

UNCLASSIFIED

AD 274 039

*Reproduced
by the*

**ARMED SERVICES TECHNICAL INFORMATION AGENCY
ARLINGTON HALL STATION
ARLINGTON 12, VIRGINIA**



UNCLASSIFIED

NOTICE: When government or other drawings, specifications or other data are used for any purpose other than in connection with a definitely related government procurement operation, the U. S. Government thereby incurs no responsibility, nor any obligation whatsoever; and the fact that the Government may have formulated, furnished, or in any way supplied the said drawings, specifications, or other data is not to be regarded by implication or otherwise as in any manner licensing the holder or any other person or corporation, or conveying any rights or permission to manufacture, use or sell any patented invention that may in any way be related thereto.

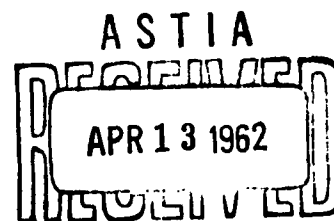
CATALOGED BY ASTIA
AS AD NO. 274039

BRL

N-62-3-1
NOX

REPORT NO. 1160
FEBRUARY 1962

PROCEEDINGS OF THE FOURTH SHOCK TUBE SYMPOSIUM
18 - 20 APRIL 1961



Sponsored by the Ballistic Research Laboratories ASTIA A

Department of the Army Project No. 503-04-002
Ordnance Management Structure Code No. 5010.11.815
BALLISTIC RESEARCH LABORATORIES



ABERDEEN PROVING GROUND, MARYLAND

ASTIA AVAILABILITY NOTICE

Qualified requestors may obtain copies of this report from ASTIA.

BALLISTIC RESEARCH LABORATORIES

REPORT NO. 1160

FEBRUARY 1962

PROCEEDINGS OF THE FOURTH SHOCK TUBE SYMPOSIUM
18 - 20 APRIL 1961

Sponsored by the Ballistic Research Laboratories

Compiled by

George D. Teel

Department of the Army Project No. 503-04-002
Ordnance Management Structure Code No. 5010.11.815

ABERDEEN PROVING GROUND, MARYLAND

FORWARD

This volume contains the papers presented at the Fourth Shock Tube Symposium which was held 18 - 20 April 1961 at the Aberdeen Proving Ground, Maryland. The Ballistic Research Laboratories was host to this affair. The previous three (3) Shock Tube Symposiums were sponsored by the Air Force Special Weapons Center, Kirtland Air Force Base, New Mexico and the proceedings are published in SWR-TM-57-2, SWR-TM-58-3 and SWR-TM-59-2.

Tuesday, Wednesday and Thursday, 18, 19 and 20 April 1961
Aberdeen Proving Ground, Maryland

PROGRAM OF THE FOURTH SHOCK TUBE SYMPOSIUM

Sponsored by
Ballistic Research Laboratories

AGENDA

Tuesday, 18 April 1961 - Moderator: James F. Moulton
US Naval Ordnance Laboratory

"Official Welcome" - Brig. Gen. John H. Weber, Commanding General
Aberdeen Proving Ground, Maryland

Col. Richard R. Entwistle, Director
Ballistic Research Laboratories

"MOL Model Nuclear Airblast Simulator"
William S. Filler, U. S. Naval Ordnance Laboratory

"The Soil Filled Shock Tube"
Andrew Thompson, Ballistic Research Laboratories

"A Shock Tube Modified to Produce Sharp-Rising Overpressures of 400
Milliseconds Duration"
D. R. Richmond, V. R. Clare, V. C. Goldizen and C. S. White,
Lovelace Foundation

"A High Explosive Operated Shock Tube with Facilities for Testing
Structures" L. O. Larsson,
Royal Swedish Fortification Corps, Stockholm, Sweden

LUNCH

Moderator: T. H. Schiffman
Armour Research Foundation

"Volume Detonation in Shock Tubes"
J. J. Swatosh and A. H. Wiedermann, Armour Research Foundation

"High Pressure Loading Device for Evaluating Blast Closure Performance"
A. H. Wiedermann, Armour Research Foundation

"Techniques for Producing Long-Duration Loads in the NCEL Blast Simulator"
S. K. Takahashi and W. A. Shaw, Naval Civil Engineering Laboratory

"ARC Heating Technique for Shock Tube Driver"
L. Y. Lamb and G. R. Russell, Aerospace Corporation

"A Diaphragm for Liquid Driven Shock Tubes"
E. Terner, Armour Research Foundation

Wednesday, 19 April 1961 - Moderator: Roman Birukoff
A.F. Special Weapons Center

"A Method for Measurement of Temperature of Air Under Nonequilibrium
Conditions"
O. L. Anderson, United Aircraft Corporation

"Centerline Gradients in Axisymmetric Ducts"
Solomon Ciolkowski, Grumman Aircraft Engr. Corporation

"Pressure and Heat-Transfer Instrumentation Used in the NOL Hypersonic
Shock Tunnels"
P. M. Aronson, U. S. Naval Ordnance Laboratory

"Pseudo Stationary Behavior of Turbulence"
Heinz Reichenbach, Ernst Mach Institut, Freiburg, Germany

"Localized Shock Velocity Measurement Techniques"
Dr. Ralph L. Haslund and Robert J. Charlson, Boeing Airplane Company

"Development of a Miniature Dynamic Pressure Gage"
Kenneth Kaplan, Broadview Research Corporation

LUNCH

Moderator: Jack Kalso
Defense Atomic Support Agency

"Aerodynamic Force and Moments Measurements in the NOL 4-Inch Hypersonic
Shock Tunnel No. 3"
David M. Bixler, U. S. Naval Ordnance Laboratory

"Measurements in the Hypersonic Shock Tunnel at the I. S. L."
Herbert Oertel, German-French Research Institut, St. Louis, France

"The Pressure Inside Open Shelters from Entering Shock Waves"
Miss Hjordis Celander, Research Institute of National Defense, Stockholm,
Sweden

"Shock Wave Decay in Tunnels"
Robert O. Clark, Ballistic Research Laboratories

"Shock Tube Blast Loadings of Scaled Model Naval Vessels"
E. V. Gallagher and T. H. Schiffman, Armour Research Foundation

Thursday, 20 April 1961 - Moderator: E. E. Minor
Ballistic Research Laboratories

"A Preliminary System for Production of High Energy Pure Gas for Hypersonic Wind Tunnel Applications"

J. E. Minardi and C. E. Pax, University of Dayton

"Study of Gas Ionizing Shocks by Streak Schlieren Methods"

G. D. Kahl and D. B. Sleator, Ballistic Research Laboratories

"Experimental Technique for Tailored Operation of a Combustion Driven Shock Tunnel"

H. Weisblatt and R. F. Flagg, AVCO Corporation

"Republic 24-Inch Hypervelocity Wind Tunnel"

Dr. Walter Martin, Republic Aviation Corporation

"A Shock Tube Facility for Real Gas Studies"

R. J. Heyman and Stewart Chapin, Martin Company

TABLE OF CONTENTS

	<u>Page</u>
"NOL Model Nuclear Airblast Simulator" by William S. Filler.....	1-23
"The Soil Filled Shock Tube" by Andrew Thompson.....	24-35
"A Shock Tube Modified to Produce Sharp-Rising Overpressures of 400 Milliseconds Duration" by D. R. Richmond, V. R. Clare, V. C. Goldizen and C. S. White.....	36-59
"A High Explosive Operated Shock Tube with Facilities for Testing Structures" by L. O. Larsson.....	60-88
"Volume Detonation in Shock Tubes" by J. J. Swatosh and A. H. Wiedermann.....	89-111
"High Pressure Loading Device for Evaluating Blast Closure Performance" by A. H. Wiedermann.....	112-130
"Techniques for Producing Long-Duration Loads in the NCEL Blast Simulator" by S. K. Takahashi and W. A. Shaw.....	131-157
"ARC Heating Technique for Shock Tube Driver" by L. Y. Lamb and G. R. Russell.....	158-183
"A Method for Measurement of Temperature of Air Under None- quilibrium Conditions" by O. L. Anderson.....	184-195
"Centerline Gradients in Axisymmetric Ducts" by Solomon Ciolkowski.....	196-210
"Pressure and Heat-Transfer Instrumentation Used in the NOL Hypersonic Shock Tunnels" by P. M. Aronson.....	211-247
"Pseudo-Stationary Behavior of Turbulence" by Heinz Reichenbach..	248-260
"Localized Shock Velocity Measurement Techniques" by Dr. Ralph L. Haslund and Robert J. Charlson.....	261-274
"Development of a Miniature Dynamic Pressure Gage" by Kenneth Kaplan	275-287
"Aerodynamic Force and Moments Measurements in the NOL 4-Inch Hypersonic Shock Tunnel No. 3" by David N. Bixler	288-304
"Measurements in the Hypersonic Shock Tunnel at the I. S. L." by Herbert Oertel.....	305-316

TABLE OF CONTENTS (continued)

	<u>Page</u>
"The Pressure Inside Open Shelters from Entering Shock Waves" by Miss Hjordis Celandar.....	317-338
"Shock Wave Decay in Tunnels" by Robert O. Clark.....	339-344
"Shock Tube Blast Loadings of Scaled Model Naval Vessels" by E. V. Gallagher and T. H. Schiffman.....	345-365
"A Preliminary System for Production of High Energy Pure Gas for Hypersonic Wind Tunnel Applications" by J. E. Minardi and C. E. Pax.....	366-375
"Study of Gas Ionizing Shocks by Streak Schlieren Methods" by G. D. Kahl and D. B. Sleator.....	376-394
"Experimental Technique for Tailored Operation of a Combustion Driven Shock Tunnel" by H. Weisblatt and R. F. Flagg.....	395-412
"Republic 24-Inch Hypervelocity Wind Tunnel" by Dr. Walter Martin	
"A Shock Tube Facility for Real Gas Studies" by R. J. Heyman and Stewart Chapin.....	413-457
"Breaking Diaphragms With Linear Shaped Charges" by Jere D. Dando.	458-470

NOL MODEL NUCLEAR BLAST SIMULATOR

William S. Filler
Explosions Research Department
U. S. Naval Ordnance Laboratory

ABSTRACT

The Naval Ordnance Laboratory has in the past year designed, constructed, and begun the evaluation of a 180-foot long, explosive-driven conical shock tube for the Bureau of Ships. The objective of this work has been to determine the feasibility of constructing a yet larger device capable of producing blast waves "in the laboratory" corresponding to those produced by full-scale nuclear explosions. An ideal charge-weight amplification of nearly 130,000 was embodied in the design of the model tube through the use of a cone angle of close to $3/5$ of one degree. The cone is 30" in diameter at the wide end. A 6", 53-caliber naval gun, its muzzle coupled to the mouth of the 180-foot cone frustum, was used to contain the high explosive detonation. Up to 5 pounds of pentolite, in the form of 1" diameter, 9" long cylinders, supported away from the gun barrel wall by styrofoam, have been fired repeatedly without plastic deformation of the gun barrel.

Excellent pressure-time records have been obtained for peak shock pressures up to the 250 psi region. Positive durations in the 20 to 50 millisecond range have been recorded. These blast-wave characteristics are identical to those from a free-air blast of approximately 75 tons of pentolite high explosive.

Details of the model cone and the test results are presented, as they apply to the design and construction of a full-scale nuclear air-blast simulator.

INTRODUCTION

A method for simulating the airblast from nuclear explosions has long been sought. Such a facility would provide a means for studying damage to structures from nuclear blasts without the complication of

radiation effects or of being restricted to a few remote areas for testing. But most important, the facility could be operated repeatedly and the obtaining of target response data would no longer be solely dependent on relatively infrequent nuclear bomb tests. (As a matter of fact, for the past two and one half years the frequency of such tests has been zero.)

The blast wave which we would like to simulate starts at the shock front with an instantaneous rise of pressure to a peak value, followed by a smooth decay in pressure lasting on the order of a second. The pressure of the peak drops from an initially high value as it moves out from the origin. The blast wave is a traveling wave which exerts a dynamic, as well as a static, pressure on objects as a result of the forward motion of the mass of air in the wave.

Several techniques have been developed in recent years for loading beams and structures with impulsive static loads that have a pressure-time configuration similar to nuclear blasts. Also, plane-wave shock tubes have been constructed which produce fairly long-duration pressure waves. Proposals have also been made for devices which employ a combination of high explosives and propellants to produce long-duration blasts in the open over limited areas. None of these techniques provide a means of simulating all the essential features of a nuclear blast wave simultaneously.

The present paper describes an explosive-driven, conical shock tube in which a small quantity of high explosive, fired under heavy confinement near the apex, produces a sector of a true spherical blast wave that has all of the characteristics of a spherical blast in the open from a much larger quantity of explosive.

The shock tube (Figure 1) is a frustum of a right circular cone 180' long. Coupled to the small end is a "retired" 6", 53-caliber Navy gun barrel of vintage 1923. Up to 5 pounds of high explosive is fired in the gun.

This facility was constructed to study and solve many of the operational and engineering problems which are involved in the application of the conical shock tube technique to full-scale nuclear blast simulation.

It was sponsored by the Bureau of Ships, Preliminary Design Branch, Ship Protection Section, for the purpose of providing a facility that would be capable of testing portions of ship structures under nuclear blast loads. It is clear, however, that Army, Air Force and Civil Defense groups could all make use of this facility for the testing of vehicles and structures above and below ground that might be subjected to nuclear blast loads.

PRINCIPLE OF OPERATION

The principle of operation of the conical shock tube is illustrated in Figure 2. Consider a sphere of explosive. After initiation at the center any sector of this sphere expands in a way that is identical to any other sector. Suppose that we were to remove a sector of this sphere of explosive and place it at the apex of a conical steel enclosure of the same angle as that of the charge. And suppose also that the walls of this enclosure extend well beyond the charge and are strong enough to withstand the detonation and blast. When the cone of explosive is initiated, it will expand within the confines of the conical enclosure in the same manner as it would if it were part of the full sphere.

The net effect is that blast characteristics of a full sphere of explosive detonated in the open is produced identically in a conical tube employing only a fraction of the amount of explosive. In fact, the fraction would be the ratio of the weight of the charge used in the conical tube to the weight of the full sphere. Or what amounts to the same thing, the ratio of the spherical angle of the cone to that of a sphere. In the remainder of this paper it will be convenient to refer to the reciprocal of this ratio, as the amplification of a conical shock tube.

If α is the plane angle of a cone then A , the amplification of the cone, is determined by dividing the spherical angle of a sphere, or 4π steradians, by the spherical angle of the cone, given in terms of the plane angle of a cone:

$$A = \frac{4\pi}{2\pi(1-\cos\alpha/2)} = \frac{2}{1-\cos\alpha/2}$$

Of course we know that there are energy losses, mainly in the firing block, that limit the attainable amplification.

Before the 180' model facility was even contemplated, a number of small conical shock tubes had been operated successfully. The most intriguing results were obtained with a 2-degree cone that was 18' long and had a theoretical amplification of 10,000. When 7.5 grams of pentolite was fired in the cone, a blast wave characteristic of 45 pounds of pentolite fired in free air was obtained -- an amplification of about 3000; and the pressure-time records were excellent. In the case of the 180' cone an angle of 637/1000 of a degree was employed. This gave a theoretical amplification of 129,600.

FIRING BLOCK DESIGN

Any explosive-driven conical shock tube has, from a design point of view, two distinct components; namely, a suitable firing block to contain and direct the high explosive detonation gas products, and an expansion tube of the required strength and uniformity. The firing block problem was novel and required special attention from the start, since practically no data of the sort needed was available. As a result of both small-scale tests at the Naval Ordnance Laboratory and the Naval Weapons Laboratory, Dahlgren, it was found that only slight plastic deformation in steel or brass resulted when a cylindrical charge was fired in a cylindrical hole three times the charge diameter. Light styrofoam was used to support the charge axially. The outer diameter could be as small as eight times the charge diameter. For example, results obtained with 1/4" diameter pentolite (2" long and weighing 4 grams) in a brass cylinder with 3/4" I.D. were very similar to results with 1 1/2" diameter pentolite (9' long and weighing 10 pounds) in a 5" gun. The I.D. of the 5" gun increased an average of 30/1000 after a single shot.

For the 180' cone the requirement was established that no plastic deformation result from repeated firings. Further tests at Dahlgren with a 6" gun (Figure 3) and a 1" diameter charge showed that this requirement

could be met. Also, hydrodynamic calculations carried out on the IBM 704 calculator predicted pressures at the wall of a 6" gun (using a 1" diameter charge) no greater than the stress capability of the gun, and these pressures lasting only for microseconds. It was on this basis, plus the fact of availability, that the 6", 53-caliber bag-loader gun was chosen.

The interrupted screw breach (Figure 4) associated with bag-loader guns has provided us with a convenient means of repeated opening, loading, and sealing of the explosion gases, thus far. The explosive loading operation consists of tying 15" long by 1" diameter cylinders of pentolite to styrofoam trays shown in Figure 4. Each cylinder weighs about 0.7 pound, so that for a full load of nearly 5 pounds, seven cylinders are pushed into position end to end, making up a total length of just less than 9". A distance of approximately 1 1/2' is maintained between the end of the charge and the breach block mushroom head. A plastic cased electric detonator is inserted in the end of the last cylinder and the leads are brought out through the breach block fuse hole.

It was decided to use the gun and mount as is. This was not only economical but greatly simplified installation, since only a stable platform was then required. Also, the train and elevation controls helped in the final alignment. Incidentally, I was told by the authorities at Dahlgren from whom we obtained the gun that these were the last of the 6" bag loaders in the Navy and that we were only 2 months ahead of the scrapping torch.

The coupling of the gun muzzle to the cone (Figure 5) was accomplished by welding an extension to the gun muzzle. This extension is free to slide in an "O" ring seal as the gun recoils. The full load recoil is only 3/16 of an inch. This seal has worked excellently. A spacer ring is provided between the gun extension and the cone end flange. When this ring is removed, the gun can be swung in train for maintenance purposes.

CONE DESIGN

Now, passing on to the shock tube proper, the right circular cone shape provides maximum strength in the radial direction. However, any cross-section shape could be used, provided it is the same throughout the length of the cone. For shock diffraction studies, a semi circular shape against a solid surface would be more convenient and make for better utilization of the working area

The shock pressure load requirement ranges from 2000 psi at the junction point with the gun where the cone is 6" in diameter, down to 200 psi at the far end where the cone is 30" in diameter. This is shown in Figure 6. Design loads were increased above "normal" at the far end to allow for the higher shock pressures resulting from reflection from the door when this was closed. Since no significant unbalanced lateral forces are involved, the entire cone (Figure 7) is mounted simply on a wide flange I-beam to provide rigidity.

The cone was made by the Bethlehem Steel Company in Baltimore. It was fabricated in three 60' sections and assembled at the NOL site. The taper of the cone was chosen, for manufacturing convenience, to be a round number - 1" diameter increase per 7.5' of length. This is how the odd angle for the cone of 637/1000 of a degree came about. The cone sections vary in wall thickness. The first section next to the gun is 3/4" thick, the middle section, 3/8", and the last section, 1/2". The door at the far end, when closed, prevents the blast from escaping, and nearly complete muffling of the blast results. A noise no louder than a rifle report is heard in the vicinity of the cone, even when a full 5-pound load of high explosives is fired.

MEASUREMENTS AND RESULTS

Gauge ports (Figure 8) are located at 120 and 180' from the imaginary geometrical cone apex corresponding to the spherical charge center. These distances are the true distances which must be used for blast performance evaluation, although the 26.5' long gun barrel replaces the first 45' of the geometrical cone. The gauge port plugs (Figure 9) were shaped to match the curvature of the inside of the cone. Piezoelectric gauges at the wall surface and in the flow were used to detect pressures.

The support for the pencil gauge in the flow proved inadequate for the larger loads and, on the first 3.45-pound shot, were bent, and the gauges were torn from the mounts. Only data from flush, wall gauges is reported here, although the few pencil gauge values obtained so far agreed well with the wall gauge values. Pressure-time records obtained with this instrumentation are shown in Figure 10.

A substantial body of data has been collected for 0.69-pound loads; also some data has been obtained for shots with 1.38-, 3.45-, and 4.83-pound loads. To show the reproducibility of the data, the table (Figure 11) lists the peak pressure and positive duration results for the 0.69-pound shots at the 180° port. By scaling all peak pressure data to 4.83 pounds, all data collected to date could be smoothed on a single peak pressure distance curve and compared with the standard peak pressure reduced distance curve for pentolite. This is shown in Figure 12. The equivalent weight was calculated from the scaling relation $R : W^{1/3}$ for constant pressure. This came out to be very nearly 150,000 pounds or about 75 tons. An efficiency of nearly 24% is indicated. These results are summarized in Figure 13.

To evaluate positive duration data, standard high explosive and nuclear data were scaled to the simulated weight of charge produced from the cone peak pressure data. The lower part of Figure 13 shows how the scaled data compare with the measured data from the cone. No significance should be attached to the degree of agreement or disagreement shown here, since the spread in most positive duration data, as well as the lack of agreement between data from various workers, is very great. The question of how closely the tube duration data agrees with free air duration results must inevitably be answered in ball-park terms. In this sense the 180° cone looks rather good.

For the full load shots, high temperatures exist behind the shock front as the blast passes the gauge station. These may have caused an error due to temperature sensitivity of piezoelectric materials, making the positive durations shorter than they may in fact have been. This is especially true for the closest gauge when exposed to peak shock pressures of hundreds of psi. For this reason such data was not included here. Efforts in the future will be directed to increase the thermal insulation of the gauges.

In regard to possible non-uniform flow due to wall effects, it should be remembered that at any given point in the cone the boundary layer takes time to develop as the shock wave passes. The pressure of the shock front recorded by the wall gauge is that of the actual shock flow before boundary layer development. Losses to the boundary, however, must eventually affect the entire shock wave.

In the near future additional data will be obtained in the 180' cone with pencil gauges in the flow and with dynamic pressure gauges developed by Broadview Research Corporation. A paper dealing with these gauges by Ken Kaplan of Broadview is included in this document.

FULL-SCALE FACILITY

The purpose of this work, as was stated earlier, is to facilitate the design of a nuclear blast simulation facility. In what follows I will discuss the blast, dimensional, and operational requirements of such a facility, and the configurations of conical shock tubes which can meet such requirements.

The blast wave in air from a nuclear weapon has a characteristically long duration in its positive pressure phase. At a distance of 1/2 mile from a 20-KT free-air explosion the positive duration is about 1/3 of a second. Megaton blasts have positive durations on the order of seconds. Megaton blasts greatly extend the damage radius compared with kiloton blasts, but this is due mainly to the maintenance of higher blast pressure levels out to greater distances. Few targets, to be defeated, require the extremely long durations of megaton blasts. Thus, a nuclear simulation facility that can generate a blast wave comparable to a 20-KT blast will meet the needs of the vast majority of target response problems. Since the conical shock tube in its basic form, must extend out to the distance at which desired blast characteristics would be found from a full-sized open blast, a cone length on the order of 2000' would seem to be adequate.

Next, we must consider target size requirements. A target located in a conical shock tube can probably occupy $1/3$ to $1/2$ the cross-section area of the cone without serious wall interaction effects. The greater the cross-section area of the test region at a given distance along the tube, however, the lower the cone amplification.

This is a major consideration in determining the general cone configurations having semicircular cross sections and diameters of 25 and 75'. For the 25' diameter semicircle, a 1000-pound quantity of high explosive will have to be fired to achieve the desired effect. A practical firing block could be made up from surplus 16" gun barrels presently available at Dahlgren. The heavy initial lengths of three guns secured together to make a 100' long tube would be adequate for this purpose, according to our firing block scaling information. For a simulated 6- or 7-KT blast, a single unmodified 16"-gun barrel would serve the purpose admirably. This summer at Dahlgren, firing tests are planned with a 16"-gun barrel.

If a 75' diameter semicircle is required as a working space for a 20-KT blast, this can be obtained by using 10,000 pounds of high explosive in a firing chamber. For a 100' length of charge, as above, a three-fold increase in firing block inner diameter is required, or about a 5' hole size. In place of modified surplus gun barrels, fabrication of the entire firing block would be required.

Mechanical design of the cone proper is a straightforward problem, using scaled blast loads and the design experience gained with the 180' cone.

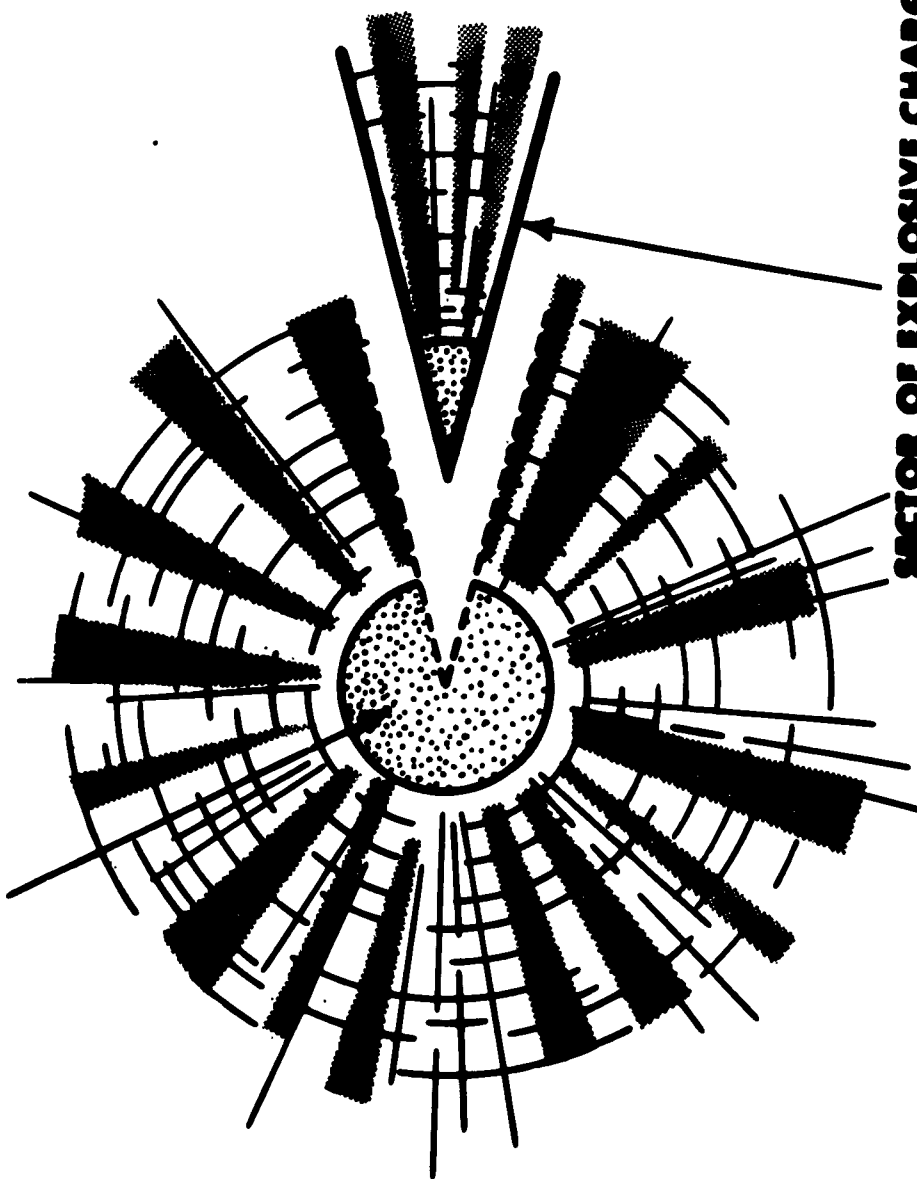
SUMMARY

In summary, a model nuclear blast simulation facility employing the conical shock tube technique has been constructed and operated. It produces a 75-ton blast wave with 5 pounds of explosive as the driving means. The successful solution of many of the engineering and operating

problems of this 180' facility indicates the feasibility of constructing and operating a 20-KT blast simulation facility. Such a facility would be on the order of 2000' long, use a 1000 pound driving charge and would have a working space in the form of a 25' diameter semicircle. A 10,000 pound driving charge would provide a 75' diameter semicircular working space.



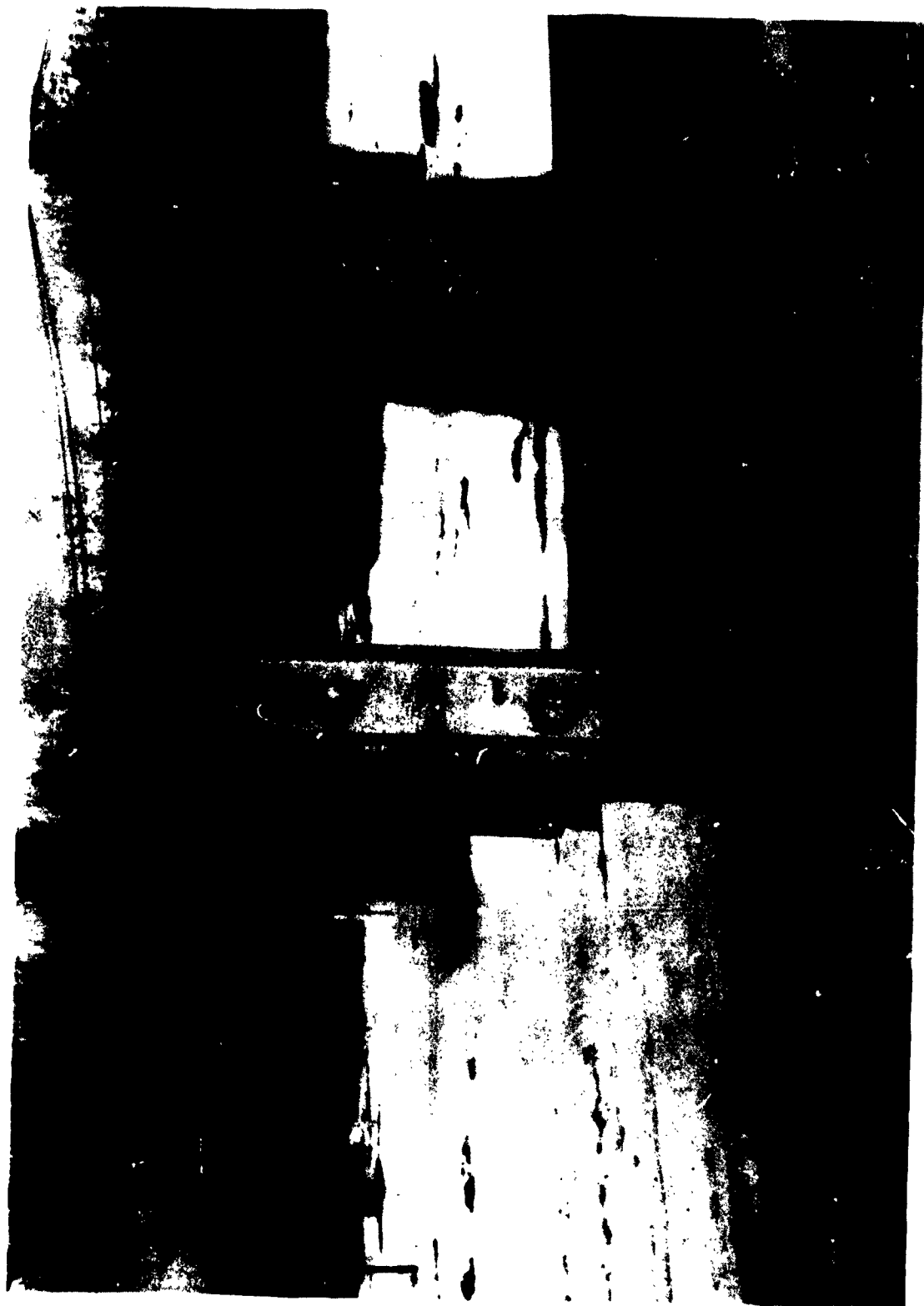
EXPLOSIVE CHARGE FIRED IN AIR

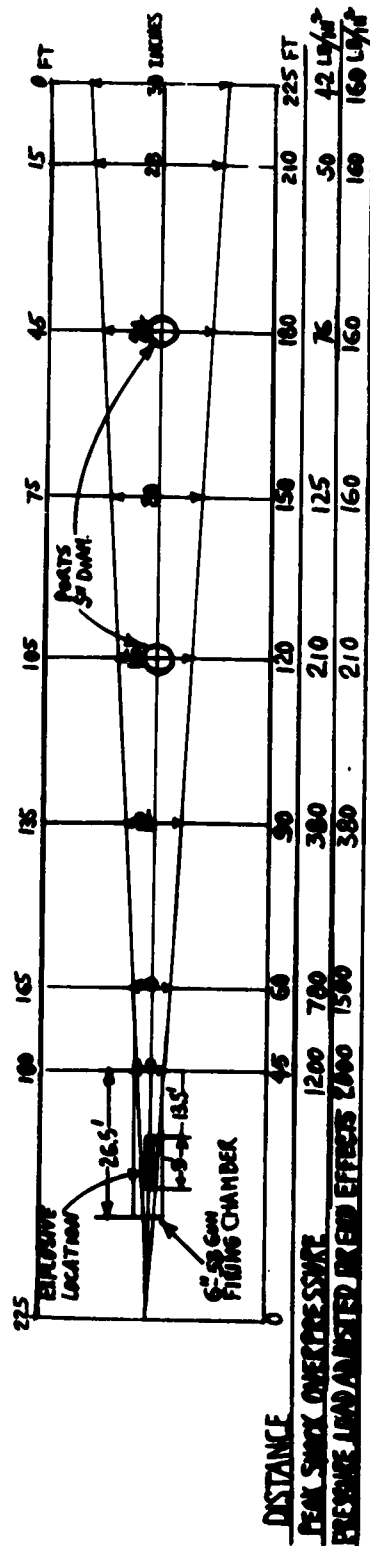


**SECTOR OF EXPLOSIVE CHARGE
WHEN FIRED IN CONE PRODUCES
EQUIVALENT BLAST WAVE**



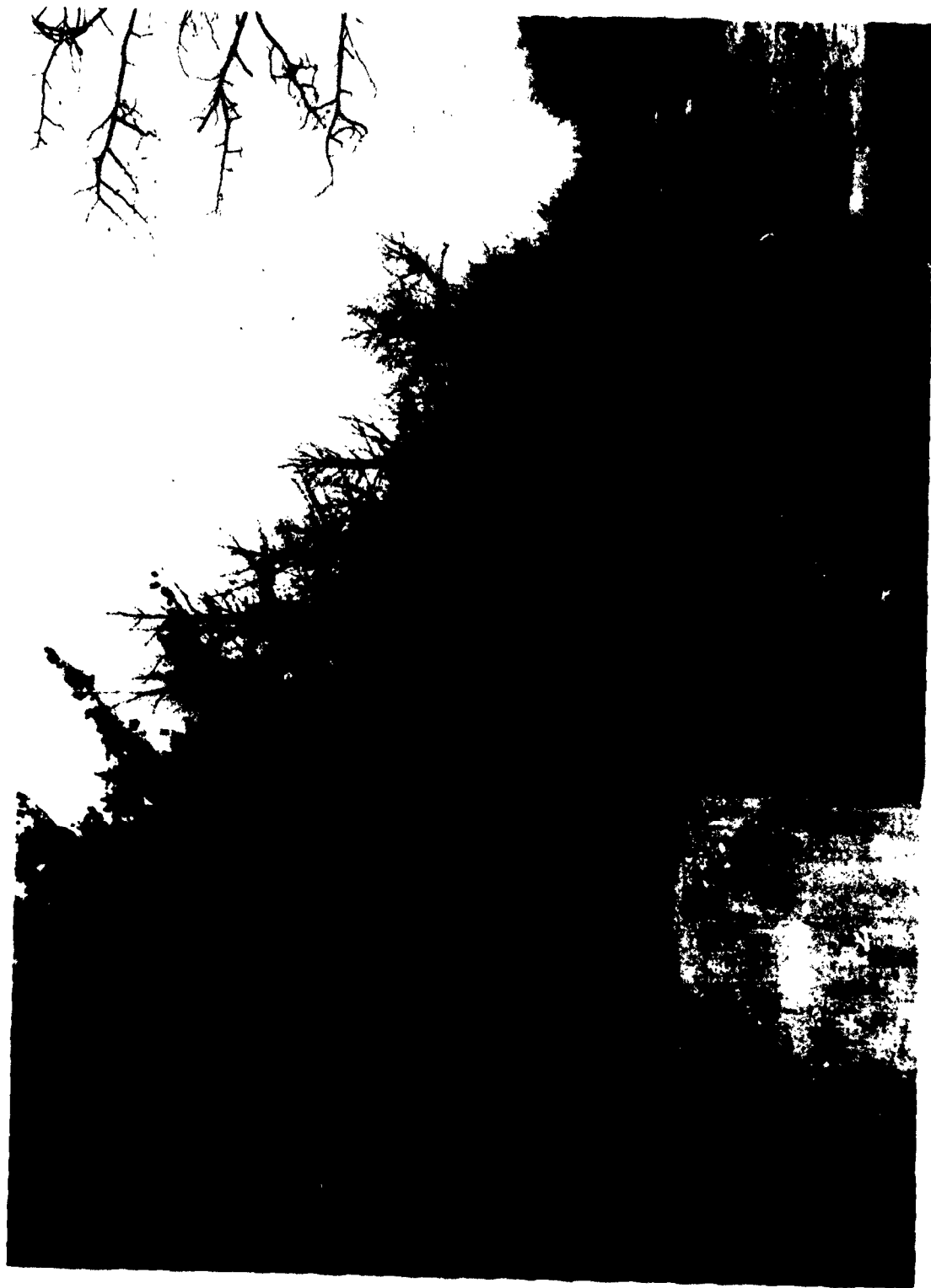






LENGTH SCALE - 20 FEET/1-INCH
HEIGHT SCALE - 2 FEET/1-INCH

100 FOOT CONICAL SHOCK TUBE DESIGN SPECIFICATION SKETCH







PRESSURE-TIME RECORDS FROM 180 FT CONE

DISTANCE FT	PEAK PRESSURE PSI	POSITIVE DURATION MSEC
120	64.3	22.6
180	27.1	42.3
120	246.5	15.1
180	66.9	38.5



1.38 LB PENTOLITE



10 MSEC TIMING INTERVALS



4.83 LB PENTOLITE

TYPICAL DATA

CHARGE WEIGHT - 0.69 LB.

DISTANCE - 180 FEET

PEAK PRESSURE

18.5

19.1

16.4

17.1

17.4

17.6

AVG. 17.7 lb/in²

POSITIVE DURATION

44.1

54.1

50.7

44.1

58.8

-

AVG. 50.4 msec.

**1-LB PENTOLITE
IN FREE AIR**

**5-LB PENTOLITE
IN 180 FT CONE**

- DATA OBTAINED AT 120 FT STATION
- x DATA OBTAINED AT 180 FT STATION

**NOTE: AVERAGE DATA FOR 0.69, 1.38,
3.45 & 4.83-LB SHOTS COMBINED
IN ONE CURVE BY SCALING ALL
DATA UP TO 4.83 LB.**

P (LB/IN²)

R (FEET)

EFFICIENCY BASED ON PEAK PRESSURE EQUIVALENT WEIGHT

DESIGN AMPLIFICATION	CHARGE WEIGHT	CHARGE WEIGHT SIMULATED	AMPLIFICATION	EFFICIENCY
129,600	4.83 lb.	148,000 lb.	30,700	23.7 %
DURATION OF POSITIVE PHASE				
DISTANCE MEASURED IN 180 FT. CONE SCALED FROM HE SCALED FROM 1 KT NUCLEAR			180 FEET 50.4 MSEC. 34.4 52.9	

THE SOIL FILLED SHOCK TUBE

A. A. Thompson
Ballistic Research Laboratories

Here at the Ballistic Research Laboratories some experiments are being conducted to test the feasibility of soil filled shock tubes. This work was stimulated from a need to simulate and study seismic waves of various shapes that would be present close to a nuclear explosion. Also, of course, there is a need to study plane wave propagation, where the particle motion is only in the direction of propagation.

The largest diameter earth shock tube presently at Ballistic Research Laboratories, is three feet, and the length is 6 feet. The tube is buried in a vertical position, and open at the bottom to a sand clay mixture.

Movement of the tube is minimized by concrete which surrounds and is an integral part of the tube.

A stainless steel sheet lines the inside of the tube. The shock wave of the desired shape is generated by a powerful thruster. This shock wave, transmitted to the sand column, is produced by an explosive located in a closed chamber above a steel piston resting on a steel plate on top of the sand column.

A series of experiments was conducted to test the tube, the loading mechanism, and the measuring techniques in the sand column at stresses up to 500 psi. The resulting records are being analyzed to determine the dynamic stress-strain relations, the shape of the wave front, the attenuation, and the reflections of the wave progressing through the confined soil column.

In addition an attempt is being made to determine the effect of friction, at the tube sidewalls, on the wave shape and the effect of this friction on the wave front. In the future, instrumented structures will be placed in the tube to study soil structure interaction and the criteria for damage to buried structures.

The attempt to get high stresses and accelerations of long durations for simulation purposes was more successful than expected, and consequently, gages have been prepared to measure stresses of over 1000 psi. and accelerations of over 1000 g. The peak value of stress that can be simulated for study is presently limited by the gage capabilities and the strength of the shock tube wall, rather than the loading technique. Following are some results which illustrate the type of measurements being obtained and analyzed.

A diagram of the gage positions for Shots 4 and 5 is given in Figure 1.

The one inch thick steel plate, used at the top of the sand column as the plane wave source shown in Figure 1, was deformed during Shot 5. It has been replaced by a four - inch thick plate that should not be deformed by the 1,000,000 pound loads being applied.

Figure 2 gives the stress, acceleration and particle velocity at 3" from the source on Shot 5. Here is shown a peak stress of 500 psi. falling rapidly to 300 psi. where it stays fairly constant. The peak accelerations are 300 g. and fall rapidly, and the peak particle velocities are 20 ft. per sec and fall not so rapidly. This sequence is similar to the seismic measurements measured close to the earth surface during the passage of an intense air wave resulting from a large explosion. The next figure gives us these same measurements at 27" from the plane wave source, or only 2 feet from these first measurements. The peak stresses have dropped from 500 to 300 psi. and spread out. The accelerations have dropped from 300 g. to 30 g. or a 10 times decrease in a distance of 2 feet and the initial positive acceleration phase has spread out in duration. The velocities have dropped from 20 to 6 ft. per second. These measurements show large attenuations and changes of wave shape occurring close to the plane wave source, that are characteristic of how the air induced wave from large explosions are attenuated with depth from the surface in a sandy medium.

The second stress peak, which is easily seen in Figure 3 is a reflection from the bottom of the tube. Although the tube is open at the bottom, an effective increase in acoustic impedance is present where the sand is no longer confined in the tube. This type of reflection may be unexpected, since, for an air shock tube, where the wave diverges at the end of the tube, a rarefaction or negative wave would be reflected back up the tube instead of the positive reflected wave actually measured in our sand filled shock tube. Possible means of eliminating this reflection shown in Figure 3, will be explored. The most obvious means, of course, would be to increase the tube's length.

Figure 4 gives the stress-strain curve for shots 4 and 5. The large area between the loading and unloading curves shows the extremely plastic nature of the propagation, and gives a measure of energy loss or soil hysteresis during the passage of the wave. Accordingly, it can be understood why such large attenuations were observed in Figures 2 and 3, showing the seismic measurements at two distances from the source.

Since the sand for Shot 5 was a great deal more compacted than for Shot 4, Figure 4 suggests that the dynamic bulk modulus for stresses over 20 psi. increases appreciably with degree of compaction. It can be shown that this bulk modulus is related to the slope of the stress-strain curve determined in the soil shock tube. It can also be shown that the propagation velocity can be related to the slope of the stress-strain curve by:

$$C^2 = \frac{1}{\rho} \frac{dp}{de} \quad (1)$$

Where C = propagation velocity

ρ = density

p = stress

e = strain

For the first arrivals, measured values of C were about 600 feet per sec. on both Shots 4 and 5. For the first power peak (as defined by PV , where V = particle velocity) measured values of C were 138 feet per second for Shot 4 and 250 feet per second for Shot 5. Using equation (1) above, the slope of the stress-strain curve was calculated for these three velocities. The slopes are also plotted in Figure 2 for comparison. The rough agreement between the calculated and measured stress-strain slopes allow confidence in the measurements, in view of the considerable probable errors expected. The larger slopes measured for Shot 5 are due to previous compaction (or simulated depth below the surface), and to higher applied rates of stress. More experiments are planned to separate the effects of these two causes.

To measure attenuation of the wave traveling down the tube, the total work, E , done on any unit imaginary surface in the medium perpendicular to the path of seismic wave propagation, has been calculated at various distances from the plane wave source. This calculation has been accomplished by the formula:

$$E = \int_0^t PV \, dt^*$$

where P = radial stress

V = radial particle velocity

and t = time

Figure 5 shows E plotted against distance (r) from the plane wave source for Shot 5. The attenuation of energy in the direction of propagation is represented by the slope of this energy-distance curve $\left(\frac{dE}{dr}\right)$. If all measurements are made in the direction of propagation, it is normally assumed that the area under the dynamic stress-strain curve can be used, within limits, to estimate the attenuation.

* See page 8 of BRL Memorandum Report No. 1267.

Accordingly the area under the stress-strain curve for Shot 5 has been integrated to estimate the attenuation. In Figure 5, at one point on the E vs r curve, a slope, derived from the area under the dynamic stress-strain curve at this value of r , is plotted for comparison. Since the stress-strain measurements were made at the edge of the tube, the slope, derived is plotted on the E vs r curve determined near the edge of the tube. In this case, the attenuation as determined by the stress-strain curve hysteresis loop agrees reasonably well with that determined from the E vs r curve. In Figure 5, the values of E measured at the tube center are usually greater than the value of E measured near the tube edge. This difference in E results from the effects of friction at the tube sidewalls, as discussed earlier in the paper.

Although a smooth stainless steel liner is used inside the shock tube to reduce friction, the recent experiments have shown some friction still exists, and therefore more effort is required. This fact had been anticipated, and work has been contracted that includes finding adequate methods of friction reduction. The Atlantic Research Corp. has experimented with a number of methods of reducing wall-friction. The most successful consisted of a layer of Teflon powder inserted between the soil column and the polished surface of the confining tube. By this means, the wall-friction has been reduced, to about 10% of the value observed without the lubricating layer. It may be possible to find a substitute for the expensive polished metal surface and Teflon powder. The adequacy of this system for reducing wall friction has not yet been demonstrated in dynamic tests. Such dynamic tests have been planned at the Atlantic Test Station using a one foot diameter tube so that several accelerometers placed at different locations with respect to the wall, could be used simultaneously. The Atlantic Research, Hyge Shock Tester will apply a force to the soil surface in this tube. A diagram of this planned set up is shown in Figure 6. The force applied can rise to a maximum in a few milliseconds and maintain that value approximately

constant for 30 milliseconds or longer, depending on the stress wave shape desired. The Hyge Shock Tester shown at the top in this figure can produce a thrust of 40,000 pounds. The 10-foot long shock tube, whose inside diameter is 10-in. is securely fastened to the concrete foundation by means of two 8-inch structural channels straddling the 3-foot diameter hole. To minimize reflections, it is intended to fill the bottom of the 3-foot diameter hole with sand to a depth of 4 feet below the end of the shock tube not shown in this figure. Experiments will be run in the instrumented tube both with and without the Teflon powder. The information obtained should supply needed information for the earth shock tube experiments being conducted at Ballistic Research Laboratories.

A need for better control of the wave shape being generated in the 3-foot diameter ERL shock tube has become apparent from past experiments. Steps have been taken to improve this control. It is anticipated that stress waves of any desired shape will be producible. There will probably be several changes necessary before the earth shock tube takes its final form. Such a facility should supply information strongly needed in plane wave propagation studies, also the facility should increase the effectiveness of Army Ordnance to destroy buried structures.

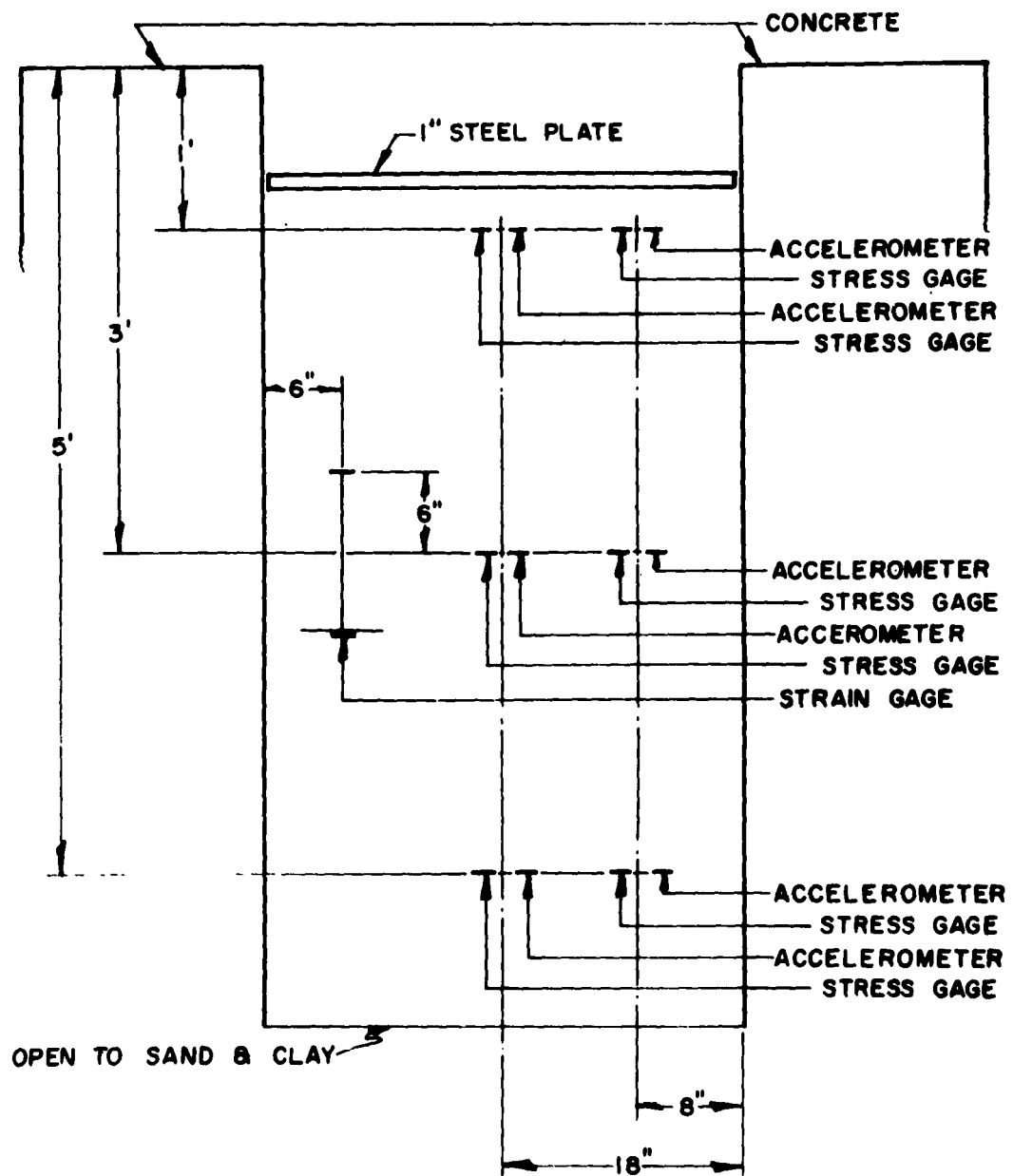


FIG. 1-GAGE POSITIONS IN SAND FILLED SHOCK TUBE

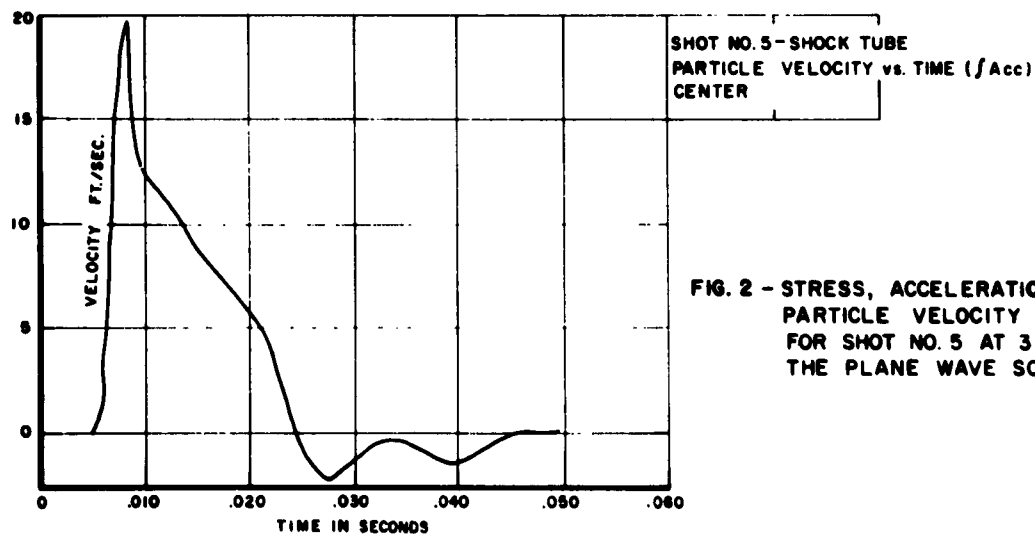
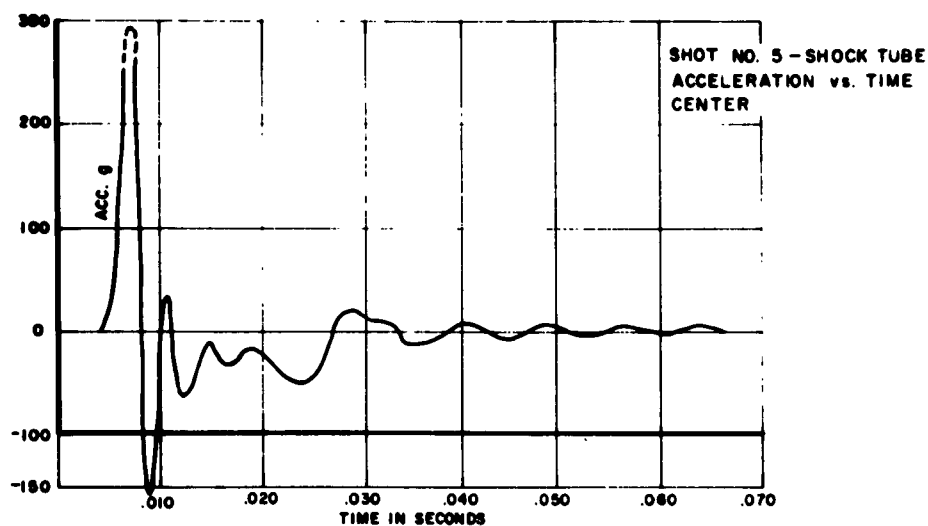
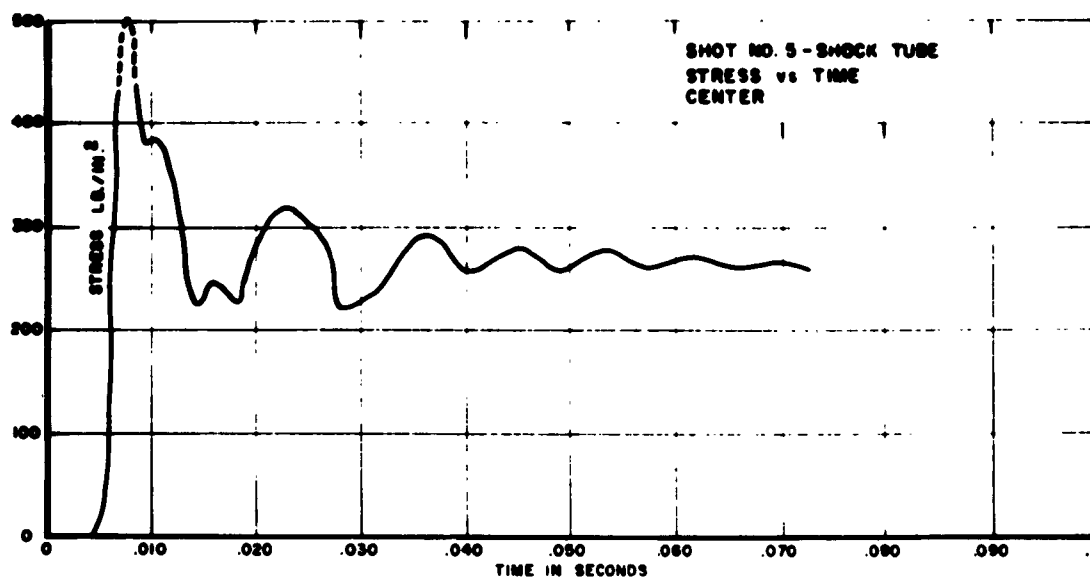


FIG. 2 - STRESS, ACCELERATION, AND
PARTICLE VELOCITY vs. TIME
FOR SHOT NO. 5 AT 3" FROM
THE PLANE WAVE SOURCE

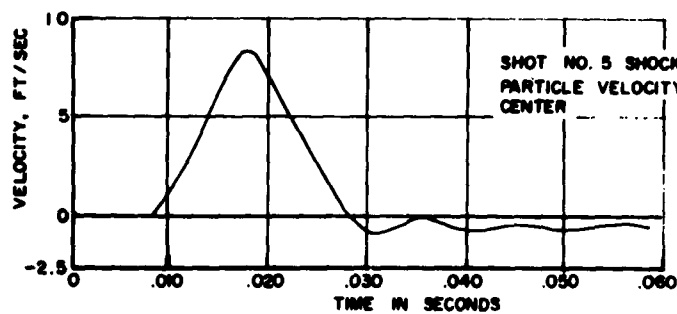
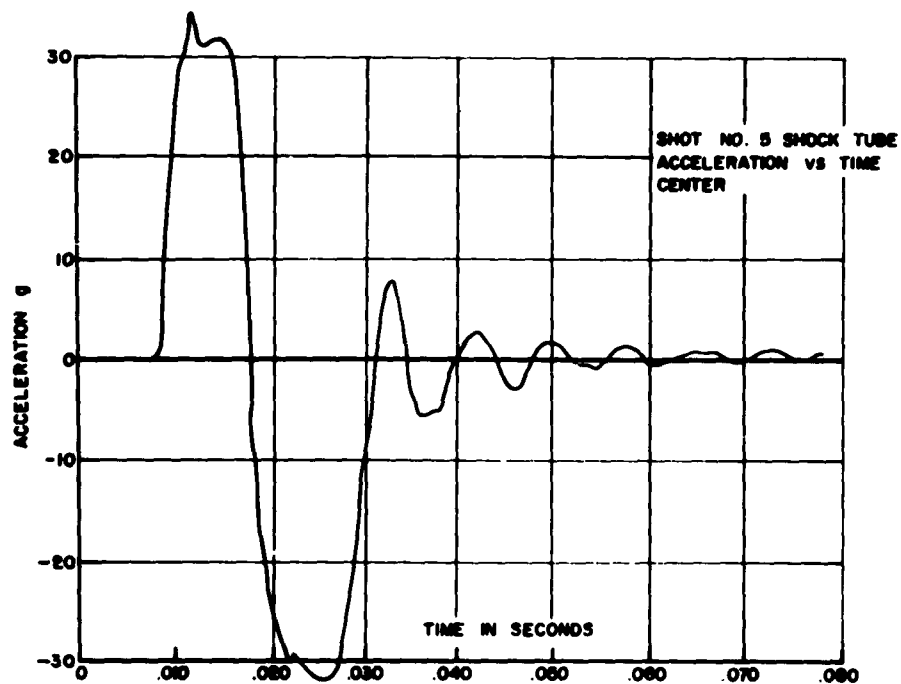
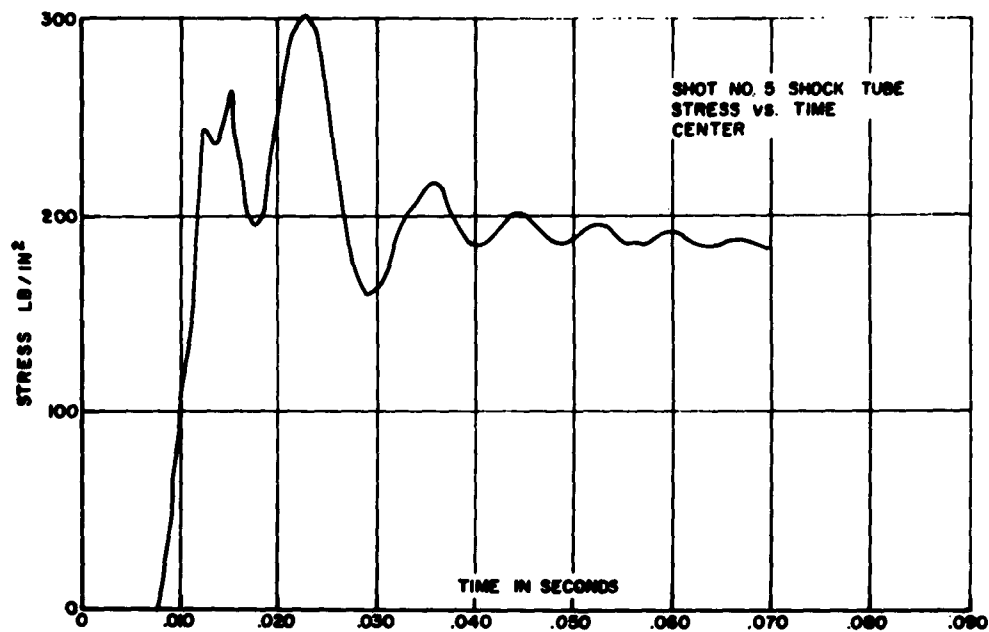
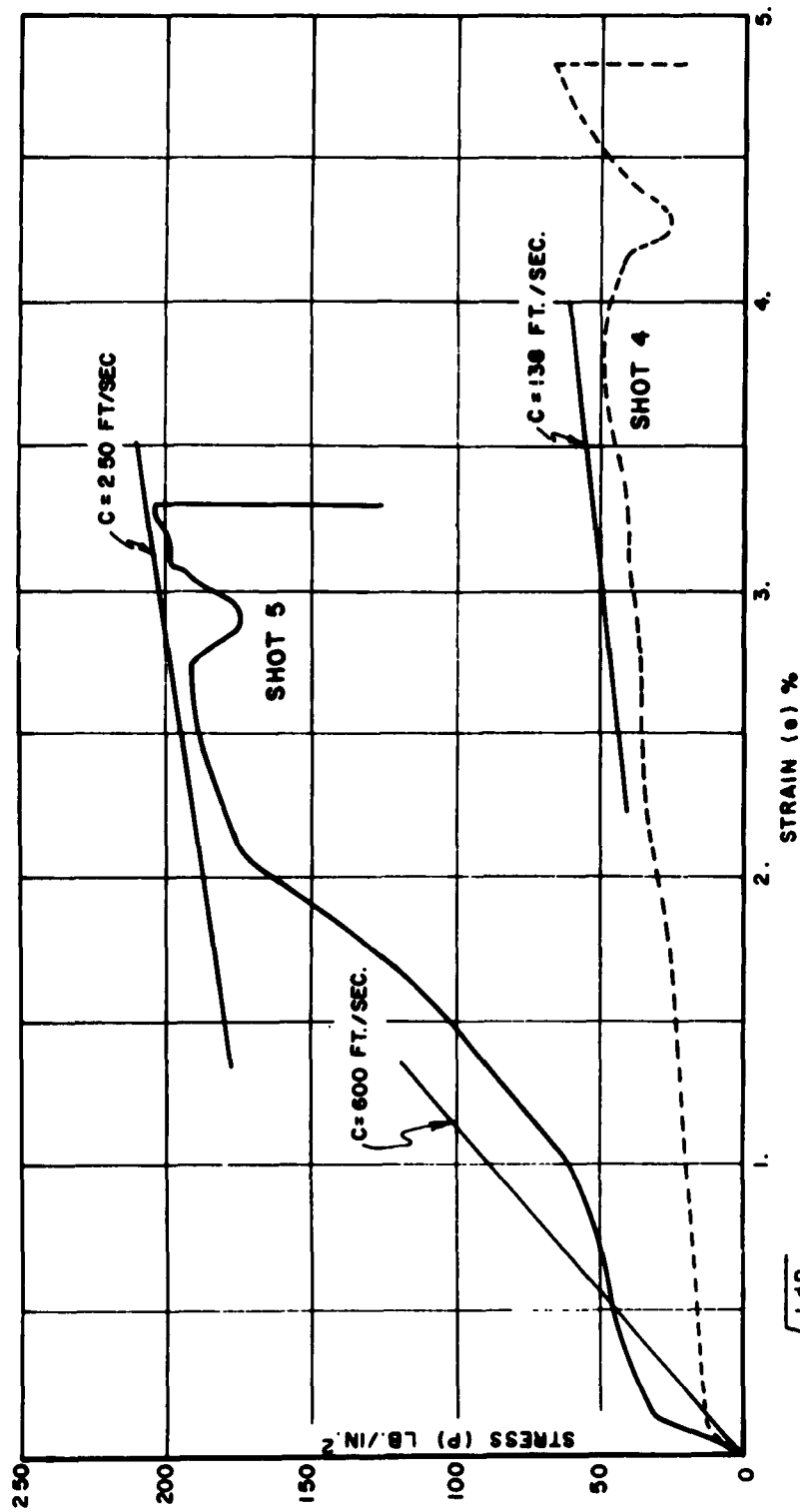


FIG. 3-STRESS, ACCELERATION AND
PARTICLE VELOCITY VS TIME FOR
SHOT NO 5 AT 27" FROM THE CENTER
OF THE PLANE WAVE SOURCE.



$$C = \sqrt{\frac{1}{\rho} \frac{dP}{de}}$$

WHERE:

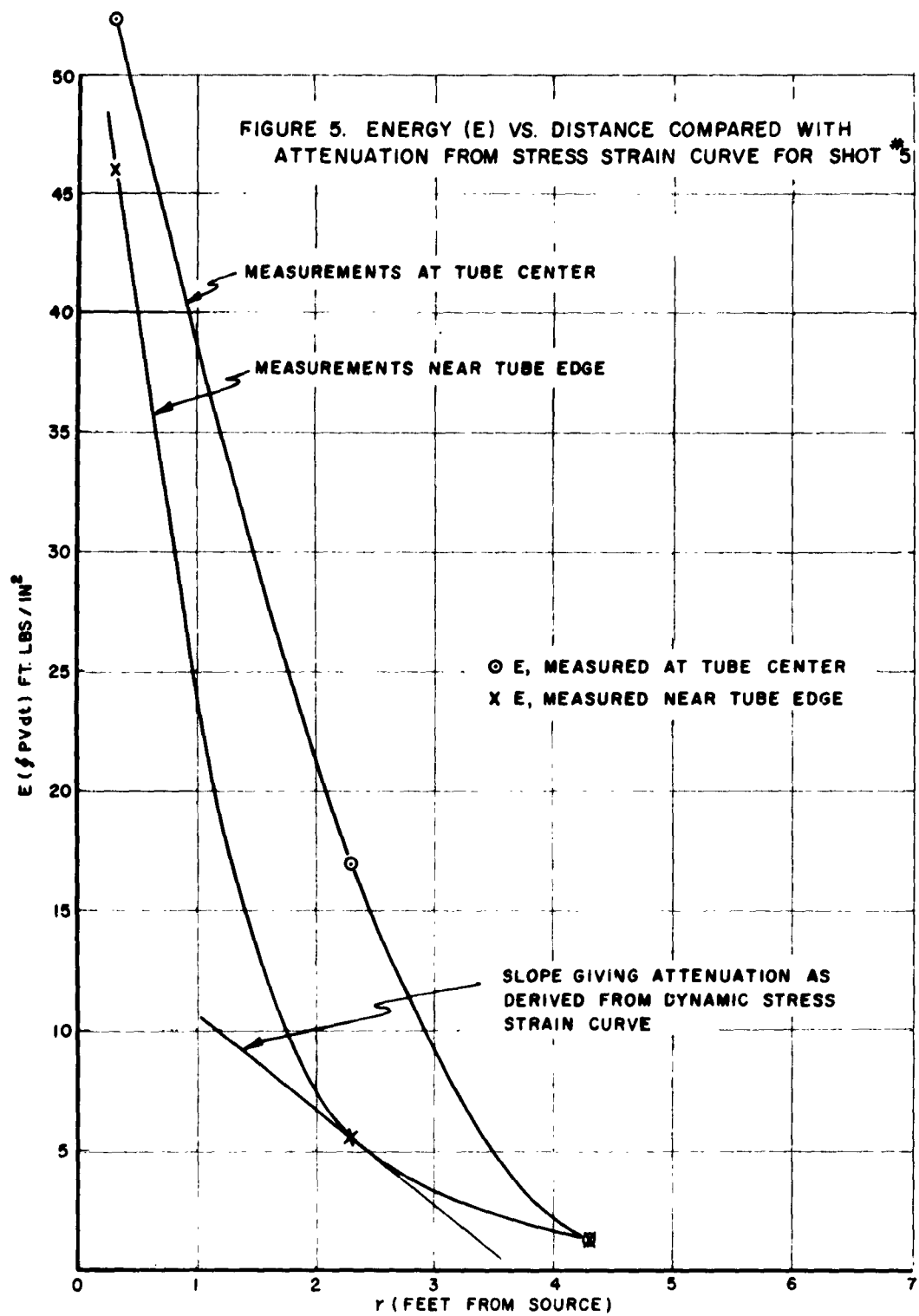
C = PROPAGATION VELOCITY

ρ = DENSITY

P = STRESS

e = STRAIN

FIG. 4 - DYNAMIC STRESS vs. STRAIN CURVE FOR SHOT NO. 4 AND NO. 5 MEASURED AT 27" FROM THE SOURCE NEAR THE EDGE OF THE TUBE, WITH THE SLOPE OF THE STRESS-STRAIN CURVE CALCULATED FROM THREE MEASURED PROPOGATION VELOCITIES AND DENSITIES.



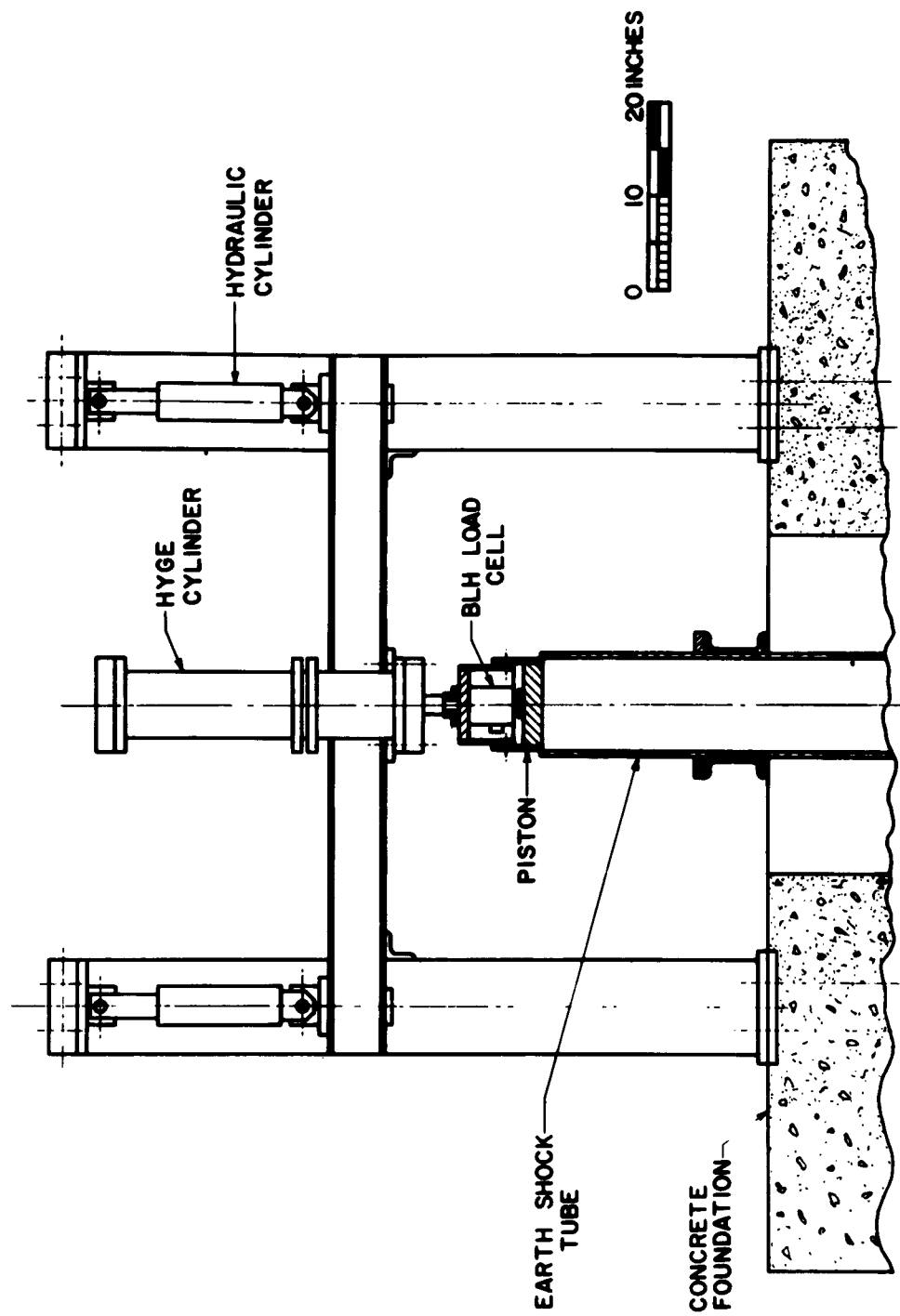


FIG. 6. HYGE SYSTEM FOR SOIL SHOCK TUBE PROGRAM

A SHOCK TUBE UTILIZED TO PRODUCE SHARP-RISING OVERPRESSURES OF
400 MILLISECONDS DURATION AND ITS EMPLOYMENT IN
BIOMEDICAL EXPERIMENTATION

D. R. Richmond
V. R. Clare
V. C. Goldizen
D. E. Pratt
R. T. Sanchez
C. S. White

Lovelace Foundation for Medical Education and Research

ABSTRACT

A shock tube employed for blast biology studies is described along with the results of one series of experiments.

The shock tube is air-driven and utilizes Mylar plastic diaphragms. The compression chamber is 17.5 ft in length and 40.5 in. I.D.; it reduces in diameter to 23.5 in. over a 3-ft-long transition section just upstream of the diaphragm station. The expansion chamber consists of 30 ft of 23.5 in. I.D. tubing followed by 22 ft of 40.5 in. I.D. tubing. It is closed distally by a steel end-plate to generate high pressures from the reflected shock. Three vents in the expansion side of the system serve to control the duration of the overpressure and to eliminate multiple reflections by bleeding off the reflected shock as it travels upstream.

An interspecies correlation is presented based on mortality data from six species of experimental animals with an extrapolation to a 70 kg animal.

INTRODUCTION

The shock tube has proven to be a valuable tool in studying the biological effects of air blast⁽¹⁻⁵⁾. By appropriate modifications, the device can be made to generate a wide variety of wave forms some of which closely resemble those recorded inside structures exposed to full-scale nuclear detonations^(6,7). The capability of creating and

reproducing at will a desired variation in environmental pressure has made it possible to initiate comparative interspecies experimentation without which there can be no clear understanding of hazardous and non-hazardous wave forms. In this light, it is well to emphasize that the air-driven shock tube has an unusual versatility and offers many other advantages. For example, it has become possible to achieve the precision in performance that is quite critical for biological experimentation. Too, with proper care, there need be no complications due to secondary missiles, hot gases, and toxic fumes which often plague explosive-driven tubes. Finally, pressure-time recording instruments, as well as those employed to monitor pathophysiological processes, can be mounted just outside the test chamber in close proximity to the animal under study.

It is well now to turn to the two main purposes of this paper; namely, first to describe a shock tube assembled to produce single pressure pulses that rise almost instantaneously to a maximum and endure for about 400 msec, which is a wave form quite comparable to those produced under certain circumstances by nuclear detonations; and second, to present mortality data on six species of animals all exposed in a similar geometry to similar pressure-time phenomena that varied among the species mostly with respect to the magnitude of the overpressure.

METHODS

Geometry of the Shock Tube

Figure 1 presents a diagram of the blast tube. The over-all length is approximately 70 ft. The compression chamber measures 17 ft 5 in. and has an internal diameter of 40.5 in. The driver reduces in diameter from 40.5 in. to 23.5 in. over a 3-ft long transition section at its diaphragm end. The expansion chamber is 53 ft 4 in. in length, of which 30 ft is 23.5 in. I.D. tubing followed by 22 ft of 40.5 in. I.D. tubing. The increase in diameter of the expansion chamber from 23.5 in. to 40.5 in. occurs rather abruptly over a span of little over 1 ft.

As noted in Figure 1, the driver is stationary since it is "nested" in a massive reinforced concrete back-stop. Consequently, the various components on the expansion side are on casters to facilitate diaphragm replacement. The end of the tube is closed by a 2-in. thick steel plate - the end-plate.

Three vents, each 10x14x8 in., are located at the upstream end of the 40.5 in. tubing of the expansion chamber. These vents serve to "tailor" the wave form and will be discussed later.

The diaphragms employed are 40x40 in. sheets of polyester plastic film (Dupont Mylar). They have holes pre-drilled to match the bolt holes in the flanges. For their insertion they are simply bolted between the appropriate flanges. Mylar sheets of 0.010 and 0.0075 in. thickness are employed, a predetermined number being used to hold a given pressure in the driver section.

Diaphragms are ruptured by lead pellets from a sawed-off 12-gauge shotgun mounted on the tube. The gun fires straight down through the tube, through holes appropriately placed in the top and bottom of the tube. The diaphragms under pressure obligingly bow-out in the path of the shotgun blast. Since the shot passes out of the tube through the vent in the under side, it is not carried downstream where it might interfere with the test.

Photographic views taken of the blast tube are presented in Figures 2,3 and 4. As seen in Figure 3 access into the end of the tube, for animal placement, is accomplished by separating the tube at the distal most 24 in. flanges.

The shack seen near the end-plate houses the pressure-time recording instruments and the equipment necessary to operate the shock tube.

Instrumentation

In these particular experiments pressure-time variations were measured by Quartz piezo-electric gauges (Model 401)* that were shock mounted flush with the inside of the tube. Gauges were routinely placed at the end-plate and at short distances upstream from the end-plate. The signal from a gauge was fed through low noise cable with an amplifier-calibrator* into

* Purchased from Kistler Instrument Corporation, North Tonawanda, N.Y.

an oscilloscope (Tektronix Model 535A) having a Type L or Type 53/54C pre-amplifier plug-in unit. This oscilloscope has a single sweep circuit which prevented retriggering after the desired trace was recorded.

In using the oscilloscope, the horizontal sweep was externally triggered by the signal from another "trigger gauge" of Barium Titanate* located just upstream of the recording gauge. Pre-triggering the sweep allowed a reference trace of base line to be photographed during the time the shock travelled from the "trigger gauge" to the recording gauge. To insure sufficient voltage to trigger reliably the oscilloscope sweep, the signal from the trigger gauge was amplified. A power supply (Type 105) with amplifiers* (Type 104A) was used for that purpose.

The sweep on the face of the oscilloscope was photographed for the permanent pressure-time record with a Polaroid Land Camera mounted in a periscope assembly. The components that make up a channel of instrumentation are shown in Figure 5. Available at present are 8 channels of pressure-time measuring gear plus three channels for monitoring the pressures within biological systems.

Calibration of Gauges

The quartz piezo-electric gauges were statically calibrated using a small pressure vessel. Their dynamic performance was also checked on a 12-in. - diameter calibration shock tube. Barium titanate and lead zirconate crystal gauges were calibrated on the calibration shock tube by measuring their voltage out-put at various shock pressures. The latter were computed from measuring the speed of the shock with a Hewlett-Packard Electronic Counter that was started and stopped by gauges placed 18 in. apart.

Biological Material

Table 1 summarizes the number of animals from each of the 6 different species that were employed in this study, along with their body weights and ages. Of the total of 569 animals, 140 were mice;

* Purchased from Atlantic Research Corporation, Alexandria, Va.

TABLE 1
ANIMALS USED IN THIS STUDY

Species	Number of animals	Body weight	Age, months
Mouse (Webster strain)	140	22 g \pm 1.9*	1 - 1-1/2
Rat (Sprague-Dawley)	164	192 g \pm 25	2 - 2-1/2
Guinea pig (English short haired)	96	445 g \pm 37	3-1/2 - 4
Rabbit (New Zealand White)	104	1.97 kg \pm 0.26	2-1/2 - 3
Dog (Mongrel)	35	15.1 kg \pm 3.1	---
Goat (Mixed breed)	30	20.5 kg \pm 3.6	4 - 5

* Mean and standard deviation

164, rats; 96, guinea pigs; 104, rabbits; 35, dogs; and 30, goats. Their body weights ranged between 22 g for the mouse to 20 kg for the goat.

All animals were exposed to the overpressure against the end-plate. Except for a few of the mice and rats that managed to turn end-for-end in their cages, all animals were right-side-on to the incident shock front. The dogs and goats were restrained in harness - the mice, rats, guinea pigs, and rabbits in wire mesh cages as described in a previous study⁽⁴⁾.

RESULTS

Pressure-time Records

Illustration of four piezo-electric gauge records are presented in Figure 6. The upper two records were from gauges 1 and 2 located face-on flush with the inside of the end-plate, while the lower two records were from gauges 3 and 4 side-on at 3 in. and 9 in. upstream from the end-plate. As seen in the figure, the face-on gauges see the incident and reflected shock pressures as one step, whereas those gauges side-on resolve the shocks as two pressure steps. It can also be noted from the record of gauge 2 that the rise time of the pressure on the end-plate was less than that of the gauge. The oscillations seen on the records to damp out rapidly were, of course, due to the natural frequencies of the quartz crystal gauges.

The duration of the overpressure (near 400 msec) can be read from the record of gauge 4 since the oscilloscope that recorded the out-put of that gauge was run at a fairly slow sweep-speed of 50 msec/cm.

The magnitude of the incident and reflected shock fronts obtained with a range of compression chamber pressures between 17 psi to 170 psi was plotted and is shown in Figure 7. The reflected shock pressures from 25 psi to nearly 60 psi were sufficient for the compilation of the dose-response curves. The durations of the overpressures over that range of reflected pressures were between 350 to 412 msec.

Mortality

The 24-hr lethality obtained with the sample of animals exposed at the various driver pressures and the associated mean incident and reflected pressures are given in Table 2. Previous studies have shown that the mortality was best correlated with the reflected shock pressures⁽⁴⁾. Since plotting the per cent mortality against the reflected pressure produced a sigmoid curve, the probit analysis was applied to the data which transforms it into a straight line⁽⁸⁾. The general form of the probit equation of this type was:

$$Y = a + b \log X$$

when Y was the per cent mortality in probit units, X was the reflected shock pressure, and a and b were the intercept and slope constants, respectively. The LD₅₀ (the pressure associated with 50 per cent mortality) was obtained by substituting the probit value of 5 (equal to 50 per cent mortality) for Y in the appropriate probit equation and solving for X. The LD₅₀'s obtained in this manner, the standard errors of the LD₅₀'s and the probit regression line equations are listed in Table 3. The LD₅₀'s in order of increasing species weights were as follows: mouse, 30.7; rat, 36.3; guinea pig, 34.5; rabbit, 29.6; dog, 47.8; and goat, 53.0 psi. The trend was for the LD₅₀'s to increase with the species size. The probit regression lines with the data points are presented graphically in Figure 8.

The LD₅₀'s fell into three groups according to statistical tests that compared them for significant differences. The mouse and rabbit were not significantly different from one another at the 95 per cent confidence level; neither were the guinea pig and rat, nor the dog and goat. However, each pair, as grouped above, were different statistically from one another. That is, the mouse and rabbit were significantly below the rat and guinea pig who were below the dog and goat.

Appropriate statistical tests that compare the slopes of the six probit mortality curves revealed that they were essentially parallel at the 95 per cent confidence level. This may be interpreted to mean that the same type of stimulus was instrumental in killing the animals from each species⁽⁸⁾.

TABLE 2

MORTALITY AS RELATED TO THE MAGNITUDE OF
THE INCIDENT AND REFLECTED SHOCK FRONTS

Compression chamber pressure psi	Incident shock psi	Reflected shock psi	Mortality	
			No. dead Total	Per cent
Mice:				
58	10.2 (9.5 - 11.0) *	27.2 (25.4 - 27.9) *	7/40	17.5
65	11.2 (10.9 - 11.4)	28.9 (28.6 - 29.1)	8/30	26.7
70	10.9 (10.5 - 11.2)	31.6 (31.3 - 31.9)	18/30	60.0
80	13.3 (13.2 - 13.4)	35.6 (34.7 - 36.6)	18/20	90.0
130	19.0 (17.5 - 18.5)	50.8 (49.5 - 52.2)	20/20	100.0
Rats:				
70	11.4 (10.9 - 11.9)	30.4 (30.0 - 30.8)	2/30	6.7
80	13.8 (13.4 - 14.1)	34.4 (33.8 - 34.7)	12/34	35.3
95	13.6 (12.7 - 14.0)	38.6 (37.9 - 39.6)	35/50	70.0
105	15.4 (15.0 - 15.8)	42.2 (40.3 - 43.2)	35/40	87.5
130	18.0 (17.5 - 18.5)	50.8 (49.5 - 52.2)	10/10	100.0
Guinea pigs:				
65	10.9 (10.6 - 11.0)	29.0 (28.6 - 29.8)	1/24	4.2
80	12.0 (11.0 - 12.4)	33.9 (33.2 - 34.3)	9/24	37.5
80	13.4 (12.8 - 14.0)	35.8 (35.5 - 36.5)	18/24	75.0
95	13.5 (11.3 - 14.7)	39.9 (38.1 - 41.0)	21/24	87.5
Rabbits:				
48	9.2 (8.7 - 9.8)	22.8 (20.0 - 24.7)	1/20	5.0
58	10.5 (9.6 - 10.9)	26.9 (25.0 - 29.1)	10/28	35.7
75	12.2 (11.5 - 13.6)	32.6 (30.5 - 34.6)	16/24	66.7
80	13.1 (12.5 - 13.6)	36.6 (35.2 - 38.3)	17/20	85.0
95	14.3 (14.0 - 14.7)	40.5 (40.4 - 40.5)	12/12	100.0
Dogs:				
95	14.7 (13.9 - 15.1)	39.2 (39.0 - 39.4)	0/5	0
115	16.6 (16.0 - 17.4)	44.1 (42.2 - 44.9)	1/10	10.0
130	17.7 (16.9 - 18.4)	48.1 (46.8 - 49.6)	6/10	60.0
150	19.0 (18.2 - 19.9)	53.0 (50.0 - 55.3)	9/10	90.0
Goats:				
130	16.7 (15.9 - 17.8)	44.9 (44.0 - 46.2)	2/10	20.0
150	18.2 (16.2 - 19.3)	51.4 (47.3 - 56.2)	4/10	40.0
170	19.4 (19.0 - 20.1)	56.9 (56.6 - 57.4)	3/5	60.0
170	20.3 (20.0 - 20.7)	59.3 (58.7 - 60.1)	4/5	80.0

Computed LD₅₀'s: Mice, 30.7 psi; rats, 36.3 psi; guinea pigs, 34.5 psi; rabbits, 29.6 psi; dogs, 47.8 psi; goats, 53.0 psi.

* Mean and range.

TABLE 3

SUMMARY OF THE RESULTS FROM THE PROBIT ANALYSIS

Species	LD ₅₀ psi	Standard error of the LD ₅₀ , psi	Probit equation constants	
			intercept, a	slope, b
Mouse	30.7	±0.56	-23.63	19.25
Rat	36.3	±0.61	-23.82	18.48
Guinea pig	34.5	±0.64	-28.50	21.78
Rabbit	29.6	±0.90	-13.63	12.67
Dog	47.8	±1.06	-49.47	32.43
Goat	53.0	±2.79	-16.68	12.57

Interspecies Correlation Between LD₅₀ Reflected Pressures and Species Weight

A log-log plot of the LD₅₀'s versus the mean body weight of each species appears in Figure 9. The regression line equation, calculated by the method of least squares that best fit the data, was:

$$\text{Log LD}_{50} = 1.3673 + 0.06939 \log \text{BW}$$

where

LD₅₀ = the reflected pressure required for 50 per cent lethality, psi

BW = mean body weight of the species, grams

1.3673 = the intercept constant

0.06939 = the slope constant

According to Figure 9 there is fair agreement between the calculated line and the measured points save for the rabbit whose point was noticeably low for its weight. The standard error of the regression estimate was 0.0602 log units or 13.9 per cent.

Included in Figure 9 is the calculated point for a 70 kg animal. It was obtained by simply solving the regression equation for a body weight of 70,000 g. In other words, this predicts 50.5 psi to be the LD₅₀ reflected pressure for a large animal the size of man exposed against a reflecting surface to a single-pulse overpressure rising almost instantaneously to near a maximum and enduring for about 400 msec.

DISCUSSION

By way of discussion, remarks in three areas are indicated; i.e., (a) the general behavior of the pressure source, (b) the wave form achieved using the shock-tube hardware described, and (c) the biological implications of the data.

The General Behavior of the Pressure Source

A study of Table 2, which gives the mean and range of the incident and reflected shock overpressures for the several experiments, shows that the pressure source utilized did not function perfectly as far as reproductibility of overpressures were concerned. For example, the variation in incident shocks for the different pressure groupings

ranged from a few tenths of a psi to a maximum of 3.4 psi (see the guinea pig data for 95 psi compression chamber pressure). In the latter case the mean incident shock pressure was 13.5 psi with a minimum 2.2 psi below and a maximum 1.2 psi above the mean, respectively. Variability for reflected shocks, as could be expected, was somewhat greater, but only ranged from a few tenths of a psi to a maximum of 8.9 psi for the goat exposure involving a compression chamber pressure of 150 psi. The maximum reflected shock was 4.1 psi above the mean while the minimum was 4.1 psi below the mean of 51.4 psi. Though this last variability represents a performance about ± 10 per cent from the mean pressure, it is indeed the maximal "misbehavior" of the shock tube. In most cases, the variability was much less as a study of the data in Table 2 will show. In fact, judging from earlier experience, the reproducibility performance noted in the present study is considered quite good indeed.

The Wave Form Achieved

Before the vent holes were added to the distal section of the shock tube, the wave form had many undesirable characteristics: first, the duration of the overpressure was longer than desired; second, there was considerable "crowning" of the overpressure after the development of the reflected shock, that is, the maximal pressure developed was considerably above the reflected shock pressure; third, marked oscillations in the overpressure occurred during the falling phase of the pulse. These were many in number and the amplitude of the oscillations was high.

After addition of the vents, all of these untoward characteristics were improved, though the wave form achieved is, from one point of view, still not exactly that desired. For example, attention is directed to the lower righthand trace in Figure 6 which shows the pressure pulse in its entirety on a somewhat compressed time scale. The reader will note that the maximal overpressure achieved is still somewhat above (about 5 psi) the reflected shock pressure of near 36 psi. Also, the pressure oscillations present represent a swing in pressure of about 19 psi, occurring in 20 msec; this involves a variation of about $1/2$ the

magnitude of the reflected shock pressure. Also, if 20 msec is taken for the half-cycle time, the frequency of this portion of the oscillation is 25 cps.

Thus, wave forms, having the characteristics of the pattern just discussed, raises uncertainties as regards assessing the biological implications of the pressure pulse, which uncertainties would be markedly lessened if the wave forms were "clean"; e.g., the crowning and pressure oscillations were absent. This point will be pursued later.

However this may be, it can be said from another point of view that the wave forms recorded in the present study are similar to some of those seen in full-scale operations in Nevada and are, therefore, quite desirable⁽⁶⁾. In truth, there is need for knowing the biology of both "clean" and "unclean" pressure pulses and in this light the present study contributes a great deal.

Biological Implications of the Data

At least two interesting questions arise in the biological area: first, what portions of the pressure pulse contribute to injury and second, what faith may or may not be put in extrapolating interspecies data to larger animals?

With regard to the first question, it is now clear that the animal poorly tolerates very "fast"-rising overpressures compared with "slow"-rising pressure pulses of the same magnitude⁽⁴⁻⁶⁾. This fact directs attention to the rising phase of the overpressure as critical and implies that damage is associated with shock loading. If indeed this is so and the animal suffers damage from the initial pressure rise, then any after-coming pressure variations might well enhance the injury. Also involved, of course, is the amplitude and frequency of the pressure oscillations, particularly as the latter may "match" the natural frequency of the thorax-abdominal system of a given species.

Also, if shock loading is one of the critical factors biologically, one would expect that any degrading of the average rate of pressure rise - all other factors being equal - would be associated with increased

tolerance to overpressure. Such is the case empirically. Guinea pigs, for example, exposed at increasing distances from the end-plate of a shock tube show an increase in P_{50} from 37 psi against the end-plate to 57 psi at 1 ft from the end-plate; e.g., the pressure rises in two rapid steps instead of one⁽⁴⁾. Likewise, dogs tolerate without fatality well over 150 psi if the time to P_{max} is 30 msec or longer, even though the pulse duration is as long as 5 to 20 sec⁽⁵⁾.

Involved in the biological interpretation of the hazards of overpressure is the duration of a single, "fast"-rising overpressure. Data are at hand which indicate that, within limits, the duration of such a pulse of overpressure is significant; e.g., for the dog about 220 psi enduring for 1.8 msec is fatal, whereas only 75 psi is fatal when the duration is 11.8 msec; for smaller animals, duration is important only for shorter intervals like fractions of a millisecond to 1, 2, or 3 msec⁽⁹⁾.

Currently, data simply are not at hand to allow a more definitive and quantitative interpretation of those characteristics of pulses of overpressure which define hazard clearly. It remains for future work to systematically spell out the criticality of rates of pressure rise, overpressure duration, step loading with two or more shocks in the rising phase of a pulse, and finally the biological meaning of oscillating overpressures.

Last, there remains the question of extrapolating interspecies blast data to larger (or smaller) animals. There is little to be said except that one should approach the extrapolation of data to any given species, including man, with considerable caution. First, it should be noted that all the animals used in the work described here were mounted against a reflecting surface and any extrapolation should keep this fact in mind. Second, the shock overpressures related or correlated with the interspecies mortality were the reflected shock pressures and one should not confuse an incident or local static-free field pressure - corresponding to the incident pressures reported here - with the

reflected shock. Third, exactly what the pressure reflection would be when an incident wave strikes an animal in the open is not currently clear to the authors and certainly the data presented do not bear upon this point.

Fourth, the extrapolation set forth in Figure 9 applies strictly to the pulse form studied and to an overpressure duration of about 400 msec. Fifth, for these conditions, it is not known whether man is more or less tolerant than might be implied by the 70 kg point marked in Figure 9. A few data do exist for the human case which relate 235 psi⁽⁹⁾ and 450 psi⁽¹⁰⁾ with human mortality, but these concern only high explosive-produced overpressures of a few msec duration and do not apply at all to the longer duration case. It would seem, therefore, that the extrapolation indicating that a 400 msec single, sharp-rising overpressure of 50.5 psi applies to as large an animal as man and might well be considered a tentative figure subject to all the conditions mentioned above. In the meantime, one must await the results of further experimental work to define more definitively man's tolerance to blast.

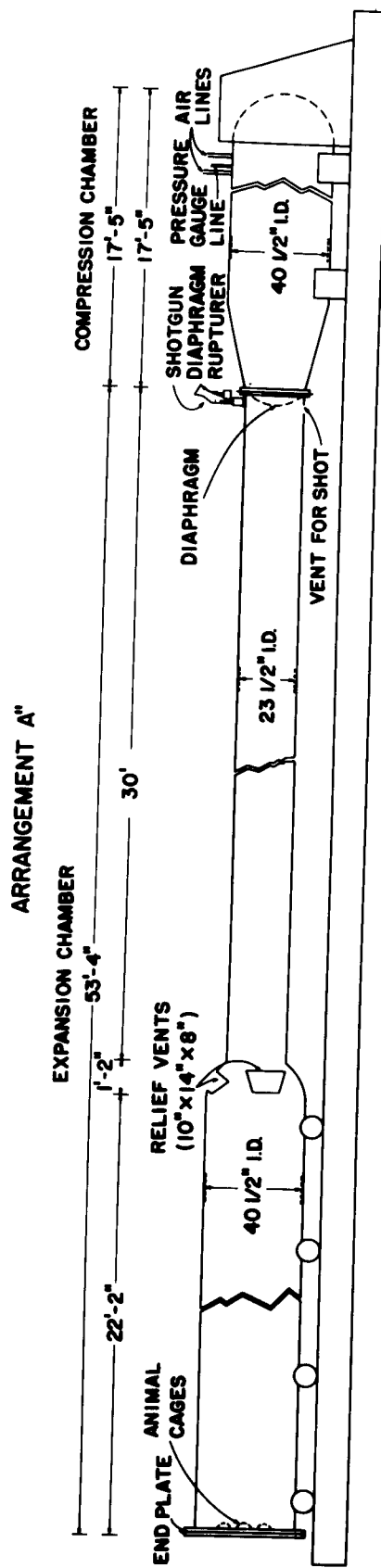
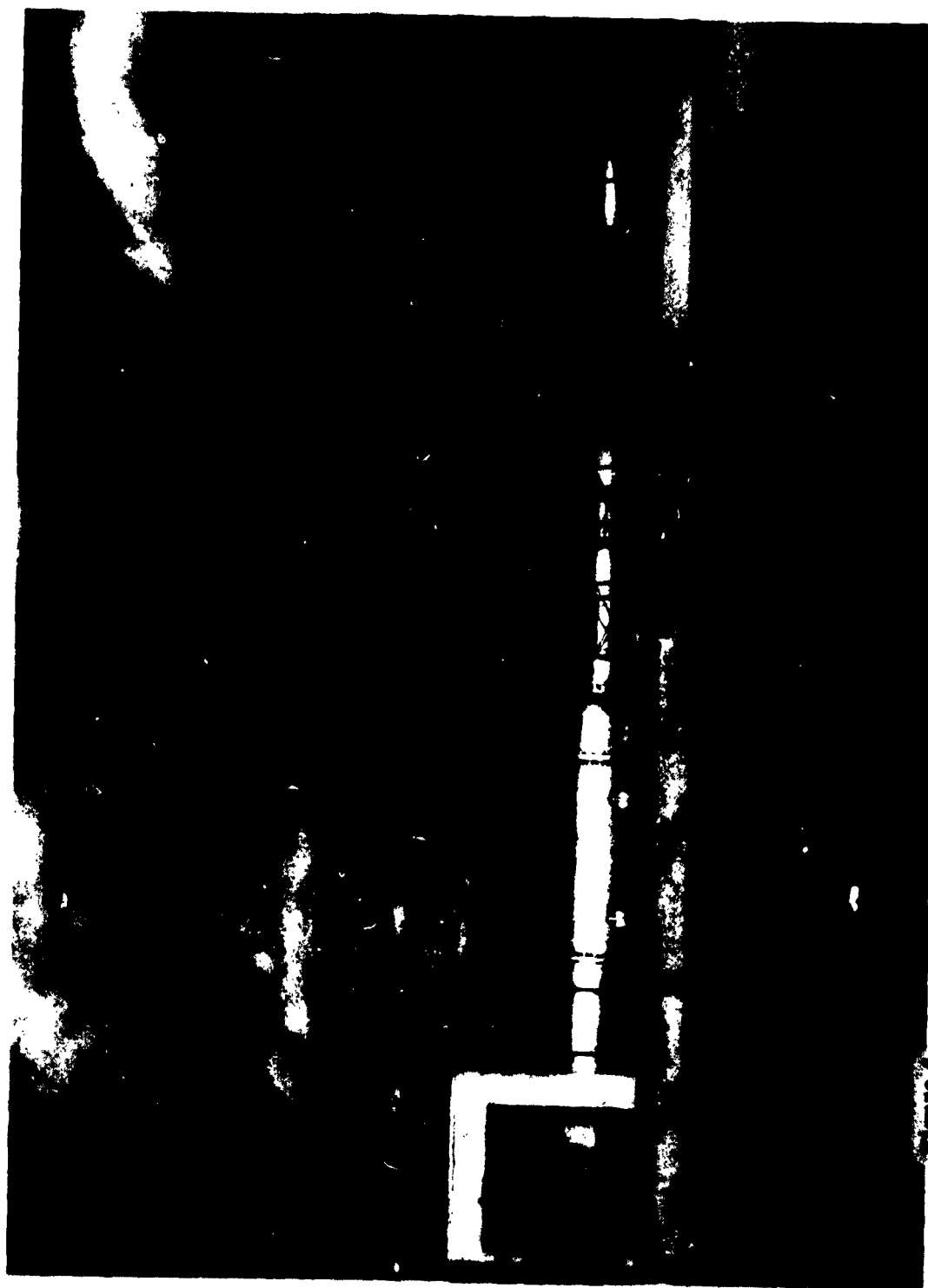


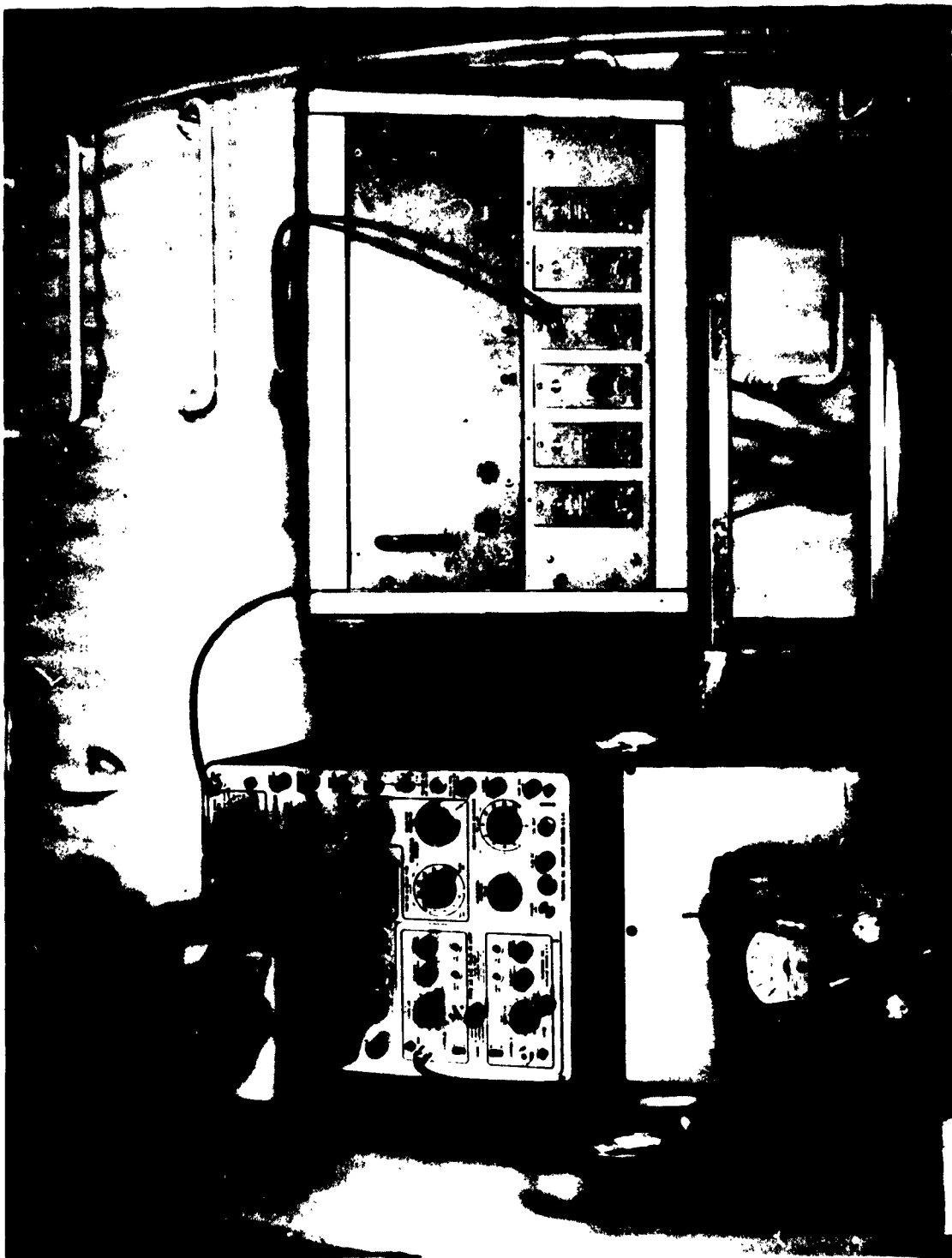
Figure 1



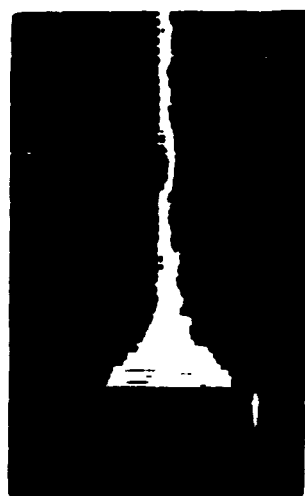
Figure 2





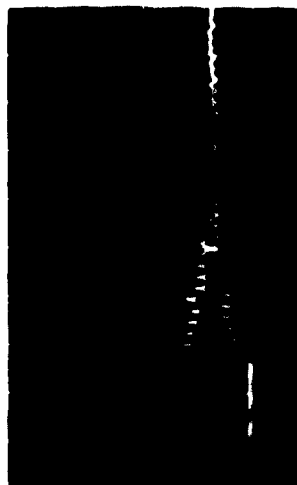


PRESSURE-TIME RECORDS QUARTZ PIEZO GAUGES



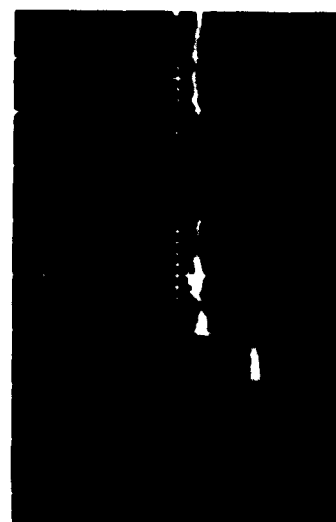
18.7
psi/cm

0.2 msec/cm
Gauge 1 Face-on at End Plate



45.4
psi/cm

0.1 msec/cm
Gauge 2 Face-on at End Plate



26.0
psi/cm

0.5 msec/cm
Gauge 3 Side-on 3" from End Plate



22.6
psi/cm

50 msec/cm
Gauge 4 Side-on 9" from End Plate

Figure 6

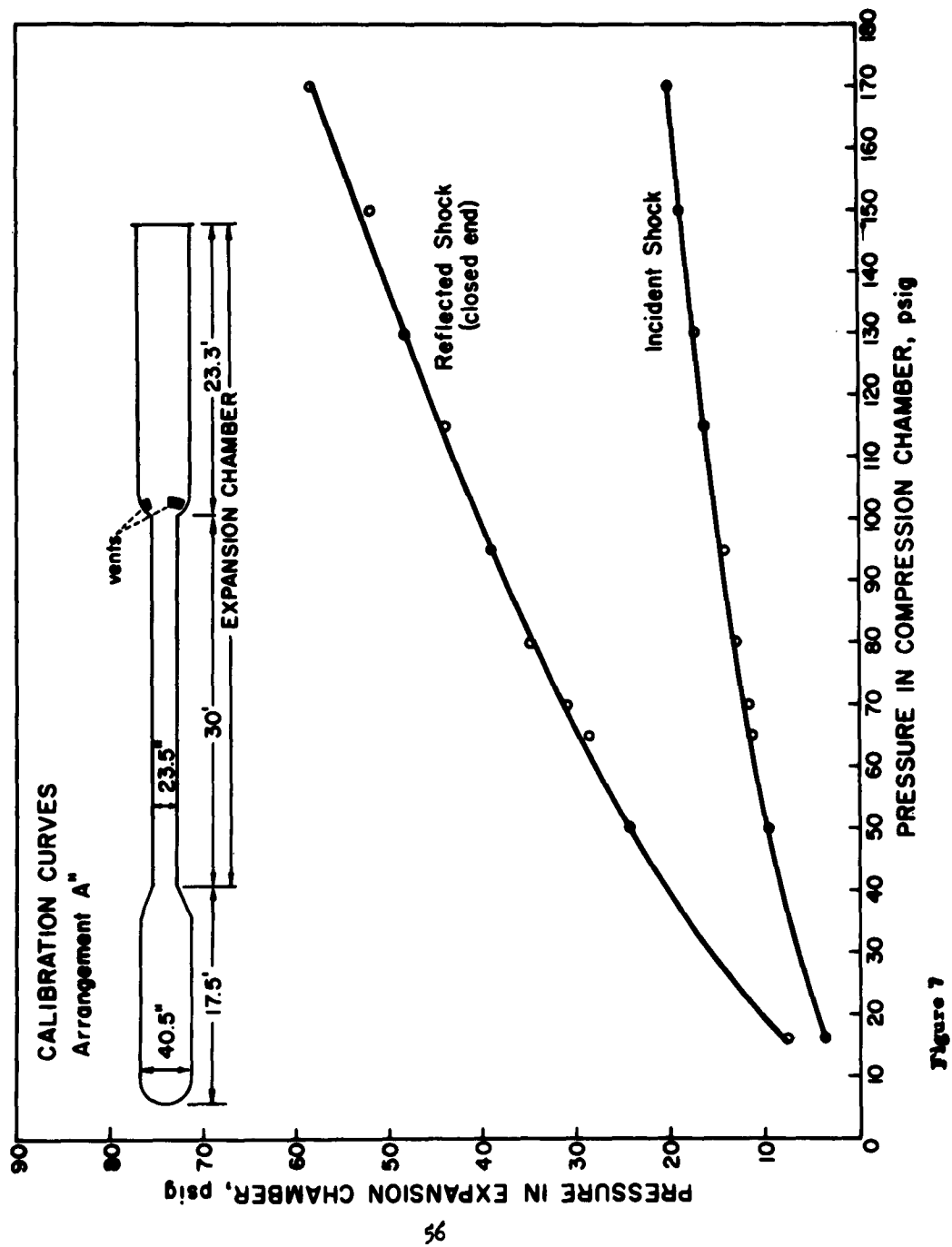


Figure 7

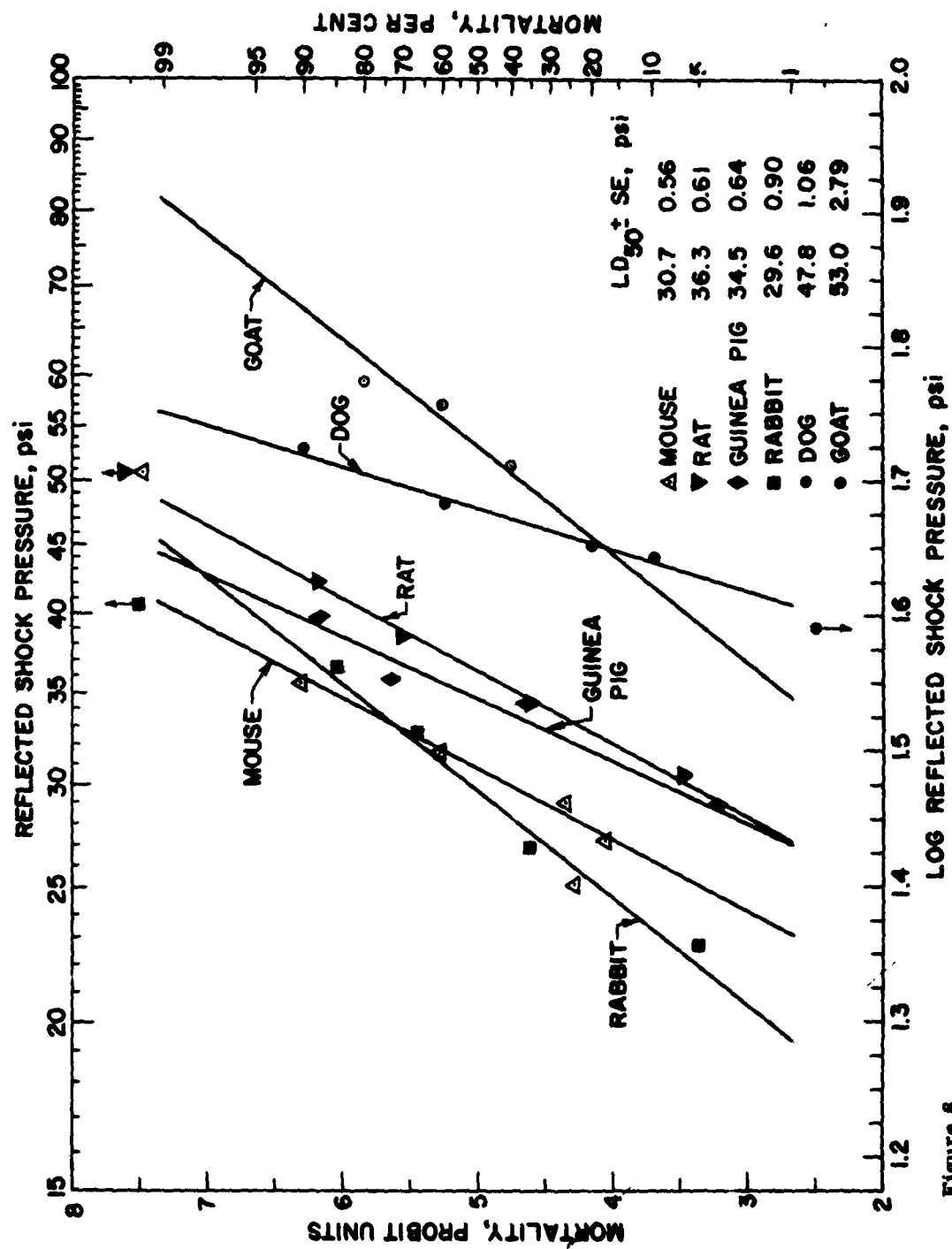


Figure 8

RELATION BETWEEN BODY WEIGHT AND FAST-RISING
OVERPRESSURES OF 400 MILLISECONDS DURATION
NEEDED TO PRODUCE 50 PERCENT MORTALITY

Animals exposed side-on against the
plate closing the end of a shock tube

REGRESSION EQUATION

$$\text{Log (LD}_{50}) = 1.3673 + 0.06939 \log (\text{BW})$$

Where LD₅₀ = Pressure required for 50% mortality, psi

BW = Average body weight of the group, grams

Standard Error of Estimate: 0.0602 log units (13.9 %)

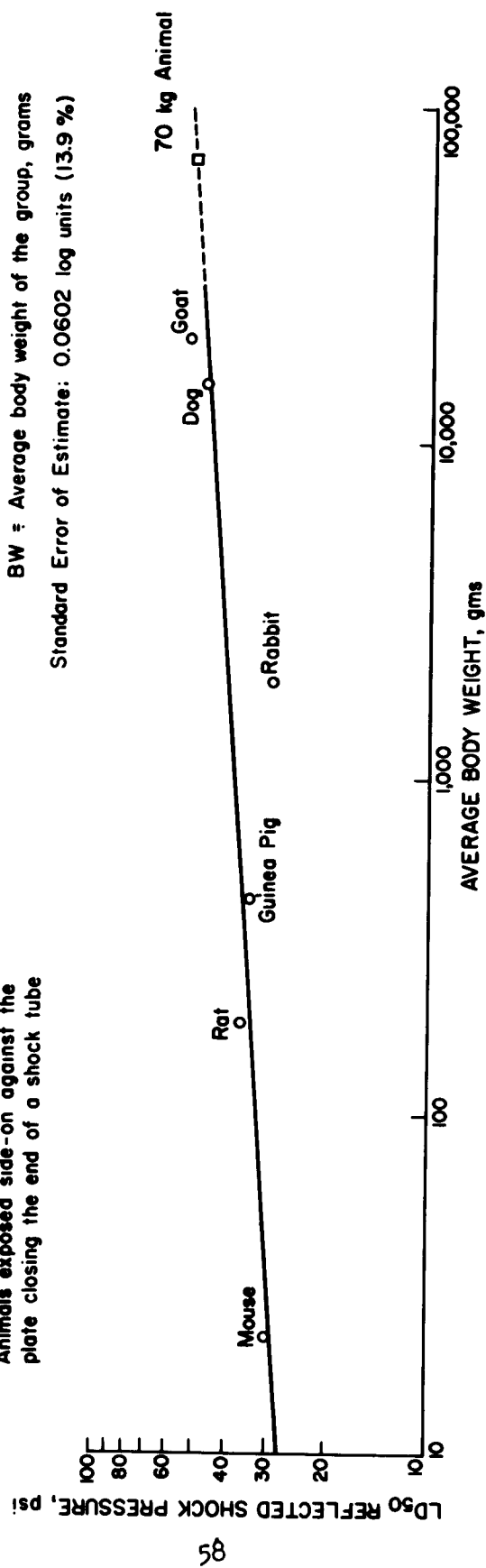


Figure 9

REFERENCES

1. Cassen, B., Curtis, L. and Kistler, K. "Initial studies of the Effect of Laboratory Produced Air Blast on Animals". J. Aviat. Med. 21:38-47 (1950).
2. Celander, H., Clemedson, C., Ericsson, U. and Hultman, H. "The Use of Compressed-air-operated Shock Tube for Physiological Blast Research". Acta Physiol. Scand. 32:6-13 (1955).
3. Richmond, D.R. and Taborelli, R.V. "Some Results of a Shock Tube for Biomedical Investigation". pp. 56-69. Proceedings of Second Shock Tube Symposium, Report SWR-TM-58-3, Air Force Special Weapons Center, Air Research and Development Command, Kirtland Air Force Base, New Mexico, March 5-6, 1958.
4. Richmond, D.R., Taborelli, R.V., Sherping, F., Wetherbe, M.B., Sanchez, R.T., Goldizen, V.C. and White, C.S. "Shock Tube Studies of the Effects of Sharp-rising, Long-duration Overpressures on Biological Systems". pp. 171-194. Proceedings of Third Shock Tube Symposium, Report SWR-TM-59-2, Hqs. Air Force Special Weapons Center, Kirtland Air Force Base, New Mexico, March 10-12, 1959.
5. Richmond, D.R., Wetherbe, M.B., Taborelli, R.V., Chiffelle, T.L. and White, C.S. "The Biologic Response to Overpressure. I. Effects on Dogs of Five to Ten-second Duration Overpressures Having Various Times of Pressure Rise". J. Aviat. Med. 28:447-460, 1957.
6. White, C.S., Chiffelle, T.L., Richmond, D.R., Lockyear, W.H., Bowen, I.G., Goldizen, V.C., Merideth, H.W., Kilgore, D.E., Longwell, B.B., Parker, J.T., Sherping, F. and Cribb, M.E. "The Biological Effects of Pressure Phenomena Occurring Inside Protective Shelters Following Nuclear Detonation". Operation Teapot Report, WT-1179, U.S. Atomic Energy Commission, October 1956.
7. Richmond, D.R., Taborelli, R.V., Bowen, I.G., Chiffelle, T.L., Hirsch, F.G., Longwell, B.B., Riley, J.G., White, C.S., Sherping, F., Goldizen, V.C., Ward, J.D., Wetherbe, M.B., Clare, V.R., Kuhn, M.L. and Sanchez, R.T. "Blast Biology - A Study of the Primary and Tertiary Effects of Blast in Open Underground Protective Shelters". Operation Plumbbob Report, WT-1467, U.S. Atomic Energy Commission, June 30, 1959.
8. Finney, D.J. Probit Analysis. A Statistical Treatment of the Sigmoid Response Curve. 2nd Edition, Cambridge University Press, New York, 1952.
9. Desaga, H. "Blast Injuries". Chap. XIV-D. German Aviation Medicine, World War II, Vol II, pp. 1274-1293, U.S. Government Printing Office, Washington, D.C., 1950.
10. Fisher, R.B., Krohn, P.L. and Zukerman, S. "The Relationship Between Body Size and the Lethal Effects of Blast". Ministry of Home Security Report R.D. 284, Oxford University, Oxford, England, 1941.

A HIGH-EXPLOSIVE OPERATED SHOCK TUBE

WITH FACILITIES FOR TESTING STRUCTURES

L. O. Larsson

Research Department, Royal Swedish Fortification Administration
Stockholm, Sweden

INTRODUCTION

Most shock tubes talked about seem to be shock tubes of the classical type with high-pressure and low-pressure chambers. Therefore, my presentation of the high-explosive operated shock tube used by the Research Department of the Royal Swedish Fortification Administration, is perhaps a bit out of the way. Nevertheless, it has proved to be very useful for our purposes, i.e. testing structures and structural elements, such as concrete beams, slabs, shelter doors, rapid-closing valves, etc., and performing certain model tests. Besides being a cheaper and often more convenient way than performing full scale tests with nuclear weapons, for a little country without such possibilities the shock tube facility offers the only way of getting similar loadings.

DESCRIPTION OF THE SHOCK TUBES

At present we have two high-explosive operated shock tubes. The first one, Shock Tube I (Figures 1 and 2)⁽¹⁾, was built in 1953 and turned out to be very useful for different investigations in the field of fortifications (protection structures). It has a length of 1.0 m. and a diameter of 1,0 m. The span of producible loadings was, however, found often to be too limited. Peak overpressure < 14 atm and pressure phase duration < 12 ms. The loading characteristics are shown in Figure 3. Moreover, the space of the test section is too restrictive for tests of reinforced concrete beams and similar elements.

Therefore, a second shock tube, called Shock Tube II^{*}, was built in 1956 on the basis of the gathered experiences from the first one. It is best described by referring to Figures 4 and 5. The two main parts

* Both shock tubes I and II were designed by S. G. A. Bergman and S. Granstrom.

of the Shock Tube II are the long steel tube in which the blast is generated, and the test section, where the objects to be tested are inserted. The dimensions of the very tube are: length 40 m. and diameter 1.5 m. (see Figure 4). The tube wall is 10mm. thick. There are three stations in the tube for placing the high-explosive charges. Here the tube is surrounded by heavily reinforced concrete fundamentals, which are placed on vibration isolating layers, and serving as supports. This arrangement allows the detonation of charges up to 10 kg of TNT located in the centre of the tube section.

The tube is provided with dilatation gliding joints between the concrete fundamentals in order to avoid temperature stresses that could be disastrous if added to the blast loading induced stresses. Positions and dimensions of the concrete fundamentals are shown in Figure 4. The fundament closest to the concrete structure of the test section is separated from this one only by a vibration isolating layer. These two concrete bodies are held together with four strong steel tubes, the ends of which are rubber isolated to minimize the vibrations transmitted to the test section. The tube fundament surrounds here the steel tube along a length of 10 meters to make it withstand the pressure of the reflection zone at the end of the tube when - as in most cases - this is closed.

The test shaft is reached from the sides as well as from the deck above the test section. On the deck there is a telfer capable of lifting test objects weighing up to 7.5 metric tons and placing them in the shaft. In many tests the objects are placed at a wall or as forming part of a wall which is placed so that the tube is closed at the test end. (Of course the wall itself could be a test object, e.g. a reinforced slab). The wall is pressed against the tube end with the aid of a clamping device consisting of four parallel hydraulic jacks (Figure 6) with a total pressure force of 900 Mp. In the test shaft a well-fitting piece of tube can be placed so as to make the tube continue through the test section. This makes it possible to use the tube without a reflecting wall, if desired.

Close to the test section there is a room for the necessary recording and measuring apparatus. After a blast the tube is filled with detonation gases, which are ventilated out by a fan.

BLAST LOADING CHARACTERISTICS

The blast loadings producible in Shock Tube II have been investigated by use of piezoelectric pressure gauges of a special fashion* (Figures 7 and 8). To meet the often very severe conditions in our tests a rugged type of gauge⁽²⁾ has been developed by surrounding a tourmaline crystal gauge (made for use in water) with water.

A typical pressure-time record of a blast in the shock tube is shown in Figure 9, where also three well-known parameters are defined, the front overpressure (at the same time peak pressure for this type of curve) \hat{p} , the positive (pressure phase) impulse i_+ and the positive (pressure phase) duration t_+ . The calibration diagrams referred to have been drawn for the case of closed tube end at the test section. The above parameters consequently refer to reflexion (see Figures 10 - 12). The calibration records available to-day show that in Shock Tube II it is possible to generate blast loadings with peak pressure up to 50 kgf/cm^2 ($\approx 715 \text{ psi}$), positive impulse up to 235 gfs/cm^2 ($\approx 2.94 \text{ psi-sec}$), and positive duration up to 100 ms. The predominant tendency is that the higher the used TNT charge and the shorter the distance from the charge to the reflexion wall, the higher the peak pressure of the loading. The impulse depends in the same way upon the size of the charge, but charges less than about 1 kg of TNT produce the same impulses when placed at the 10-meter and the 20-meter distances. Bigger charges produce at the 10-meter distance lower impulses than at the 20-meter distance. This anomaly of the 10-meter curve - which seems real - might be explained by incomplete development of the flow produced by big charges near the reflexion wall. As regards the positive duration, the tendency is decreasing with increasing charge at the 10-meter and the 20-meter distances, and the opposite at the 40-meter distance. (The 40-meter curve is partly dashed, because the experimental data here

*This measuring device and technique were developed by the author, who also made the calibrations of the shock tubes.

(not yet checked) are remarkably higher than is indicated by the curve.) In Figures 13 - 15 the pressure, impulse and duration curves for the different charge locations are brought together for comparison.

The calibration described aimed primarily to a study of the characteristics of the first overpressure phase. Records extended over longer times show also a secondary wave pattern (Figure 16), which seems, however, to be of little importance in most of our present shock tube applications. The secondary shock fronts and waves have much less pressure than that which is characteristic of the first overpressure phase. By placing some sort of grid at the open end of the shock tube, waves originated there could most likely be extinguished more or less completely. The arrival time of the second front has been evaluated from the records and is diagrammed as a function of the charge, with charge location as parameter (Figure 17). Some other curves are also shown for comparison. The 10-meter and the 20-meter distances give constant arrival times, but at 40 m. the time increases with increasing charge. In the former case with constant time the forming mechanism might be associated with a shock front reflexion at the contact surface between the air and the detonation gases. This hypothesis is being investigated with the aid of the characteristic method. In the latter case with varying arrival time the mechanism seems to be more complicated.

BLAST SIMULATION FACILITIES

In conclusion, the capacity of Shock Tubes I and II to simulate loadings from big charges detonating in free air is demonstrated in Figure 18. The left column shows the overpressure phase of the loading in the shock tube for given charge and distance. The right column indicates the equivalent free charge and distance which produce approximately the same loading*. The equivalent charges and distances are chosen so that the loadings agree as to peak pressure and impulse. The durations of the loading in the shock tube and the loading of the free charge then differ. The loading in the tube has namely longer duration than the loading from

* The values of the blast loading characteristics of the free air blast taken from Reference 3.

the free charge. The last part of the overpressure phase of the former contains, however, only a comparatively small amount of impulse, so this discrepancy can be expected to be of very little importance. The intention is here only to estimate the order of magnitude of the simulated charges. A charge of TNT in the tube Q_T can consequently be said to correspond to a free charge Q . The effectiveness of the shock tubes can then be expressed as follows:

Shock Tube I Q/Q_T approx. 10^3

Shock Tube II Q/Q_T approx. $10^3 - 10^4$

EXAMPLES OF APPLICATIONS OF THE SHOCK TUBE LOADINGS

A series of concrete slabs (1.5 x 1.5 m.) with and without reinforcement has been tested in the shock tube in order to investigate the behaviour of slabs subjected to blast loading, to study the fracture mechanism, and to gain information for design calculations (see Figure 19).

Door constructions offer a difficult problem in connection with field fortifications for troops. The requirements are among others that the troops themselves shall be able to build doors from simple material. Nevertheless, the doors shall give good protection against blasts from nuclear weapons. Door constructions consisting of a number of plank layers laid with differently directed fibers and joined with nails and/or glue have been tested (Figure 20).

The Swedish Civil Defence Administration has issued construction specifications for standard population shelters and has recently modernized the shelter types earlier used. In the living areas of towns with a population over some 50,000 inhabitants every new-built living block for more than two families shall be equipped with a standard shelter (in the basement) capable of resisting blast loadings of 1 atm overpressure (≈ 14 psi). In smaller places the protection level shall be 0.5 atm overpressure. As part of the work with the specifications for these shelter constructions, test series with models in the scale 1:5 have been performed. Figure 21 shows various

models used in these tests. The investigation has included shelters with roofs supported by mountable columns. The idea is that in peace time the columns shall be taken away to provide more effective space. The aim of the tests was among other things to investigate the behaviour of the columns, the effects of various reinforcements in the roof slabs, and how failure develops.

A troop shelter of corrugated plate has been tested in a model scale of 1:10 with the shock tube arranged for passing blasts. Figure 22 shows a model of the "Group Helmet", a transportable shelter to be dug down by the troop to get radiation and blast protection.

The list of shock tube applications could be extended further, but as one last example I would like only to mention the use in the development of the rapid-closing air-intake valves for high-qualified big underground shelters. These valves close in a few milliseconds and let only a small amount of impulse come through.

CONCLUSION

Shock Tube II, 1.5 m. in diameter, is not the biggest one with respect to the diameter size, but as far as we know at present no shock tube capable of stronger loadings over a test section of this size exists anywhere. Nevertheless, the need of test loadings of still higher pressure, say 70 atmospheres, and longer duration, say 2 seconds, for the solution of several high-protection problems in the field of fortifications, has directed our efforts to the intricate task of constructing a new blast simulating device with this capability.

REFERENCES

1. Bergman, S. G. A., Granstrom, S. and Larsson, L. O. The Shock Tube - A Blast Loading Test Bench. Royal Swedish Fortification Administration, Technical Note No. B 16, March 1956.
2. Larsson, L. O. Measuring of Shock Wave Pressure in Air and Water. Swedish National Committee for Mechanics, Section for Detonics and Combustion, Luctures at Conference on Effects of Explosives on Solids 19-20 March 1959, pp. 3:1-14 + 7 pp. ill.
3. Granstrom, S. A. Loading Characteristics of Air Blasts from Detonating Charges. Transactions of the Royal Institute of Technology No. 100, Stockholm 1956.

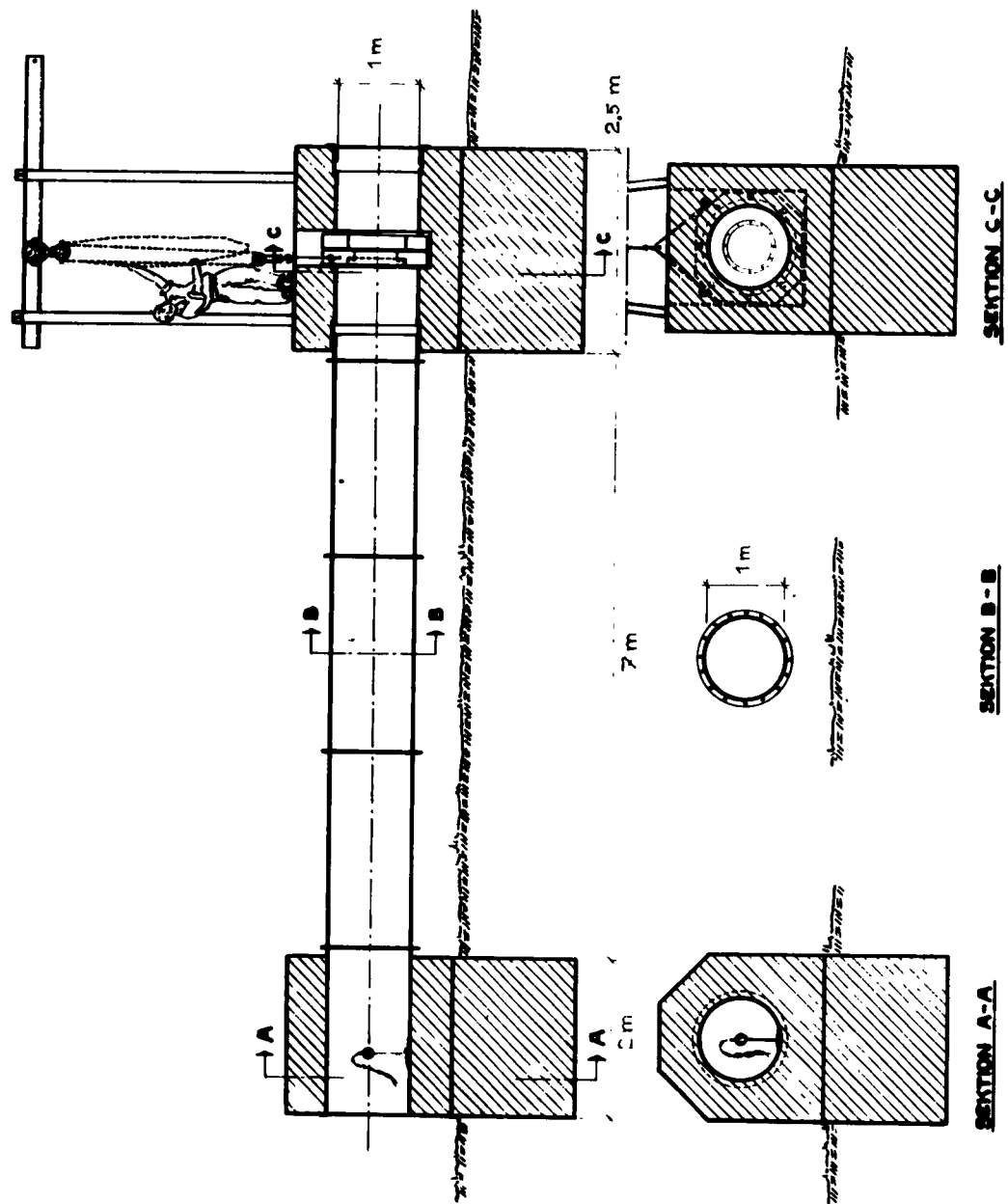


Figure 1. Sections of Shock Tube I



Figure 2. View of Shock Tube I

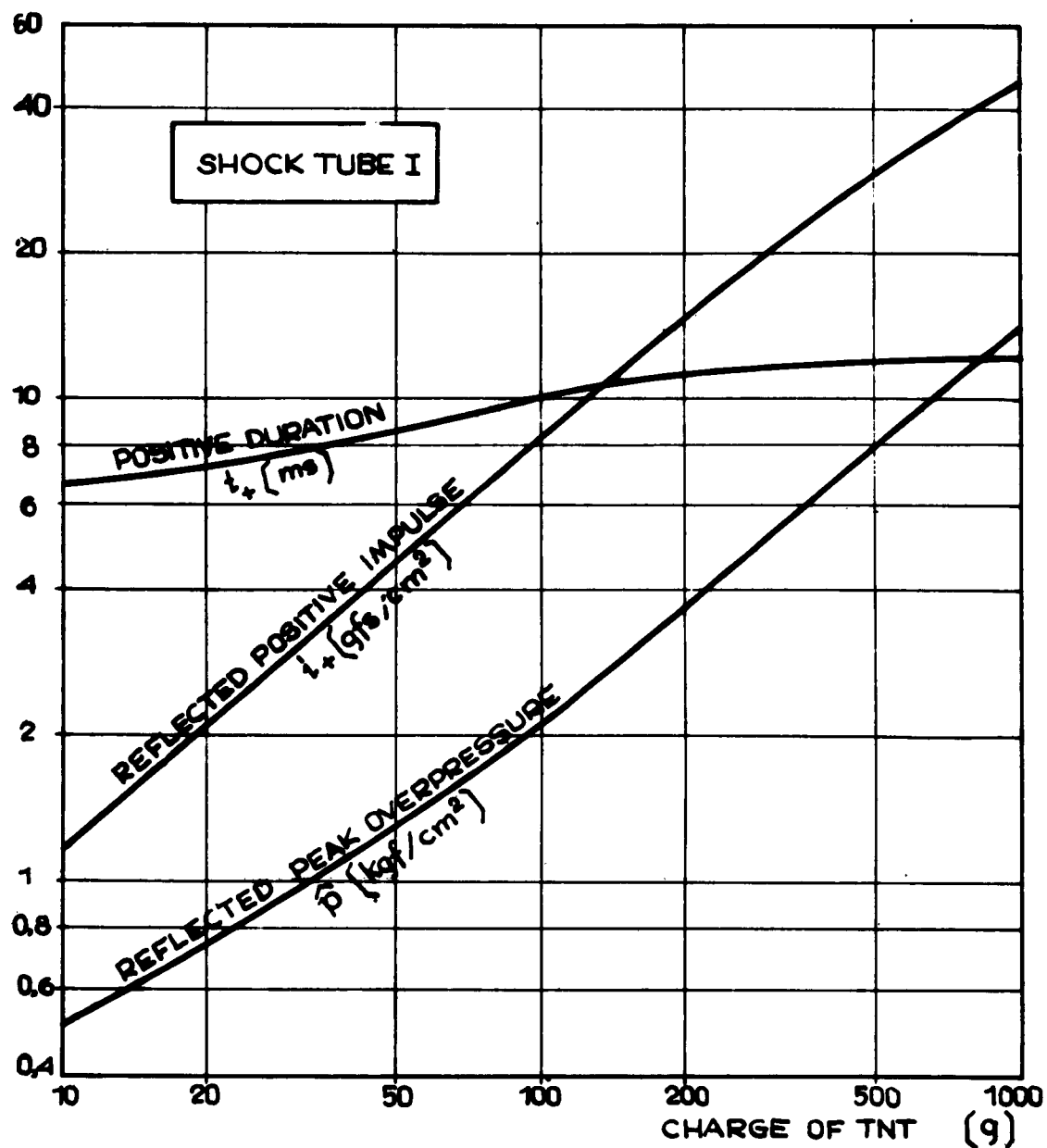


Figure 3. Characteristics of Blast Loadings in Shock Tube I

Diagram of the test shaft showing dimensions and locations of charges. The shaft is a long horizontal cylinder with a diameter of 1.5 m. A test shaft is attached to the left end. The shaft is divided into sections with the following dimensions and charge locations:

- Section 1: 40 m long, with a charge located 40 m from the left end.
- Section 2: 17 m long, with a charge located 17 m from the left end.
- Section 3: 3 m long, with a charge located 3 m from the left end.
- Section 4: 46.5 m long, with a charge located 46.5 m from the left end.
- Section 5: 8.5 m long, with a charge located 8.5 m from the left end.
- Section 6: 15 m long, with a charge located 15 m from the left end.
- Section 7: 2.5 m long, with a charge located 2.5 m from the left end.
- Section 8: 2.5 m long, with a charge located 2.5 m from the left end.

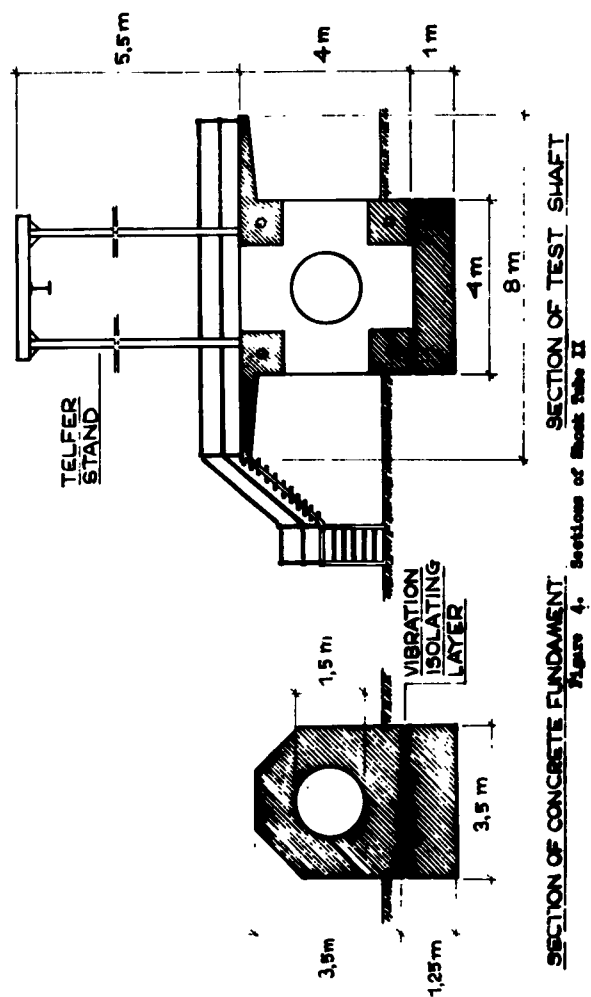




Figure 5. View of Shock Tube II



Figure 6. Clamping Device of Shock Tube II Consisting of Four Parallel Hydraulic Jacks

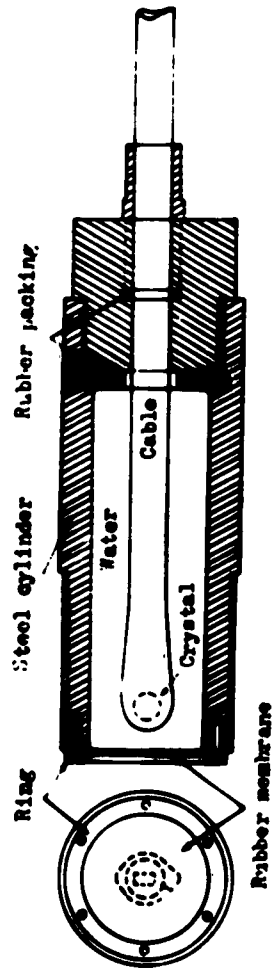


Figure 7. Section of Tourmaline Crystal Gauge

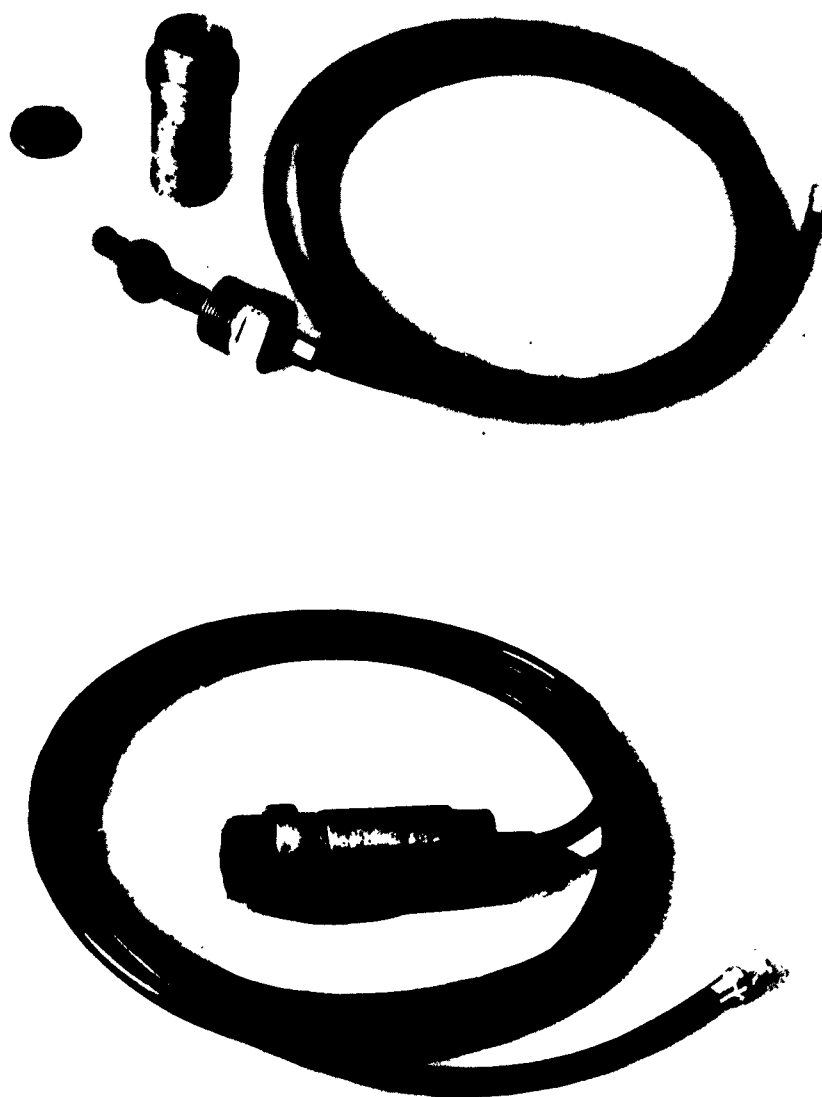


Figure 8. Photograph of Tourmaline Crystal Gauge

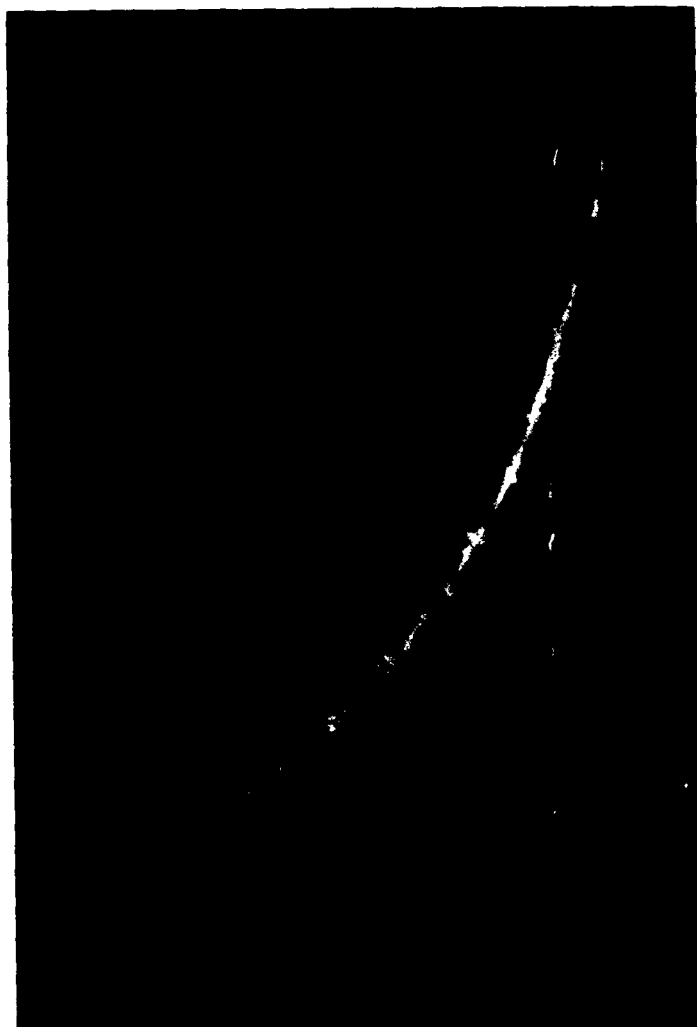


Figure 9. Typical Blast Pressure-Time Record
of the Positive Pressure Phase

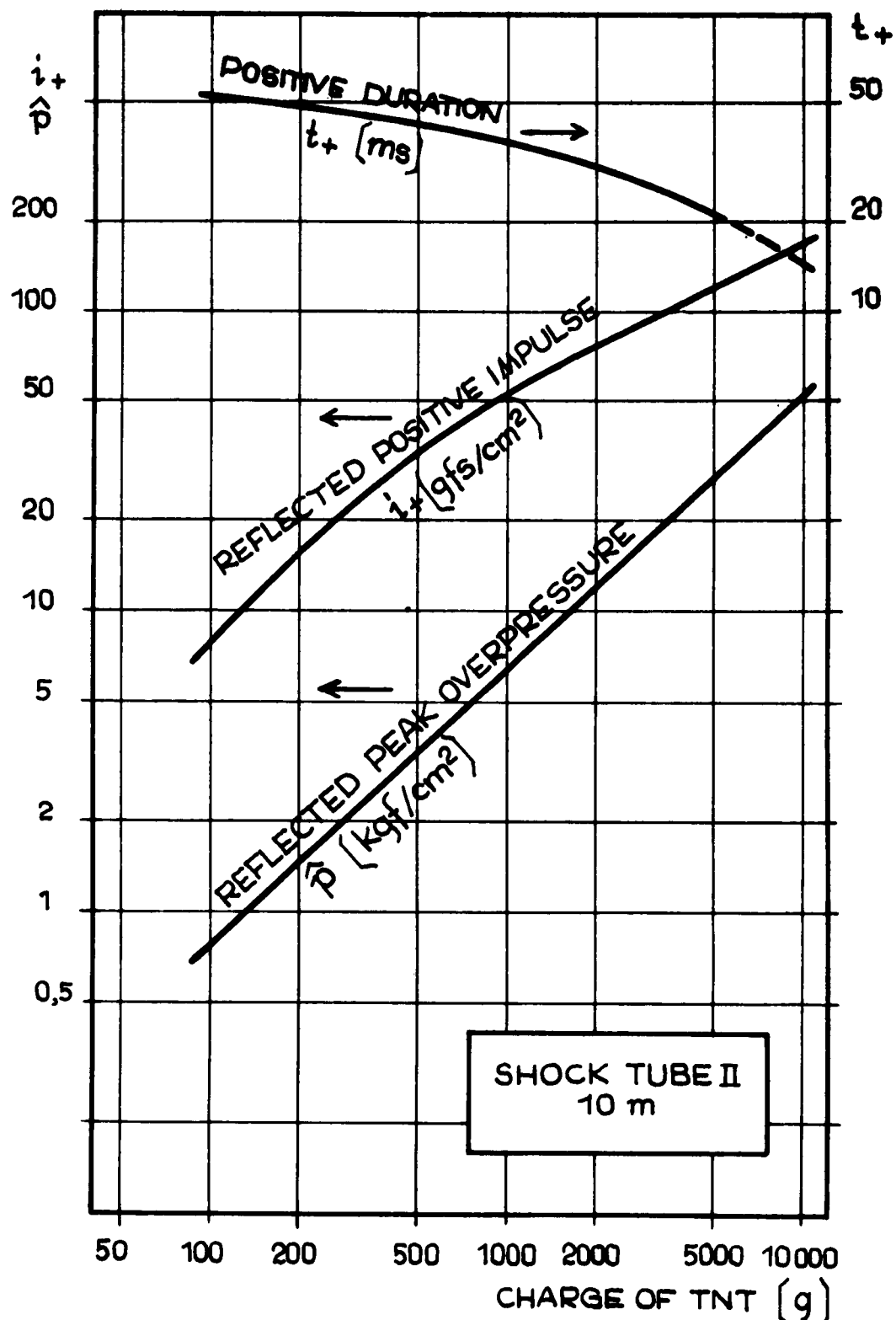


Figure 10. Characteristics of Blast Loadings in Shock Tube II (Distance from Detonating Charge 10 meters)

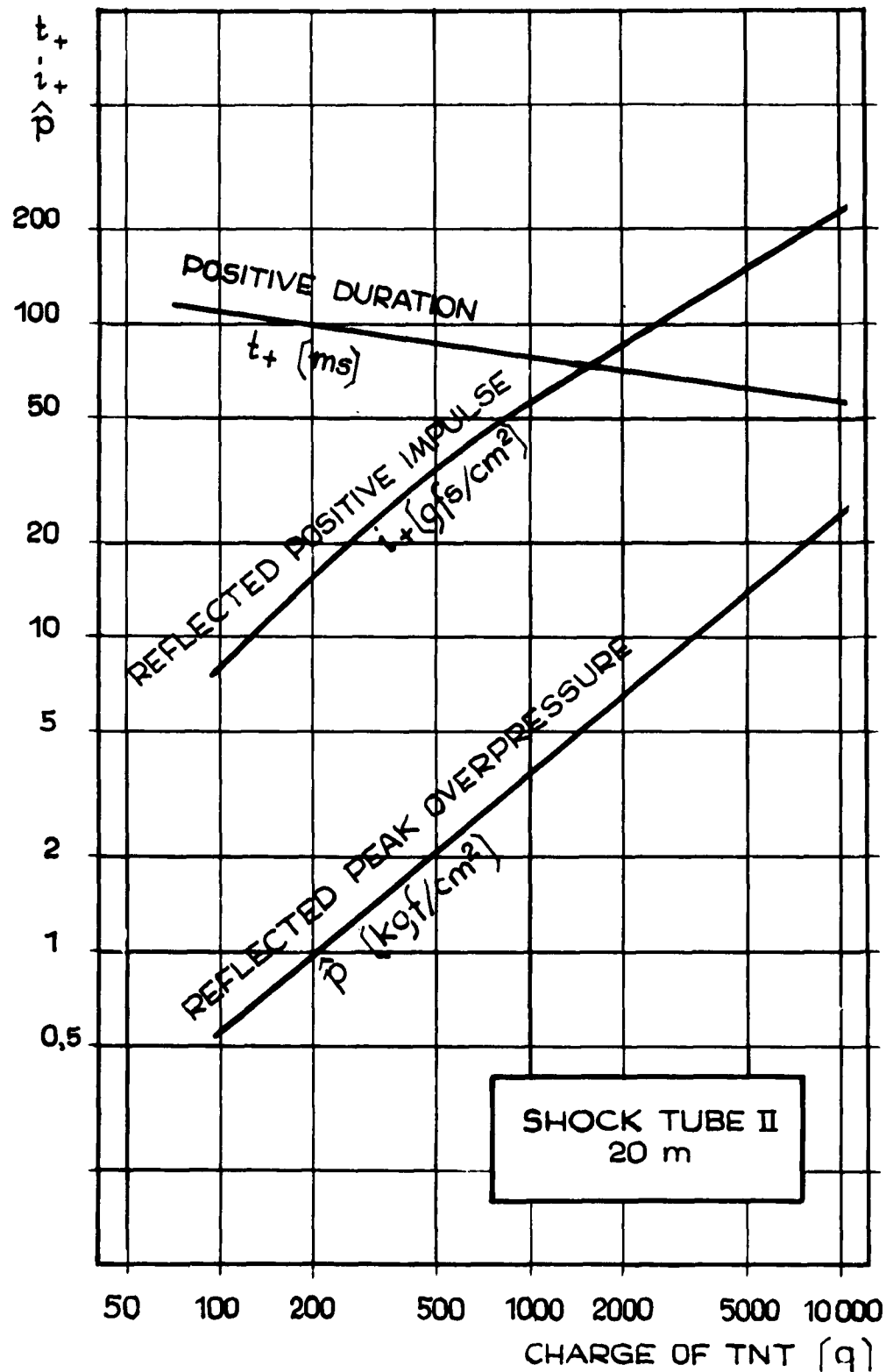


Figure 11. Characteristics of Blast Loadings in Shock Tube II (Distance from Detonating Charge 20 meters)

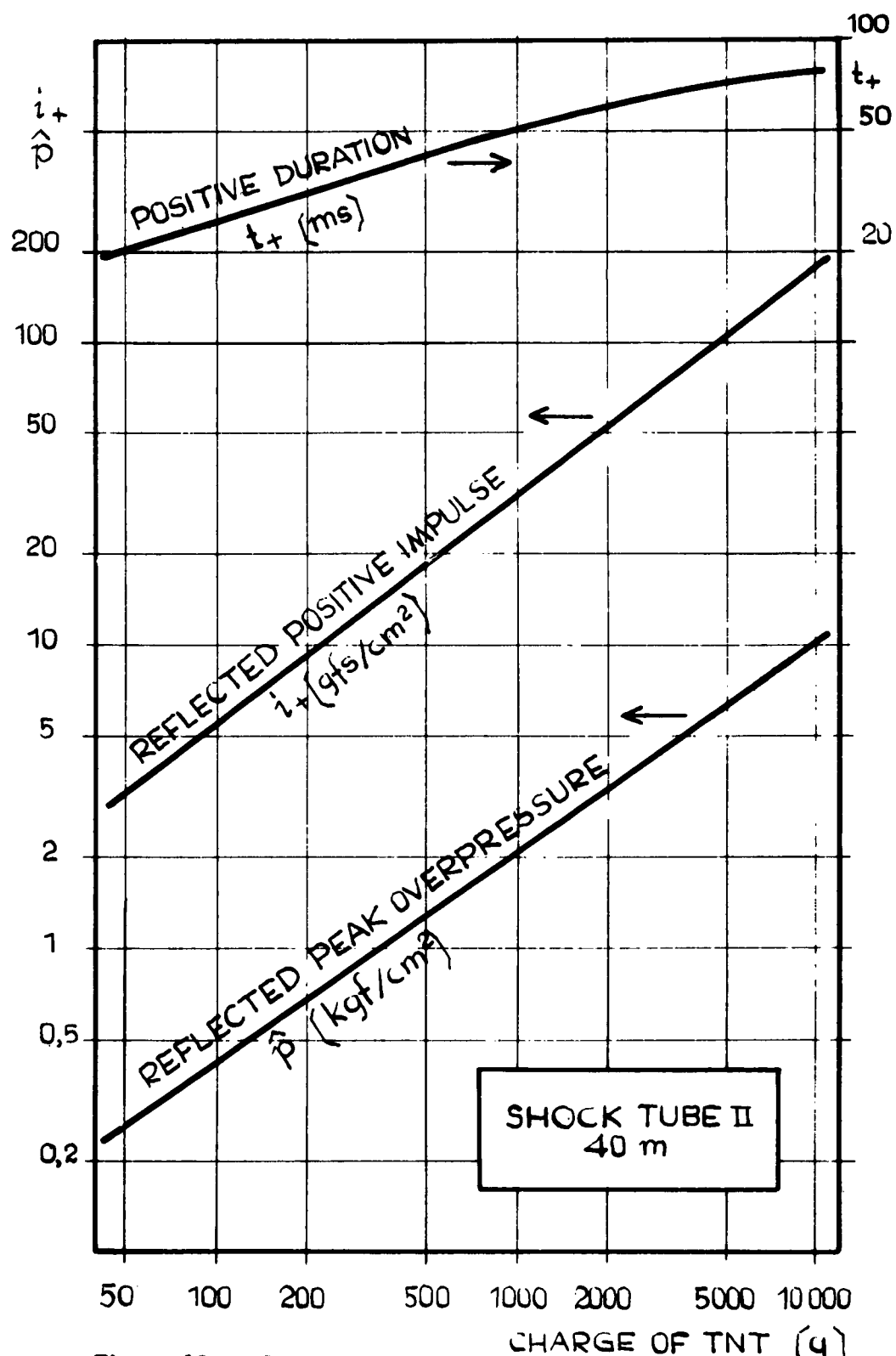


Figure 12. Characteristics of Blast Loadings in Shock Tube II (Distance from Detonating Charge 40 meters)

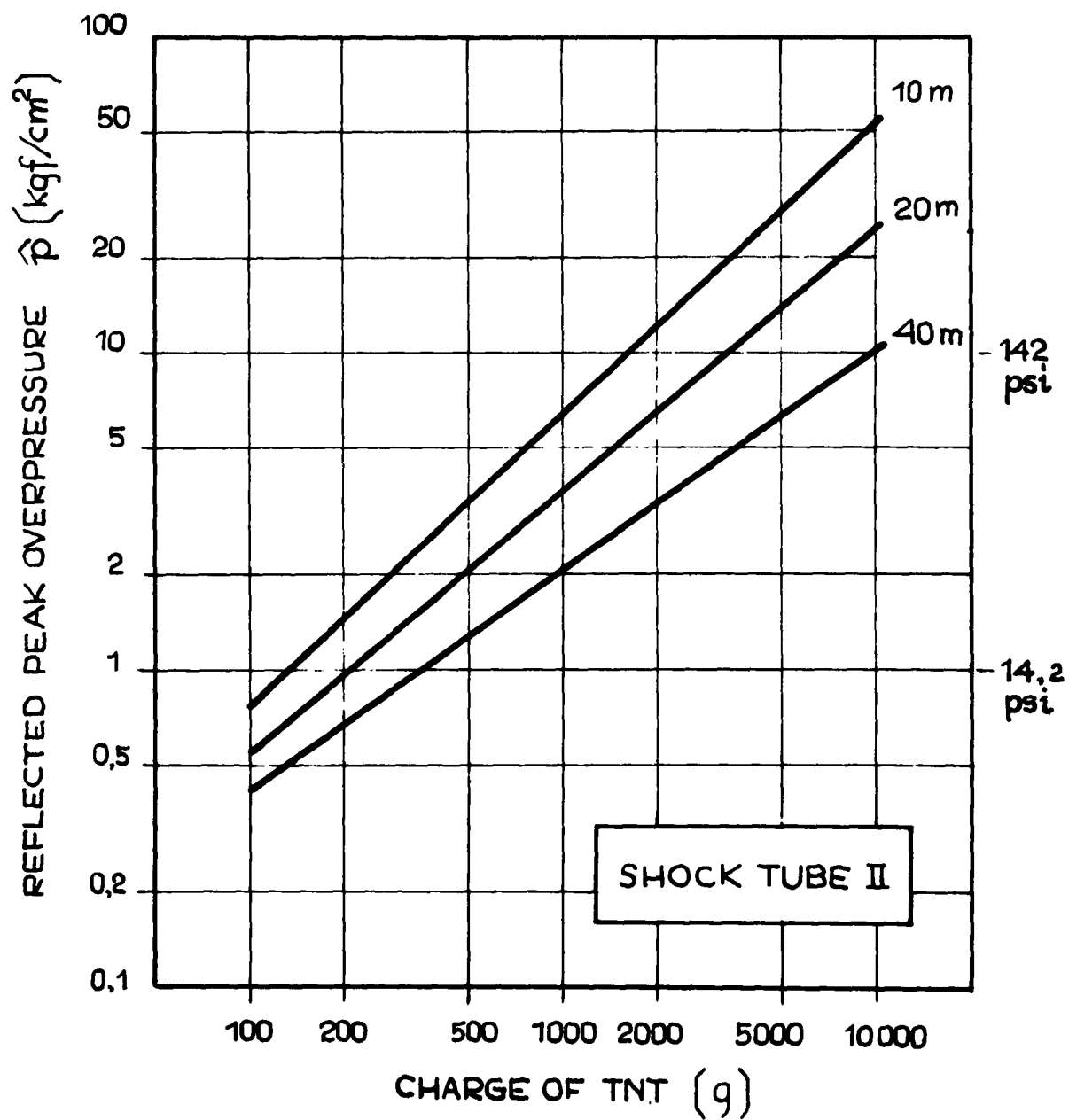


Figure 13. Peak Overpressures of Blast Loadings in Shock Tube II

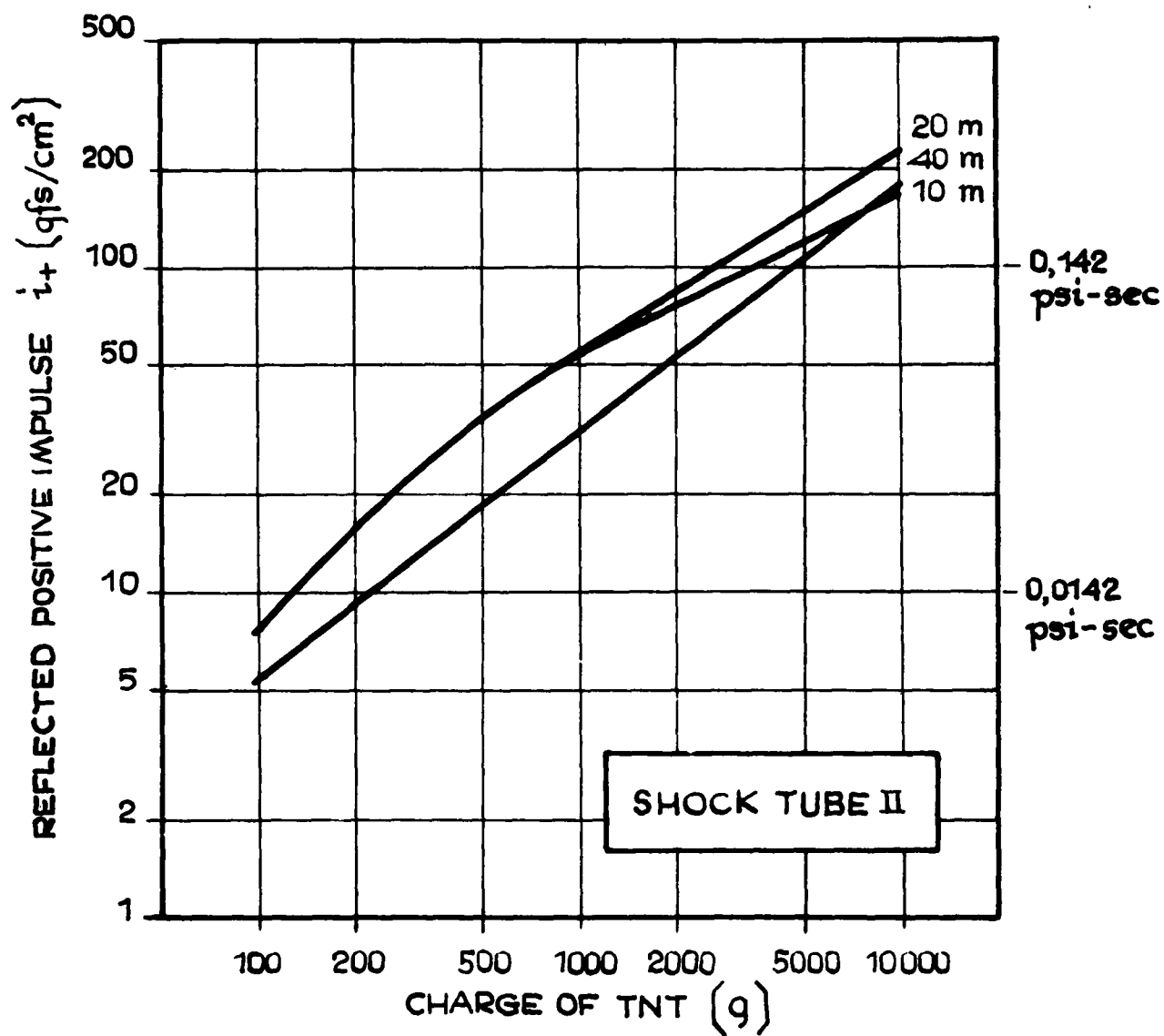


Figure 14. Positive Impulses of Blast Loadings in Shock Tube II

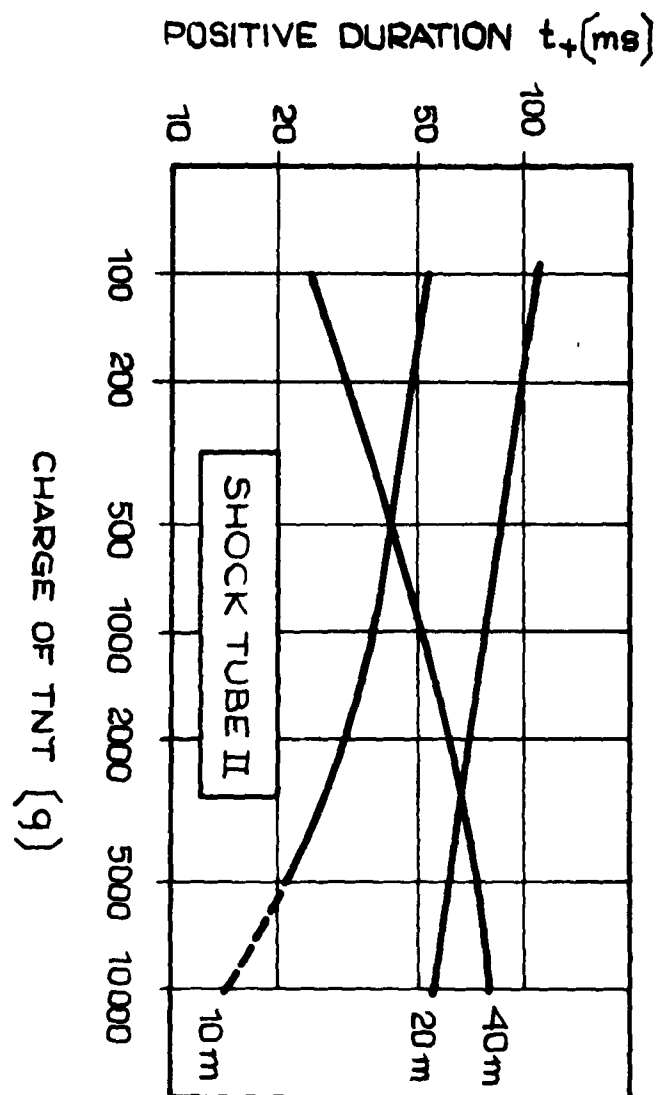


Figure 15. Positive Durations of Blast Loadings in Shock Tube II

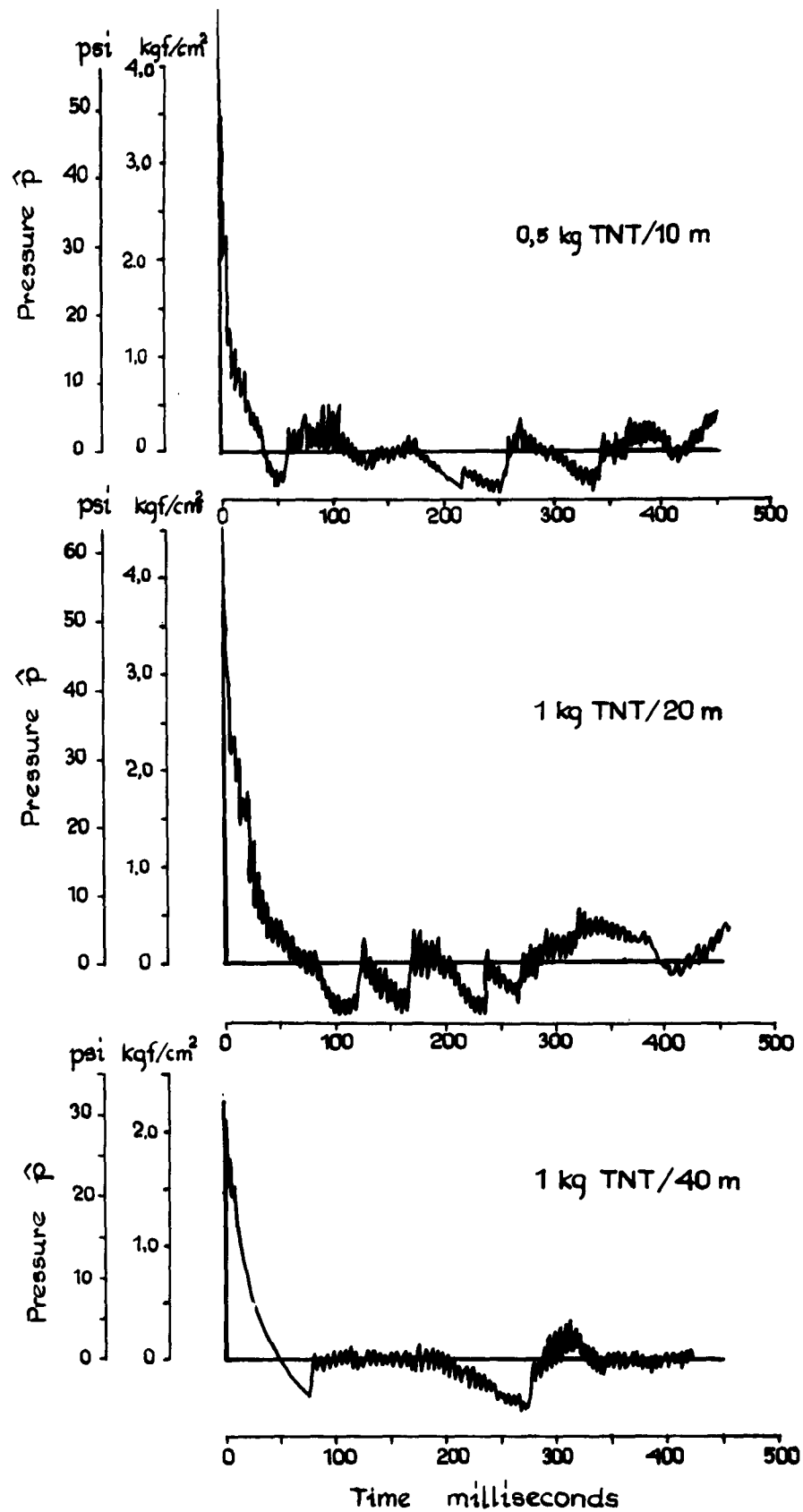


Figure 16. Extended Pressure-Time Records

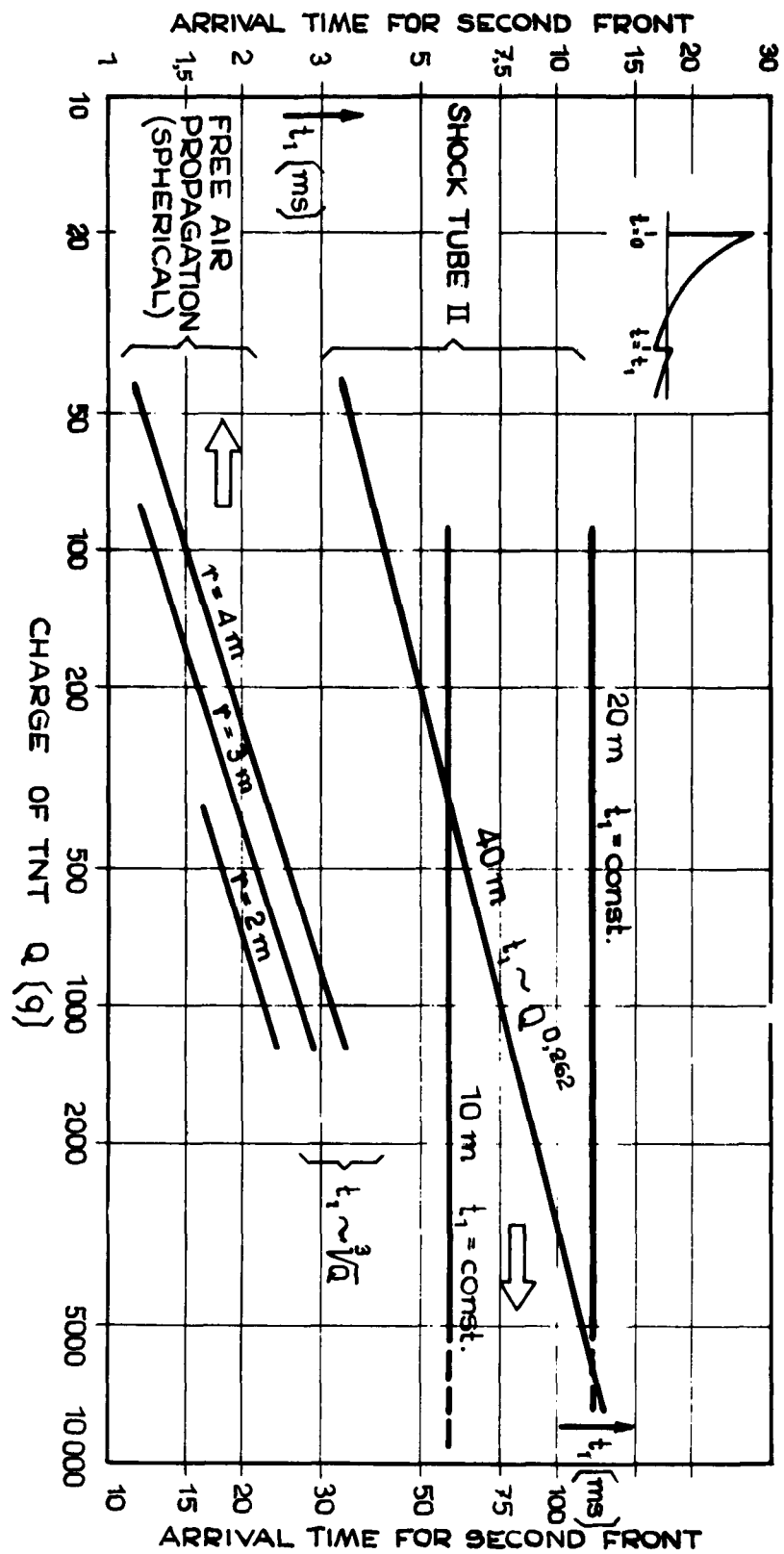


Figure 17. Arrival Time of Second Front

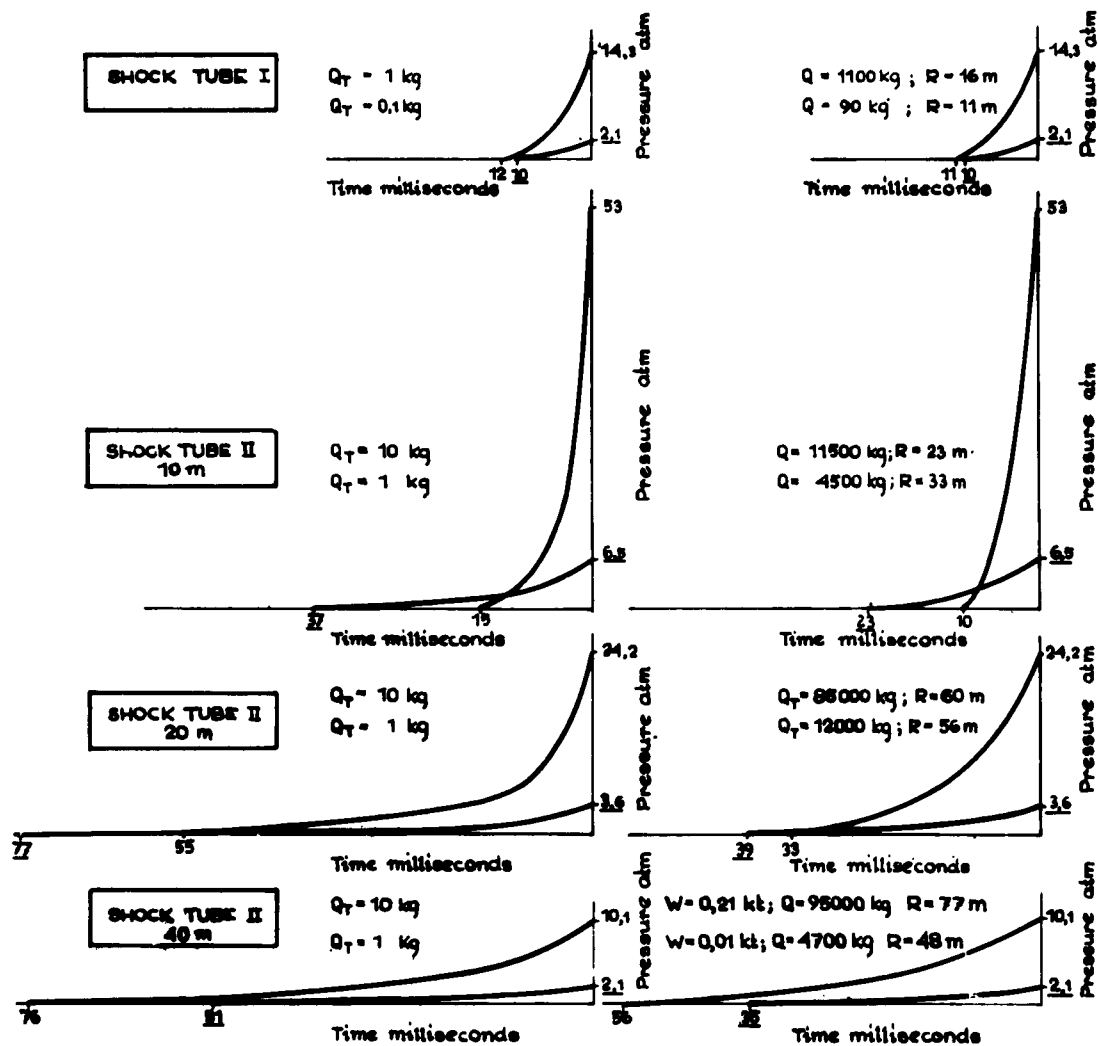


Figure 18. Blast Simulation Capacity of the Shock Tubes: Comparison Between Blast Loadings (the Positive Pressure Phase) Producing in Shock Tubes I and II and Loadings from Free Charges.

Q_T = Charge TNT Used in Shock Tube

Q = Free TNT Charge

W = Yield of Nuclear Weapon



Figure 19. Concrete Slabs Tested in Shock Tube II



Figure 20. Wooden Doors Tested in Shock Tube II

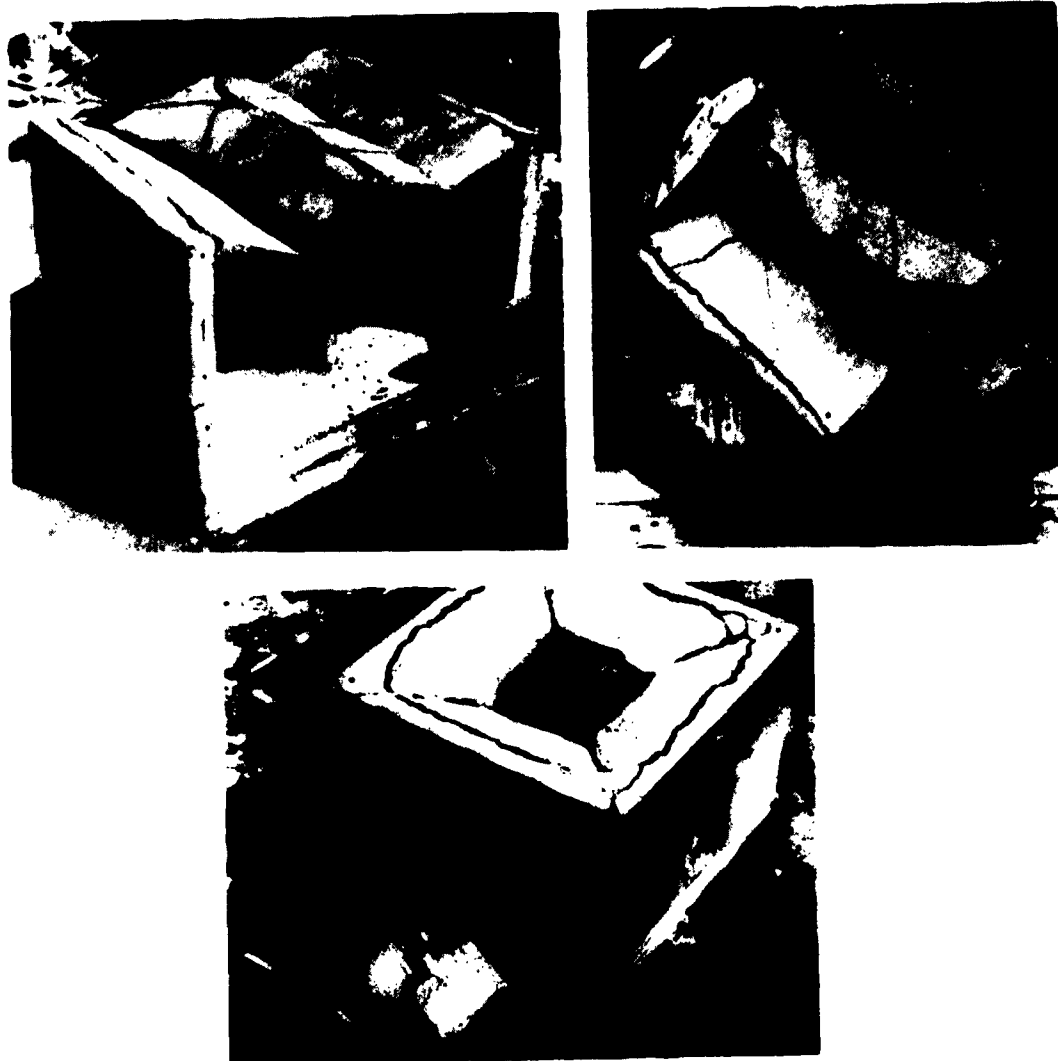


Figure 21. Models of Standard Shelters for Living Blocks Tested in Shock Tube II

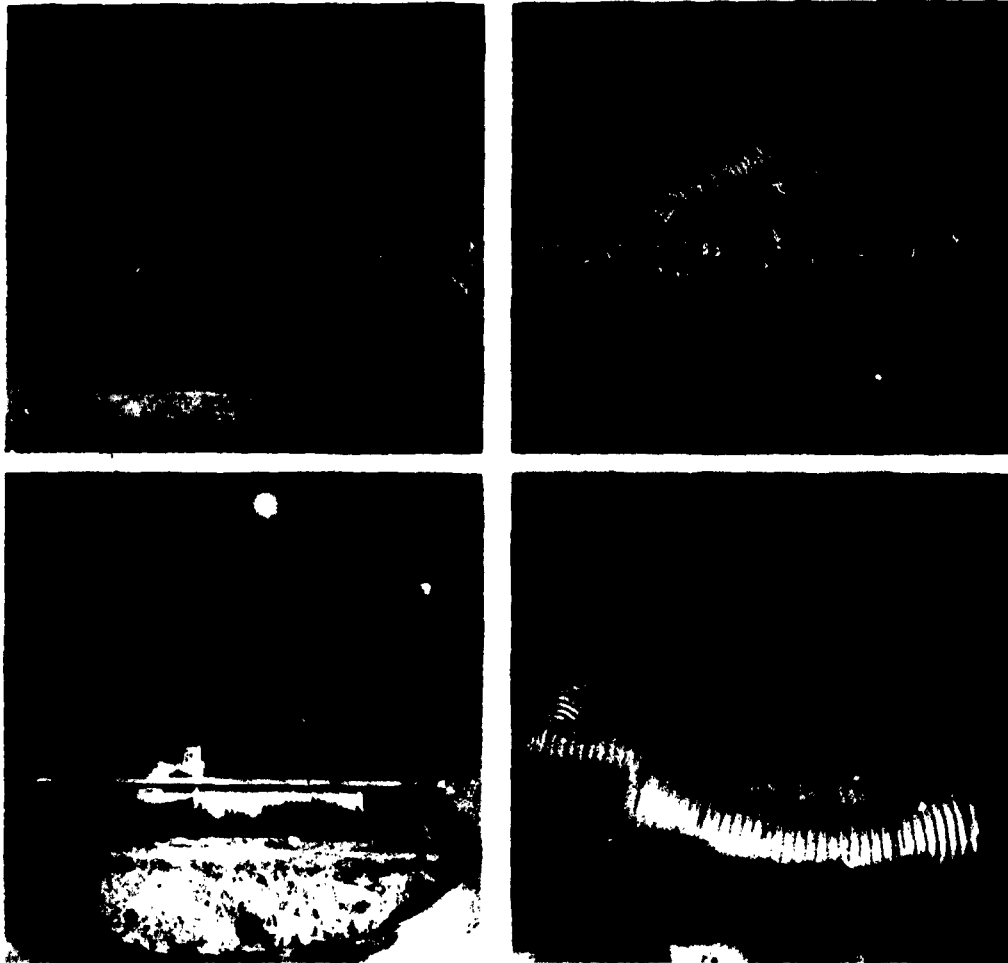


Figure 22. Models of Troup Shelter "Group Helmet" Tested in Shock Tube II

VOLUME DETONATION IN SHOCK TUBES

J. Swatosh, Jr.
A. Wiedermann
Armour Research Foundation

INTRODUCTION

This paper concerns itself with a relatively new method of arranging an explosive charge in shock tubes such that it greatly increases their present capabilities. Some experiments were conducted in the Air Force's Two and Six-Foot Diameter Shock Tubes using "volume detonations" and they indicated substantial increases in overpressure and duration at the test section without increasing the strength of the detonation chamber of the shock tube. The results of these experiments plus the analytical analysis made indicate that there is a hydrodynamic correlation between explosive "volume detonation" and compressed gas-rupturing diaphragm systems.

The detonation of an explosive charge is the most common method of generating shock waves in large diameter shock tubes. In the Air Force six-foot diameter shock tube primacord explosive is most often used because it is safe and easy to handle yet highly efficient. Other methods of shock wave generation, such as compressed gas or explosive gas mixtures require diaphragm and/or balloon-bag systems. These systems, because of their size, require elaborate diaphragm holding and rupturing mechanisms as well as extremely large pumps to handle the quantities of gases necessary to obtain substantial shock wave overpressures. These systems are at best complex and time consuming to operate and therefore do not lend themselves to efficient shock tube operation. Explosive gas mixtures are also extremely dangerous when handled in the quantities necessary for large diameter shock tubes.

Currently, the primacord charge is spirally wound on a vertical frame, Figure 1. The frame is located within the detonation or compression chamber of the shock tube. This type of charge arrangement is referred to as a pancake or plain charge. The pressures and durations

that are obtained at the test section are primarily a function of the distance between the explosive charge and the test section, and the amount of explosive charge. The limitations of such a system are then determined by the physical size and strength of the shock tube. Size or the length of the shock tube limit the durations which can be obtained. When the distance between the charge and the test section is increased the positive wave duration increases in general also. There is also a restriction on the length of shock tube required downstream of the test section. This length determines the time required for reflected shock waves to reach the test section or rarefaction waves in the case of open end shock tubes. The physical strength of the detonation chamber determines the maximum amount of explosive which can safely be detonated and thus a limitation is put on the maximum pressures which are obtainable at the test section.

By placing primacord in a spiral on a vertical frame within the compression section, it was possible to produce in the test section peaked pressure waves up to 70 psi at about 10 ms duration or 50 psi at about 30 ms and 5 psi at about 100 ms. In other words, for these pressure ranges the actual blast wave for a 1/8 KT air burst is duplicated in the test section of the shock tube.

A method of expanding the capabilities of the shock tube without increasing the physical strength of the present detonation chamber is investigated in this paper. How can one place additional explosives in the detonation chamber so as not to impair the safety of the shock tube yet increase the pressure in the test section?

By arranging the primacord strands parallel to the longitudinal axis of the shock tube one obtains a "volume" of explosive. In this configuration considerably more primacord can be placed in the detonation chamber and still not exceed the maximum wall loads per unit area. When a plane charge configuration is used the loads are concentrated in a single diametrical plane. In a volume charge the loads are distributed over the entire volume surface. The length of tube, detonation chamber, which contains the "volume" of explosive can be regarded as a compressed gas

compression chamber without a diaphragm. The burning rate of primacord is relatively fast (20 ft/ms) in comparison to the speed of sound and the speed of the rarefaction waves in the detonation phenomena. The exploding primacord may then be treated similarly to a rupturing diaphragm sytem, i.e., instantaneous release of energy creating a shock phenomenon.

NOMENCLATURE

The following is a list of nomenclature used in the following discussions.

α density ratio,

$$\alpha = W_e/W_1 = \rho_e/\rho_1$$

β explosive energy per unit mass, 20×10^6 ft-lb/lb.

C_1, C_4 local sound velocity, ft/sec

$C_{v_1}, C_{v_4}, C_{v_e}, C_{v_i}$ specific heat, const. vol., Btu/lb-°F.

$C_{p_1}, C_{p_4}, C_{p_e}, C_{p_i}$ specific heat, const. press., Btu/lb-°F.

$\gamma, \gamma', \gamma''$ gas mixture constants, see equation 7

K_1, K_4 ratio of specific heats (C_p/C_v)

L_c compression chamber length, ft.

L_T distance to test section, ft.

P_1, P_4, P_e, P_i pressure, psia

Q energy per unit volume, ft-lb/ft³

$\rho_1, \rho_4, \rho_e, \rho_i$ local density, lb/ft³

R_1, R_e, R_i universal gas constants

t_o positive wave duration, ms

T_1, T_4 temperature, °R

u_1, u_4 partical velocity, ft/sec

W_1, W_e weight

Subscripts designations are:

e explosive

i inerts

1, 2, 3, 4 flow field

SHOCK TUBE EXPERIMENTS

Volume detonation experiments were conducted in both the two and six-foot diameter shock tubes. Tubular pipe frames were constructed to slide into each of the shock tubes. Primacord was taped to these frames as shown in Figures 2 and 3. The purpose of the frames were to distribute the primacord strands as evenly as possible in the detonation volume. Thus making the air-charge mixture as homogeneous as possible. All of the strands were spidered together at the end. In this configuration all strands were simultaneously ignited with a single blasting cap.

The explosive charges were placed at one end of the shock tube as shown in Figure 4. Pressure gages were located in the walls of the detonation chamber to record the detonation pressures. They were also placed at various locations along the length of the shock tube to record the overpressure and duration of the shock wave traversing the tube.

Several different charge lengths or volume lengths were shot, namely, $L_c = 5'$, $10'$ and $20'$. These were fired in both the two and six-foot diameter shock tubes. Several different size charges were also fired. The size or quantity of explosive used was measured as the ratio of weight of explosive, W_e , to the weight of air, W_a , in the compression chamber. Thus one obtains the relatively charge density $\alpha = W_e/W_a$. In the six foot shock tube charge densities up to $1/2$ were fired and in the two-foot shock tube charge densities up to 1 were fired.

The results of these experiments are shown on Figures 5 and 6. Figure 5 is a plot of peak overpressure in the shock tube as a function of distance from the charge. Distance from the charge has been normalized in terms of compression chamber lengths. Figure 6 is a plot of the total positive wave duration as a function of normalized distance from the charge. The pressures and durations scale with L_c as one would expect.

It was observed from the records obtained that the wave phenomenon was very similar to that of a rupturing diaphragm system. There was a flat top wave until rarefaction waves caught up with the shock front and then a peaked wave traversed the tube. This is evidenced on Figure 5 by the constant pressure up till $L_T = 3 L_c$. At $L_T = 3 L_c$ the rarefaction

waves catch up to the flat top shock front and attenuation of the shock front occurs. As this peaked wave traverses the shock tube it obviously attenuates too.

The duration of the positive phase of the blast waves behaves similar to standard diaphragm systems with the exception of the apparent independence on charge density. The positive phase duration appears to depend only on the length of compression chamber or charge length. The positive phase duration is shown as a band on Figure 6. This was done because there seemed to be an indiscriminant scatter of data points following this band. In general the duration of a blast wave is difficult to pinpoint. The duration data procured here was no exception. There was considerable scatter.

One can readily see the increased capability of these shock tubes using volume charges. Before, it was only possible to obtain pressures to 70 psi with a duration of 10 ms. With a volume charge 10 ft long ($L_c = 10'$) and a density ratio of $1/2$, ($\alpha = 1/2$) one obtains a pressure of 70 psi with a duration of approximately 70 ms.

Pressure and duration can be measured at any point in the shock tube, not only at the test section. In other words, the detonation chamber can be relocated at any desired distance from the test section. For any predesired peak pressure and duration values the distance between the charge and test section, L_T , can be chosen, see Figure 4, such that with the proper values of L_c and α , any predesired peak pressure and duration can be obtained within the limits of the values expressed by Figures 5 and 6.

CLOSED BOMB EXPERIMENTS

For some time there has been an interest in even higher peak pressures and durations than those already attainable in the two- and six- foot diameter shock tube with volume detonations. Scaled megaton detonations are now of interest in the area of underground protective construction.

There is thus a need to still further increase the capabilities of these larger shock tubes. To compensate this need some experiments were conducted to determine what pressures or charge densities are required in the detonation chamber to produce the desired shock waves.

These experiments were conducted utilizing a 7-inch diameter x 24-inch long closed bomb. In this closed bomb charge densities up to $\alpha = 4$ were detonated. From previous experience the maximum charge density that the present six-foot diameter shock tube could safely contain is $\alpha = 1/2$. Charge densities of $\alpha = 1$ were safely detonated in the two-foot diameter shock tube. Without strengthening the detonation chambers larger charges cannot be fired.

Once again the primacord strands were evenly distributed over the length of the closed bomb and across its diameter. Pressure sensors were placed in the walls of the bomb to record the detonation pressures. The results of these closed bomb experiments plus the compression pressures recorded in the shock tube experiments are plotted on Figure 7. The average pressure P_4 , is plotted as a function of the charge density α . The curve shown is the average or static detonation pressure in the compression chambers and closed bomb. It should be noted that there are local variations in pressure which may be 100 per cent greater than the average pressure shown on Figure 7. These high pressures are the result of the reflection phenomenon of the initial shock waves produced by the detonation of the primacord strung the length of the compression chamber. Their magnitudes vary depending upon the location of the primacord strands with respect to the recording gages. They are also of very short duration.

The average detonation pressures in the compression chambers of both the two- and six-foot diameter shock tubes were identical for similar charge densities α .

Upon comparing the average pressure in the closed bomb with the average pressure in the shock tube compression chamber it was observed that the closed bomb pressures are somewhat lower at the comparable charge densities. The pressure difference has not been plotted in Figure 7,

instead the average or best fit curve is shown. The difference in pressure can be attributed to several factors. First, the ratio of surface area to charge density is much greater in the closed bomb as compared to the shock tubes. More energy therefore per charge is being lost in heat conduction through the walls. Secondly, and perhaps the most important is the accuracy with which one can read the shock tube records. Since the bomb is fairly well sealed it contains the pressure longer than the shock tubes and thus one is able to determine the average pressure more accurately, that is to say, one has a longer pressure duration with which to determine the average pressure. In the shock tube the average pressure is by comparison quickly relieved and it is difficult to determine exactly what is the average pressure. In any event the closed bomb experiments give a general indication of the magnitude of pressures one can expect in compression chambers with the detonation of larger charge densities.

The duration of the average pressure in the shock tube compression chamber is dependent upon the location of the measuring station in the compression chamber. It also is a function of the compression chamber length. For these experiments the measurements were obtained near the closed end of the compression chamber where one would expect the duration to be longest.

Utilizing this data an analytical analysis is made in the following section to determine what overpressures can be expected downstream in the shock tube from these larger compression chamber pressures.

ANALYSIS

After the detonation of an explosive charge there is a mixture of gases and inerts in the vicinity of the explosion. The gases present are composed primarily of the air originally surrounding the explosive and the explosive gases. These explosive (primacord) gases are chiefly N_2 , CO_2 , CO , H_2O , CH_4 , O_2 , OH , NO , H , etc. The inerts in the system are from the explosive wrapping and from undetonated explosive. The above then are the elements which are in the detonation or compression chamber of the shock tube. To perform a chemical analysis of the actual physical properties of this gaseous mixture would be a very difficult, if

not impossible, task. Therefore, using a few basic assumptions plus experimental results in a simplified analysis one is able to determine the ratio of specific heats, local sound velocity, shock overpressure, particle velocity, etc. Knowing these quantities one is able to predict the magnitude of the shock waves developed.

The following assumptions are made in this analysis. First, all of the energy of the explosive is released instantaneously upon detonation. The burning rate of primacord is approximately 20×10^3 ft/sec. If the compression chamber is 20 feet in length it would take one ms for the primacord to burn, assuming it were ignited at one end. It would take a minimum of 7 ms for sound waves to travel 20 feet in the same medium. Secondly, the problem will be treated similar to a rupturing diaphragm system. This assumption follows from the first. Third, the energy losses through the walls in terms of heat will be considered negligible. Fourth, the air, explosive gases and inerts are thoroughly mixed and considered homogeneous.

The basic shock tube flow problem is illustrated in Figure 8. The area indicated 1 is the ambient stream (air) in front of the shock wave. The area indicated 2 is the flow immediately behind the shock wave and forward of the interface. The flow directly behind the interface and forward of the initial rear facing rarefaction waves is indicated 3. The area indicated 4 is the compression chamber's high pressure gas mixture. The particles in areas 1 and 4 are assumed to be at rest (i.e., $u_1 = u_4 = 0$) for these experiments.

COMPRESSION CHAMBER PRESSURE

After the detonation of the explosive charge in the compression chamber the energy of the driver gas mixture may be written as follows

$$Q = \beta \rho_e \text{ (energy per unit volume)} \quad \text{eq. 1}$$

or in terms of specific heats

$$\beta \rho_e = (T_4 - T_1)(C_{v1} \rho_1 + C_{ve} \rho_e + C_{v1} \rho_1) \quad \text{eq. 2}$$

Using Dalton's Law of Partial Pressures one obtains the compression chamber pressure

$$P_4 = P_1 + P_e + P_i \quad \text{eq. 3}$$

where P_1 , P_e , P_i are the partial pressures of the air, explosive gases and inerts. Assuming the gases are ideal, using the perfect gas law $P = T \rho R$ equation 3 can be written

$$P_4 = T_4 (\rho_1 R_1 + \rho_e R_e + \rho_i R_i) \quad \text{eq. 4}$$

The change in pressure across the imaginary diaphragm is found from equation 4 by subtracting P_1

$$P_4 - P_1 = (T_4 - T_1) \rho_1 R_1 + T_4 (\rho_e R_e + \rho_i R_i) \quad \text{eq. 5}$$

Substituting the temperature terms of equation 2 into equation 5 and rearranging the terms one obtains

$$P_4 - P_1 = \frac{\rho_1 R_1 \beta \rho_e + \beta \rho_e \left[\rho_e \frac{R_e}{R_1} + \rho_i \frac{R_i}{R_1} \right] R_1}{C_{v1} \rho_1 \left[1 + \frac{C_{ve} \rho_e}{C_{v1} \rho_1} + \frac{C_{vi} \rho_i}{C_{v1} \rho_1} \right]} + T_1 \left[\rho_e \frac{R_e}{R_1} + \rho_i \frac{R_i}{R_1} \right] \quad \text{eq. 6}$$

Let

$$\alpha = \frac{\rho_e}{\rho_1}$$

$$\gamma = \frac{\rho_i}{\rho_e} = \frac{\rho_i}{\rho_1} \frac{\rho_1}{\rho_e} = \frac{\rho_i}{\rho_1} \frac{1}{\alpha}$$

$$\gamma' = \frac{C_{ve}}{C_{v1}} + \gamma \frac{C_{vi}}{C_{v1}}$$

$$\gamma'' = \frac{R_e}{R_1} + \gamma \frac{R_i}{R_1}$$

eqs. 7

Assume further that the specific heats remain constant in the range of charge densities considered. Substituting these constants into equation 6 one obtains after simplifying

$$\frac{P_4 - P_1}{P_1} = \frac{\rho_1 [K_1 - 1] \beta}{P_1 [1 + \alpha \gamma']} + \alpha \gamma'' \quad \text{eq. 8}$$

Equation 8 is an analytical expression for the compression chamber pressure in terms of the charge density α . All of the constants are known from the ambient conditions with the exception of γ' and γ'' . These two unknowns represent the physical properties of gaseous mixture in the compression chamber. In order to determine the magnitude of these unknowns equation 8 was curve fitted with the experimental results described before. Using a trial and error method the values of γ' and γ'' were found to be

$$\gamma' = 0.8$$

and

$$\gamma'' = 0.2$$

eqs. 9

Figure 7 is a comparison of the actual experimental results and equation 8 using the values of γ' and γ'' shown in equations 9.

COMPRESSION CHAMBER GAS CONSTANT

The gas constant of the gaseous mixture in the compression chamber, (i.e., indicated area 4) is by definition

$$K_4 = \frac{C_{p_4}}{C_{v_4}} = \frac{\rho_1 C_{p_1} + \rho_e C_{p_e} + \rho_i C_{p_i}}{\rho_1 C_{v_1} + \rho_e C_{v_e} + \rho_i C_{v_i}} \quad \text{eq. 10}$$

dividing by $\rho_1 C_{v_1}$ and simplifying

$$K_4 = \frac{K_1 + \alpha \frac{C_{p_e}}{C_{v_1}} + \alpha \gamma \frac{C_{p_i}}{C_{v_1}}}{1 + \alpha \gamma'} \quad \text{eq. 11}$$

if $C_{v_e} \approx C_{v_1}$ and $R_e \approx R_1$ then equations 7 can be simplified to

$$\gamma' \approx \frac{C_{v_e}}{C_1} (1 + \gamma) \quad \text{eqs. 12}$$

and

$$\gamma'' \approx \frac{R_e}{R_1} (1 + \gamma)$$

Making these substitutions in equation 11 and simplifying

$$\frac{K_4}{K_1} = \frac{K_1 + \alpha \gamma' \left[1 + \frac{\gamma''}{\gamma'} (K_1 - 1) \right]}{K_1 (1 + \alpha \gamma')} \quad \text{eq. 13}$$

Equation 13 is plotted on figure 9. It should be noted that the limiting values of K_4 are 1.4 when $\alpha = 0$ (i.e., no explosive) and 1.1 as $\alpha \rightarrow \infty$.

SPEED OF SOUND IN COMPRESSION CHAMBER

The compression chamber sound velocity is found using the equation of a perfect gas.

$$C_4^2 = K_4 R_4 T_4 = \frac{K_4 P_4}{P_4}$$

or

$$C_4^2 = \frac{K_4 P_4}{\rho_1 + \rho_e + \rho_1} = \frac{K_4 P_4}{\rho_1 [1 + \alpha (1 + \gamma)]}$$

dividing by C_1^2 and rearranging term

$$\frac{C_4}{C_1} = \left[\frac{K_4}{K_1} \frac{P_4}{P_1} \frac{1}{1 + \alpha (1 + \gamma)} \right]^{\frac{1}{2}} \quad \text{eq. 14}$$

By actually measuring the weight of the primacord wrapping it was found to be approximately 10% of the total weight of the primacord prior to detonation.

After detonation one would expect the weight to be even less because of the burning process. The term $\gamma = \frac{P_1}{P_e}$ therefore is a very small quantity.

After dropping the γ term equation 14 becomes,

$$\frac{C_4}{C_1} = \left[\frac{K_4 P_4}{K_1 P_1 (1+\alpha)} \right]^{\frac{1}{2}} \quad \text{eq. 15}$$

Equation 15 is plotted on Figure 9 also.

SHOCK FRONT PRESSURE

Knowing the values of K_4 and C_4 in the compression chamber one can readily compute the shock front pressure from the classic equation below.

$$\frac{P_2}{P_1} = \frac{P_4}{P_1} \left[1 - \frac{(\mu_1 - 1) \left(\frac{P_2}{P_1} - 1 \right)}{\sqrt{(\mu_1 + 1)(1 + \mu_1 \frac{P_2}{P_1})}} \right]^{\frac{K_4 - 1}{2}} \left(\frac{C_1}{C_4} \right)^{\frac{2K_4}{K_4 - 1}} \quad \text{eq. 16}$$

where

$$\mu_1 = \frac{K_1 + 1}{K_1 - 1}$$

Equation 16 has a complex algebraic form and an explicit solution for $\frac{P_2}{P_1}$

has not been obtained. One can, however, plot equation 16 and obtain curves holding $\alpha = \text{constant}$. It should be noted from equations 8, 13 and 15 that P_4 , K_4 and C_4 are all functions of α . Holding α constant one must curve fit equation 16 to find the explicit value of P_2 which satisfies equation 16.

The results of equation 16 are plotted on Figure 10. At the lower values of charge density the analytical expression agrees rather well with the experimental results. At higher charge densities or at larger values of compression chamber pressure the analytical and experimental curves diverge. The authors are of the opinion that in the lower range of compression chamber pressures, where the agreement is best, the experimental results are good. At the higher pressure, however, only a few data points were available and could be in error. The experimental curve also has a curvature which is contrary to the phenomenon. It is, therefore suggested that the theoretical prediction is probably not as contrary as Figure 10 suggests.

ACKNOWLEDGEMENTS

The authors wish to posthumously acknowledge Mr. Eric Wang of AFSC. Mr. Wang's interest and suggestions were extremely valuable to the completion of this and many other shock tube programs.



Fig. 1 PANCAKE CHARGE



Fig. 2 VOLUME CHARGE, 6-FOOT SHOCK TUBE

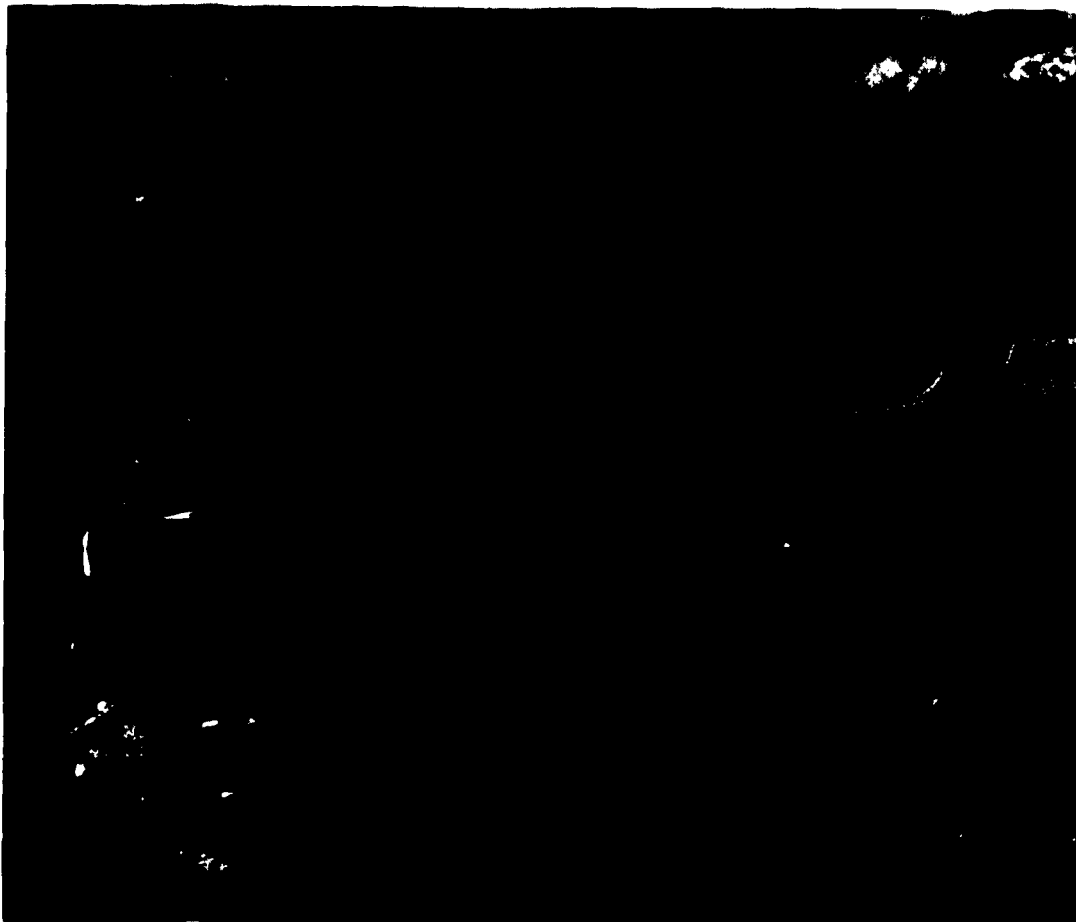
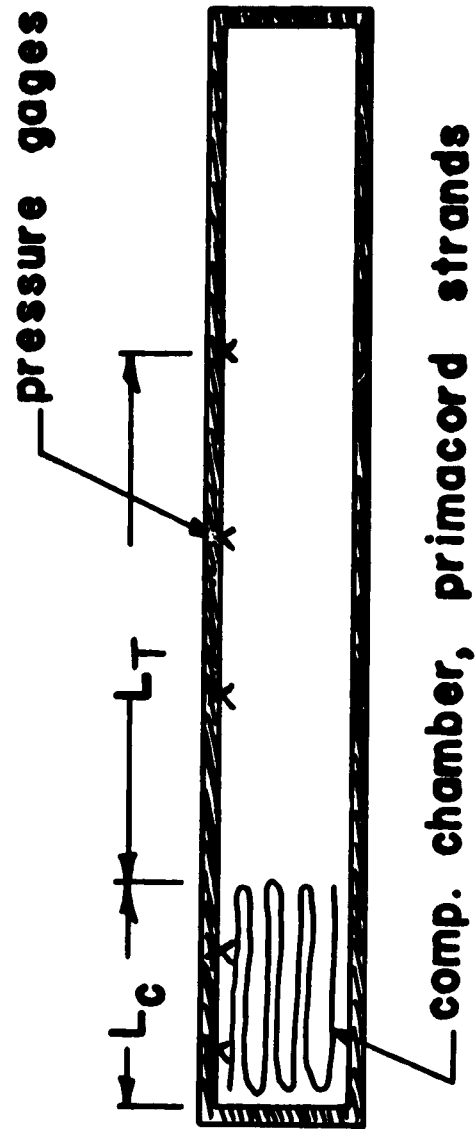
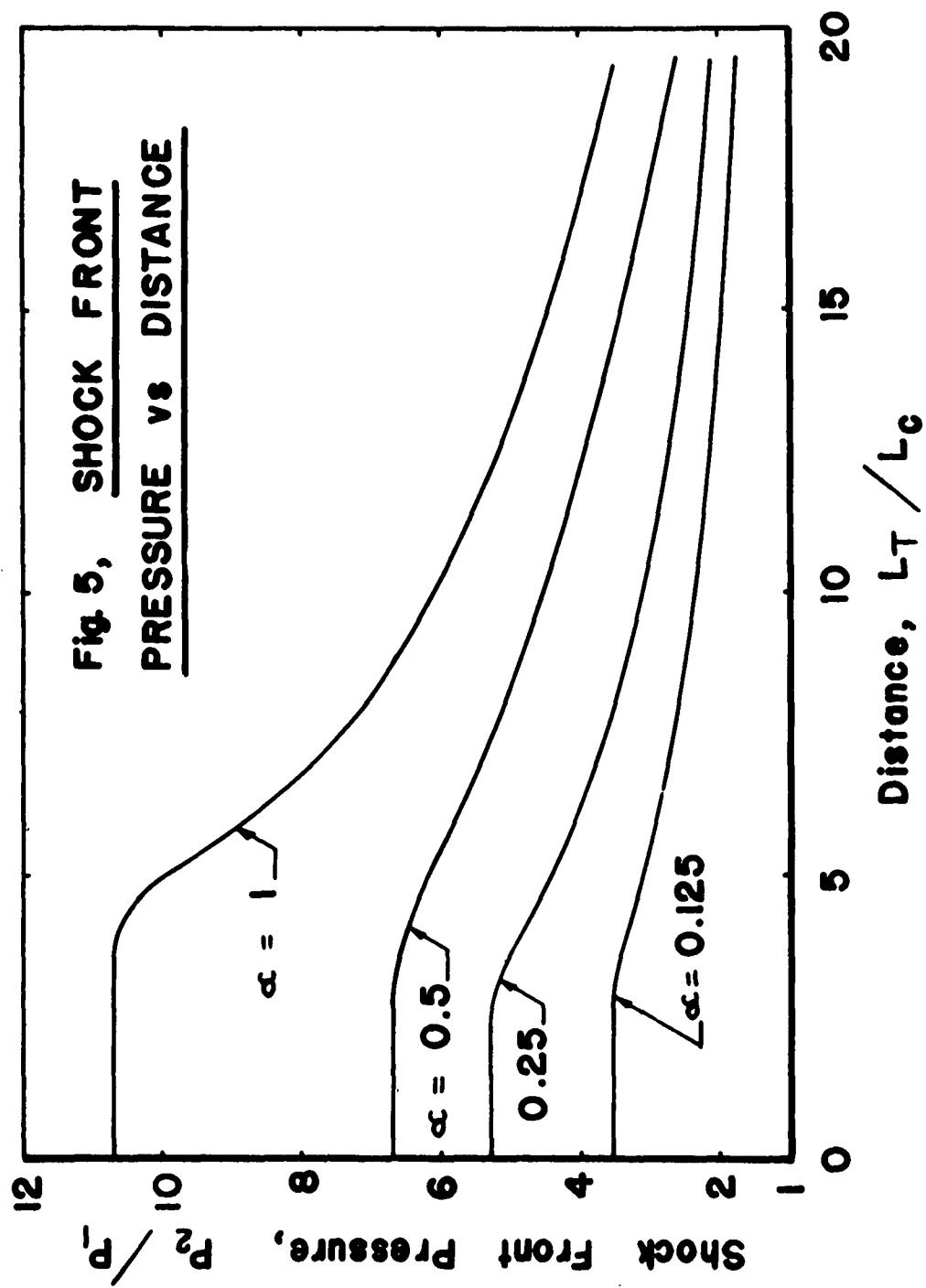
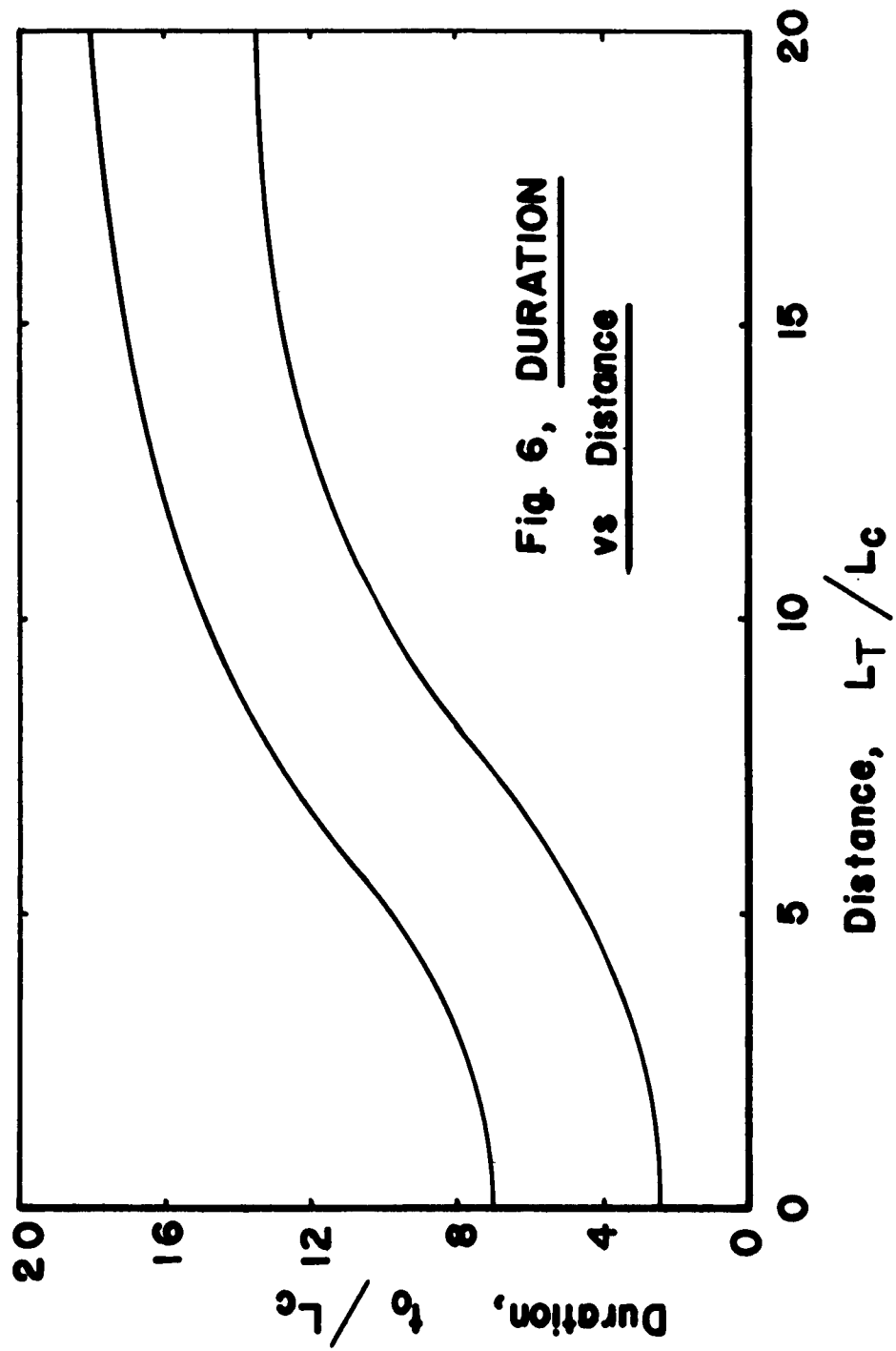


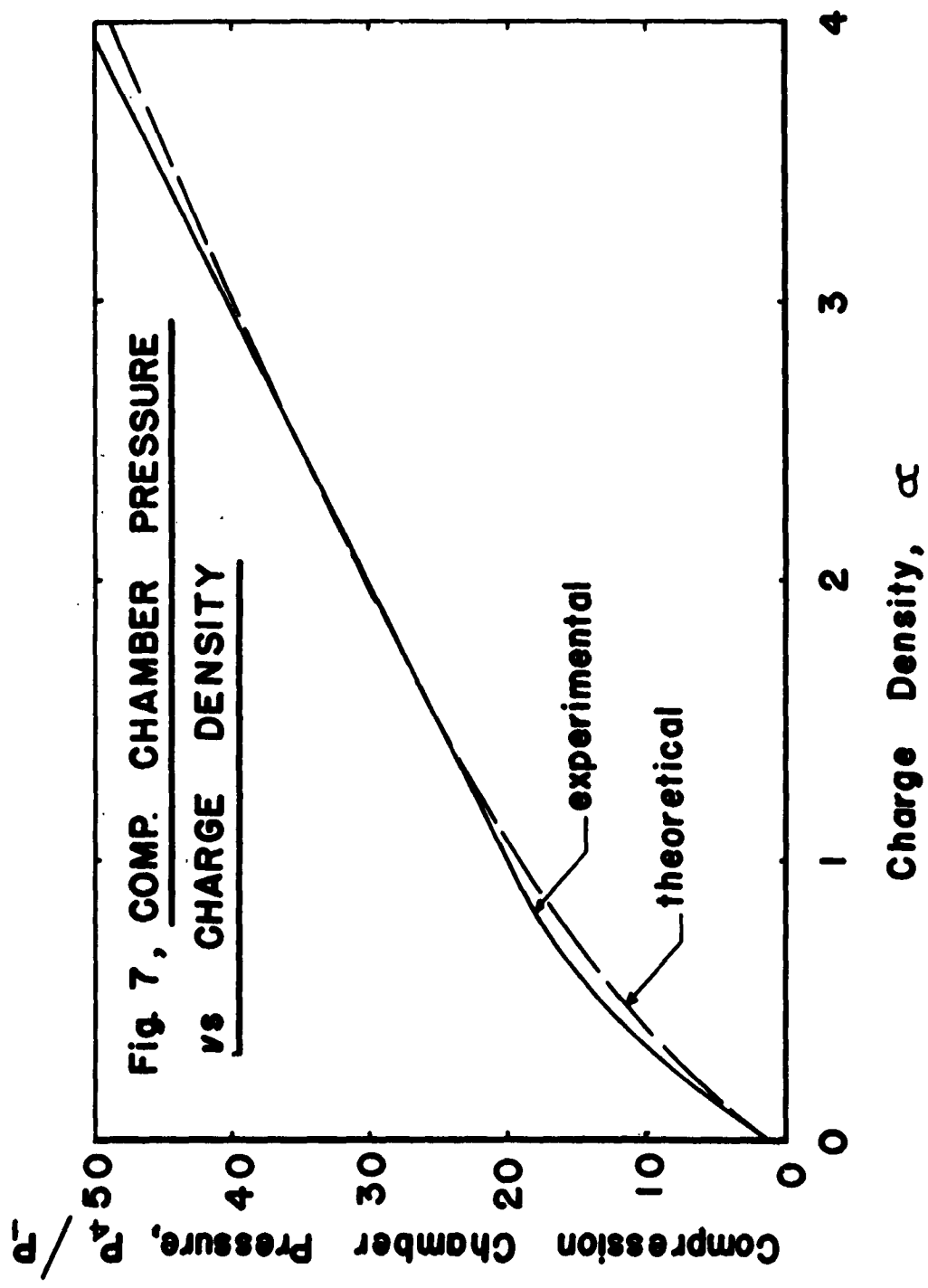
Fig. 3 VOLUME CHARGE, 2-FOOT SHOCK TUBE

Fig 4, SHOCK TUBE SCHEMATIC









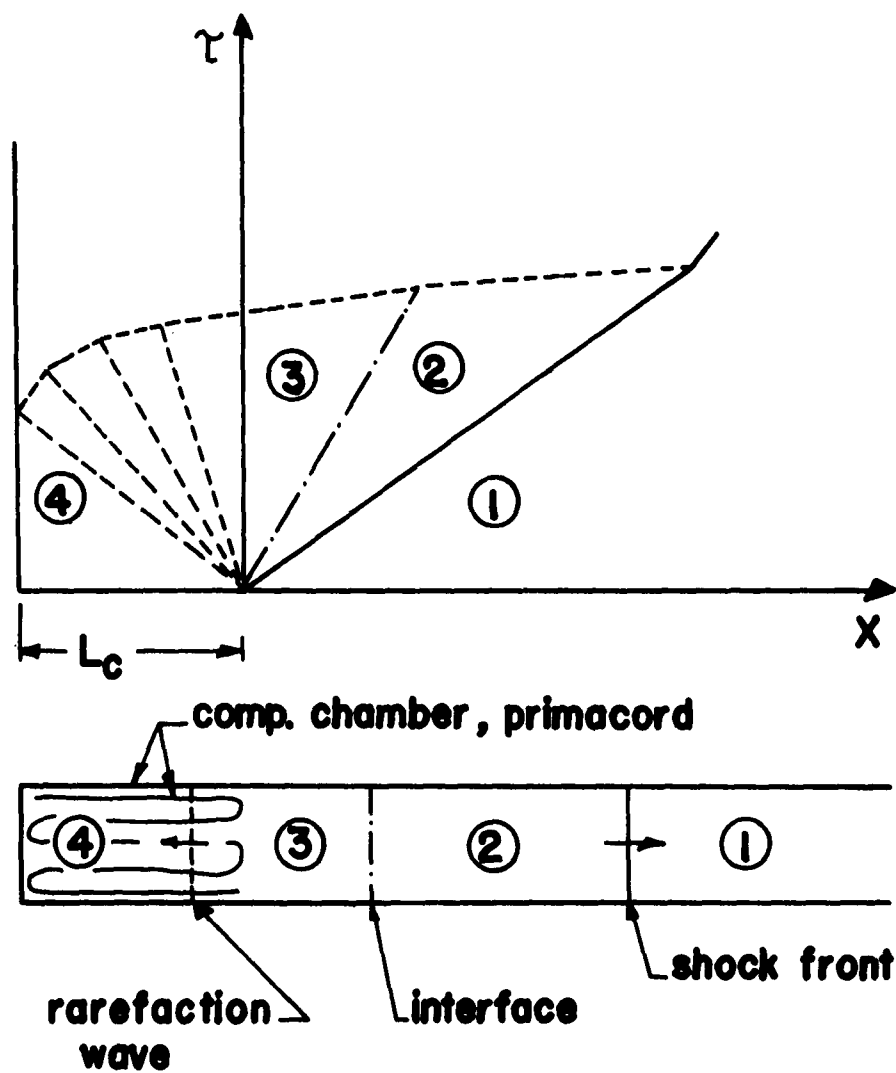
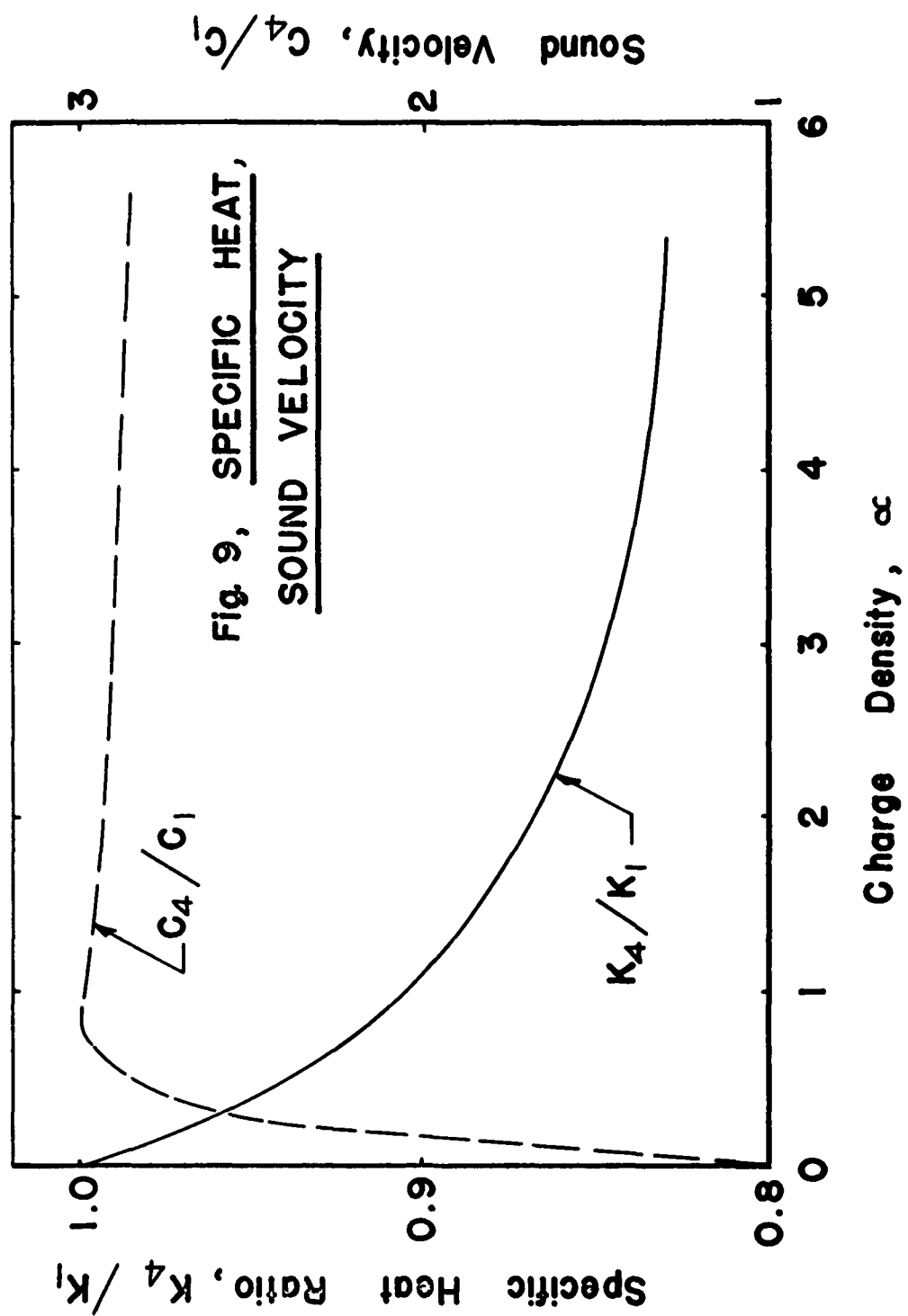
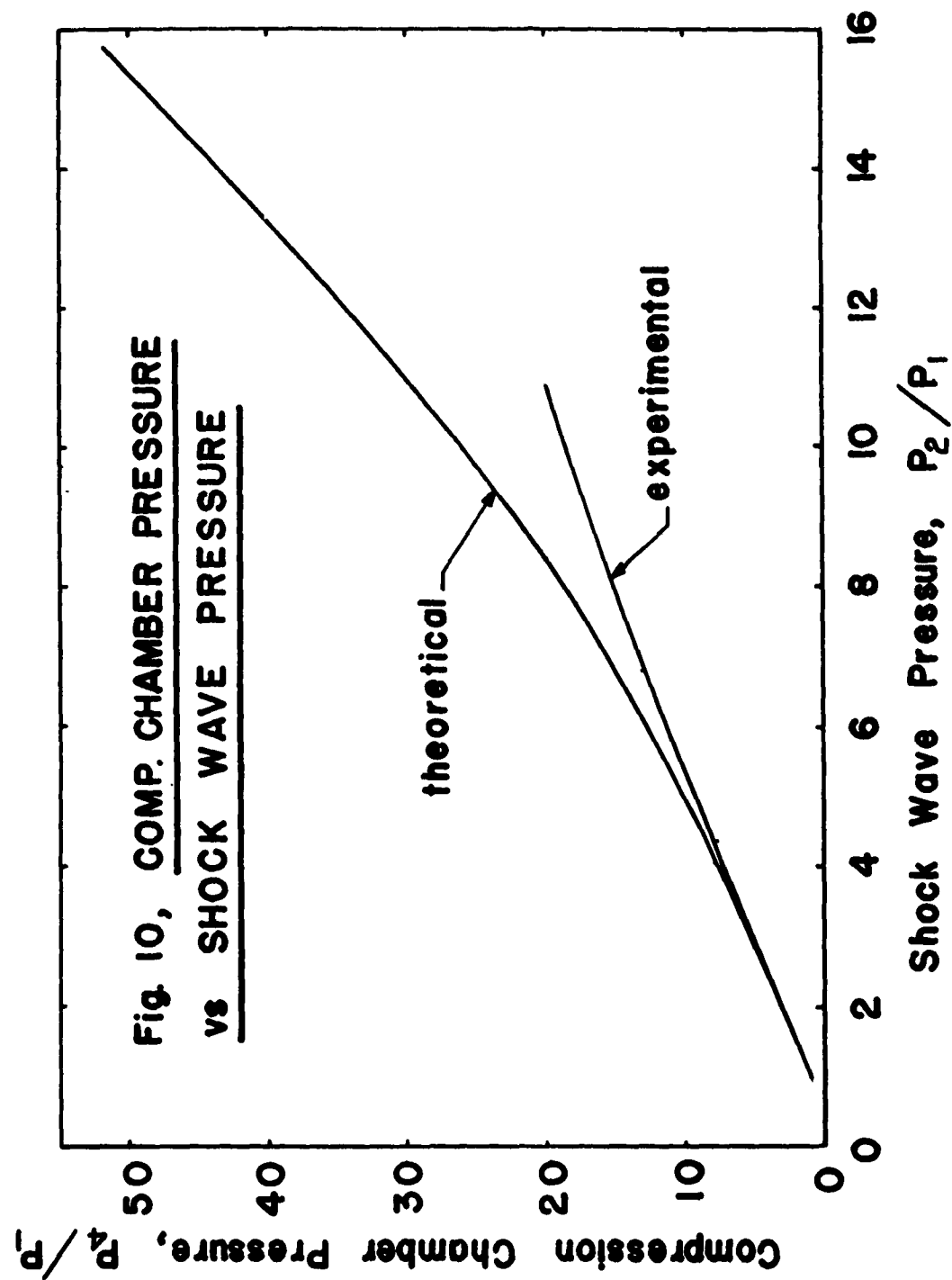


Fig. 8, SIMPLE SHOCK TUBE FLOW





HIGH PRESSURE LOADING DEVICE FOR EVALUATING
BLAST CLOSURE PERFORMANCE

A. H. Wiedermann
Armour Research Foundation

ABSTRACT

This paper describes the performance of a loading device which is capable of simulating the high pressure transient loads acting on blast closures for superhard facilities. The device utilizes the "volume detonation" concept, together with a control orifice to vary the pressure decay. The response of the blast closure influences the pressure decay, hence the equations which govern the gas-dynamic system are coupled to the equations which govern the motion of the valve head.

The theoretical performance of this loading device is compared with the actual performance which was observed during an evaluation of the performance of a 24-inch blast closure for hardened Minuteman facilities.

INTRODUCTION

Hardened underground facilities require fresh air for personnel and equipment purposes. Thus, the air handling systems of these facilities are connected to the ground surface by a number of intake and exhaust ducts. These ducts are provided with blast valves for the purpose of sealing off the facility from the atmosphere under nuclear attack conditions. As a necessary step in insuring that this countries retaliatory capability does indeed exist, it is essential that these blast valves or closures be evaluated under simulated attack conditions.

The Air Force 6-foot shock tube has been used to proof-test prototype blast valves for the Atlas and Titan II facilities under simulated conditions. The maximum load on the valve head were of the order of several hundred pounds per square inch. The strength of the large shock

tube does not permit its use as a loading device for blast valves which require peak loads in excess of approximately 300 psi.

The requirements for the Minuteman facilities results in peak loads on some of its blast valves which are in excess of this value. Therefore another device or technique had to be developed so that these valves could be tested.

Recent experiments at the Air Force Shock Tube Laboratory on close bomb systems indicate that suddenly applied loads of the order of 1000 psi can be achieved by detonating explosives (primacord) in a closed volume. The magnitude of the pressure depends upon the quantity of explosive, per unit volume. The pressure is relatively uniform throughout the volume since the explosive is distributed throughout the volume. The time decay of the pressure can be controlled in part, by allowing the gas to leak out of the detonation chamber through suitable orifices.

It is the purpose of this paper to describe the performance of a loading device which is capable of simulating the high pressure transient loads which act on blast valves for superhard facilities.

DESCRIPTION OF THE LOADING DEVICE

The loading device consists physically of a detonation chamber, that is a heavy cylindrical tube, which is connected to the blast valve. An orifice plate or flange seals off the other end of the detonation chamber. Slide 1 presents a schematic diagram of the loading device. This paper deals with blast valves which consist of a translating mass of piston as the sealing mechanism. The application of the high pressure load on the valve head sets the head in motion. The motion of the head is largely controlled by inertia effects, at least during the port closing phase of the motion. The moving mass is then arrested by some means and the valve seals off the underground facility from the atmosphere. The valve is characterized by its mass, M , and its projected area, A . The motion of the valve head increases the volume of the system and depending upon the magnitude of the increased volume, may influence significantly, the load on the valve head. This coupling effect will be discussed in detail in this paper.

The "volume detonation" technique which was discussed in some detail in the previous paper was used as the method of generating the initial high pressure conditions in the pressure vessel. A prescribed amount of explosive (primacord) is distributed fairly uniformly over the volume of the pressure vessel and then detonated. The dependence of the magnitude of the initial pressure after detonation, P_0 , upon the relative explosive density, α , (the ratio of the weight of explosive to the weight of air) is given in Slide 2. The curve represents average values since these types of explosive systems possess inherently poor reproducibility characteristics. The maximum over shot observed in this system has been approximately 100 per cent of the mean pressure (P_0).

It is desirable to minimize the size of the detonation volume, since the quantity of explosive needed, for a given peak load, is proportional to the size, and since the hazard involved in conducting such an experiment increases with the quantity of explosive needed. Furthermore the cost of a pressure vessel increases quite rapidly with the size of the vessel.

The device which is proposed here is only one of a number of systems which could be used. The explosive system could be eliminated by substituting a "shot-start" system in which the peak load is applied slowly by the use of compressed gas and in which the valve motion is restrained until the proper time. This type of system would require elaborate seals between the valve head and the valve body. The proposed system has the advantage of being simple as well as allowing other features of the valves performance, such as the transient "blow-by" or leakage pressures to be observed.

The design load which acts on the blast valve is normally determined by scaled shock tube experiments on the duct systems used in these hardened facilities. These loads are generally characterized by a suddenly applied load which is due to the reflection of the shock wave which enters the duct system. The load then decays quite rapidly due to local diffraction effects and then remains relatively constant. The degree of simulation of this load needed in evaluating the performance of a blast valve depends

upon the specific requirements of the program, however, it is generally excepted that if the peak load and the impulse, at the time of valve port closure, is conserved, then adequate simulation exist. Thus only a single orifice is needed to provide for the pressure decay in the detonation chamber. More elaborate pressure time variations could be obtained by providing a series of time dependent orifices, however, this additional complexity is generally not required.

THEORETICAL PERFORMANCE

The following paragraphs summarize an analysis of the gas dynamic system which is proposed. This analysis is necessary in order to size the experimental apparatus and takes into consideration the effects of the pressure decay due to the valve head motion, and the gas leakage through the valve and control orifices.

The analysis is of a quasi-steady type and assumes that the flow through the orifice is choked. This requires that the absolute pressure, P , in the chamber be greater than a critical amount, viz.

$$\frac{P(t)}{P_{\infty}} \geq \left[\frac{k+1}{2} \right]^{\frac{k}{k-1}}, \quad (\approx 1.8 \text{ for } k=1.2) \quad (1)$$

where

t = time

P_{∞} = ambient air pressure

k = ratio of specific heat

During the time of interest the pressure will be considerably greater than this critical amount. The quasi-steady analysis is valid if the interval of time for a significant change of the pressure is much greater than the transient time of a sound signal in the chamber. Thus no pressure gradients will be set up in the chamber. In the system which was tested a slight (about 5 per cent) pressure gradient was observed, at least for the fast decay rates. The minimum closing time was of the order of 10 milliseconds.

The analysis is based upon the assumption that the expansion process of the gas in the chamber is isentropic, and that the gas is a perfect gas. Hence, by applying the equations of motion of the valve head (assuming that the inertia force is the only retarding force) and the mass flow equation for a choked orifice, one obtains the following set of equations.

$$\frac{dm}{dt} = - \left[\frac{2}{k+1} \right]^{1/2} \frac{k+1}{k-1} \left[\frac{\frac{m}{\rho_o}}{V_o + xA} \right]^{\frac{k+1}{2}} \cdot \rho_o c_o A_o \quad (2)$$

$$\frac{d^2x}{dt^2} = \frac{AP(t)}{M} \quad (3)$$

$$\frac{P}{P_o} = \left[\frac{\rho}{\rho_o} \right]^k \quad (4)$$

$$P = \rho RT \quad (5)$$

where:

- m = mass of gas in chamber
- ρ_o = initial density (after detonation)
- ρ = density
- c_o = initial sound velocity
- A_o = area of orifice
- x = displacement of valve head
- A = area of valve head
- P_o = initial pressure (absolute)
- R = gas constant
- T = absolute temperature
- V_o = Volume of detonation chamber

In dimensionless form the variables become:

$$\tau = \frac{tc_o A_o}{V_o}$$

$$\tau' = t \sqrt{\frac{P_0 A^2}{V_0 M}}$$

$$\beta^2 = \left(\frac{\tau'}{\tau}\right)^2 = \frac{P_0 V_0 A^2}{M C_0^2 A_0^2} \quad (6)$$

$$\mu = \frac{m}{m_0}$$

$$\zeta = \frac{x A}{V_0}$$

$$\xi = -\frac{P}{P_0}$$

where: m_0 = initial mass of gas in chamber
Equations (2), (3) and become

$$\frac{d\mu}{d\tau} = -\lambda \xi^h \quad (7)$$

$$\frac{d^2 \zeta}{d\tau^2} = \beta^2 \xi \quad (8)$$

$$\xi = \left[\frac{\mu}{1 + \zeta} \right]^k \quad (9)$$

where

$$\lambda = \left[\frac{2}{k+1} \right]^{1/2} \frac{(k+1)}{(k-1)} \quad (10)$$

$$h = \frac{k+1}{2k} \quad (11)$$

The initial conditions are:

$$\begin{aligned} \mu(0) &= 1 \\ \zeta(0) &= 0 \\ \frac{d\zeta(0)}{dt} &= 0 \\ (0) &= 1 \end{aligned} \quad (12)$$

It will be informative to examine two limiting cases before investigating the general solution. These limiting cases are: (1) the case when the increase in volume due to the valve motion is negligible ($\xi = 0$) and (2) the case where there is no gas leakage ($A_0 = 0$).

The solution for the first case is readily obtained by integrating equation (7), hence,

$$\xi = \left[1 + \left(\frac{k-1}{2} \right) \lambda \tau \right]^{-\frac{2k}{k-1}} \quad (13)$$

This equation is presented in Slide 3 (for $k = 1.2$) and it should be noted that the nature of the pressure decay is very similar to that of the surface blast wave. The decay rate can be controlled by varying either A_0 or V_0 (c_0 being fixed by the relative explosive density, α).

The solution for the second case cannot be obtained readily in an explicit form, however, by the combination of analytical and numerical integration one obtains the results which are plotted in Slide 4 ($k = 1.2$). In performing the numerical integration the value of the integrand becomes infinite at the limit point ($\tau = 0$) and hence a linearized solution for $(1 - \xi) \ll 1$ was obtained, viz.

$$\tau^1 = \sqrt{\frac{2}{k} (1 - \xi)} \left[1 + \frac{(k+1)}{3k} (1 - \xi) \right] \quad (14)$$

This equation is reasonably accurate for $\xi \geq 0.9$. The pressure decay for this case does not correspond too well with the pressure decay of the surface blast wave. This is due to the fact that the increase in volume at early times is very small (i.e., the valve head velocity is initially zero). The decay rate can only be controlled by varying the volume of the chamber; all the remaining parameters are fixed.

The general solution for the coupled equations cannot be readily obtained analytically, however a linearized or approximate solution for early times can be obtained in closed form, viz.

$$\xi = 1 - \left\{ k \lambda \tau + \frac{\tau^2}{2} \left[k \rho^2 - k^2 \lambda^2 h \right] \right\} \quad (15)$$

This approximate solution is presented in Slide 5 ($k' = 1.2$) together with the exact solution for the case $\beta^2 = 0$. The accuracy of this equation is sufficient for the proposed purposes over the range of the variables presented in this slide and will permit the selection of the values of the parameters for the test apparatus.

To obtain the general solution, it is necessary to integrate the equation numerically. The following difference equations were used for this calculation.

$$\begin{aligned}
 \mu_{i+1} &= \mu_i - \lambda \xi_i h \Delta \tau \\
 \left(\frac{d\xi}{d\tau} \right)_{i+1} &= \left(\frac{d\xi}{d\tau} \right)_i + \beta^2 \xi_i \Delta \tau \\
 \xi_{i+1} &= \xi_i + \left(\frac{d\xi}{d\tau} \right)_i \Delta \tau \\
 \xi_i &= \left[\frac{\mu_i}{1 + \xi_i} \right]^k \\
 \tau_{i+1} &= \tau_i + \Delta \tau
 \end{aligned} \tag{16}$$

The results are presented in Slide 6 for $k = 1.2$.

It is of interest to examine the theoretical performance of this type of device and to determine the sensitivity of the solution to certain parameters. The value of these parameters, such as k and c_0 , may not be known very accurately. Additional calculations were made to illustrate this sensitivity and are presented in Slide 7. An examination of the predicted initial conditions from the volume detonation technique (Slide 2) shows that the value of k , at least at high pressure, is reasonably well determined. An error of less than five per cent should be expected due to the variance of the ratio of specific heats. The value of the initial (after detonation) sound velocity is probably not known to better than 10 per cent. The initial sound velocity, c_0 , is a proportionality factor in the time (τ) scale, hence one cannot expect a prediction to be much better than 10 per cent.

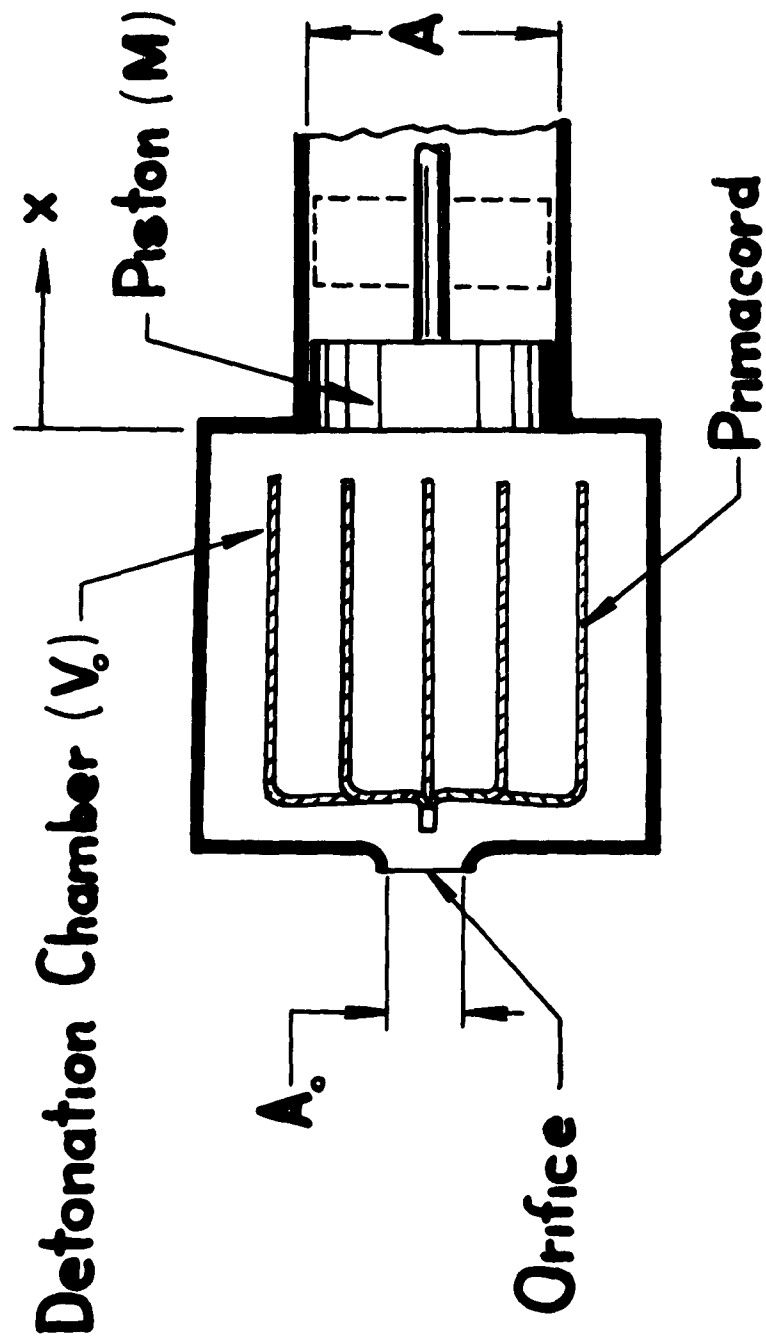
EXPERIMENTAL RESULTS

Experiments were performed in a device which was constructed to evaluate the performance of a blast valve which was being designed for use in a hardened Minuteman Facility. A chamber volume of approximately five cubic feet was used and pressures were measured at several positions along the side of the detonation chamber. A typical pressure time record is illustrated by the lower-trace in Slide 8. The characteristic overshoot and subsequent high frequency pressure oscillations due to the volume detonation techniques are shown. The large area of the valve head is subjected to these high frequency pressure oscillations, but in a random spacial manner, so that the total applied load, after the initial discontinuity, is smooth and monotonously decreasing with time.

The analysis was performed in order that the loading device could be designed and some measure of its performance could be estimated. The majority of the experiments were conducted with initial conditions which resulted in a valve of the parameter β^2 beginning in the range of approximately 0.5 to 1. Hence the experiments which were performed are limited as a means for evaluating the corrections of the analysis over the entire range of the parameter. The lower trace in Slides 9 and 10 presents a comparison of the predicted and observed pressure time variation. In each case the agreement is good, perhaps somewhat better than should be expected considering the uncertainty in some of initial conditions. The time scale in these slides is 5 milliseconds per major division.

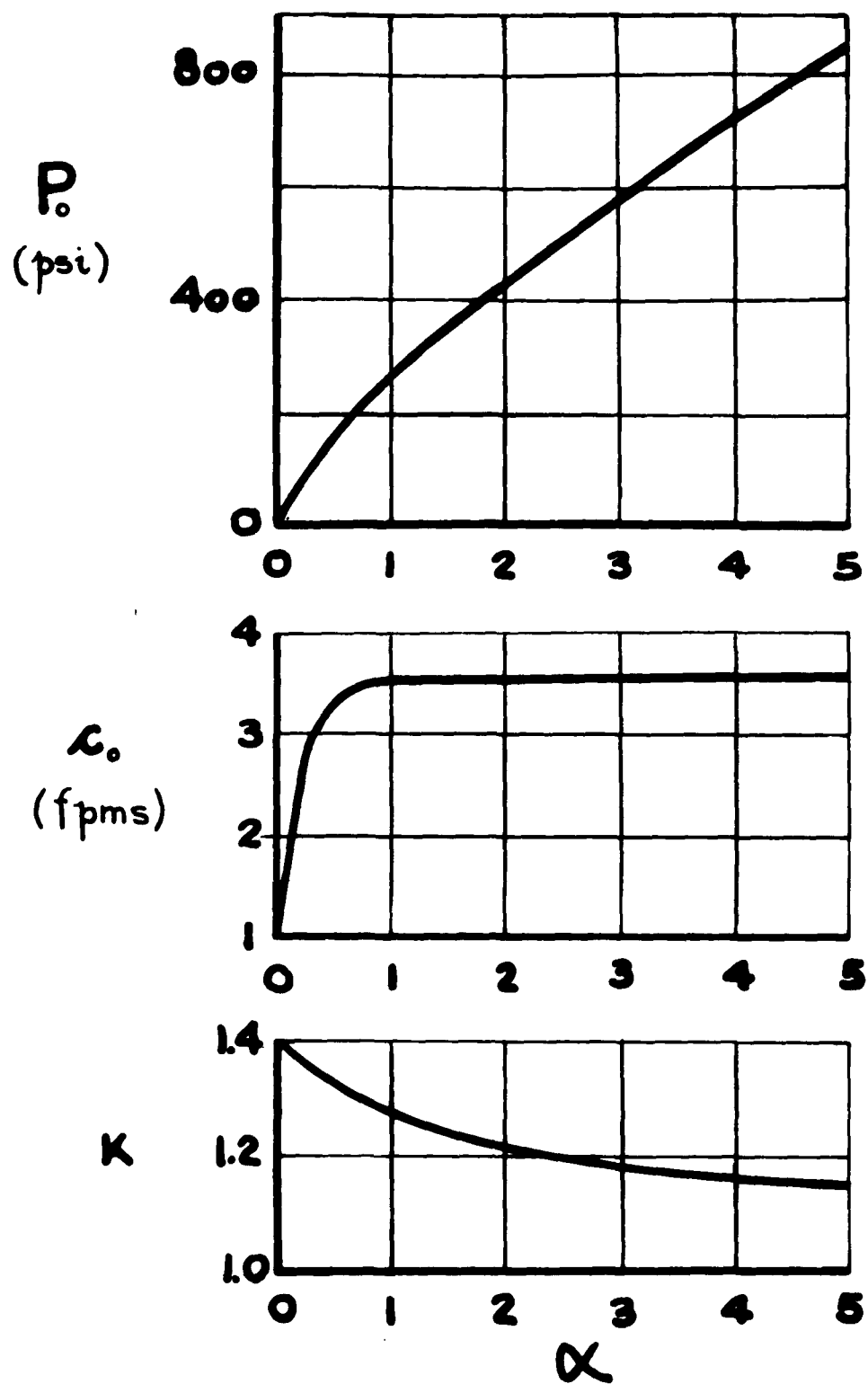
ACKNOWLEDGEMENTS

The author would like to acknowledge the Structures Division of the Air Force Special Weapons Center for the use of the material dealing with the "volume detonation" technique and the R. M. Parsons Company for the use of the experimental pressure-time records which were observed during the proof testing of a Prototype Minuteman blast valve.

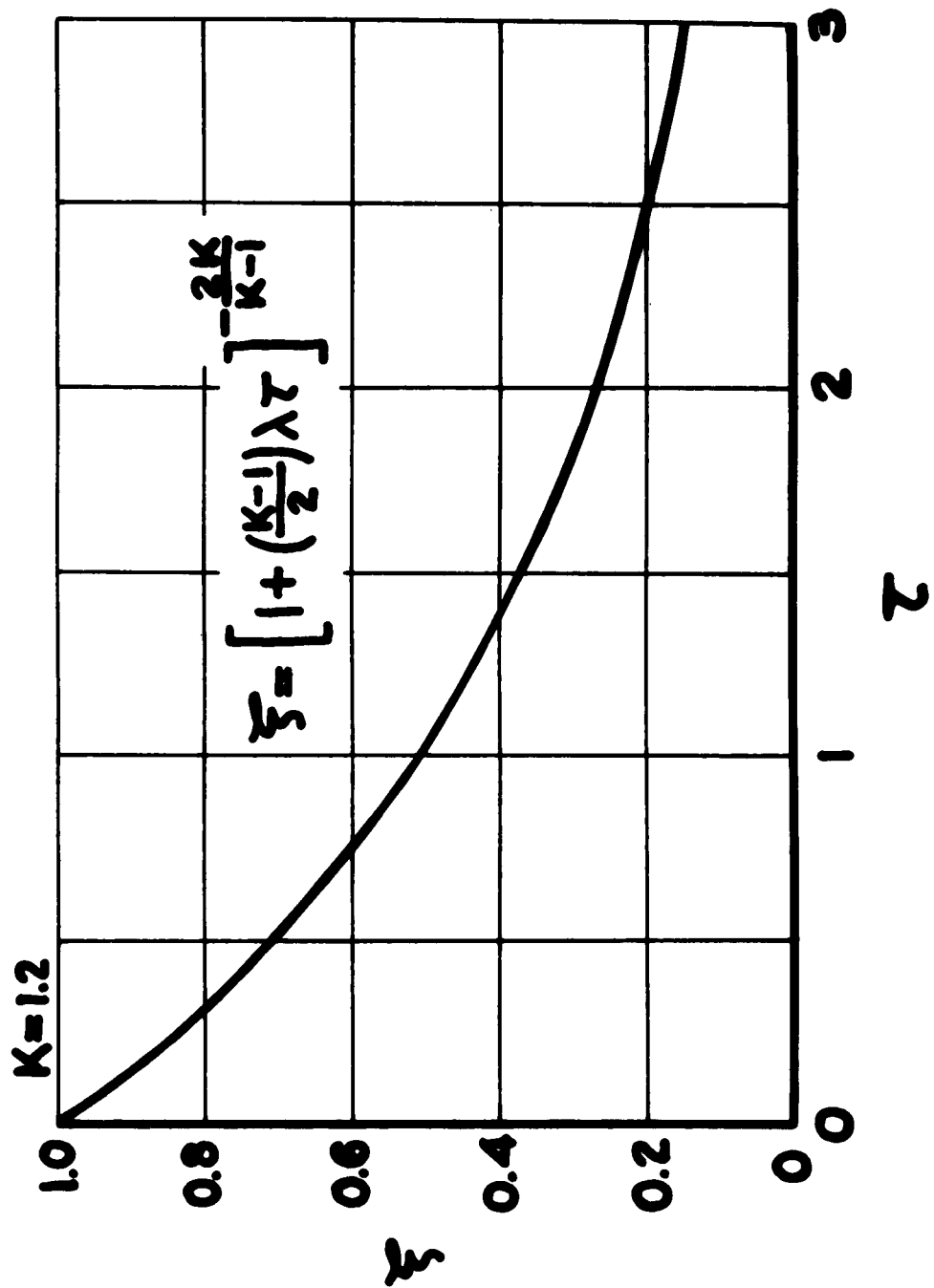


Schematic of Loading Device

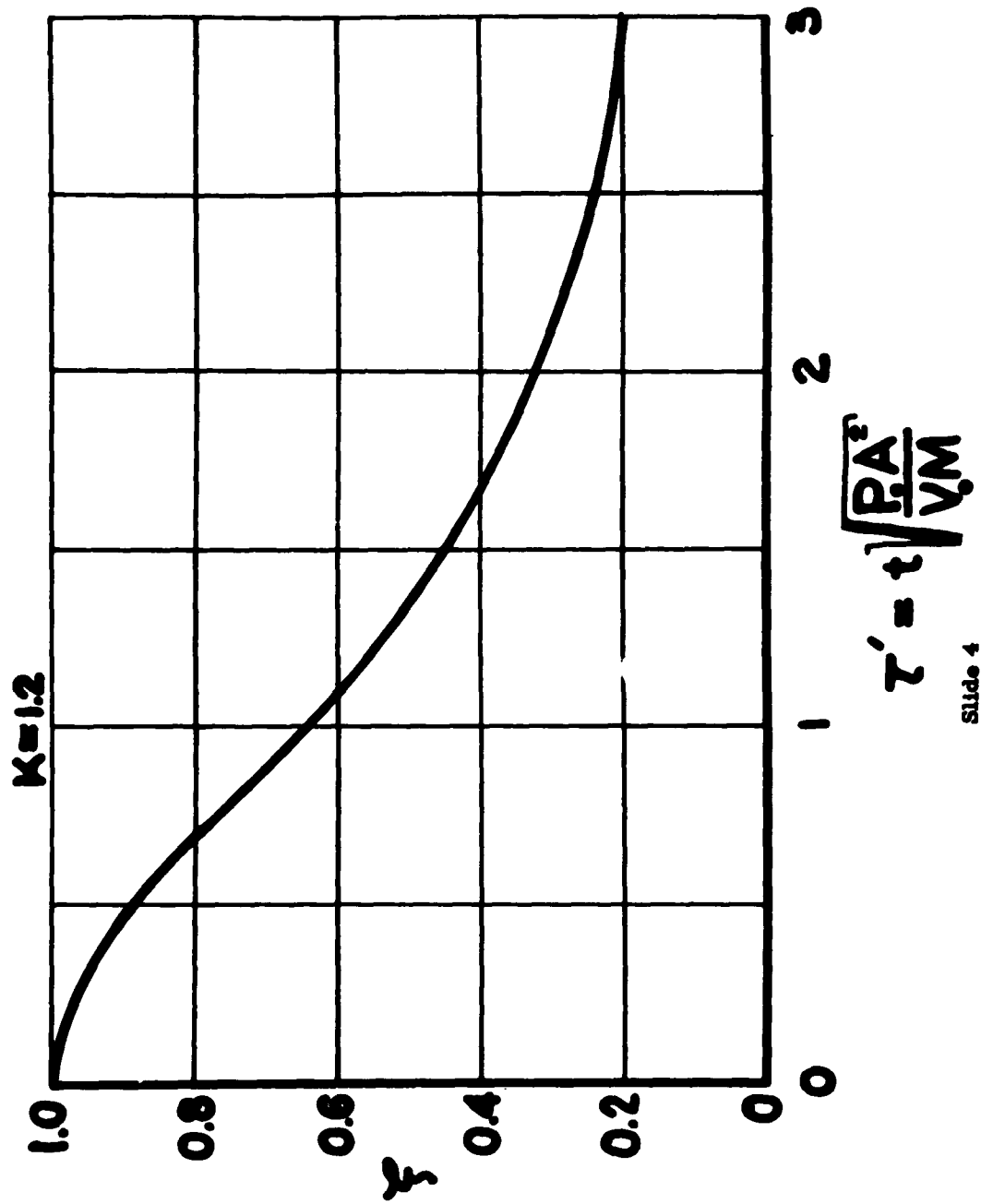
Slide 1



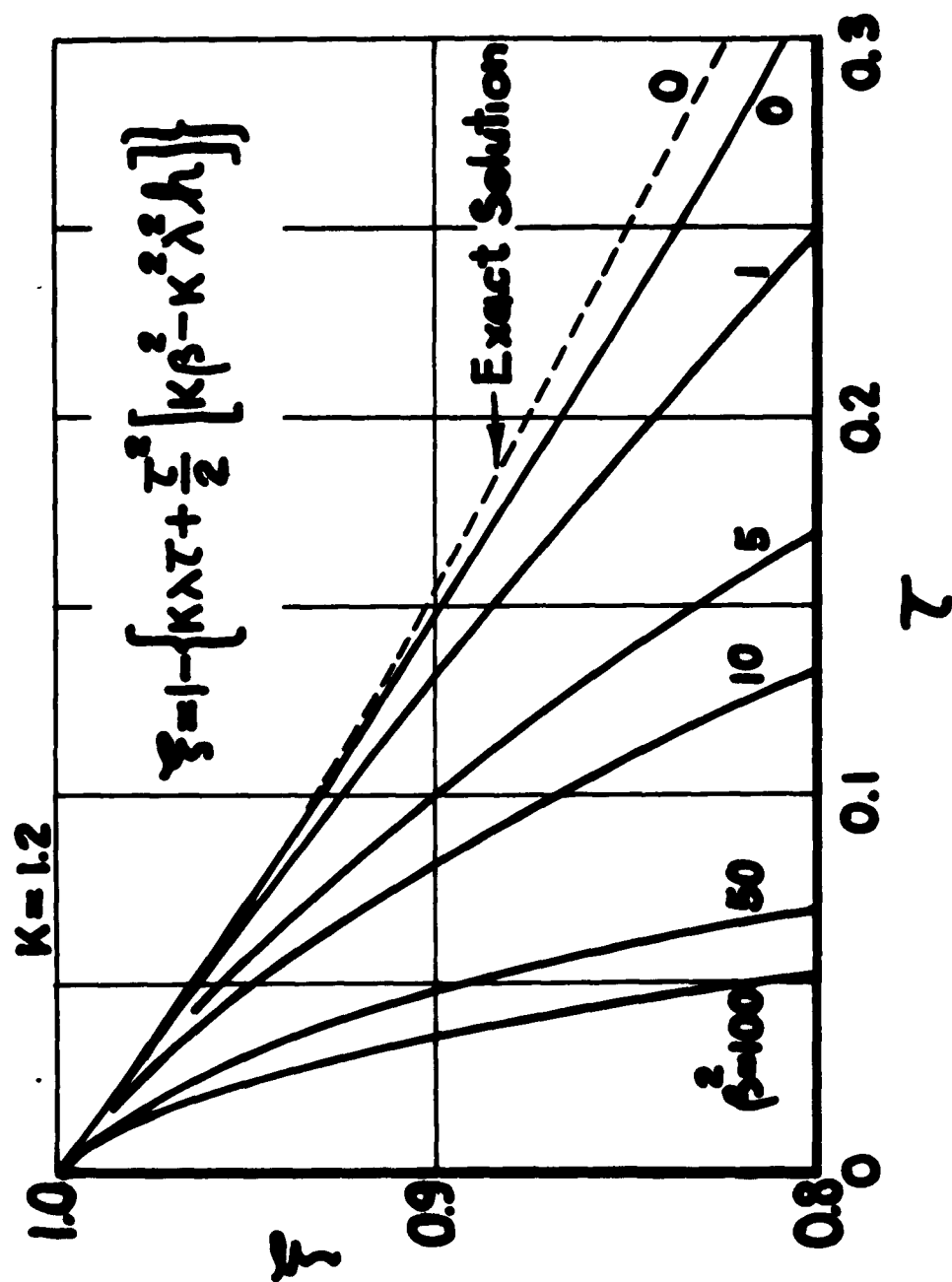
Slide 2



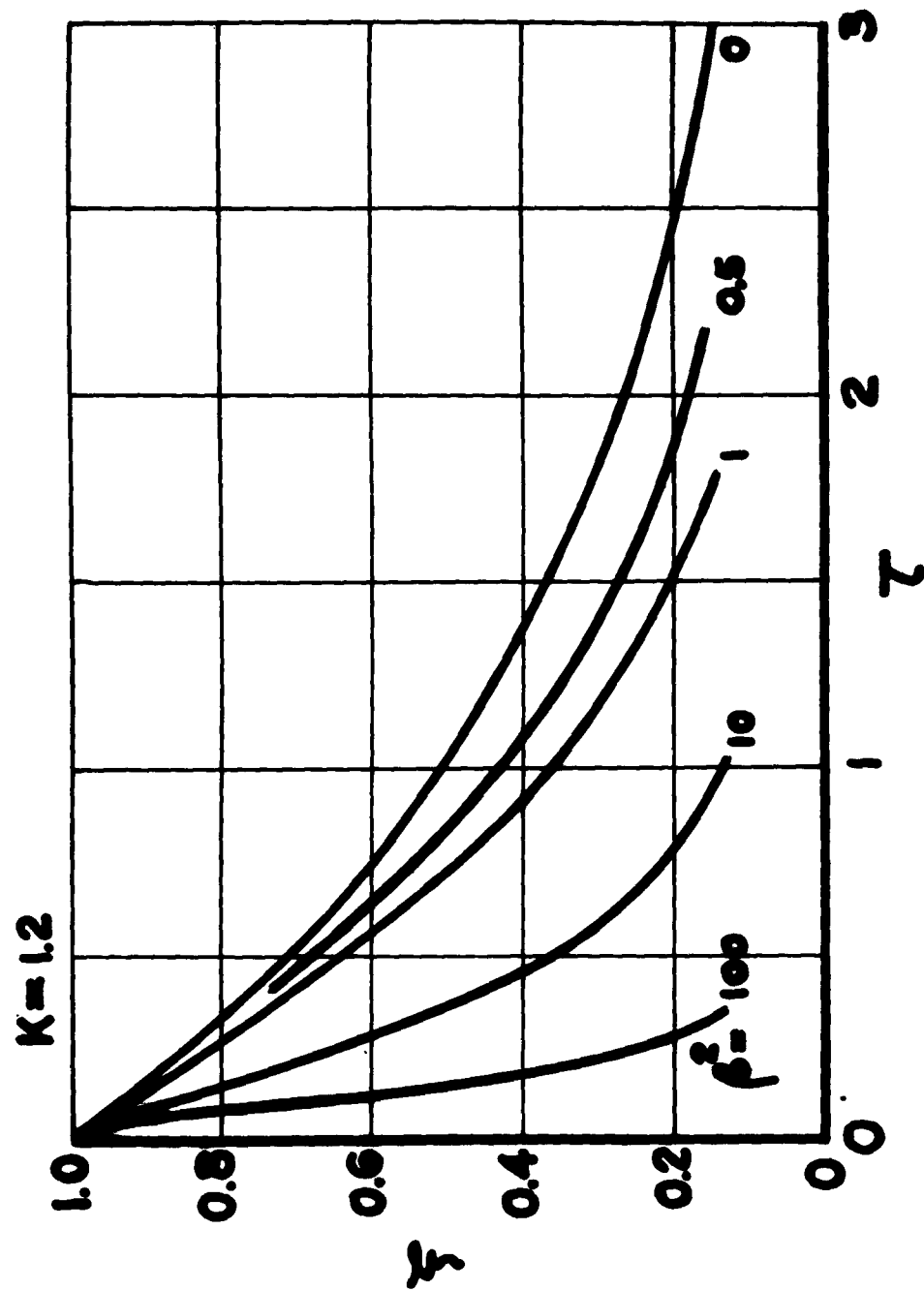
Slide 3



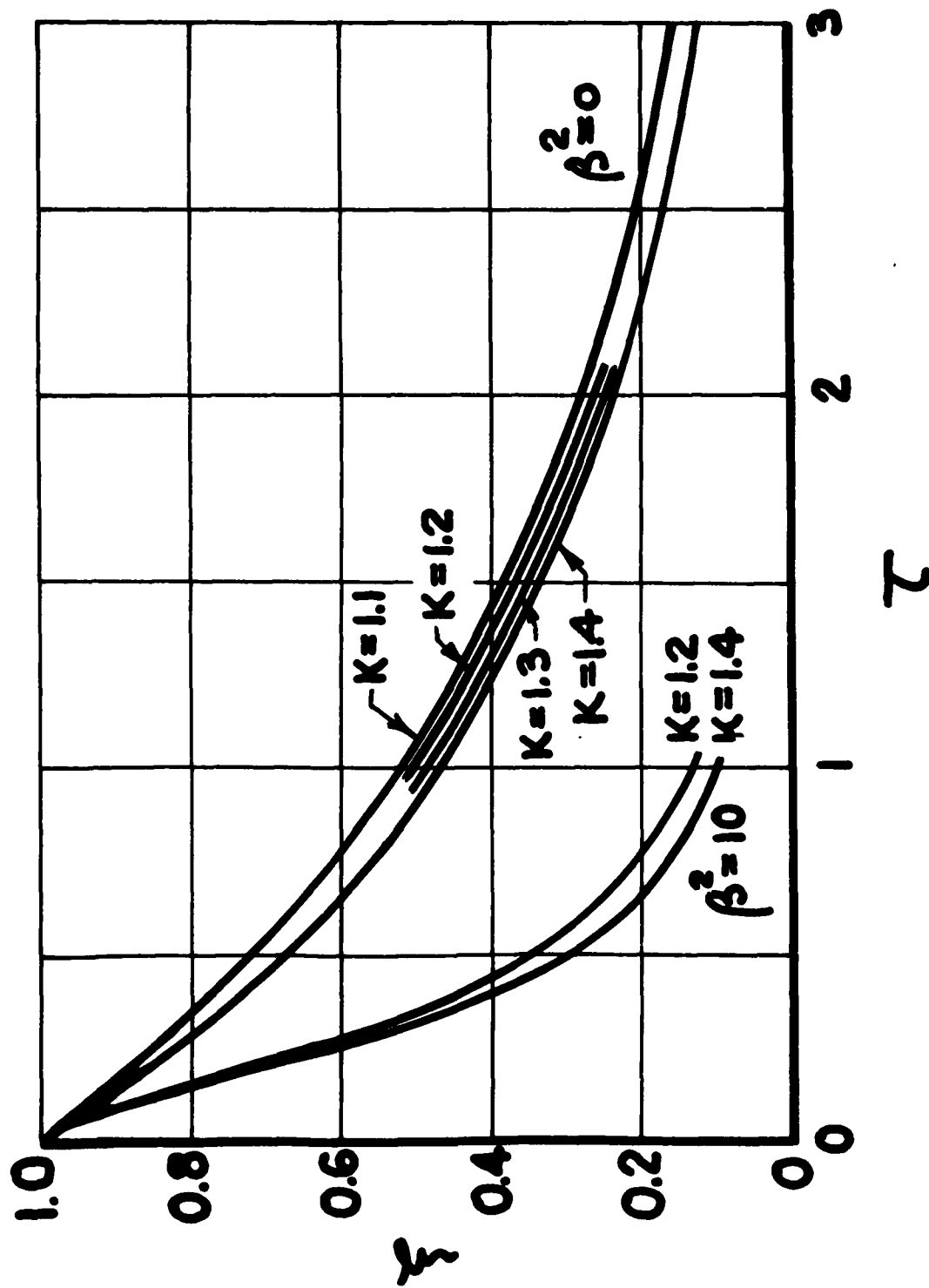
Slide 4



Slide 5

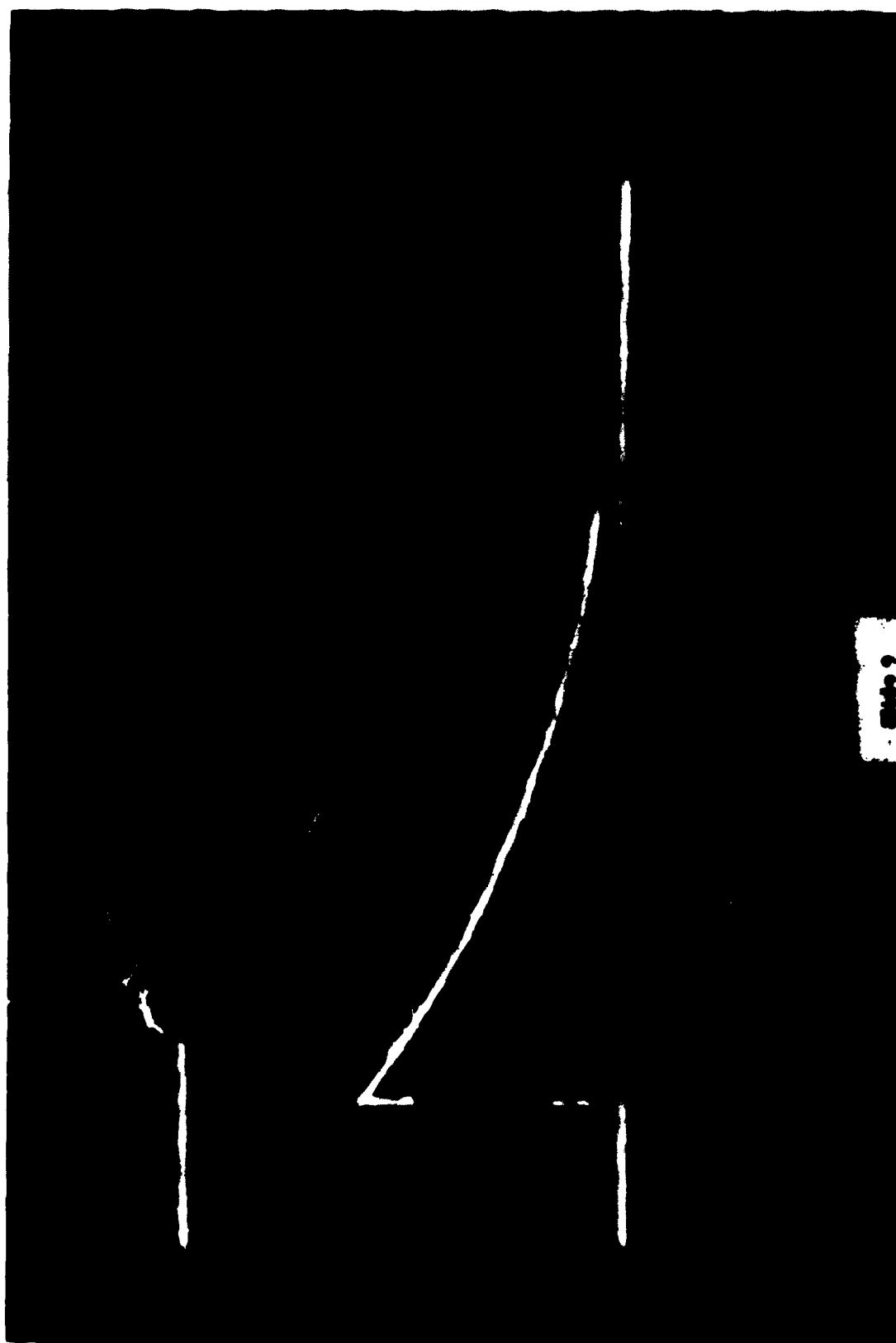


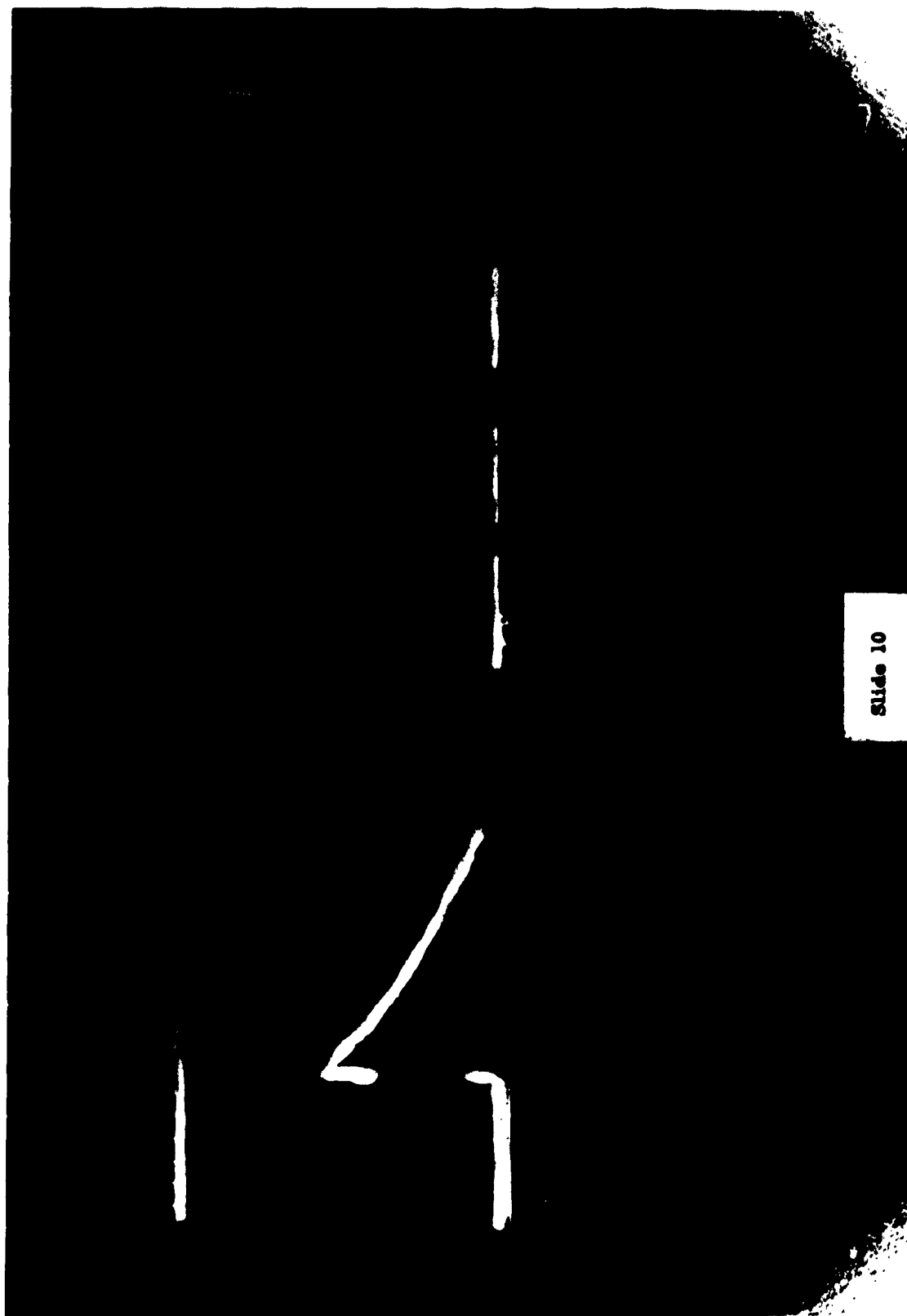
Slide 6



Slide 7







TECHNIQUES FOR PRODUCING LONG-DURATION LOADS
IN THE NCEL BLAST SIMULATOR

Stanley K. Takahashi
Warren A. Shaw
U. S. Naval Civil Engineering Laboratory

ABSTRACT

Over 400 blast load tests using explosives have been performed in the blast simulator which is located at the U. S. Naval Civil Engineering Laboratory, Port Hueneme, California. The basic explosive charge has consisted of Primacord, nitrocellulose film, and Composition C4, which are detonated by blasting caps. With this charge, the initial rate of decay of the pressure-time curve has been impossible to control due to heat loss from the gas to the simulator.

Numerous tests using additional explosive material have been conducted to overcome the effects of heat transfer and to provide better control over the initial decay in the blast pressure. Successful results were obtained using X-12, a high-energy solid propellant developed by the U. S. Naval Ordnance Test Station, China Lake, California. This propellant was tested with the explosive charge. The results showed a definite decrease of the initial decay of the pressure-time function.

INTRODUCTION

Purpose

The purpose of this paper is to discuss several approaches used to delay the initial decay of the pressure-time curve obtained in the blast simulator.

Background

For nearly three years the U. S. Naval Civil Engineering Laboratory (NCEL), Port Hueneme, California, has been operating a blast simulator^{(1)*}, Figure 1. The simulator is used to subject various test specimens to a

* Superscripts refer to items in the list of references.

uniformly distributed pressure that decays with time. Specimens tested thus far in the simulator have included reinforced concrete beams with simple and fixed ends, aluminum beams with fixed ends, steel portal-frame knee connections, steel beam-column connections, steel frames, blast closure valves, sand filters, two- and three-dimensional model arches buried in sand, electrical conduit seals, and prestressed concrete beams.

The uniformly distributed pressure in the simulator is obtained by the detonation of Primacord^{*} within a closed container, one surface of which is supplied by the test specimen. Actually, the Primacord is detonated inside a 6-inch-diameter firing tube 19 feet long. Three thousand 1/4-inch-diameter holes are distributed along the length of the tube. This firing tube, which serves as a throttling valve, is concentric with the main explosion chamber, Figure 2. Firing tubes of different orifice area may be used to provide rise-times to peak pressure in the main chamber from 0.5 to 5.0 milliseconds.

Once the peak pressure is obtained, the pressure decay may be regulated within certain limits by the use of 22 quick-opening solenoid valves. These valves are normally opened in three groups to achieve the proper decay to the pressure-time curve, Figure 3. The operation of the valves is controlled by mechanical cams, and the proper timing of the opening of the valves is set with a chronoscope.

As can be seen in Figure 3, pressure decay begins as soon as the peak values of pressure are reached. This is caused by the radiative heat transfer from the hot gases as they come into contact with the simulator. Thus, the initial decay of the pressure-time curve is not subject to control by the solenoid valves and there is an upper limit to the effective duration of the pressure curve which can be achieved. The effective load duration may be determined by extending the straight line which represents the average pressure-time curve up to the time of the maximum structural response until it intercepts the time axis.

* The properties of Primacord, as well as other explosive material discussed in this paper, are summarized in the Appendix.

In order to achieve the maximum dynamic response from a given structural member, a step pulse should be applied. However, for practical purposes, the response of a member is not decreased appreciably if the effective load duration is greater than eight times the natural period of the member^(2,3). For some of the tests, the effective simulator load duration was less than eight times the natural period of the member. Therefore, it became desirable to find a means of controlling the initial decay of the pressure-time curve in order to obtain a longer effective load duration.

Approaches to the Problem

As mentioned previously, the initial decay in pressure is caused by the cooling of the hot gases resulting from the explosion as they contact the simulator. Two general methods have been considered for preventing or delaying the initial decay of the pressure: (1) introducing additional hot gases into the simulator, and (2) introducing additional pressure at the appropriate time. Of course, the rapid cooling of the gases would be prevented if the simulator were initially at the same temperature as the gases. However, since the gases in the simulator are at temperatures of several hundred degrees Fahrenheit and since the simulator consists of some twenty tons of steel, this approach can be immediately discarded as extremely impractical. The other two approaches appeared to offer a feasible solution:

1. Introducing additional hot gases: This approach considered installing a gas generator in place of one of the quick-opening valves. Explosive and combustible material installed in the generator would serve as a source of heat which would inject additional hot gases into the main simulator chamber, thereby overcoming the loss of heat to the simulator.
2. Introducing additional pressure into the simulator: This approach considered the use of additional explosives along with the explosives normally used in the simulator. The

objective would be to find an explosive material which would provide pressure a few milliseconds after the basic explosive charge reached its peak pressure.

EXPERIMENTAL TESTS AND RESULTS

Development of the Basic Explosive Charge

The design of the blast simulator, including the development of the basic explosive charge, was accomplished by contract with NCEL⁽⁴⁾. As a result of numerous tests, it was determined that the detonation of PETN would provide satisfactory pressure conditions in the simulator. PETN is readily available in the form of Primacord, a detonating fuse in which a cover of polyethylene and a case of cotton or rayon surround the explosive core. The applicability of Primacord was particularly fortunate, since Primacord cannot be detonated by ordinary means; i.e., by dropping, burning, electrical current, or radio transmission signals. This simplified the storage requirement and handling procedures, as well as reduced the possibility of accidental detonation.

Primacord can be detonated by means of blasting caps. For more positive detonation, a small amount of Composition C⁴ (a plastic explosive) is placed between the Primacord and the blasting cap. The location of the explosives in the simulator is indicated in Figure 2. Two No. 8 Engineer's Special blasting caps, one at each end of the simulator, are used for detonation.

It was also demonstrated in early calibration tests that the addition of nitrocellulose film was helpful by contributing additional gas at a lower temperature, which aids in reducing the deposit of carbon in the simulator.

Use of the Gas Generator

The initial experimental attempt to decrease the effect of gas cooling in contact with the simulator used a gas generator, Figure 4. The generator was installed in place of one of the quick-opening valves.

Hot gases were created in the generator by the burning of nitrocellulose film, which was ignited by an igniter assembly (Figure 4) consisting of a mixture of black powder and magnesium powder placed, together with a No. 1 squib, in a bag formed of polyethylene sheet. The squib was detonated by means of a spark from a heavy-duty spark plug. The amount of nitrocellulose film to use was to be determined experimentally. The time lag before gas is delivered at the full rate would be about 50 milliseconds: however, the gas generator ignition could be controlled by the overall firing system in order to achieve proper timing of the gas delivery to the simulator.

Numerous tests with varying amounts of nitrocellulose film and different times of ignition were performed. The results were uniformly disappointing. The addition of gas into the simulator did not have the desired effect of maintaining the pressure in the early stages of the decay. In none of the tests was the pressure increased at any time over the basic curve without use of the gas generator. In fact, the addition of hot gases produced the opposite effect, resulting in a pressure curve that decayed at a faster rate than when the basic charge was used by itself. One possible explanation of this phenomena may be that the extra turbulence created by the gas flow from the generator into the simulator may actually have served in bringing more of the hot gases into contact with the simulator, thereby resulting in a more rapid cooling of the gas mixture.

Because of the negative results, further investigation of this approach was not warranted.

Use of Additional Explosives

Since the combustible material in the gas generator was unable to provide the desired results, the possibility of using additional explosive material was considered. A material which would reach a peak pressure in 5 to 10 milliseconds was desired. Scientists at the U. S. Naval Ordnance Test Station (NOTS), China Lake, California, were consulted. It was

decided to try high-energy X-12, a rocket propellant developed at NOTS, in addition to the basic explosive charge. The X-12 propellant has special properties which make its use desirable: the burning rate is independent of pressure and temperature over a limited variation of these parameters, and the propellant is relatively insensitive to shock.

There were two major problems concerned in using X-12:

1. The detonation of Primacord might initiate a high-order detonation of the propellant. This would result in the release of energy in a fraction of a millisecond and would provide considerably higher pressures than desired.
2. The propellant might fracture under the action of the shock wave. If the fracture were excessive, the additional surface area would enable the propellant to burn at a more rapid rate. This would provide erratic pressure conditions.

It was highly desirable to explore the possibility of either of these two situations occurring. Personnel at NOTS were therefore requested to perform tests which would provide information relative to these problems. Since the shock wave from the detonation of Primacord is more or less independent of the confining vessel, the initial tests were performed in the open air.

In the first series of tests, a length of Primacord (70 grains per foot) was detonated in the near vicinity of a 4-inch length of X-12 propellant. In the most severe of these tests, eight strands of the Primacord were placed in contact with the propellant and were detonated. The propellant did not detonate, although it fractured into numerous pieces which ignited and burned. This situation was considerably more severe than any condition likely to be encountered in the tests in the blast simulator. A more realistic situation was experienced with two strands of the Primacord in contact with the X-12 propellant. Again, detonation did not occur. The propellant did break into a few pieces, some of which ignited and burned.

It was believed that this fracture of the propellant was not serious enough to provide excessively high pressures, although the conditions might not be as reproducible as desired.

The second series of tests at NOTS was conducted in a 9-inch length of steel tube with a 2-inch internal diameter. A 4-inch length of X-12 propellant was placed in the bottom of the tube; Primacord was strung along the top and detonated. The clear spacing between propellant and Primacord was $3/4$ inch. Neither detonation nor ignition of the X-12 occurred.

Since consultants at NOTS felt that one of the major problems in the anticipated use of the X-12 propellant would be that of ignition, strands of quick match were strung along with the Primacord in the remainder of the tests. It was determined that two strands of quick match in this configuration would be sufficient to insure ignition of the propellant. Burning of the X-12 occurred at a slow rate since the pressure was not sufficiently high to promote rapid burning. In the most severe test, from the standpoint of detonation of the propellant, eight strands of quick match were used along with the Primacord. It is significant that detonation did not occur in any of these tests, nor did the propellant break into small pieces.

Accordingly, full-scale tests were planned in the simulator. A total of 15 tests using Primacord, nitrocellulose film, and X-12 propellant were conducted in the blast simulator. The most significant of these tests are discussed here.

Test No. 1 established the base curve for a pressure of 66 psi using Primacord and nitrocellulose film. The tracing of the initial portion of the oscillogram record is shown in Figure 5a.

Test No. 2 was performed with a 12-inch length of X-12 propellant resting on the bottom of the firing tube with a clear spacing of $13/16$ inch to the Primacord (Figure 6). Figure 7 is a perspective view of the firing tube at midspan.

Test No. 3 used a 24-inch length of X-12 in the same configuration. Figures 5b and 5c show that the propellant in this position did not make any significant contribution to the pressure-time curve. It was noted that the propellant was entirely consumed but apparently burned at such a rate that its effect was insignificant.

In Test No. 4, a 12-inch length of propellant was in contact with the Primacord (Figure 8). It can be seen in Figure 9a that the initial decay was considerably decreased. For Test No. 5, the 12-inch length of propellant was cut into 4-inch sections. There were no significant differences in the results of the two tests, as can be noted by comparing Figures 9a and 9b. The comparison of Test No. 5 with the basic test curve over the entire range is presented in Figure 10. It is noted that the propellant used in this configuration has a marked effect in increasing the pressure-time curve over the full duration of the pressure.

Test Nos. 6 and 7 used a 24-inch length of X-12 in contact with the Primacord. In the first of these tests (Figure 11a), the pressure increased slightly above the initial peak value, whereas the pressure decreased somewhat for the second of these tests (Figure 11b).

Test No. 8 used Primacord and nitrocellulose film to establish a base curve for a pressure of 120 psi. The initial portion of the pressure-time curve for this test is shown in Figure 12a. For test Nos. 9 and 10, 12-inch and 24-inch lengths respectively of X-12 propellant were placed in contact with the Primacord. The main result from these latter two tests was the elevation of peak pressure from 121 psi to 143 and 154 psi (Figures 12b and 12c). The initial decay from peak pressure is comparable for these three tests.

Table I is a summary of the test schedule and results for the most significant tests.

Table I. Summary of Test Schedule and Results

Test No.	Primacord		Nitro-cellulose Film (feet)	X-12 Propellant		Initial Peak Pressure (psi)	Remarks
	Grains per ft	Length (feet)		Length (inches)	Distance from Primacord (inches)		
1	100	31	65	0	-	66	Established base curve
2	100	31	65	12	13/16	65	Negligible effect on pressure-time curve
3	100	31	65	24	13/16	64	Negligible effects on pressure-time curve
4	100	31	65	12	0	66	Decreased initial pressure decay significantly
5	100	31	65	12	0	67	Provided step pulse for 200 milliseconds
6	100	31	65	24	0	65	
7	100	31	65	24	0	67	
8	200	33	138	0	-	121	Established base curve
9	200	33	138	12	0	143	Peak pressure elevated; rate of decay approximately the same as for Test No.8
10	200	33	138	24	0	154	" " "

DISCUSSION OF RESULTS

The tests demonstrated the feasibility of using X-12 propellant in conjunction with the basic explosive charge to provide substantial decreases in the initial pressure decay rate experienced in the blast simulator. It is significant that detonation of the propellant did not occur in any of the tests performed either at NOTS or NCEL. Thus, the likelihood of such a high-order detonation appears quite remote for the test conditions in the simulator.

For pressures in the 70-psi range, a step pulse of 200 milliseconds duration can actually be achieved. The decay of the pressure pulse in the later stages of loading can be controlled within certain limits by the quick-opening valves. Cutting the propellant into smaller lengths, as was done in Test No. 5, did not produce significant differences in pressure conditions from Test No. 4 for the first 200 milliseconds. Comparison of these two tests also indicates that there was not a significant amount of fracturing of the propellant caused by the detonation of the Primacord. If severe fracturing had occurred, the peak pressure would have been increased noticeably. This would have provided a different pressure-time behavior, which was not in evidence. The results of the tests in the open air at NOTS also support the contention that fracturing of the propellant is not a significant problem at these pressure levels. There was also no difficulty in ignition of the X-12 when the propellant was initially in contact with the Primacord. Thus, the test results for this pressure level seem to be reproducible within the expected limits of experimental variation.

For pressures in the 120-psi range, the addition of X-12 propellant provided substantial increases in the peak pressure attained as noted in Test Nos. 8, 9, and 10. The peak pressure obtained using the basic charge was 121 psi; the use of 12- and 24-inch lengths of X-12 along with the basic charge increased the peak pressure to 143 and 154 psi respectively. An explanation of this phenomenon may be that the portion of the propellant

in immediate contact with the Primacord was forced to burn at an excessively rapid rate as caused by the heat and pressure in the detonation wave. The rapid burning created increases of pressure at times earlier than desired; this resulted in an increase in peak pressure rather than an increase in pressure shortly after reaching the peak value as obtained with the basic charge.

Some exploratory tests using the propellant encased in a protective shield to prevent the rapid forced burning of the propellant were not successful in delaying the initial decay of pressure. Two approaches for sustaining the peak pressure at higher pressure levels are: (1) using a propellant of lower burning rate in contact with the Primacord, and (2) resting the propellant on the bottom of the firing tube and insuring its ignition by the use of several strands of quickmatch in conjunction with the Primacord. These tests have not yet been performed.

CONCLUSIONS

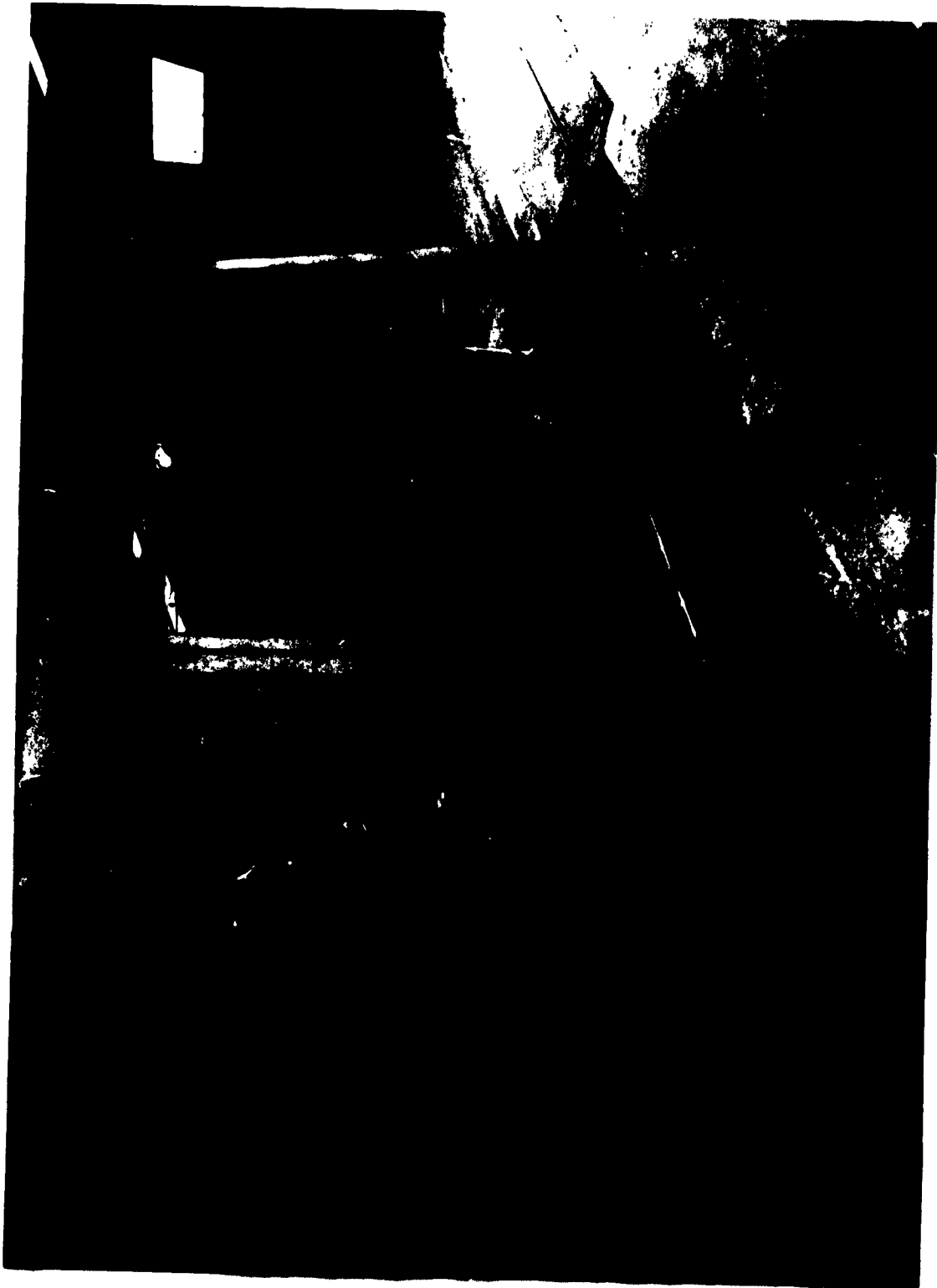
Based on the numerous tests performed at NOTS and at NCEL, the following conclusions for the test conditions encountered seem warranted:

1. There is little likelihood of detonating X-12 propellant when it is placed adjacent to Primacord.
2. Combinations of X-12 propellant, Primacord, and nitrocellulose film can be used to provide step pulses of at least 200 milliseconds duration for pressures up to 70 psi. The decay of pressure beyond these times can be controlled within limits.

Since the completion of these tests in July 1959, additional tests have been performed⁽⁵⁾ which tend to confirm the above conclusions.

ACKNOWLEDGMENTS

In addition to the contributions made by members of the NCEL technical staff, the authors would like to express their sincere appreciation for the efforts of numerous NOTS scientists, particularly those of Messrs. J. L. Bray and R. G. Sampson of the Propulsion Analysis Branch, Propulsion Development Department. Mr. Bray assisted in the full-scale tests at NCEL and in the interpretation of results.



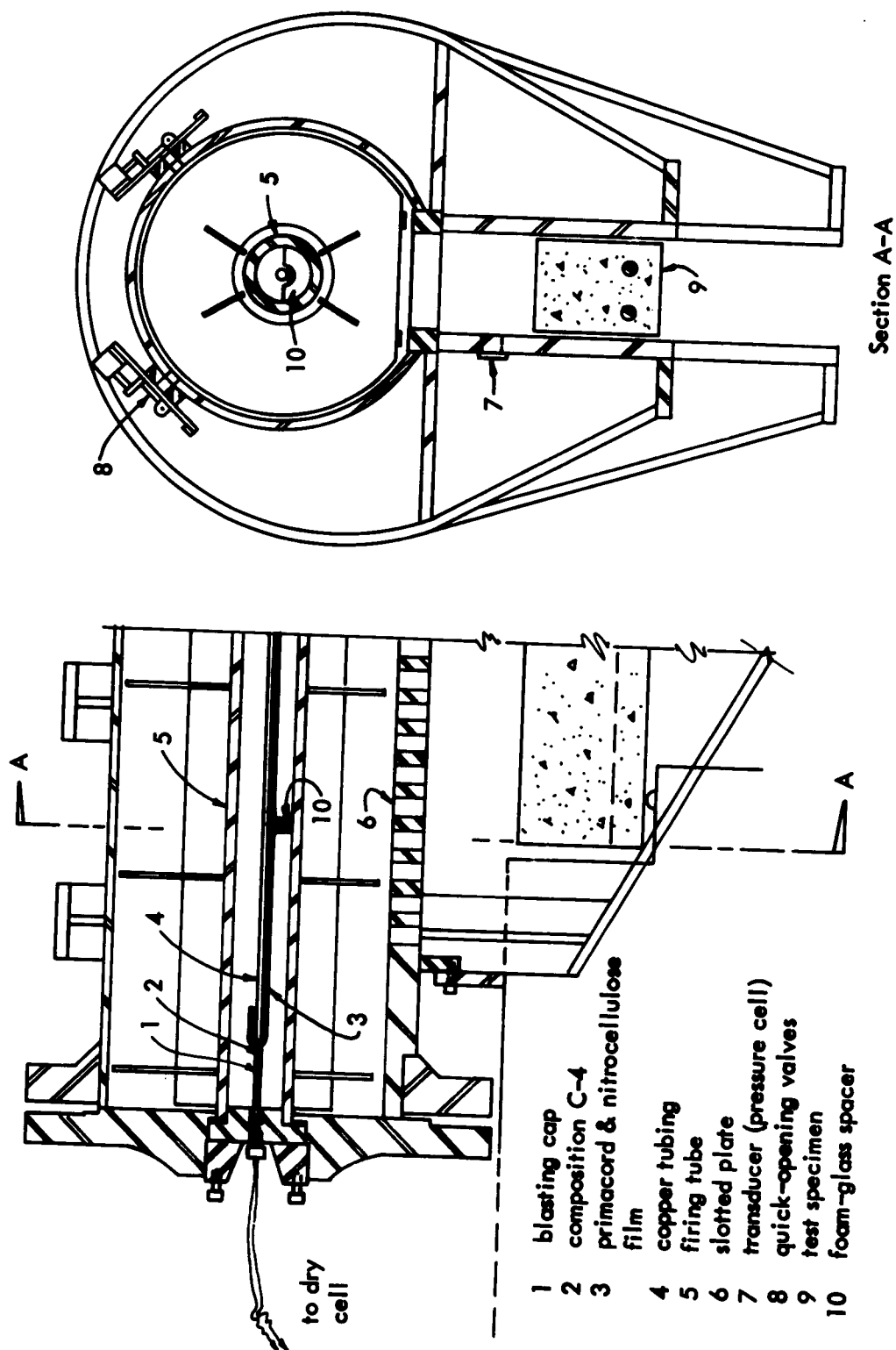


FIGURE 2. DESCRIPTIVE PARTS OF THE BLAST SIMULATOR.

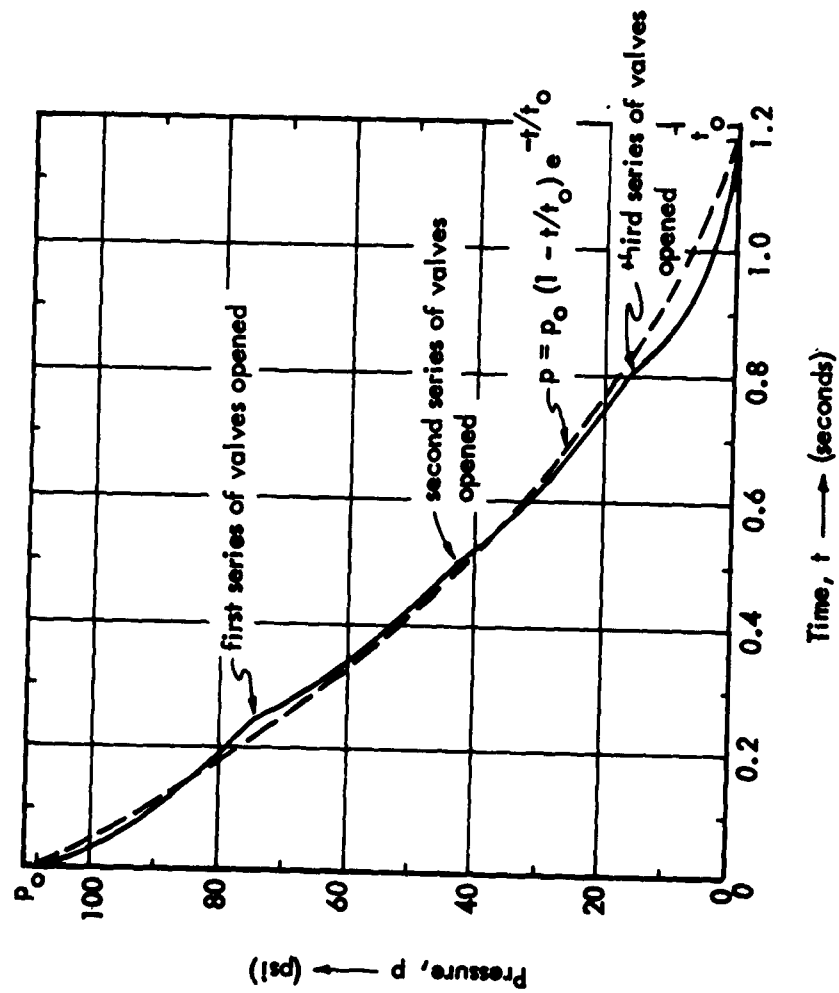


FIGURE 3. THEORETICAL AND EXPERIMENTAL BLAST PRESSURE CURVES.

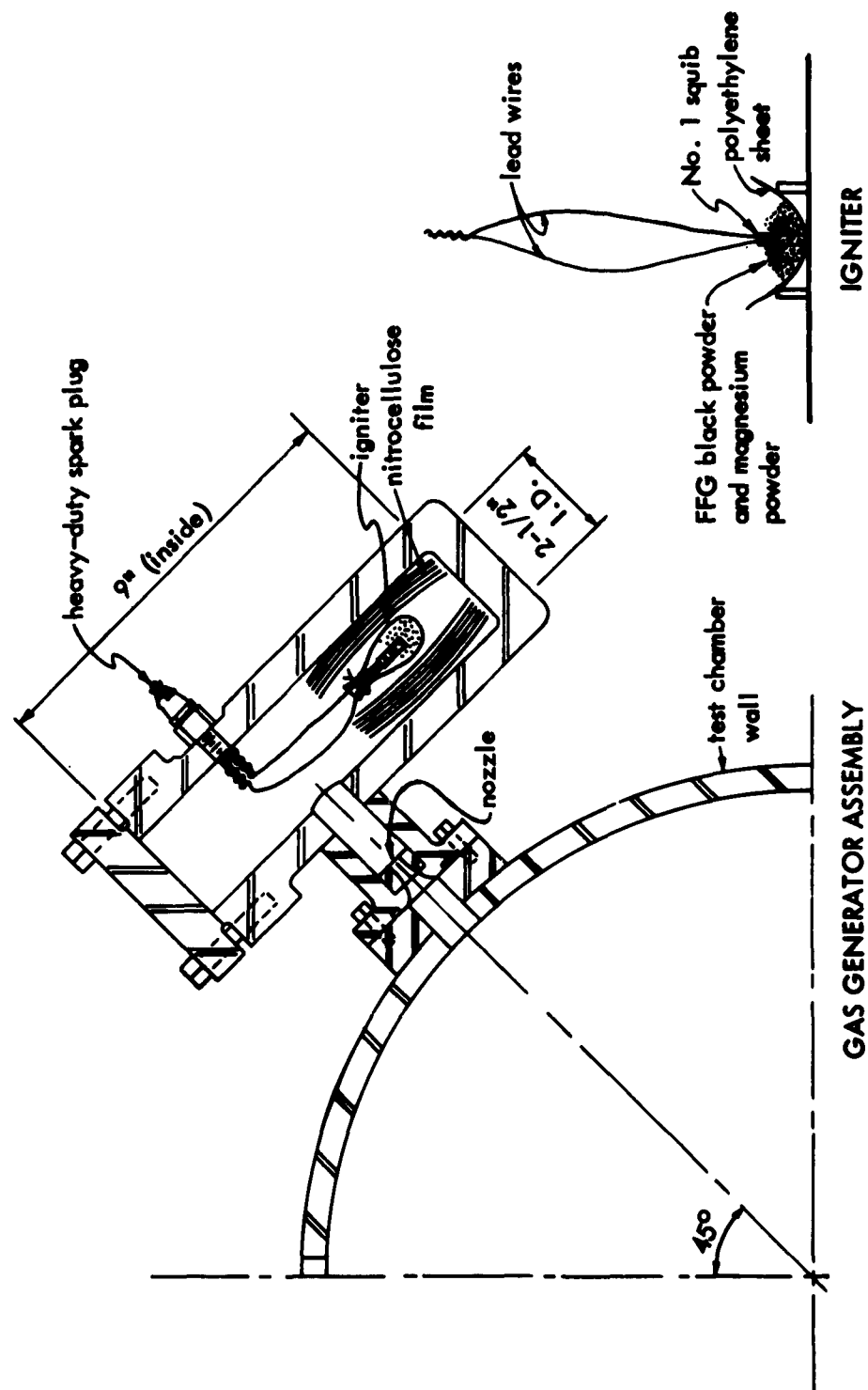
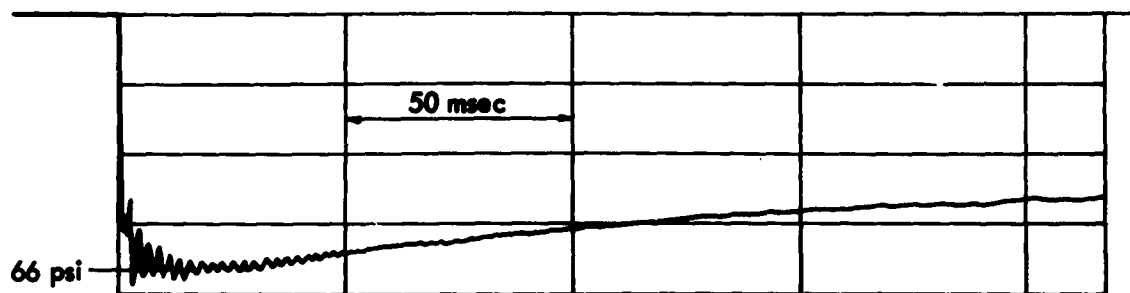
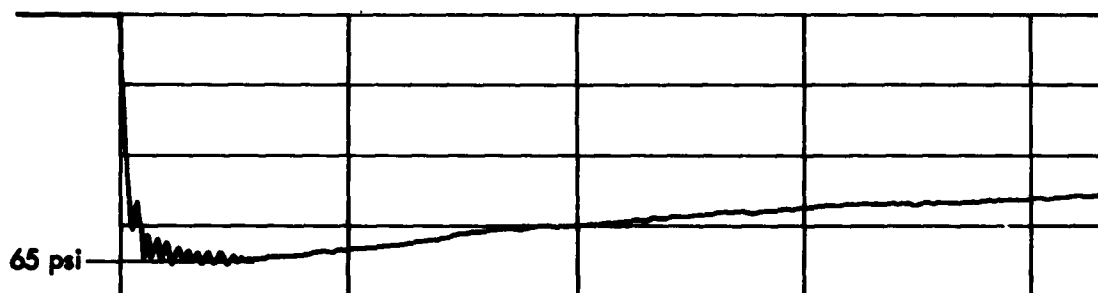


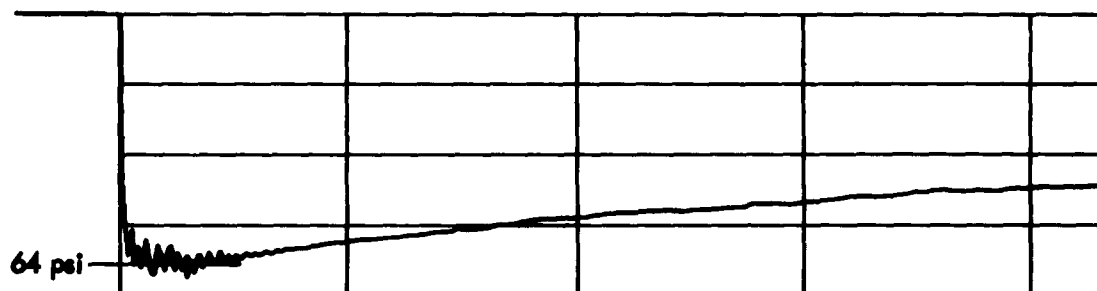
FIGURE 4. GAS GENERATOR, IGNITER, AND CHARGE.



a) Test 1: Basic explosive charge



b) Test 2: 12 inches of X-12 propellant placed 13/16" from primacord



c) Test 3: 24 inches of X-12 propellant placed 13/16" from primacord

FIGURE 5. PRESSURE-TIME CURVES FOR TESTS 1, 2, AND 3.

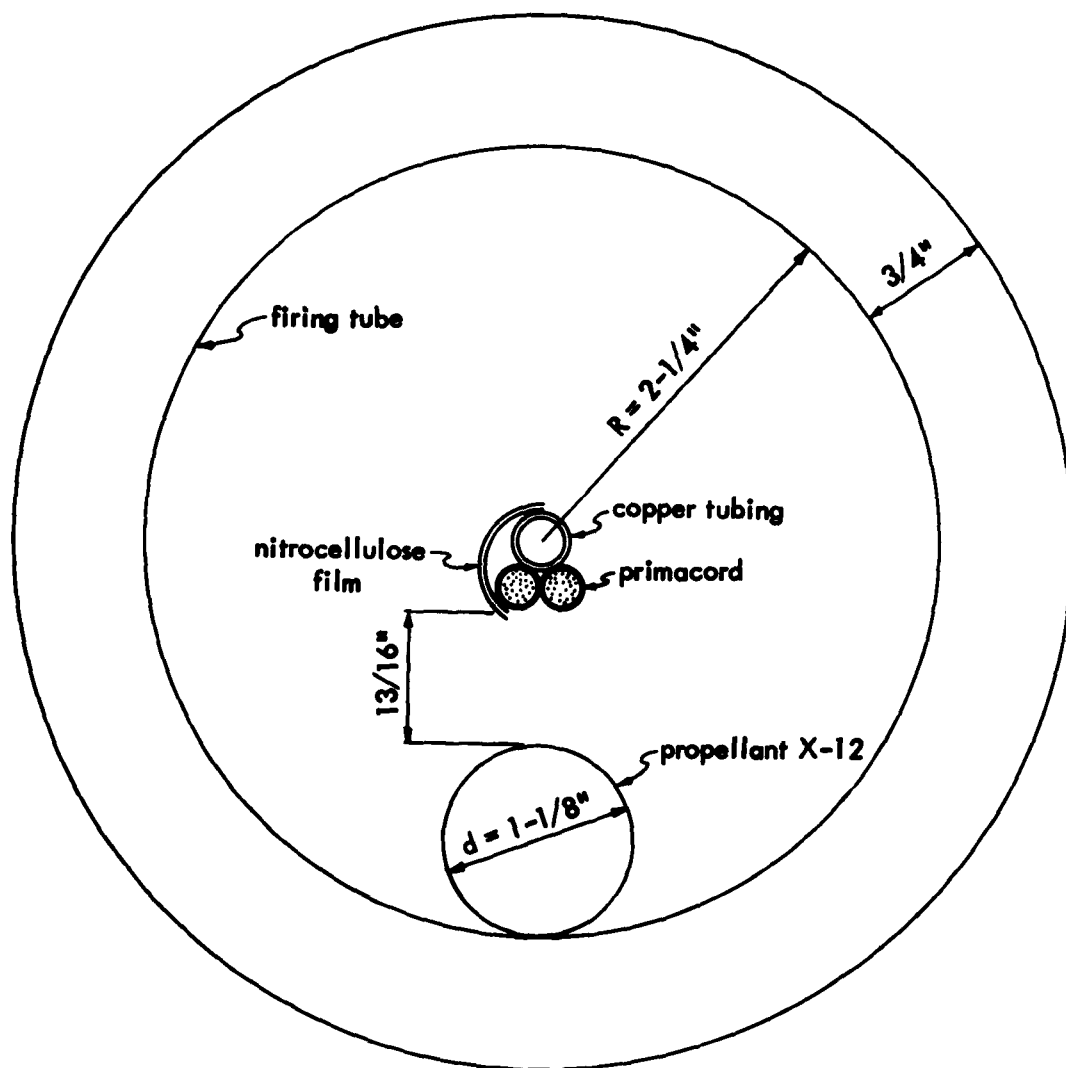


FIGURE 6. PROPELLANT LOCATED AT A DISTANCE OF $13/16"$ FROM THE PRIMACORD.

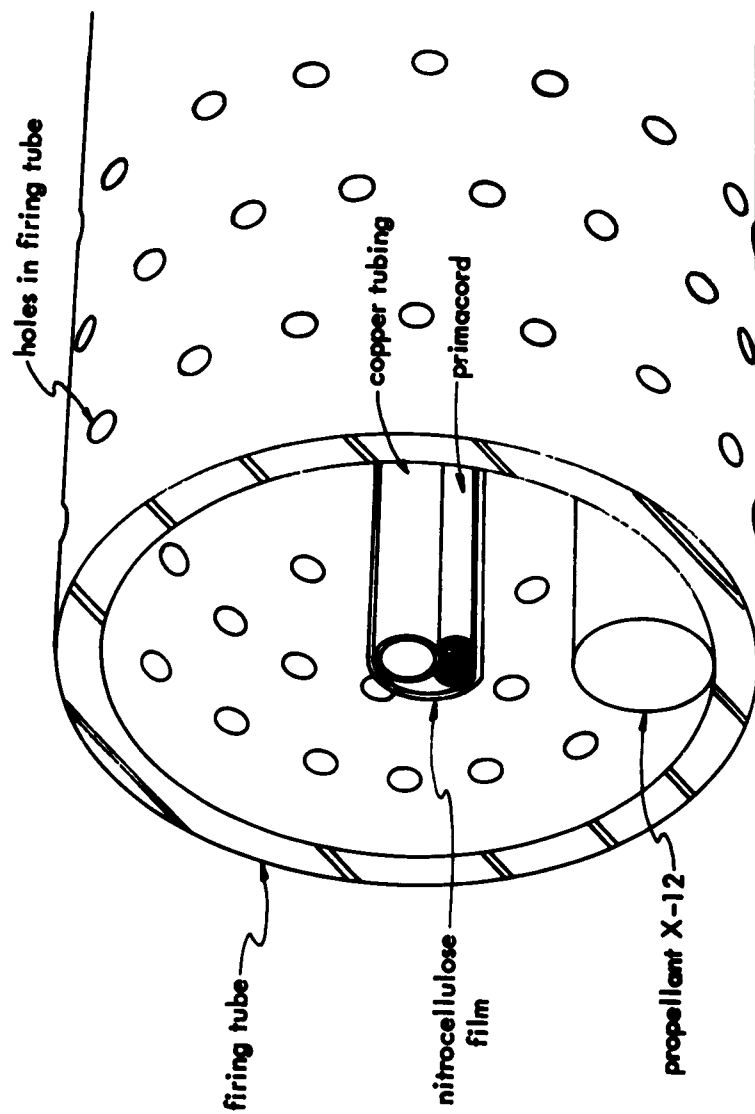


FIGURE 7. SECTION THROUGH FIRING TUBE.

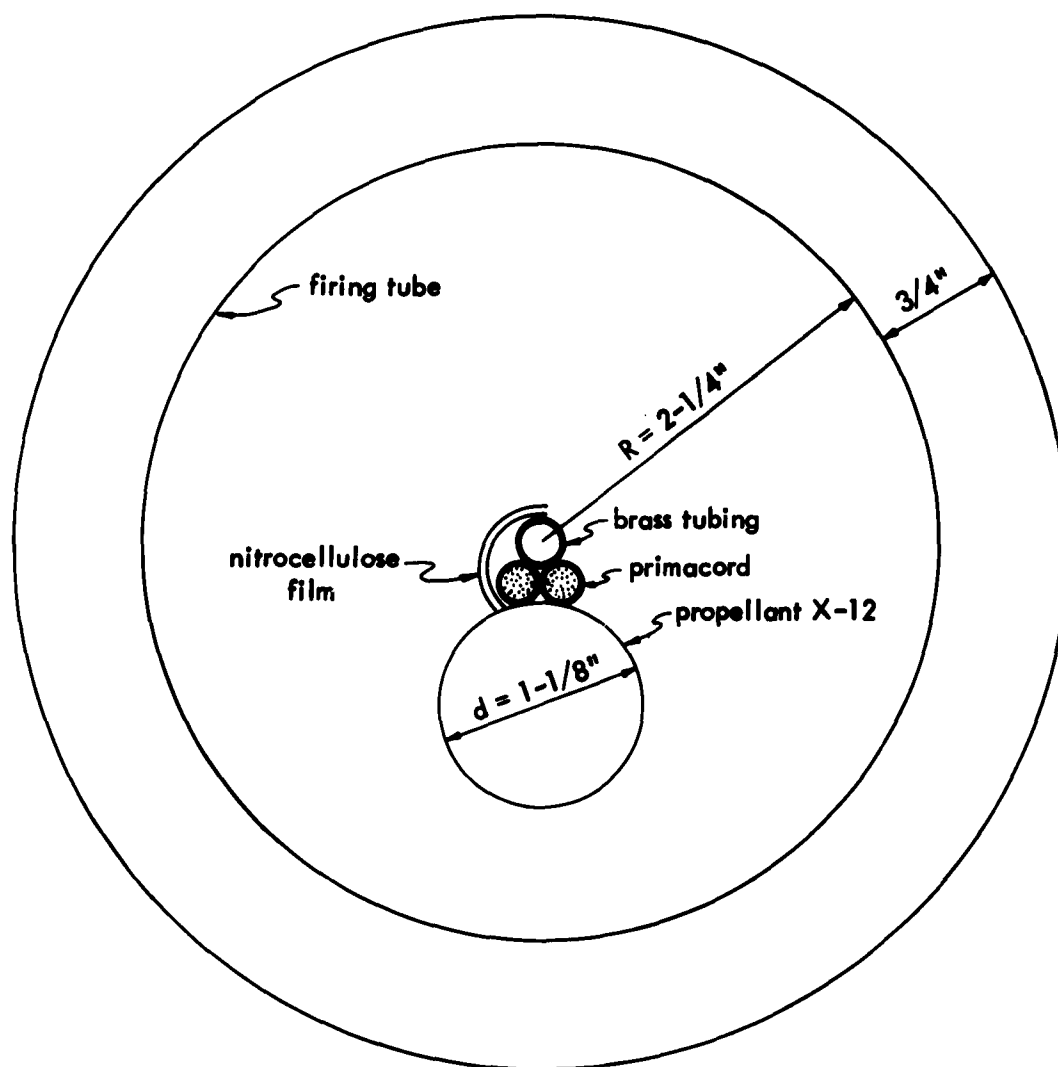
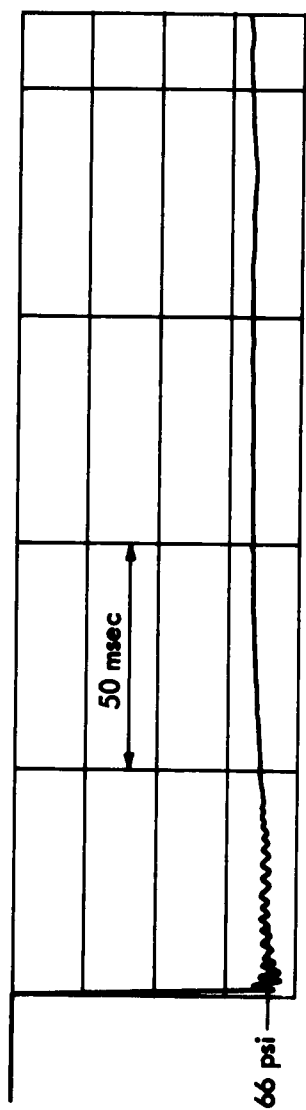
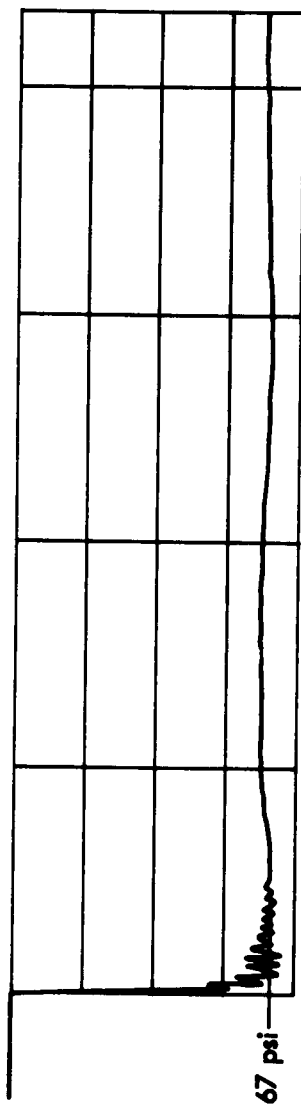


FIGURE 8. PROPELLANT IN CONTACT WITH THE PRIMACORD.



a) Test 4: 12 inches of X-12 propellant placed adjacent to primacord



b) Test 5: 12 inches (4-inch lengths) of X-12 propellant placed adjacent to primacord

FIGURE 9. PRESSURE-TIME CURVES FOR TESTS 4 AND 5.

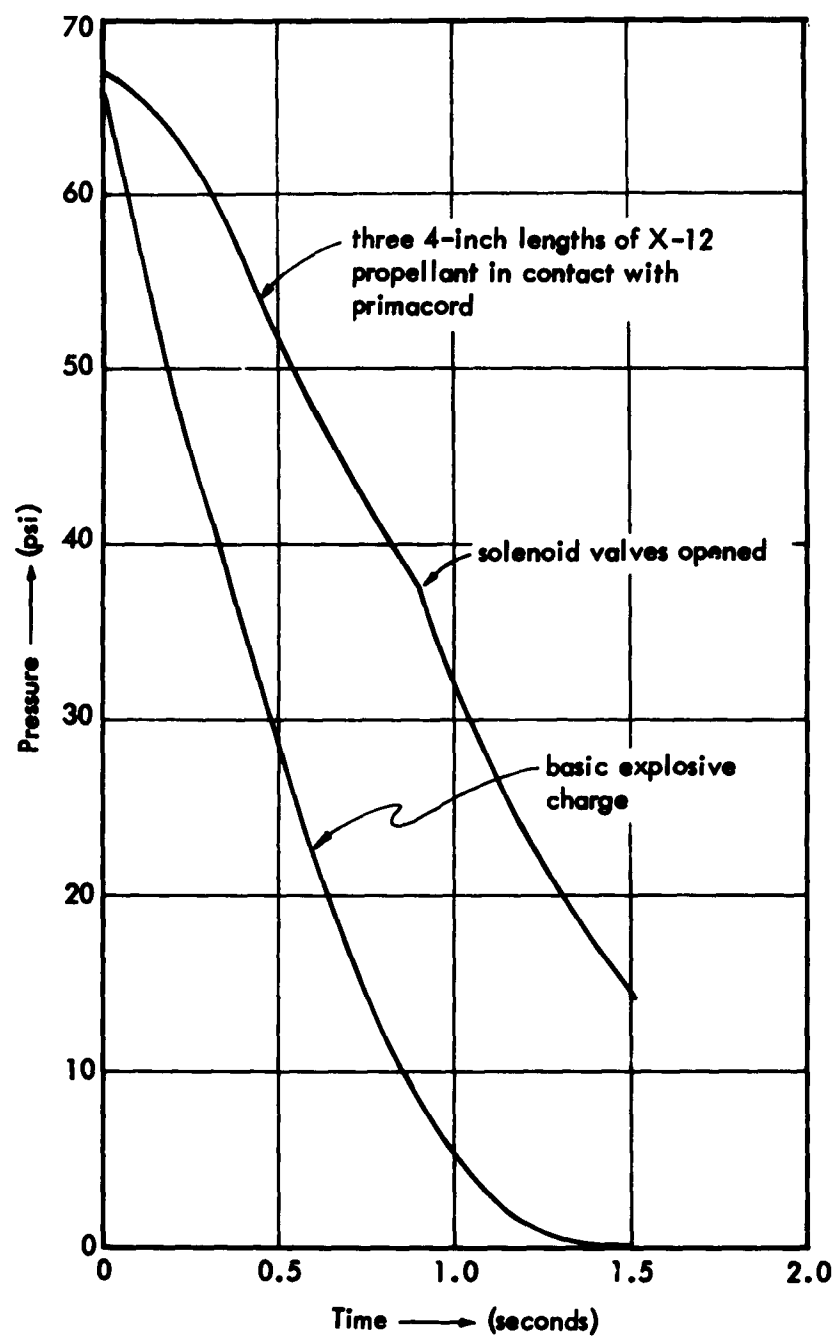


FIGURE 10. PRESSURE-TIME CURVES FOR TESTS 1 AND 5.

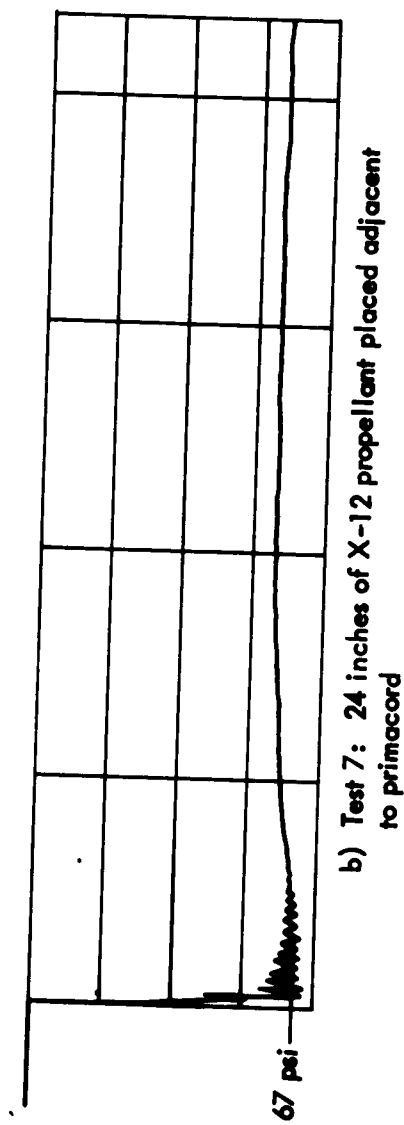
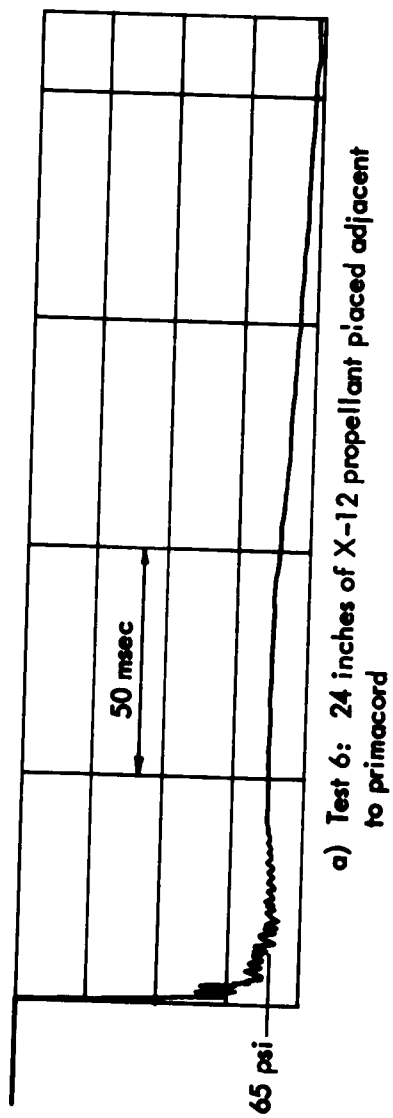
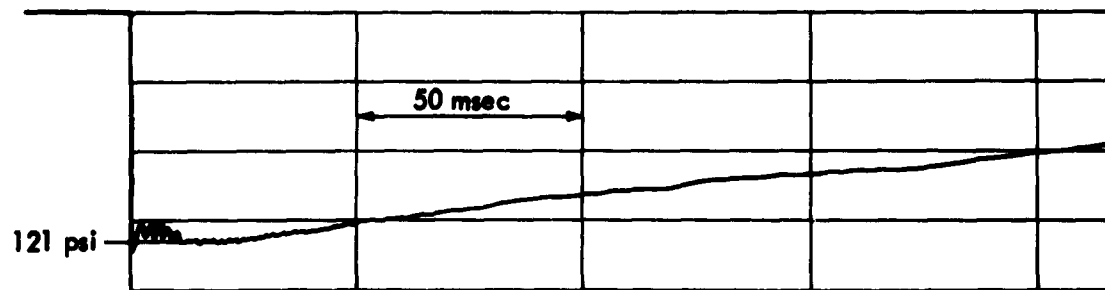
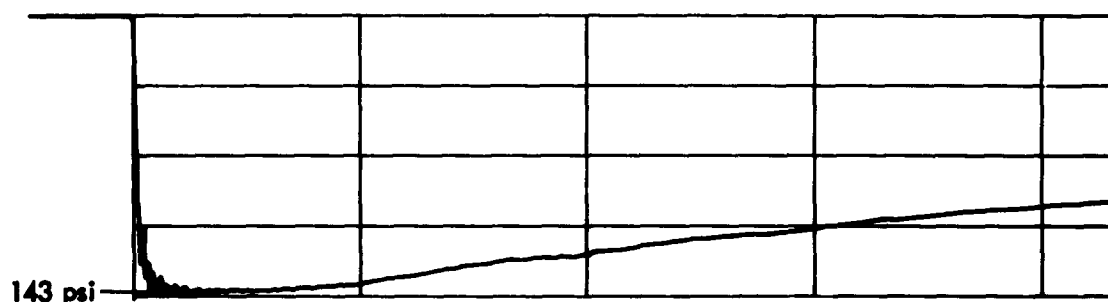


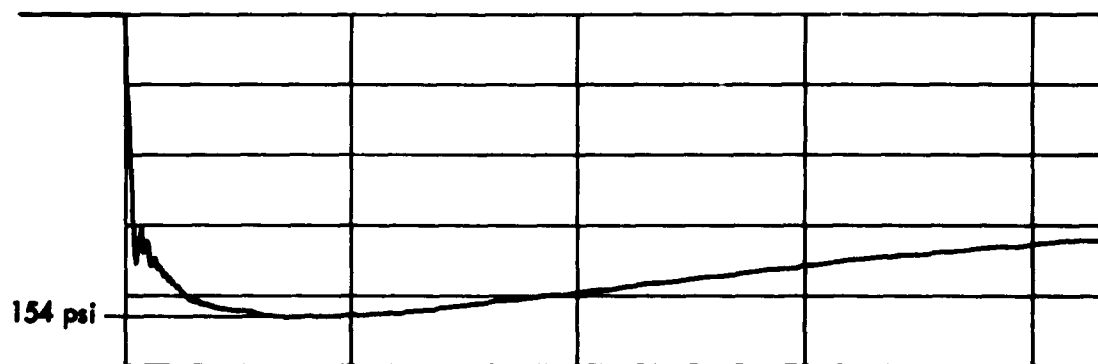
FIGURE 11. PRESSURE-TIME CURVES FOR TESTS 6 AND 7.



a) Test 8: Basic explosive charge



b) Test 9: 12 inches of X-12 propellant placed adjacent to primacord



c) Test 10: 24 inches of X-12 propellant placed adjacent to primacord

FIGURE 12. PRESSURE-TIME CURVES FOR TESTS 8, 9, AND 10.

APPENDIX I

PROPERTIES OF EXPLOSIVES USED IN THE SIMULATOR

A brief summary of the properties of the various types of explosives used is given below:

Primacord^(6,7)

Primacord is a detonating fuse comprising a high explosive core of pentaerythritetetrinitrate (PETN) contained within a waterproof sheath overlaid by reinforcing coverings. It has a high detonating velocity of about 21,000 ft per second. It is light in weight and very flexible, making it easy to handle and connect. Primacord is very insensitive and cannot be detonated by fire, friction, or ordinary shock.

Composition C⁴

Composition C⁴, also called Harrisite, is a plastic explosive. It has a high velocity of detonation at 26,000 ft per second. C⁴ catches fire easily and burns with an intense heat. It remains pliable like putty and is easy to mold at temperatures between -70°F and 170°F. Poisonous fumes are given off when exploded; thus the explosive should not be used in an enclosed, unventilated space. Composition C⁴ is easily detonated by a blasting cap.

Blasting Caps⁽⁸⁾

Electric blasting caps are small tubes, usually copper, closed at one end and loaded with a charge of various explosives. Two insulated wires connect to a bridge wire which is embedded in one of the explosives. The cap is detonated by means of an electrical current which heats the bridge wire to incandescence, thereby exploding the charge.

Engineer's special blasting caps provide a more powerful explosion than the blasting caps normally used in most applications. This special cap contains crystalline PETN and assures a more positive detonation of the Composition C⁴ and Primacord. For tests in the simulator, two No. 8 Engineer's special blasting caps are used.

Nitrocellulose Film^(9,10)

The nitrocellulose used in the simulator tests is in the form of clear, ordinary movie film. The film is a solid solution of cellulose nitrate and camphor or other plasticizer. It is highly flammable and releases toxic gases during combustion.

Black Powder⁽⁷⁾

Black powder is a deflagrating explosive, one that burns progressively over a relatively sustained period of time in comparison with a detonating explosive which decomposes practically instantaneously. It is one of the worst known explosive hazards and must be handled with extreme caution.

Black powder is manufactured in two grades: Type A which is composed of 75 percent saltpeter or potassium nitrate, 10 percent sulfur, and 15 percent charcoal; Type B which uses sodium nitrate instead of potassium nitrate. Type A blasting powder is considerably faster and slightly stronger than Type B blasting powder.

Magnesium Powder⁽¹¹⁾

Magnesium is a highly flammable solid and can cause explosions when in a finely divided state such as powder. It is a dangerous fire hazard and should be stored in a cool, well ventilated place. Magnesium can unite with oxygen to form magnesium oxide, a poisonous compound which can cause metal fume fever and gas gangrene. If the container of the magnesium powder is left uncovered, the magnesium can liberate hydrogen which is also a potential explosion hazard.

Electric Squibs⁽⁷⁾

Squibs comprise a small aluminum tube with a charge of deflagrating mixture in the bottom closed end; an electrical firing element and attached wires are sealed into the other end with waterproofing compound and sulfur. When current is applied to the wires, the firing element flashes and ignites the deflagrating compound. Intense flame, issuing from the ruptured shell, ignites the main explosive charge.

Electric squibs are considered the safest and most effective means of igniting black powder.

High-Energy X-12 Propellant⁽¹²⁾

The composition and properties of the high-energy X-12 propellant is discussed in Table 12 of the referenced report which is classified CONFIDENTIAL. The propellant used in the simulator tests is extruded in grains that are 1-1/8 inches in diameter.

Quickmatch

The quickmatch used in the tests goes under the tradename of Blackmatch. It consists of a heavy cotton cord impregnated with black powder. Its principal application is as a fuse material and the combustion characteristics are identical to those of ordinary black powder. It does not detonate and can produce an explosion only in a confined space.

REFERENCES

1. Shaw, W. A. and Allgood, J. R. "An Atomic Blast Simulator". Proceedings of the Society for Experimental Stress Analysis, Volume XVII, Number 1, 1959.
2. Allgood, J. R. and Shaw, W. A. "Elasto-Plastic Response of Beams to Dynamic Loads". NCEL Technical Memorandum 130, Port Hueneme, California, March 1958.
3. Frankland, J. M. "Effects of Impact on Elastic Structures". Proceedings of the Society for Experimental Stress Analysis, Volume VI, Number 2, May 1947.
4. Boynton Associates. "Final Report on Atomic Blast Simulator". Contract NBy-3127 with the U. S. Naval Civil Engineering Laboratory, September 1958.
5. Unreported tests performed by Boynton Associates of La Canada, California, May and June 1960.
6. "Data Sheet, Primacord Detonating Fuse". The Ensign-Bickford Company, Simsbury, Connecticut, September 1959.
7. Blasters' Handbook, DuPont de Nemours and Company, 1942.
8. Explosives and Demolitions, Field Manual 5-25, U. S. Government Printing Office, September 1954.
9. Organic Chemistry, Fieser and Fieser, D. C. Heath and Company, 1944.
10. The Condensed Chemical Dictionary, Reinhold Publishing Corporation, 1950.
11. Sax, Irving N. Handbook of Dangerous Materials, Reinhold Publishing Corporation, 1951.
12. "Some Properties of Several Double-Base Solid Propellants for Rockets". U. S. Naval Ordnance Test Station Report No. 1089 (NavOrd Report 3477), 1955, CONFIDENTIAL.

ARC HEATING TECHNIQUE FOR SHOCK TUBE DRIVER

L. Y. Lamb
G. R. Russell
Aerospace Corporation

ABSTRACT

A preliminary study of arc heating as a means of increasing the sound speed of the driver gas in a shock tube has been made. A description of the pilot facility is given together with the operational procedure. The arc unit characteristic was studied separately, and arc phenomena were observed in detail with the help of a high speed movie camera. It has been found that the problems in arc operation are nozzle erosion and premature arc blow-out. Nozzle erosion limits the maximum gas enthalpy level that can be attained with the arc. Driver temperature and pressure time histories as well as the driver axial temperature gradient have been obtained. The total efficiency and the final driver gas temperature versus power input are presented to illustrate the capability of the prototype facility. Finally, the arc-heated shock tube performance is summarized with a graph of measured shock Mach number versus pressure ratio with driver gas temperature as a parameter.

In conclusion, it was found that the plasma-jet heating scheme utilizing contemporary engineering materials is restricted by thermal stress problems to operate at about 3000°K . With improvement in design and selection of high temperature materials, substantial increase in driver gas temperature can be realized.

SYMBOLS

A	Cross-sectional area of the arc nozzle throat
a	Sound speed
C_p	Specific heat at constant pressure
E	Total Energy
h	Gas enthalpy
$^{\circ}\text{K}$	Degree Kelvin
M_s	Shock Mach number
m	Total mass of gas or material under consideration
\dot{m}	Gas mass flow (dm/dt)
P	Arc power input
p	Gas pressure
\dot{q}	Heat transfer rate $\text{cal/m}^2 - \text{sec}$
$R_1 T_o$	20.65 cal/gm ($T_o = 300^{\circ}\text{K}$, for air)
$R_4 T_o$	148.9 cal/gm ($T_o = 300^{\circ}\text{K}$, for helium)
S	Driver interior wetted surface area m^2
T	Temperature
t	Time
V	Driver internal volume
x	Distance
γ	Specific heat ratio
η	Efficiency

SUBSCRIPTS

1	Shock tube section
2	Conditions behind primary shock
4	Instantaneous driver gas condition
a	Arc unit
c	Reservoir, or arc charging condition
d	Pertaining to the driver
t	Total
s	Stagnation
in	Input

SUPERSCRIPTS

'	Final condition in driver (at time of major diaphragm rupture)
---	--

I. INTRODUCTION

The shock tube, a device useful for hypersonic simulation as well as for general physical research, has been developed extensively during recent years. Improvements in performance and versatility of this remarkable instrument are constantly being investigated. One of the ultimate goals of these studies is the achievement of higher shock Mach numbers.

Consistent with this interest, one of the important parameters to be considered is the sound speed ratio across the major diaphragm as indicated below from the basic shock tube equation for ideal gases.

$$\frac{p_4}{p_1} = \frac{p_2}{p_1} \left[1 - \frac{\gamma_4 - 1}{\gamma_1 + 1} \frac{a_1}{a_4} \frac{M_s^2 - 1}{M_s} \right]^{-2\gamma_4/(\gamma_4 - 1)} \quad (1)$$

When the pressure ratio p_4/p_1 approaches ∞ as a limit, the maximum attainable shock Mach number becomes the asymptotic value $M_{s_{\max}}$. It is then seen:

$$M_{s_{\max}} \approx \frac{\gamma_1 + 1}{\gamma_4 - 1} \frac{a_4}{a_1} = K \sqrt{\frac{T_4}{T_1}}$$

where

$$K = \frac{\gamma_1 + 1}{\gamma_4 - 1} \sqrt{\frac{\gamma_4 m_1}{\gamma_1 m_4}} \quad (2)$$

The driver and driven gas used are usually selected to be compatible with the experiment under consideration in which case K is a constant. It is noted then that $M_{s_{\max}}$ is proportional to the $1/2$ power of the

temperature ratio across the major diaphragm. It is obvious that for a conventional shock tube the only way in which $M_{s_{\max}}$ can be increased is to heat the driver gas.

For hypersonic studies employing shock tubes of reasonable dimensions, various heating methods have been considered in the in the past. These methods include combustion heating with exothermic gas mixtures and conduction heating by means of electric heating elements. The first scheme

is limited by the maximum combustion temperature of the chemical constituents. The latter scheme suffers from low attainable temperatures of the heating elements and heat losses to the driver walls. The arc heating technique is unique in this application because its heating capability is recognized as more than an order of magnitude higher than other methods previously used in driver gas heating. Arc heating is defined here as the process of conversion of electrical energy into thermal energy of the gas in the form of gas joule heating (j^2/σ). Qualitatively, the gas temperature rise is then proportional to the specific energy input to the gas. The electrical energy can be dumped into the gas in a short time interval of the order of a few milliseconds or it can be added over a longer period of time (100 milliseconds or longer).

A long duration heating scheme becomes attractive because the power requirement is not as severe. Ideally speaking, a small power supply can deliver the required energy if the injection period is made long enough. An electric arc unit such as the plasma-jet is a device within this classification.

Since arc heating does not depend on chemical reaction for the generation of heat, various gases in either pure or mixed form can be used as the driver gas. The combination of mixing inert gases to obtain various effective molecular weights and the ability to vary the gas temperature should lend itself to the tailored-interface⁽²⁾ application, which is a useful method for extending the test time for a shock tube with a short driver section. In addition, an axial temperature gradient can be imparted to the driver gas, normally with the hotter gas near the arc unit. Theoretical considerations show that compression waves from such a positive temperature gradient reinforce the shock wave as it travels down the shock tube^(3,4), which would tend to minimize the attenuation of the shock wave.

This paper describes the feasibility of using a plasma-jet of conventional design as a driver gas heater. Experimental results are presented which describe the operation of the arc unit, its coupling with the shock tube driver, the transient driver gas conditions and finally the shock tube performance using arc heated helium as a driver gas.

II. THE ARC-SHOCK TUBE FACILITY

Figure 1 is a schematic diagram of an arc-heated shock tube made up of three major components: the plasma-jet arc heater (referred to as the arc unit), the driver, and the shock tube. The arc unit is connected to a gas reservoir and the gas flow to it can be regulated to any desired pressure. The unit is separated from the driver by a thin brass diaphragm 0.001 inch thick. Separating the driver section from the shock tube is the major diaphragm, preformed from aluminum sheet stock. It is 0.008 to 0.016 inch thick, depending on the charge pressure used. To facilitate pumpdown of the shock tube section, the tube is sealed at the downstream end by a Mylar diaphragm. The driver is a steel cylinder, 1 foot long with a 4 inch inside diameter. A heat-resistant liner protects the driver walls from high temperatures and also reduces heat loss by the driver gas. A zirconium-oxide (ZrO_2) based material with the trade name of "Rokide Z" coats the interior walls of the driver. A mechanical striker, energized by a solenoid and mounted in the driver, punctures the major diaphragm from within the driver by a sharp point aligned with the center of the diaphragm. A delay timer, regulating the time of strike, can be set to a wide range of delays after arc starting. Two separate vacuum systems with mechanical pumps evacuate the driver and the shock tube section, separately. Arc power is supplied by two battery banks with potentials of 384 or 768 volts, obtainable with parallel or series connections. More than 500 kilowatts can deliver for a short duration to the arc unit. Figures 2, 3, and 4 show the facilities used in the experiments. Helium is used as the driver gas because of its inert nature, low molecular weight, and safe handling characteristics. Air is used in the shock tube driver section.

Arc power input is determined by current and voltage measurements across the arc. A fast-response pressure transducer measures the pressure built up within the driver. The driver gas temperature is measured by platinum and platinum plus 10 per cent rhodium thermocouples inserted about 1 inch into the driver gas. Shock waves are detected with ionization gauges placed 1 foot apart long the shock tube.

III. OPERATIONAL PROCEDURE

In preparation for shock tube operations, the driver is pumped down to a very low pressure while the shock tube section is maintained at a pressure predetermined for each series of experiments. The arc chamber is charged with helium at a selected charge pressure when the system is ready for firing. A thin brass diaphragm at the throat of the nozzle 0.001 inch thick, acts in effect as a shutoff valve and prevents the flow of helium into the driver. The diaphragm is in contact with the anode, and a metal whisker attached to the diaphragm contacts the cathode of the arc. This provides the initial current path and facilitates arc starting.

The sequence of operation begins with the closing of the controller switch which completes the power supply circuit of the arc unit. The current surge quickly vaporizes the metal whisker of the brass diaphragm (Figure 5) together with the portion of diaphragm spanning the throat. This action starts the arc operation and also removes the barrier between the arc chamber and the evacuated driver. As the gas is injected into the arc chamber with a tangential component, a vortex is created within the arc chamber thus maintaining arc stability during operation. Helium flows through the arc column into the driver increasing the driver gas pressure and temperature simultaneously. At a predetermined time after the arc starting, a timer switch energizes the mechanical striker and ruptures the diaphragm, thereby starting the shock formation process within the shock tube. The sequence timer then opens the controller switch and de-energizes the solenoid gas valve, thus shutting off the arc and the flow of helium successively.

IV. THE ARC UNIT

The performance of the arc unit limits ultimately the capability of the shock tube. Development has therefore been directed toward meeting the requirements of shock tube operation with high arc starting and operational pressure, high gas enthalpy, and erosion-free operation. The arc configuration used in this program is rather simple. The electrodes

consist of a cathode made of copper, with a tungsten tip insert to cut down the erosion rate and an anode of a heat-sink type design in the form of a converging-diverging nozzle. The anode has a 1/4 inch throat diameter, cut into a solid copper cylinder. Electrode erosion is one of the main concerns in arc operation, and various combinations of copper, tungsten, and graphite have been tried as cathode and anode material. Graphite, despite its favorable high temperature characteristics, is not suitable as an electrode material because fine particles which form in the process of erosion can cause severe driver gas contamination, resulting in a decrease in shock tube performance. A full-scale assembly drawing of the arc unit used in the experiments is shown in Figure 5.

Because the arc driver coupling phenomena are complex, the arc unit has been studied independently to reveal its specific characteristics. By operating the arc so that it exhausts into the atmosphere, the back pressure is constant. Equilibrium conditions can be achieved shortly after arc starting. The arc phenomena have been photographed with a high speed motion picture camera, and a transparent arc chamber has been constructed specially to permit viewing of the arc column itself. The arc starting transient lasts for less than one millisecond. Steady arc operation then prevails and the arc column can be observed to originate at the center of the cathode and to end downstream of the throat at the expanding portion of the nozzle wall. For low-power runs, the plasma makes no contact with the throat nor does the arc column fill the throat cross-sectional area completely. A linear pinch effect, produced by the arc current induced magnetic field, tends to confine the arc column into a narrow region rather than diffusing it radially. A vortex flow exists within the arc chamber and helps in centralizing the arc column, and thereby provides an envelope of relatively cool helium surrounding the hot plasma. As the power input is increased, the arc column increases in size and luminosity, eventually filling the full throat area. The gas temperature within the driver is then the resultant temperature of the hot plasma and the relatively cool gas that has been injected without benefit of the joule heating.

Two factors are of primary importance as far as the arc operation is concerned. They are joule heating within the gas and heat transfer from the gas to the nozzle walls. The joule heating is the mechanism by which the gas temperature is raised. The heat transfer to the nozzle walls represents the chief energy loss within the arc unit. At low power inputs, the arc column is rather slender and the ratio of the arc column diameter to throat diameter is small. The thermal boundary layer across the helium gas is large because the relatively cool gas surrounding the arc column acts as an insulating layer. Heat transfer to the walls does not present too big a problem. At high power inputs, the arc column diameter increases and displaces more of the cooler gas envelope. Therefore, heat lost to the wall begins to mount until at a certain power level the enthalpy of the gas in contact with the throat surface reaches the melting threshold of the throat material. At this point the nozzle walls start to ablate, eventually causing failure of the arc unit.

With respect to arc starting, it has been observed that for a given arc chamber pressure and electrode gap spacing there is a threshold electrical potential below which the arc will not be sustained after the initial current surge has destroyed the metal whiskers of the brass diaphragm. Arc stability depends on continuity of the current path through the arc column from cathode to anode. An adequate electrical potential, after the initial drop, must be maintained to overcome the large electrical impedance of the relatively cold gas during arc starting. A high charge pressure creates a large flow velocity across the electrode gap. This action tends to break up the weak arc filament formed initially. High pressure also implies high gas density and consequently high electrical impedance. Both of these factors demand a high starting electrical potential for successfully starting the arc. Typical threshold starting voltage for a helium gas with a 350 psi charge pressure is around 380 volts with an electrode gap spacing of about 1/16 inch at the closest approach.

V. ARC-DRIVER COUPLING

The arc-driver coupling phenomena are different from the arc phenomena because the arc exhausts into a closed driver. The jet back pressure, or equivalently in this case the driver pressure, changes with time. Observation of the arc operation during a run reveals that the arc column grows continuously in size and luminosity, eventually filling the whole throat area as the driver pressure is brought close to the charge pressure. This is consistent with the fact that the average enthalpy at the throat increases as the mass flow decreases. This mode of operation is nonsteady and the operating cycle is essentially a long transient. Conditions within the arc and the driver are not uniform. Because of this, the fill-up process is not easily amenable to a rigorous theoretical analysis. Therefore, only average values of density, enthalpy, etc., can be estimated for the arc and the driver conditions.

The initial rate of pressure build-up is rapid within the driver, decreasing to zero as the driver pressure approaches asymptotically the charge pressure. Although the time required for the build-up is long, the driver can be considered full when its pressure reaches 95 per cent of the charge pressure. For the driver size and nozzle configuration used in the experiments, this time interval ranges from 100 to 250 milliseconds, depending on the charge pressure and power input. The time of pressure build-up is designated as the fill time t_f , and the time interval from the onset of driver filling to rupture of the major diaphragm is called the gas dwell time t_d . The driver gas temperature is observed to be a function of time. Since heat transfer within the driver tends to lower the gas temperature, the average gas temperature drops when energy input ceases due to the lack of mass flow into the driver near the end of the driver filling process. For maximum driver performance, the dwell time for the peak average temperature should be made approximately equal to the fill time for the maximum obtainable pressure. Records of the driver pressure, temperature and the arc power input for a typical experimental run are shown in Figures 6 and 7. The driver gas temperature is measured with a thermocouple located near the center of the driver; if this temperature is taken to be the average

value, then the mass input to the driver, which is equal to the mass flow across the throat, can be calculated. Since the perfect gas assumption is permissible for helium at the prevailing temperature (encountered during the experiments) in the driver, the mass within the driver at any time is given approximately by the equation of state, expressed as follows:

$$m_4 = \frac{Vp_4}{R_4 T_4} \quad (3)$$

The average enthalpy of the gas when it enters the driver, also being the enthalpy at the exit of the arc nozzle, is given by:

$$h_a = \frac{\eta_a P}{\dot{m}_a} \quad (4)$$

The calculated arc enthalpy for a run with a fixed value of 0.8 for the arc efficiency is shown in Figure 8. The gas enthalpy is an inverse function of the mass flow. Since the mass flow decreases with time, the jet velocity decreases proportionately. Therefore, the higher gas enthalpy tends to be distributed closer to the arc unit and a positive temperature gradient can be expected in the driver gas. A measured temperature gradient, obtained separately, is shown in Figure 9. Modification of the gradient curve shape can be effected, e.g., by changing the arc injection location, the injection angle, and the number of injection points.

The driver gas average temperature and the total efficiency of the device have been measured. A single thermocouple, located near the mid-section of the driver, measures the driver gas average temperature. The total efficiency is defined as:

$$\eta_t = \frac{\text{final driver gas energy}}{\text{energy input to arc unit}} \quad (5)$$

It can be shown that

$$\eta_t = \frac{\frac{1}{2} p'_4 V}{\int_0^{t_d} P dt} \quad (5a)$$

The graphs for temperature as well as for total efficiency versus power input are shown in Figures 10 and 11.

The gas enthalpy at the throat is high toward the end of the run, and when the nozzle acting as a heat sink becomes saturated, the wall temperature of the copper nozzle can reach the melting point very rapidly. Erosion in the form of melting usually occurs for high-power runs when the threshold enthalpy level for erosion is reached during the early stage of a run. Nozzle erosion has been the chief source of difficulties because a steep rise in arc enthalpy is encountered at the end of every run. The final driver gas average temperature can be expressed as

$$T'_4 = \frac{1}{m'_4 C_p} \left[\eta_a E_{in} - S \int_0^{t_d} \dot{q}(t) dt \right] \quad (6)$$

where \dot{q} is the heat transfer rate to the surfaces of total area S . Qualitatively, \dot{q} is a function of the gas temperature and density; both of which are functions of time. It is noted then for given energy input the final driver gas temperature is a decreasing function of the dwell time t_d , if other factors are held constant in this evaluation. It is thus advantageous to minimize the dwell time for obtaining high final driver gas temperature.

It has been found that driver wall materials limit the maximum operating temperature of the driver gas at about 3000°K. Contemporary materials (such as developed for re-entry nose cones) can withstand these temperatures. For the arc heated driver, the hot gas from the arc impinges on the driver walls at the driver entrance, causing a severe local heating problem. It is this local heating that limits the final average temperature the driver will

withstand without excessive local ablation of the driver liner. Short dwell time is thus necessary to minimize the material heating problem and to reduce the total heat transfer to the walls of the driver.

With more sophisticated arc unit design, such as water cooling for the arc nozzle and throat, the arc enthalpy can be increased. New high temperature materials, such as pyrolytic graphite, can be used to protect the driver walls from overheating. It is believed that driver gas temperature in excess of 3000°K can be attained with such improvements.

VI. SHOCK TUBE EXPERIMENTAL RESULTS

Shock tube experiments to evaluate the arc-heated driver performance have been made. At high pressure ratios, the effects of driver gas temperature on shock Mach number are greatest. Therefore, the initial shock tube pressures were maintained at low values (0.1 to 0.5 millimeter Hg) in order to keep the pressure ratio high. Initial arc charge pressure varied from 200 to 500 psi.

Figure 12 shows the maximum shock Mach number and the effective temperature level obtained with the prototype arc-heated shock tube. The shock Mach number is plotted against the shock tube pressure ratio and examples of the measured driver gas average temperature are indicated. For comparison, calculated curves of the shock Mach number versus pressure ratio using ideal shock tube theory with temperature as a parameter are superimposed on the same grid. The measured temperature values are given for a few points to indicate the level of agreement with theory. In view of the fact that transient temperature has been measured with a thermocouple at one location in the driver, where a temperature gradient exists, and the ideal theory is based on a uniform driver, the temperature parameter cannot be adhered to rigidly in this comparison. Capability of the pilot model arc-heated shock tube is adequate for many areas of aerodynamics research, such as low density high enthalpy aerodynamic testing. As an illustration of the test conditions that can be achieved with a shock wave in air, Figure 13 shows a plot of the stagnation temperature and stagnation enthalpy ratio versus shock Mach number. Future shock tube performance

with this driver heating method will be highly dependent upon the development of the arc unit. The direction of such improvement is achievement of higher arc enthalpy and operating pressure. With the use of high temperature materials in the driver, an increase in driver gas temperature would be permitted with a subsequent improvement in shock tube performance.

VII. CONCLUSION

Experiments have shown that material problems constitute the main practical limitation of the attainment of very high driver gas temperature. The plasma-jet arc heating scheme in its simple form is satisfactory for the production of driver temperatures up to about 3000°K . With improvements in the arc unit and driver liner materials, driver temperatures somewhat exceeding 3000°K should be possible.

ACKNOWLEDGEMENTS

The authors are indebted to D.J. Spencer and W.R. Grabowsky of the Aerospace Corporation for advising and contributing to the development of the arc unit. Leland Von Seggern* has ably managed the electronic instrumentations and has participated in the experiments.

* Now with Aeronutronic, Division of Ford Motor Company.

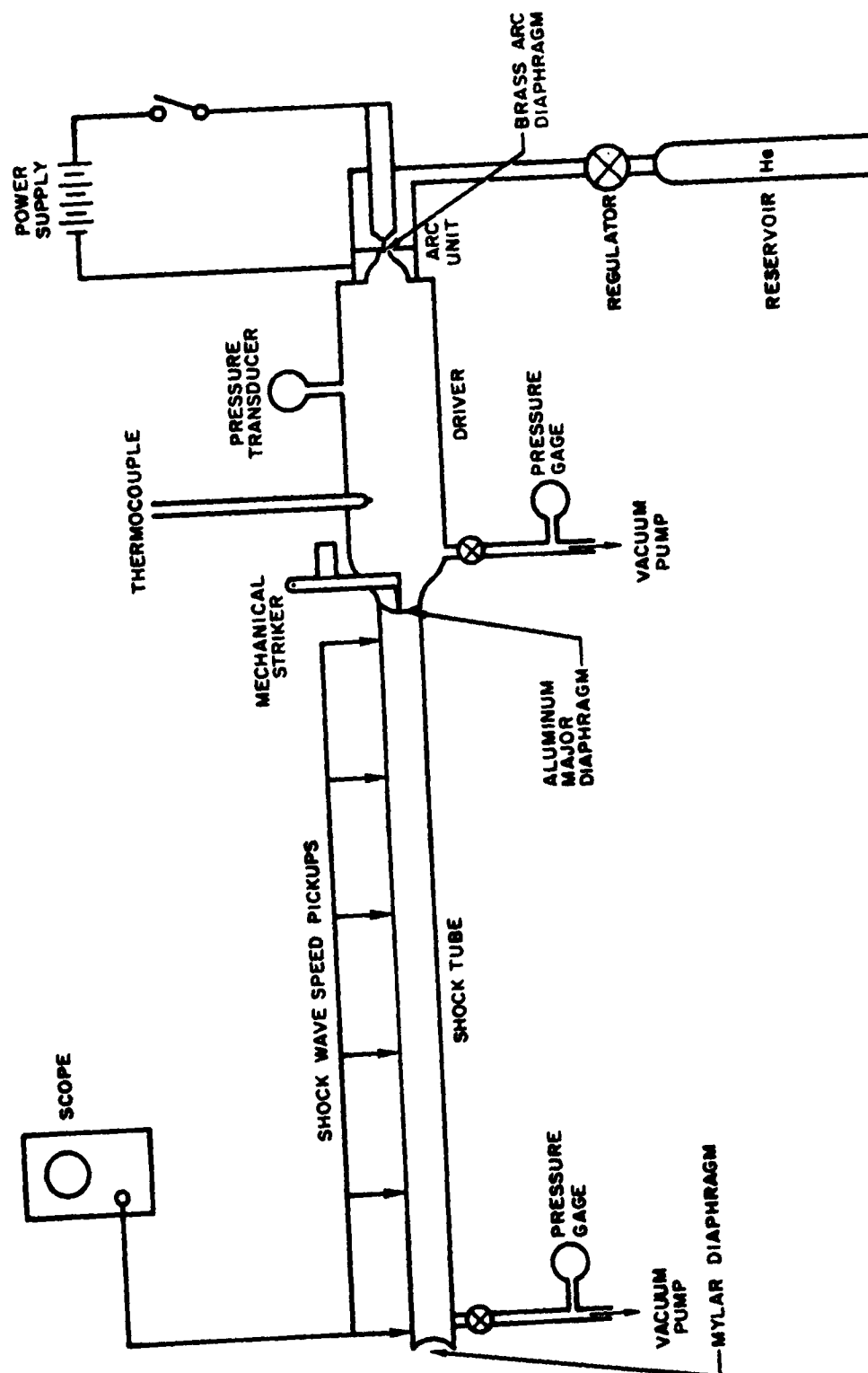


Figure 1. Schematic Diagram of Arc-Heated Shock Tube Facility.

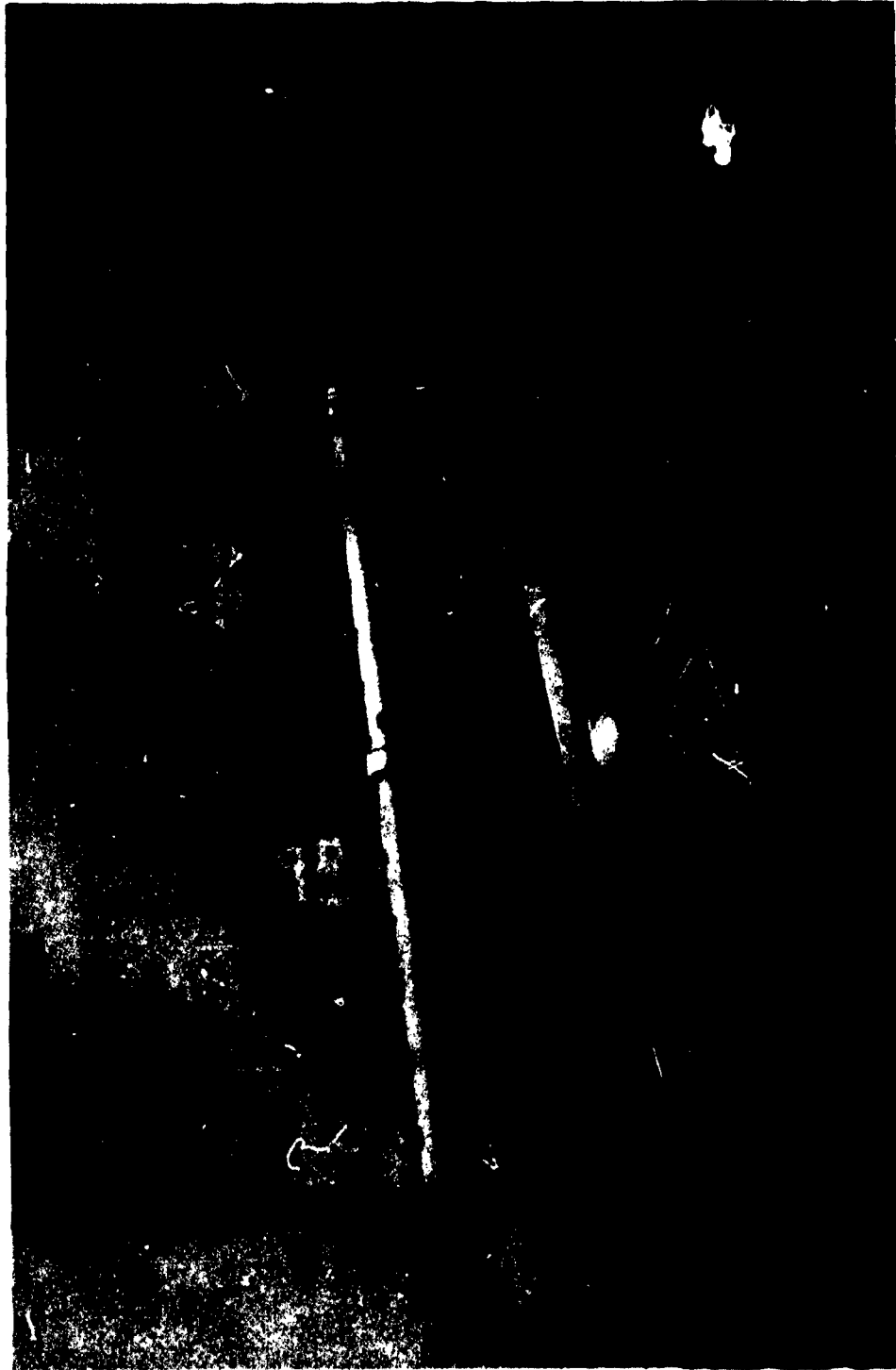


Figure 2. General View of the Arc-Heated Shock Tube Facility.

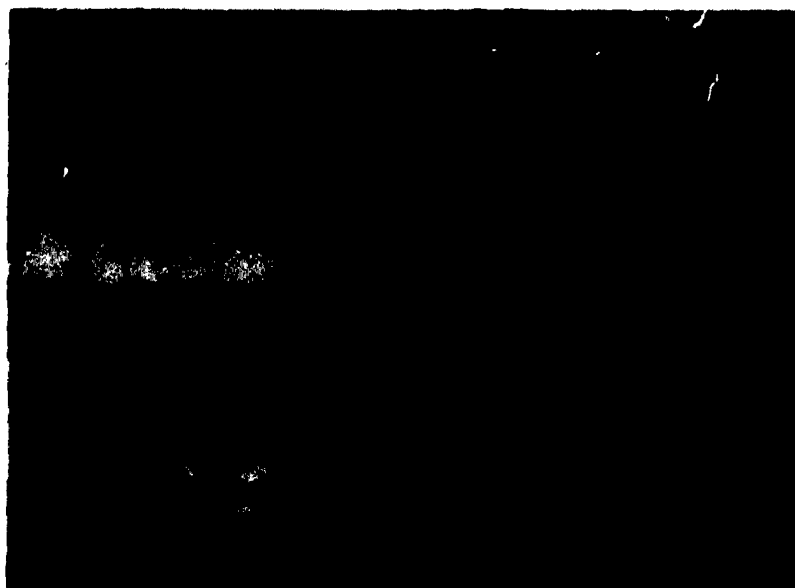


Figure 3. Close-up View of Arc-Driver Installations.

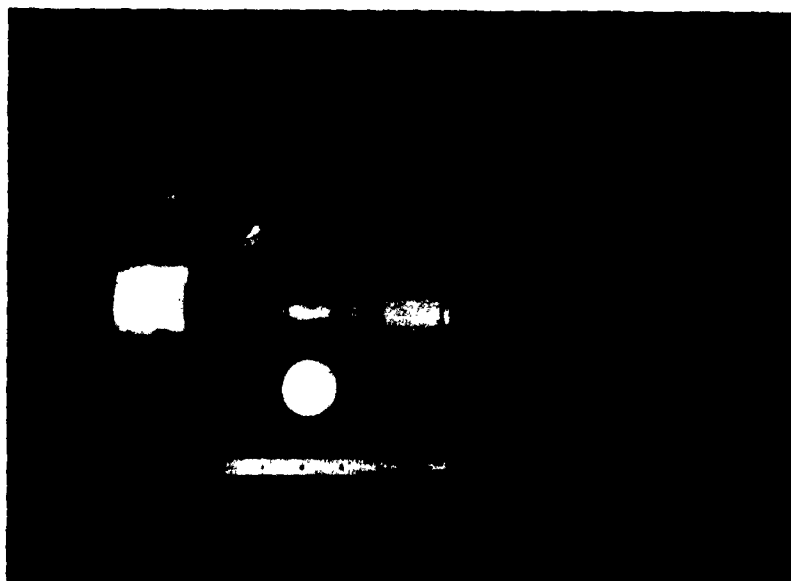


Figure 4. Disassembled View of the Basic Arc Unit.

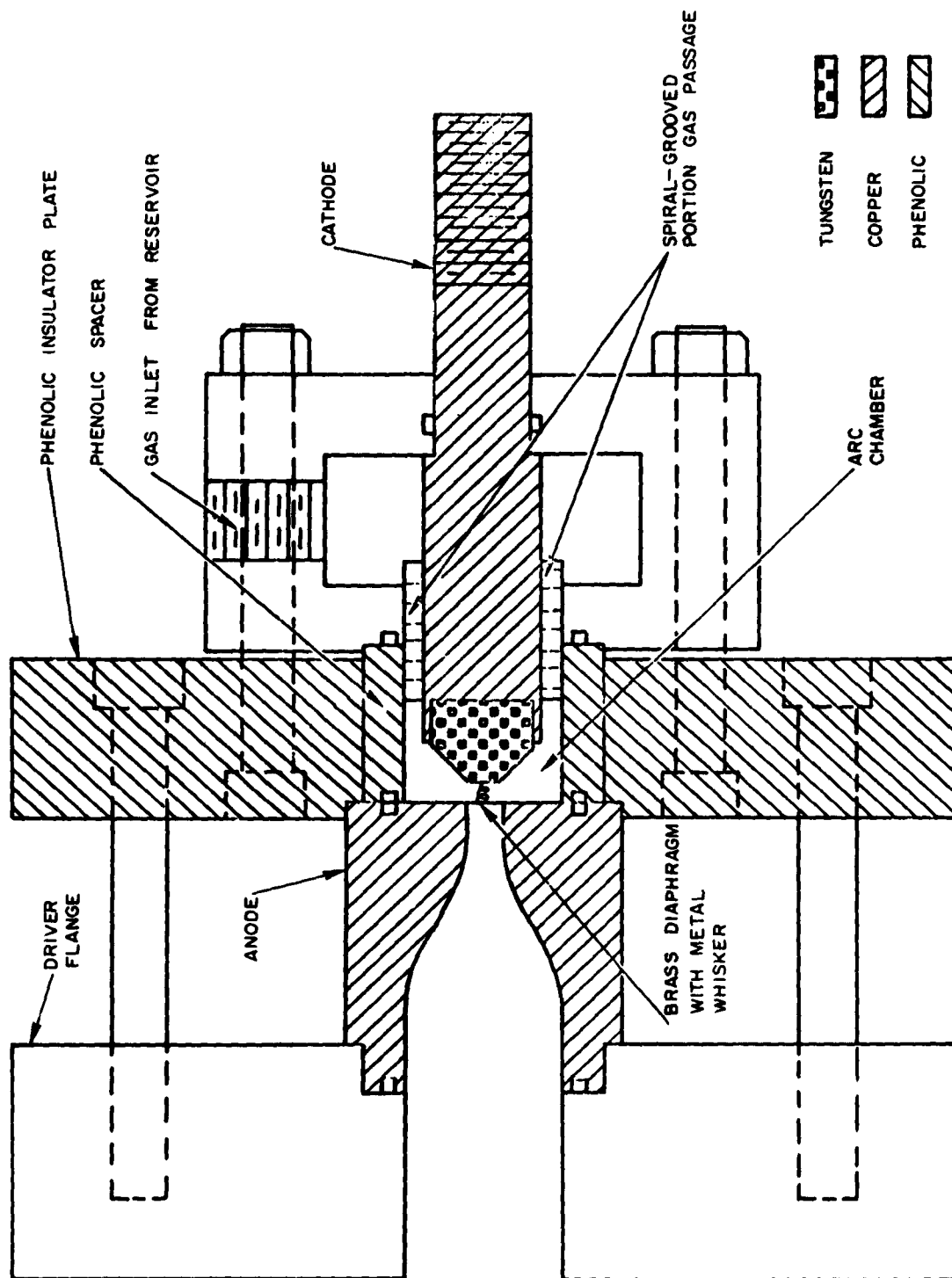
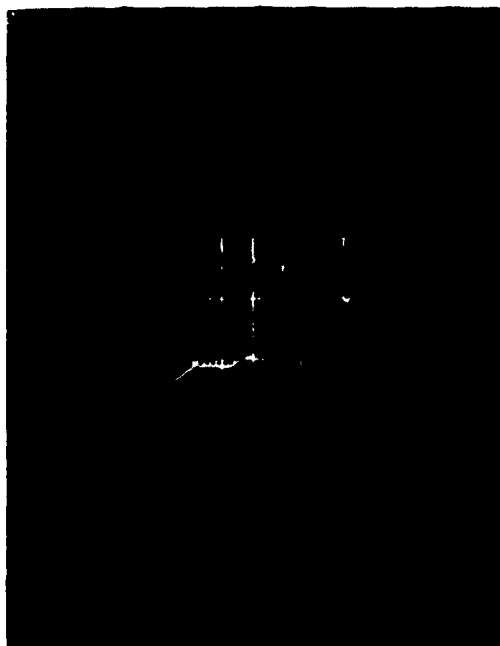


Figure 5. Basic Arc Unit Assembly Drawing.



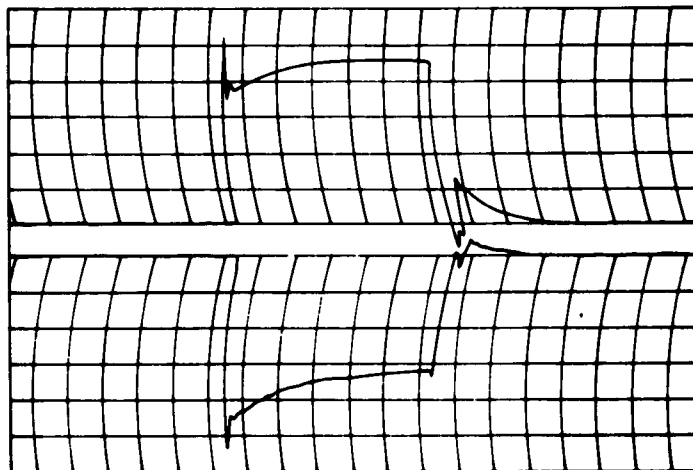
Scale

p_4 = 100 psi per division
(upper trace)

T_4 = 5 millivolts per division
(lower trace)

t = 50 milliseconds per
division (right to left)

Figure 6. Typical Driver Pressure and Temperature Records.



Scale

I = 60 amperes per
division (upper trace)

V = 10 volts per division
(lower trace)

t = 40 milliseconds per
division (left to right)

Figure 7. Typical Arc Current and Voltage Records.

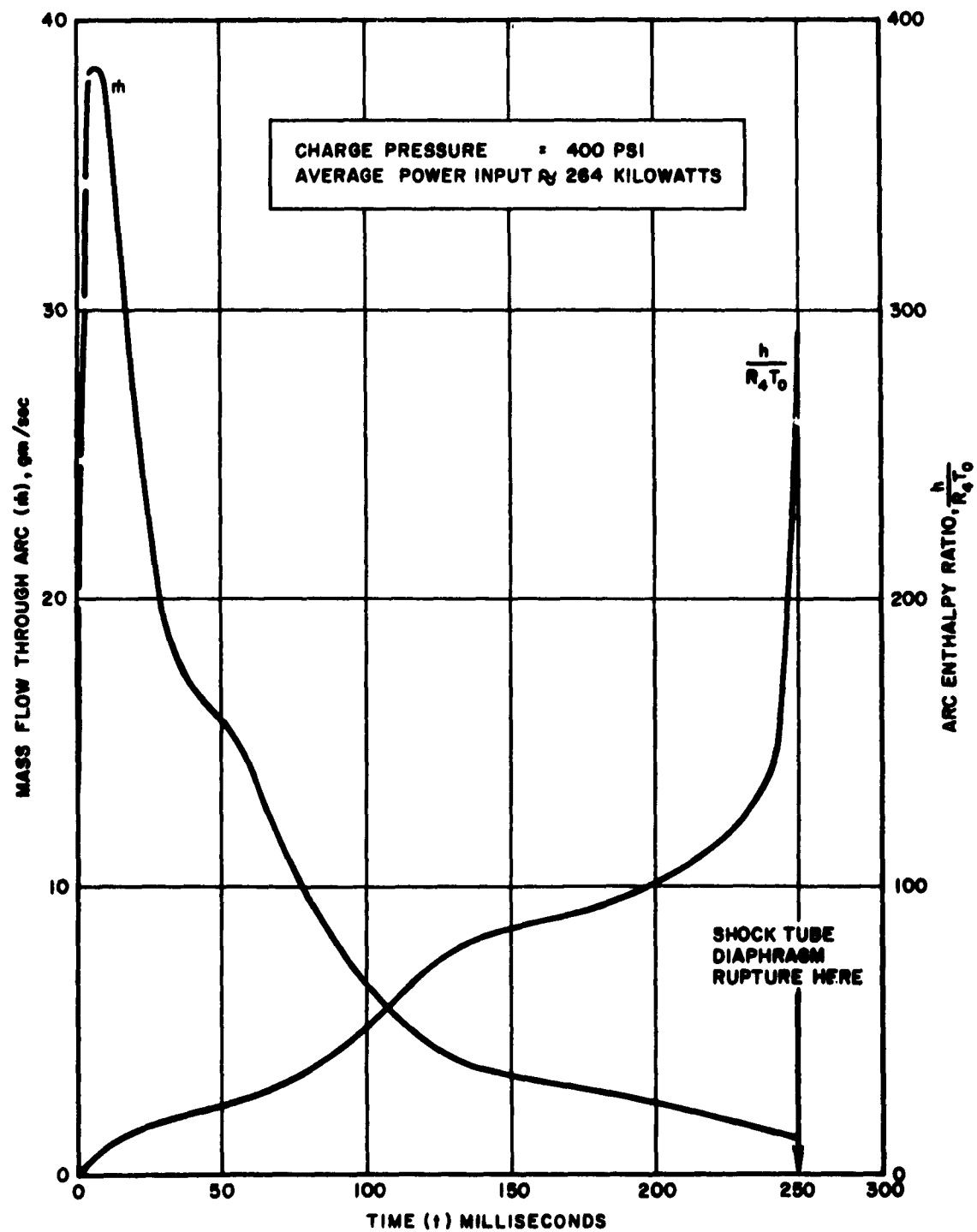


Figure 8. Typical Arc Condition with Coupling to Driver.

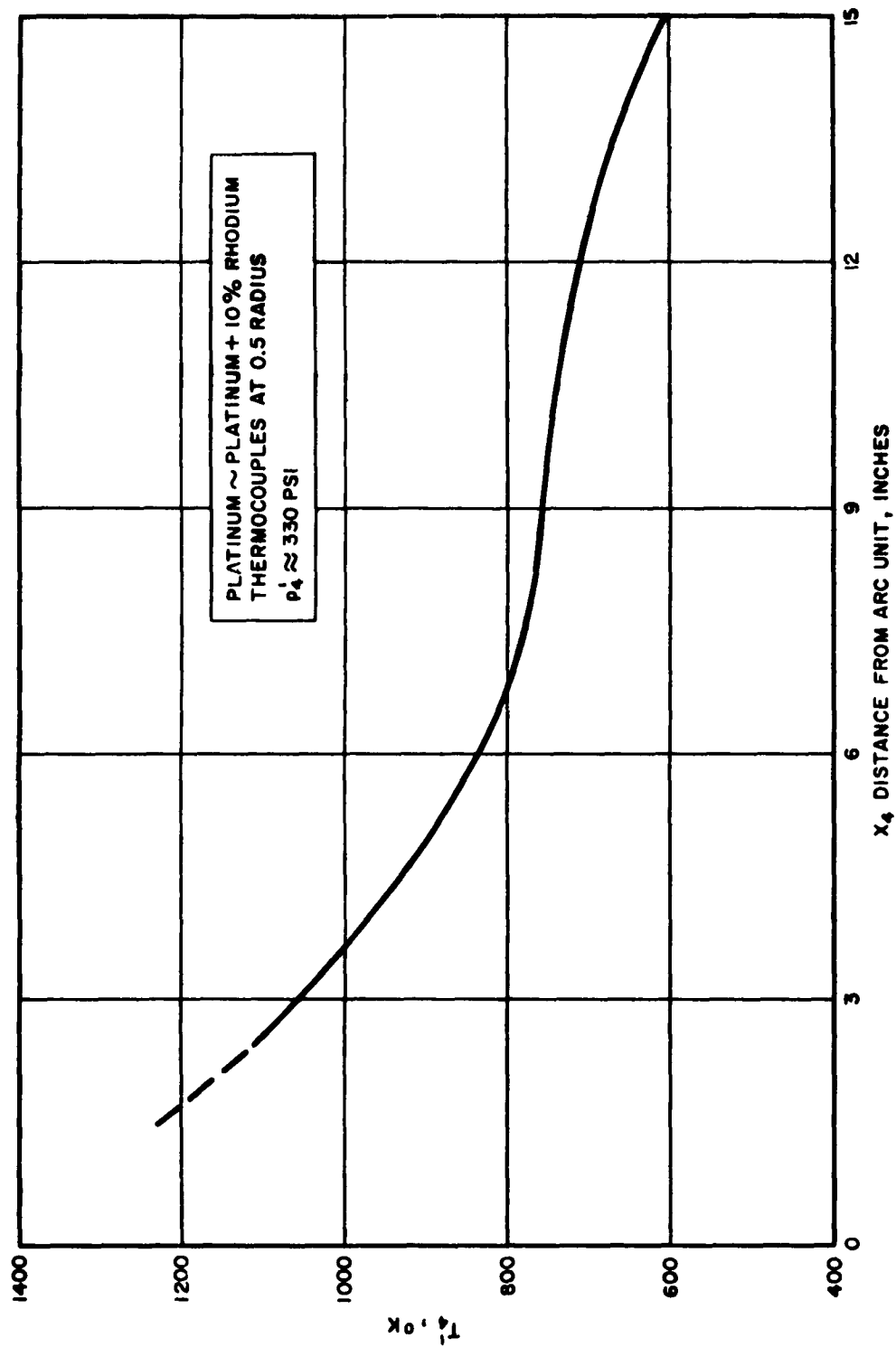


Figure 9. Measured Driver Temperature Gradient.

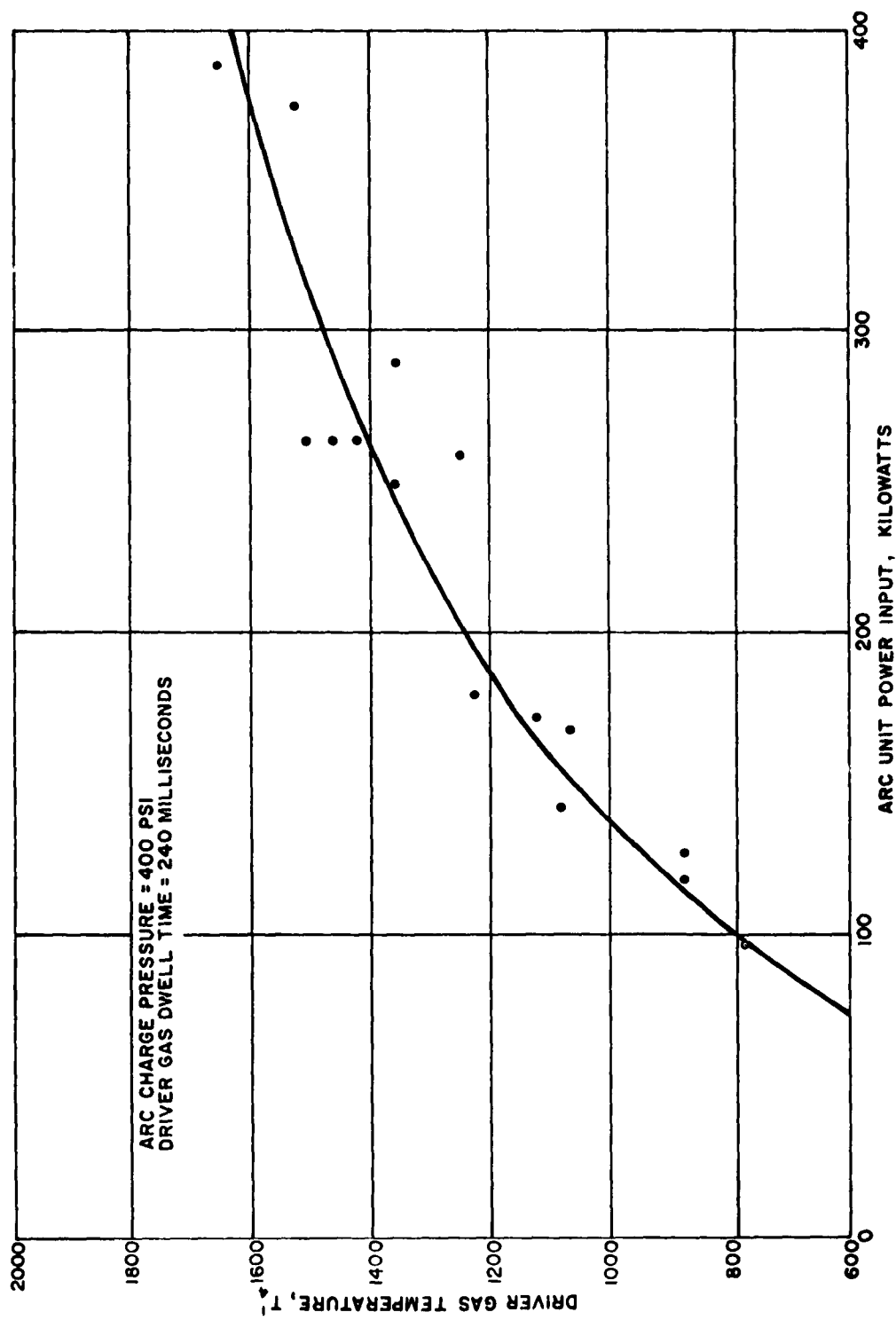


Figure 10. Driver Gas Final Temperature Versus Power Input.

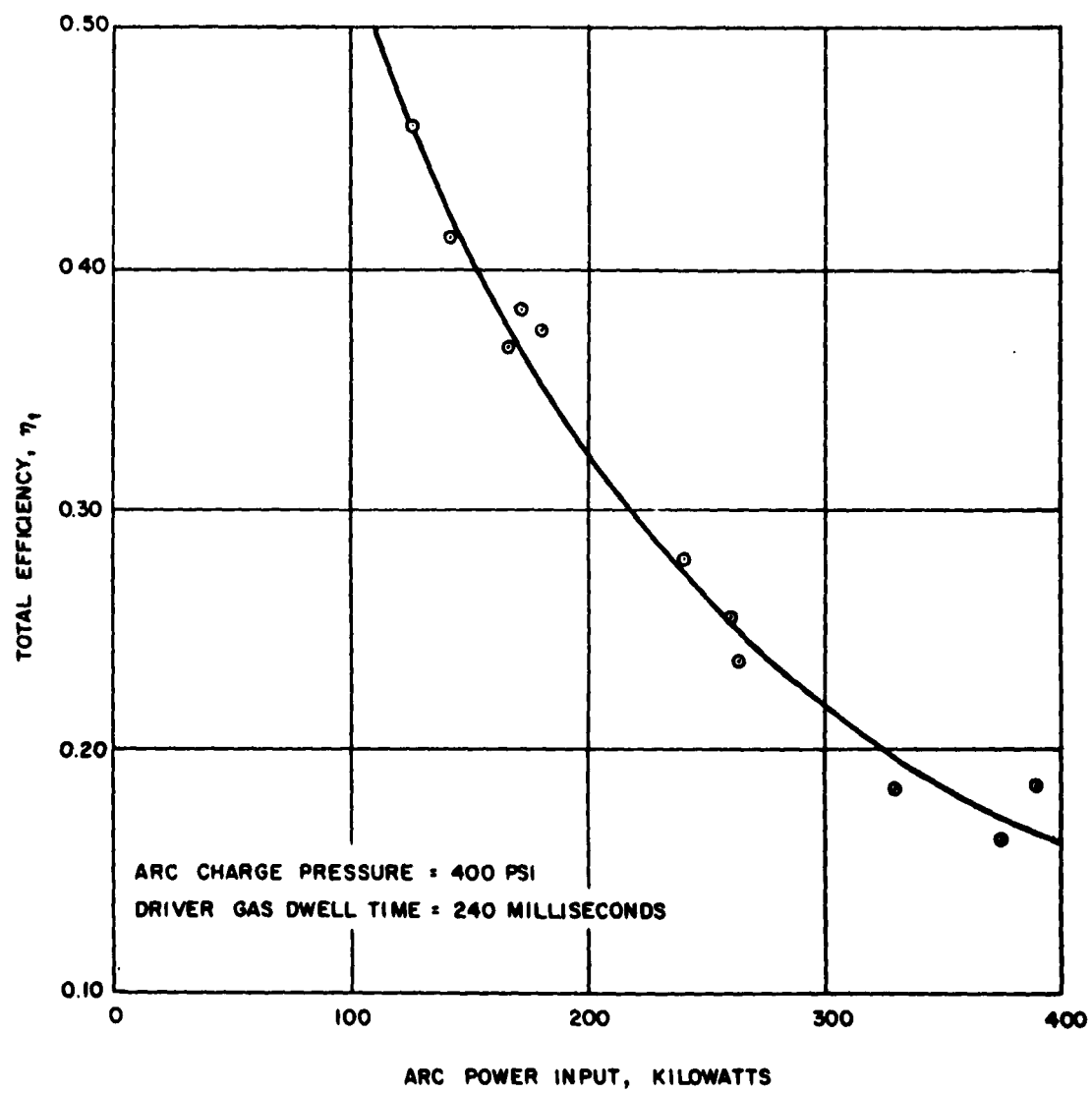


Figure 11. Arc-Driver Total Efficiency Versus Power Input.

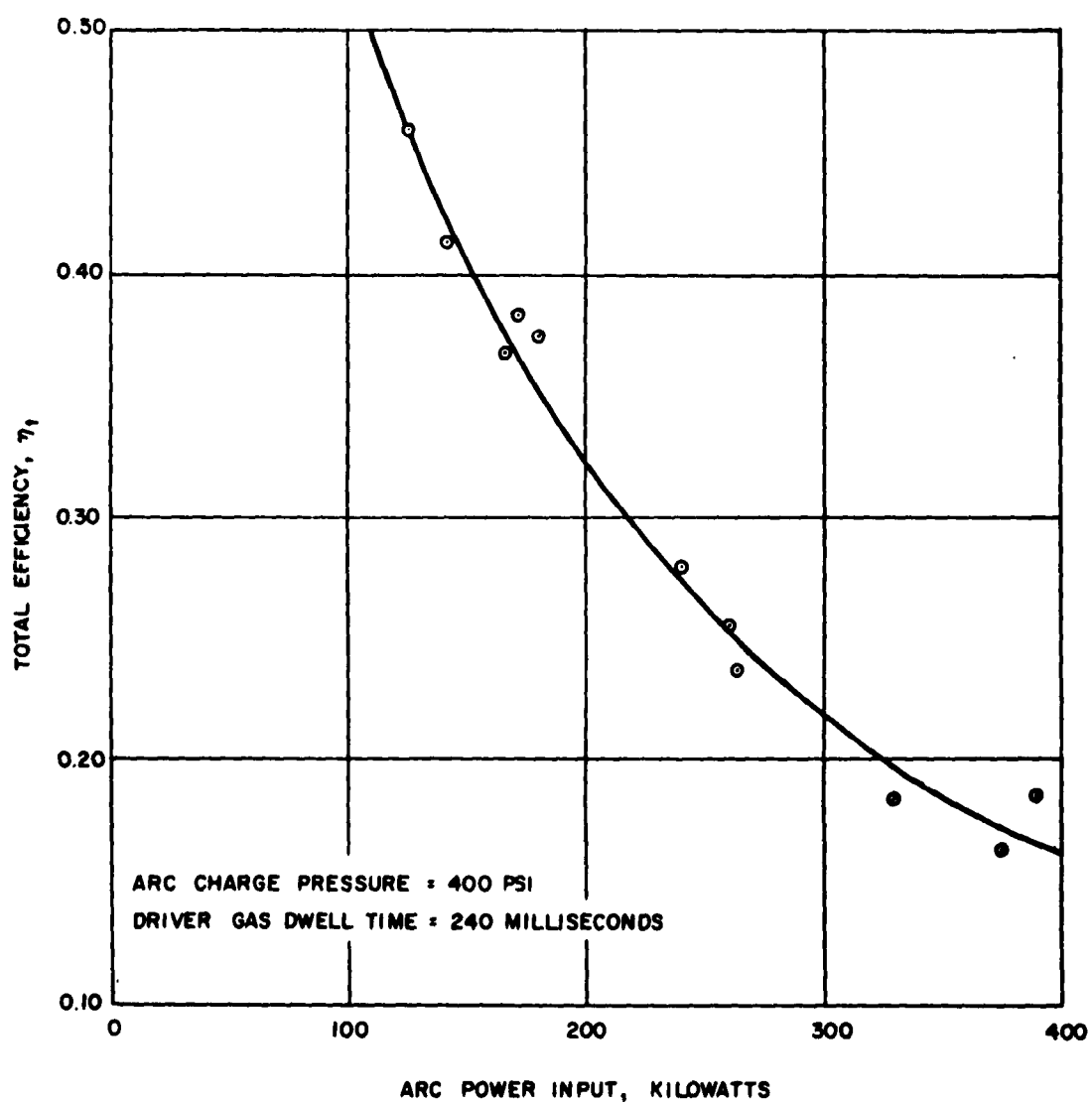


Figure 11. Arc-Driver Total Efficiency Versus Power Input.

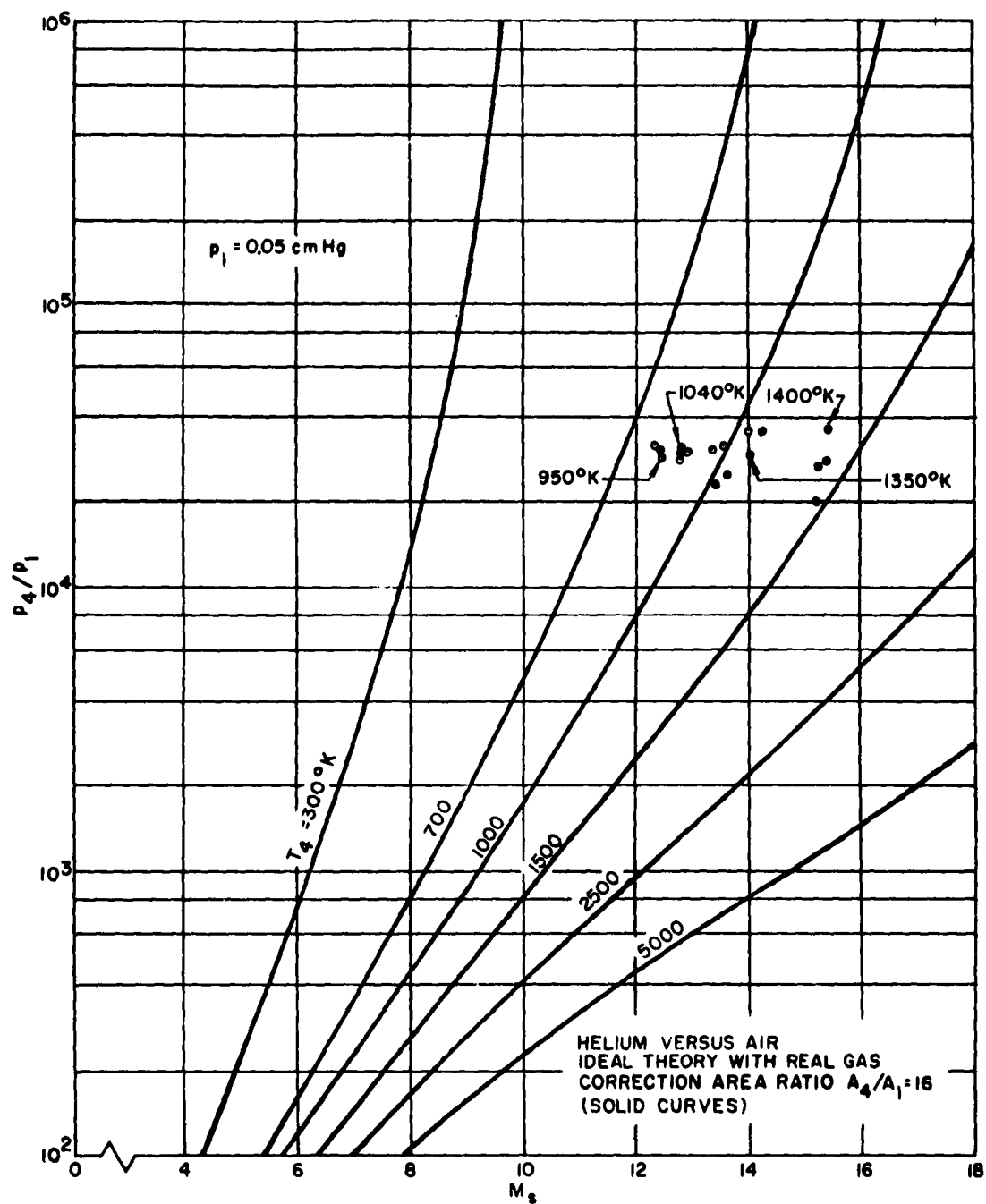


Figure 12. Shock Tube Experimental Results.

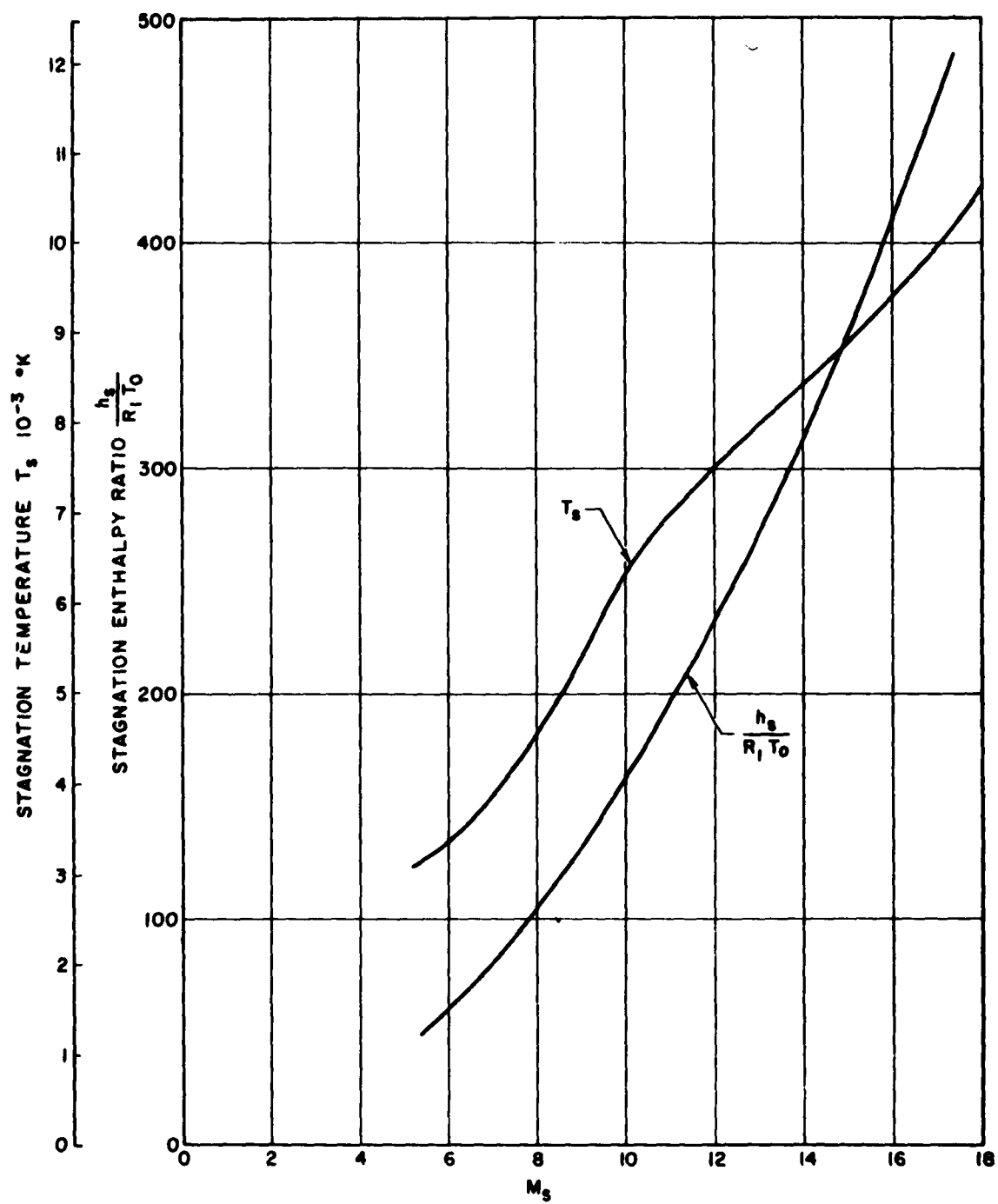


Figure 13. Stagnation Conditions Behind Normal Shock in Air,
 $p_1 = 1$ centimeter Hg.

REFERENCES

1. Resler, E.L., Lin, S.C. and Kantrowitz, A. "The Production of High Temperature Gases in Shock Tube". Journal of Applied Physics, 23 (12 December 1952).
2. Wittliff, C.E., Wilson, M.R. and Hertzberg, A. "The Tailored Interface Hypersonic Shock Tunnel". Journal of Aerospace Sciences, 26 (4 April 1959).
3. Lamb, L.Y. "Semiannual Report on High Mach Number and Materials Research Program". Space Technology Laboratories, Inc., STL/TR-60-0000-09205, 1 January - 30 June 1960.
4. Rudinger, G. Wave Diagrams for Nonsteady Flow in Ducts. New Jersey: Van Nostrand Co., 1954.
5. Lamb, L.Y. and Russel, G.R. "A Preliminary Investigation of Driver Arc Heating Technique for Shock Tube". Space Technology Laboratories, Inc., GM-TN-0165-00278, 3 September 1958.
6. Grabowsky, W.R. and Spencer, D.J. "High Temperature Arc Studies". Space Technology Laboratories, Inc., STL/TR-59-0000-09934, 31 December 1959.
7. Feldman, S. "Hypersonic Gas Dynamic Charts for Equilibrium Air". AVCO Research Laboratory (Everett, Massachusetts), January 1957.

A METHOD FOR THE MEASUREMENT OF AIR TEMPERATURE

UNDER NONEQUILIBRIUM CONDITIONS

Olof L. Anderson
United Aircraft Corporation

SUMMARY

A spectroscopic method suitable for use in shock tubes and other test facilities has been developed to measure the temperature of air or other oxygen bearing gases between 300 K and 4000 K with microsecond time resolution. This measuring technique is based on the light absorption properties of the oxygen molecule in the Schumann-Runge continuum between 1300 Å and 1700 Å. The absorption coefficients at 1470 Å and 1608 Å have been simultaneously determined from measurements in a shock tube up to 5000 K using a 2% oxygen and 98% argon gas mixture. The experimental results demonstrate that this method can be used to measure the temperature of oxygen bearing gases which are not in chemical equilibrium, although more development work is necessary to improve the accuracy of the present system.

INTRODUCTION

A major problem confronting experimentalists working in the field of high-temperature gas kinetics is the measurement of temperature, especially when the gas is not in chemical equilibrium. Although a number of experimental studies of the specific reaction rate constants for the dissociation of oxygen have appeared in the literature (References 1 and 2), very few experimental studies have been made to verify the theory of nonequilibrium flow in nozzles (References 3, 4, and 5), hypersonic boundary layers (Reference 6) and other related problems. Since temperature is an important property of nonequilibrium flows, methods of measuring this property would be of considerable use in such experimental studies.

A number of investigators have reported recently on the use of an ultraviolet light absorption technique to measure the concentration of oxygen molecules during dissociation (References 7 and 8). The object of the studies reported herein was to develop a method for extending the ultraviolet light absorption technique to measure the temperature of air during dissociation or recombination.

PHYSICAL PRINCIPLES INVOLVED IN THE METHOD

Nonequilibrium Flow

In general, a temperature cannot be defined for a gas unless the gas is in thermodynamic equilibrium. However for many gases, the internal degrees of freedom are weakly coupled. Hence it is possible for some internal degrees of freedom of the gas to be in "equilibrium" and not others. "Equilibrium" in this sense means that the energy states of that particular degree of freedom are distributed according to the laws of equilibrium statistical mechanics. Thus if a diatomic gas is in vibrational equilibrium, the population in the j^{th} energy state is given by

$$\frac{N_j}{N} = \exp \left(-j \frac{\theta_v}{T_v} \right) \left\{ 1 - \exp \left(-\frac{\theta_v}{T_v} \right) \right\} \quad (1)$$

where θ_v is the characteristic vibrational temperature of the diatomic molecule and T_v is defined as the vibrational temperature of the gas.

Furthermore, it has been experimentally verified that under most conditions, the translational, rotational, and vibrational degrees of freedom of a gas relax to an equilibrium state much more rapidly than the molecules dissociate or recombine. As an example, from Reference 7, it is estimated that at 4000 K vibrational relaxation is 90 times more rapid than dissociation or recombination relaxation and the translational, rotational, and vibrational degrees of freedom are in equilibrium with each other and their temperatures are identical.

These two facts justify the use of the vibrational temperature as a thermometer to measure the temperature of a gas when the gas is not in chemical equilibrium. Thus as a gas recombines, the heat of formation of the reaction is released and is absorbed in the remaining degrees of freedom. These degrees of freedom then instantaneously relax to a new "equilibrium" state at a higher temperature which is identical to the vibrational temperature.

Light Absorption in The Schumann-Runge Continuum

The oxygen molecule has a strong absorption continuum in the ultraviolet region between 1300 Å and 1700 Å. This absorption continuum is due to the bound-free transition from the various rotational and vibrational levels of the $X^3\Sigma_g^-$ ground state shown in Figure 1 to the $B^3\Sigma_u^-$ upper electronic state which immediately dissociates to one normal 3P and one excited 1D atom. A discussion of this process and the calculation of the absorption coefficient is given in References 9 and 10. A simplified treatment, using the reflection method which is developed in Reference 9, yields the result that the absorption coefficient of the oxygen molecule can be written in the following form,

$$k_v = \sum_j a_j(v) \exp\left(-j \frac{\theta_v}{T_v}\right) \left\{1 - \exp\left(-\frac{\theta_v}{T_v}\right)\right\} \frac{n}{n_0} \quad (2)$$

where the summation is over the vibrational energy states in the ground electronic state. Hence the absorption coefficient is a function of the vibrational temperature of the oxygen molecules and the mole concentration of oxygen molecules.

The absorption coefficient is related to the measured light intensity by the Lambert-Beer law.

$$\ln \frac{I_0}{I} = K_v (n, T_v) l \quad (3)$$

It can be shown from Equations (2) and (3) that the ratio of the absorption coefficients at two different wave lengths in the Schumann-Runge continuum is a function only of vibrational temperature.

$$\alpha = \frac{\ln (I_0/I)_1}{\ln (I_0/I)_2} = \frac{k_v (v_1)}{k_v (v_2)} = f (T_v) \quad (4)$$

The absorption coefficient was calculated as a function of wave length and temperature by the reflection method using some spectroscopic constants from Reference 10. As shown in Figure 2, the peaks of these absorption curves occur at about 1470 Å and are a very strong function of temperature. However, at about 1608 Å, the absorption coefficient is almost insensitive to temperature. These two wave lengths were therefore selected for the absorption measurements.

DESCRIPTION OF EXPERIMENTAL EQUIPMENT

A diagram of the experimental apparatus is shown in Figure 3. The ultraviolet light source consists of a hydrogen glow discharge tube with a lithium fluoride window. The discharge tube is operated at a few mm of hydrogen pressure with 2000 V across the electrodes and is pulsed for 200 microseconds at 3 amps. A vacuum ultraviolet monochromator, which is used to select the proper wave lengths of light, contains a 1 1/2 meter replica diffraction grating which has a dispersion of 6.9 Å/mm and a theoretical resolution of .02 Å. The grating has an aluminum coating with a magnesium fluoride overcoating and a blaze angle chosen to provide maximum reflectance in the ultraviolet region between 1000 Å and 2000 Å. Two photomultiplier tubes, coated with sodium salicylate, are mounted inside the monochromator to monitor the light intensity at 1470 Å and 1608 Å. The output of the photomultiplier tubes passes through a cathode follower and is then displayed on a dual beam oscilloscope where it is photographed with a Polaroid camera. The gas is heated in a 1 1/2-in. dia metal shock tube with a helium driver.

DISCUSSION OF LIGHT ABSORPTION MEASUREMENTS

The absorption coefficient of oxygen at 1470 \AA and 1608 \AA was determined from measurements in the 1 1/2-in dia shock tube for a range of temperatures between 300 and 5000 K. The results of these measurements are shown in Figures 4 and 5 for a test gas having a mixture of 2% oxygen and 98% argon. The large concentration of argon was used to provide a constant temperature heat bath in which the oxygen molecules dissociated. The temperature was calculated from the measured shock Mach number and the Rankine-Hugoniot shock relations assuming vibrational equilibrium.

The ratio of the absorption coefficients is a function only of the vibrational temperature (Equation (4)) and its value will change during vibrational relaxation. When the vibrational degrees of freedom of the oxygen molecule reach equilibrium with the argon heat bath, the vibrational temperature and, hence, the ratio of absorption coefficients remains constant. At temperatures above 2000 K dissociation of the oxygen molecules occurred and the measurements of absorption coefficients were made under chemical nonequilibrium. However, all absorption measurements used for calibration were taken in a vibrationally relaxed gas.

The experimental data shown in Figure 4 substantiates the general conclusions obtained from the theory; i.e., the absorption coefficient at 1470 \AA is very sensitive to temperature changes while the absorption coefficient at 1608 \AA is insensitive to temperature. As shown, there is some scatter of the data and more development work is necessary to improve the accuracy of the measurements.

The temperature calibration of the equipment is shown in Figure 5. When the calibration curve is determined, the spectroscopy method can be used to measure temperatures and mole concentrations of oxygen under nonequilibrium conditions when both the temperature and composition of the gas vary with time. Above 4000 K the measured curve of the ratio of absorption coefficients as a function of temperature decreases slowly

with increasing temperature and the error in measuring temperature becomes more than four times the error in measuring the absorption coefficients. Therefore, temperature measurements using this spectroscopic method above 4000 K are not believed practical.

SYMBOLS

I	Light intensity leaving test section
I_0	Light intensity entering test section
k_v	Absorption coefficient, cm^{-1}
l	Light path length, cm
n	Mole concentration of oxygen (cm^{-3})
n_0	Mole concentration of oxygen at standard conditions (cm^{-3})
N	Number density of molecules, cm^{-3}
N_j	Number density of molecules in j^{th} vibrational state
T_v	Vibrational temperature, degrees K
α	Ratio of absorption coefficients
θ_v	Characteristic vibrational temperature of oxygen (2228 K)
ν	Wave length, angstroms

FIG. 1

POTENTIAL ENERGY CURVES OF OXYGEN

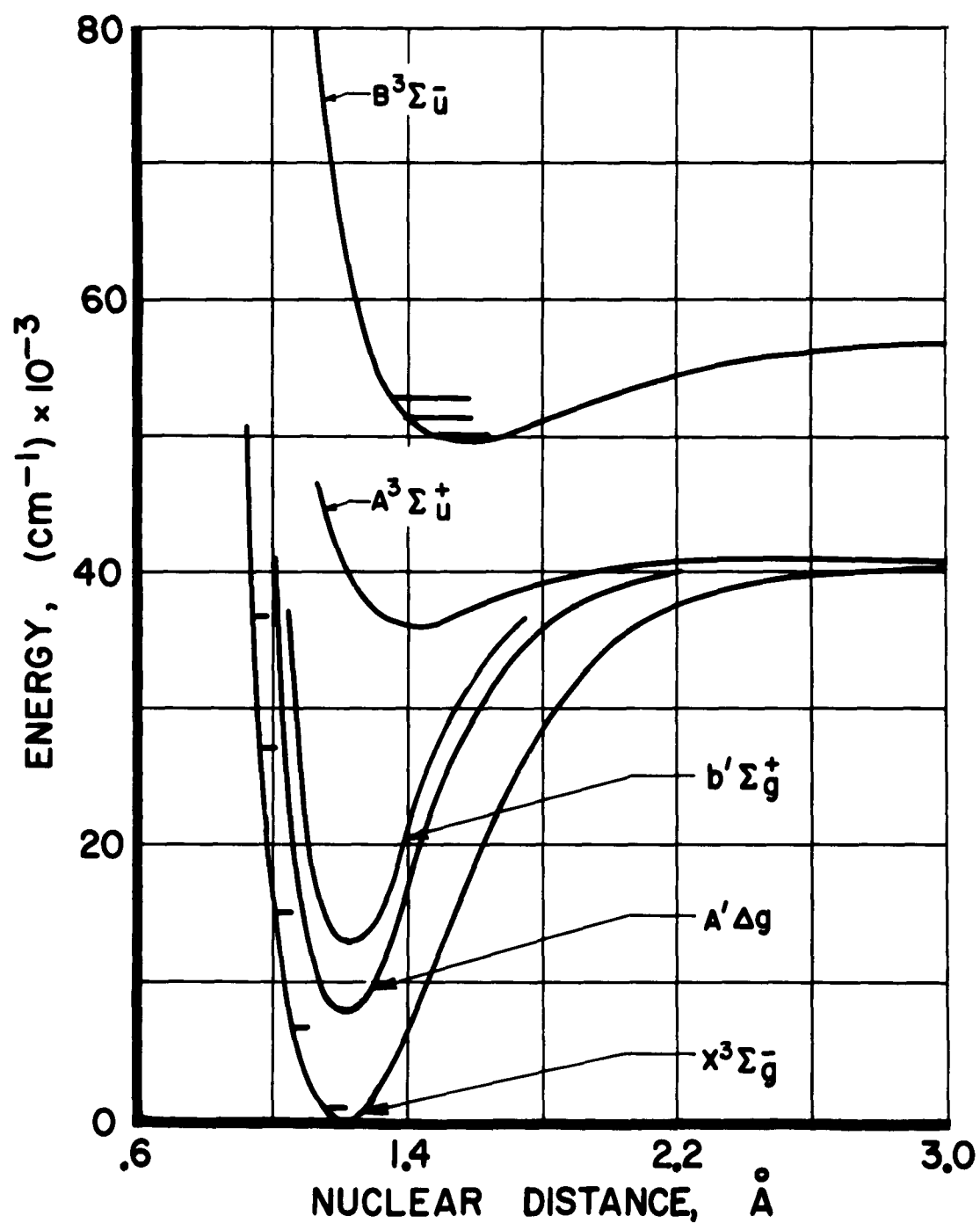


FIG. 2

ABSORPTION COEFFICIENT FOR OXYGEN IN FAR ULTRAVIOLET

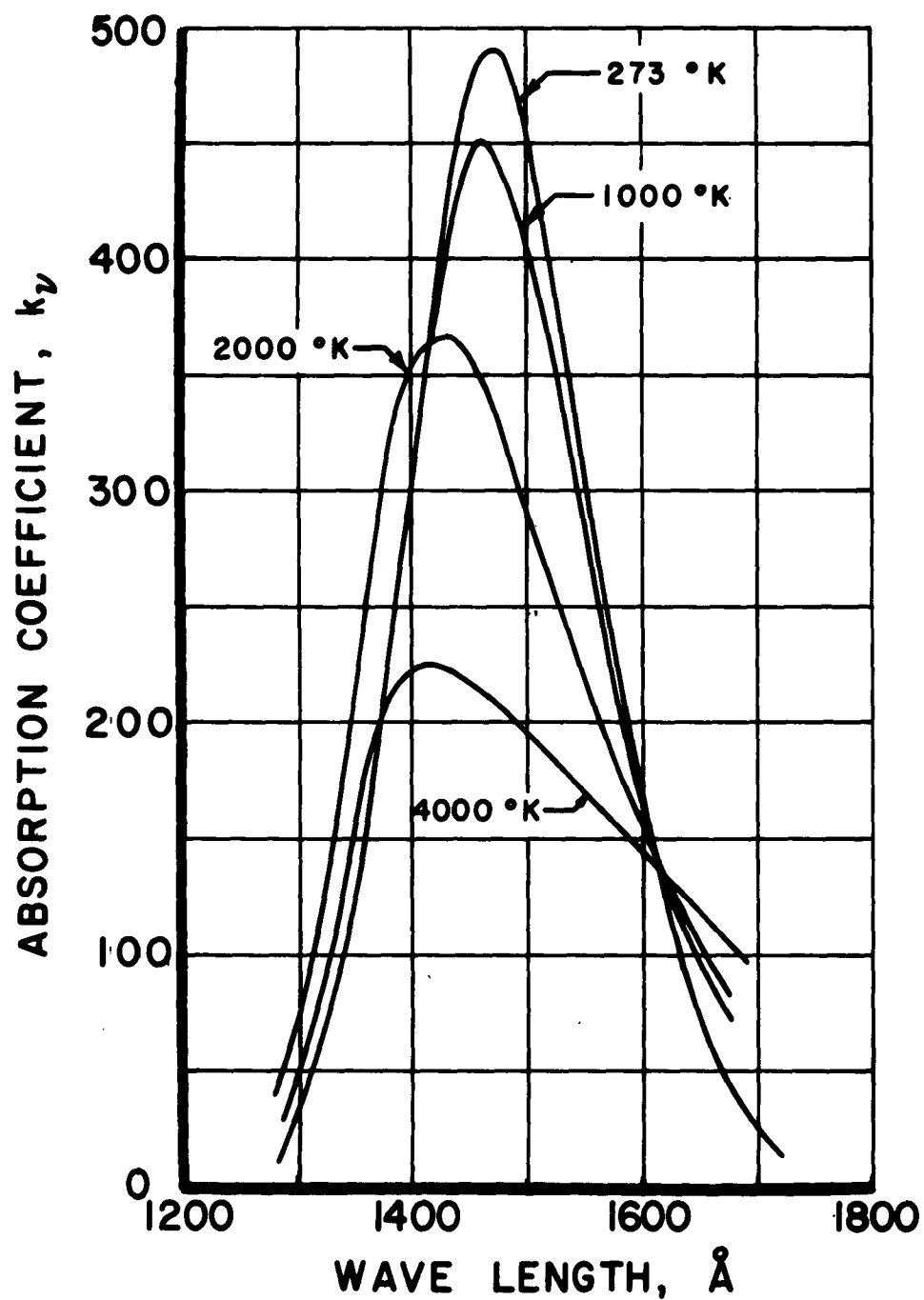


FIG. 3

DIAGRAM OF EXPERIMENTAL APPARATUS

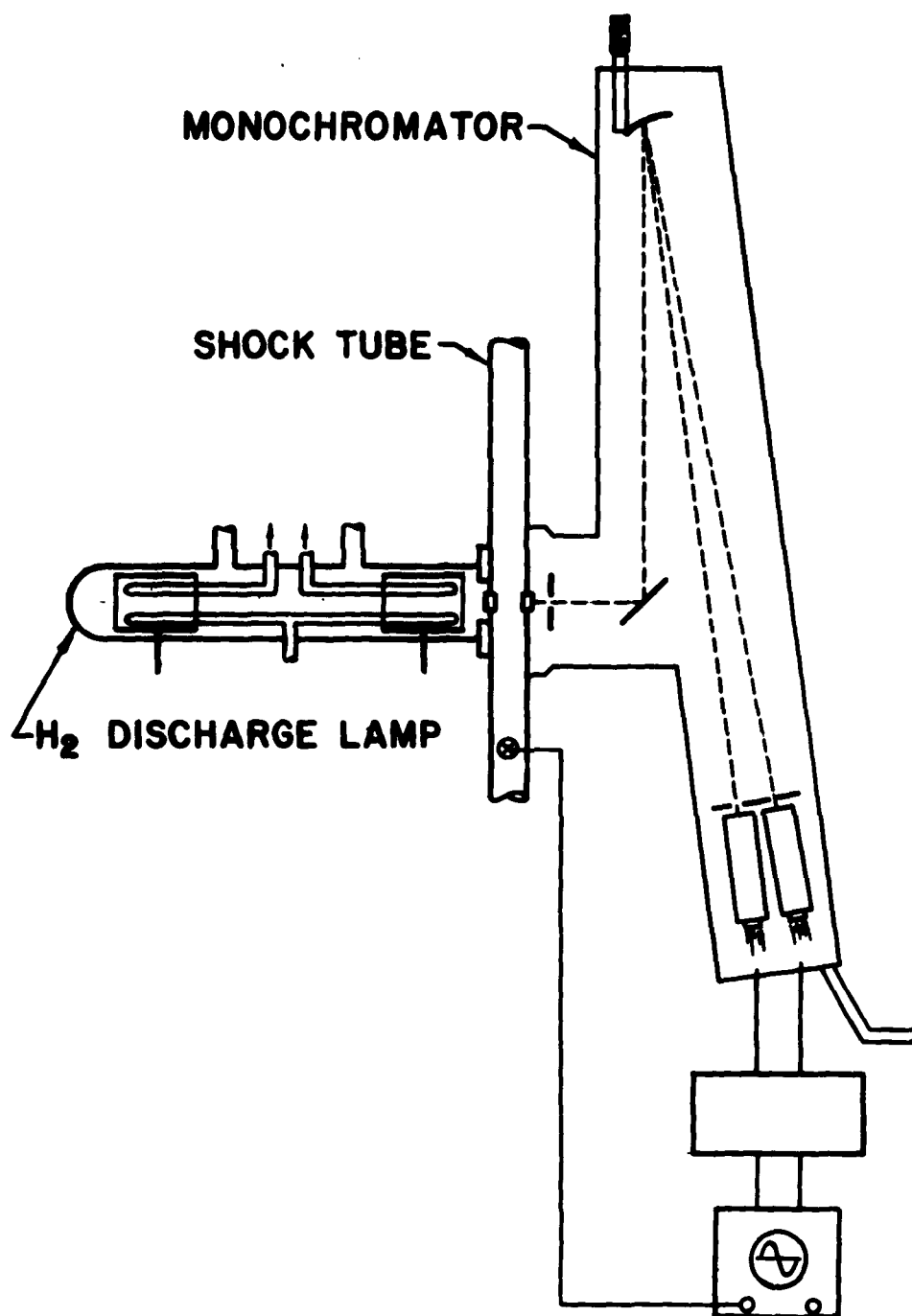


FIG. 4

TEMPERATURE DEPENDENCE OF OXYGEN ABSORPTION COEFFICIENT

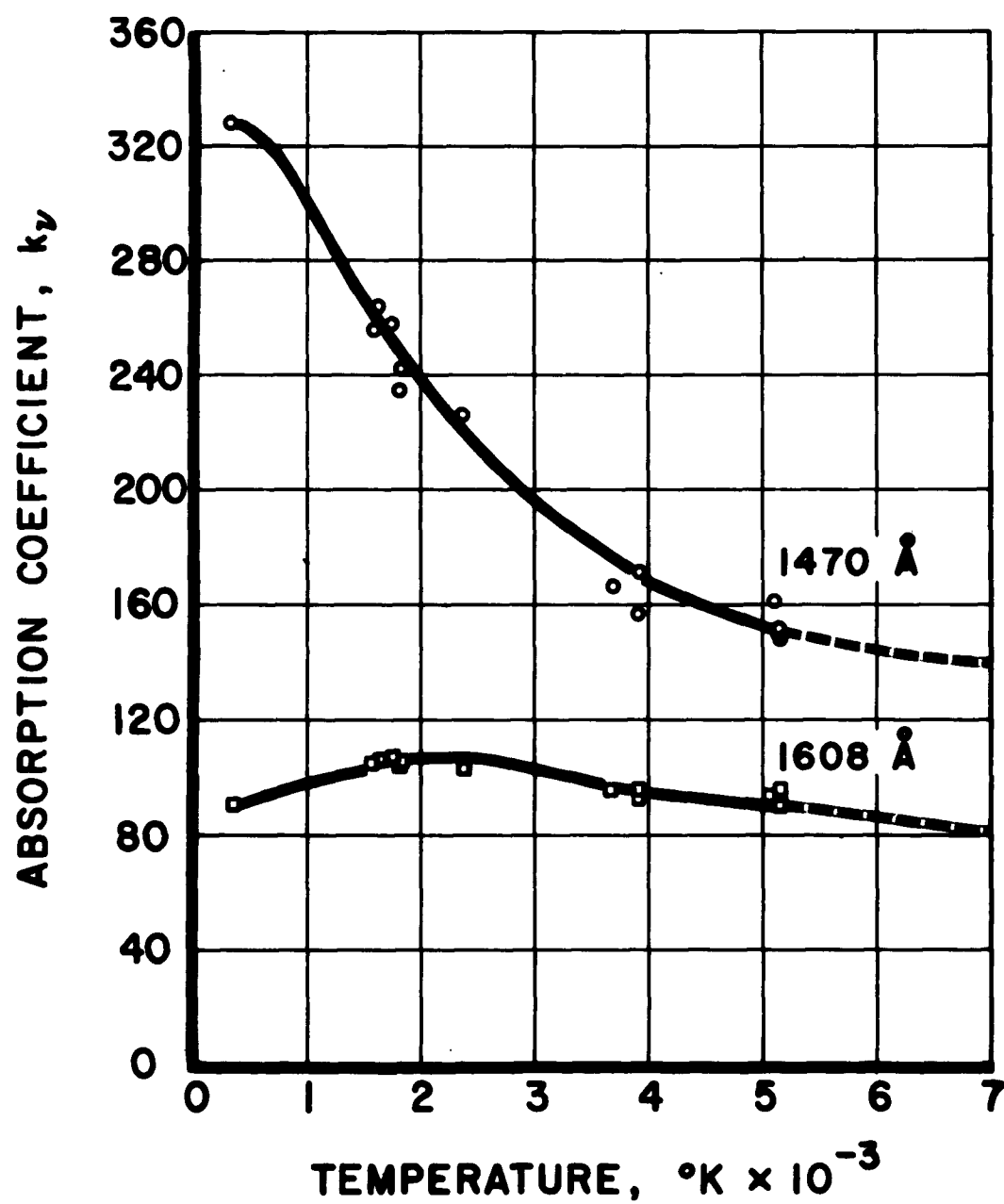
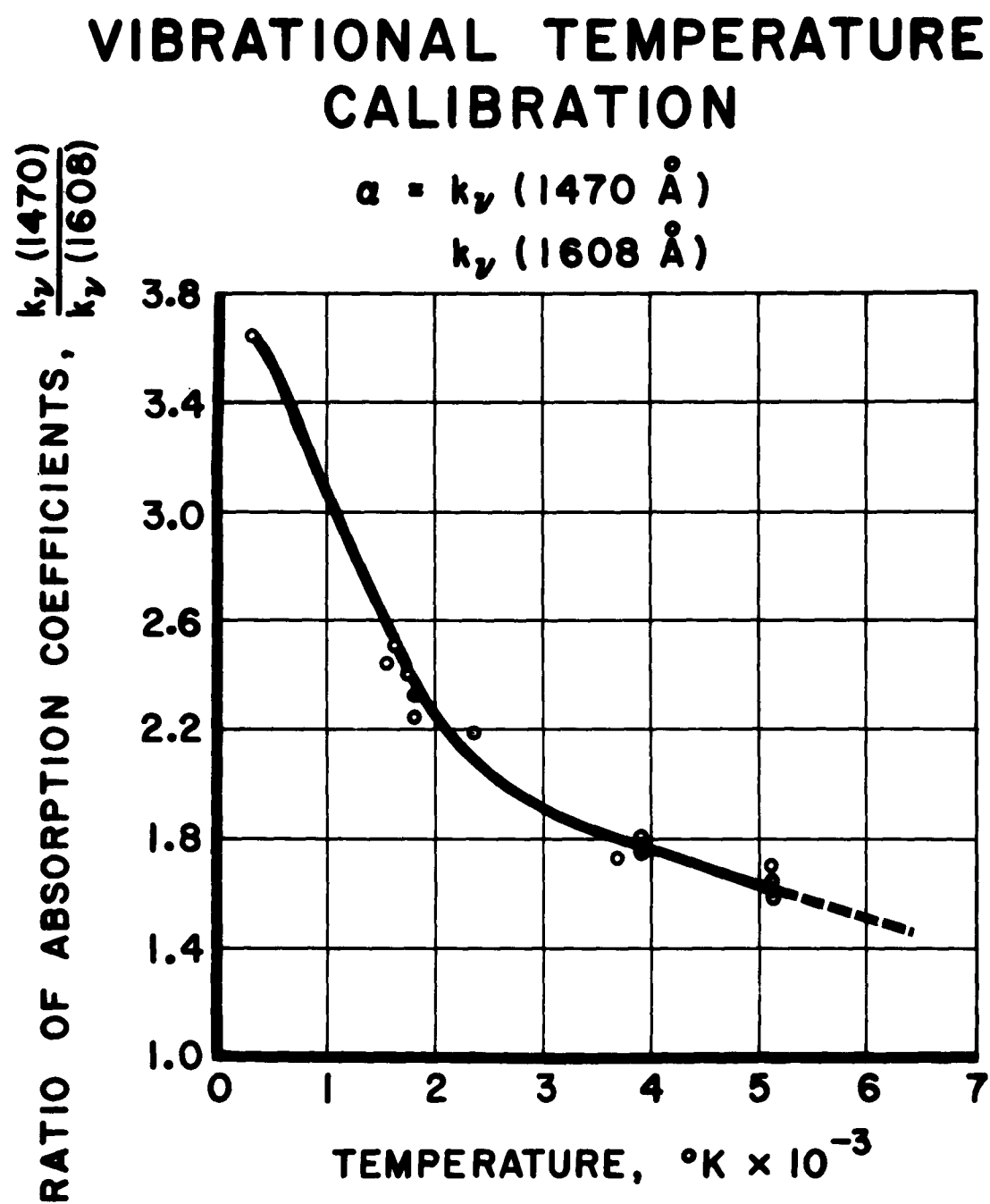


FIG 5



REFERENCES

1. Byron, S. R. Interferometric Measurement of the Rate of Dissociation of Oxygen Heated by a Strong Shock Wave. Ph.D. Thesis Cornell University, 1957.
2. Matthews, D. L. Interferometric Measurement in the Shock Tube of the Dissociation Rate of Oxygen. *Phy. of Fluids*, Vol. 2, 1959.
3. Bray, K. N. C. Atomic Recombination in a Hypersonic Wind Tunnel Nozzle. *Journal of Fluid Mechanics*, July 1959.
4. Bray, K. N. C. and Matsin, B. Recombination of Oxygen in a Nozzle: Comparison with Experimental Results of Air From General Electric Research Laboratory. University of Southampton, USAA Report No. 143, September 1960.
5. Wegener, P. P. Experiments on the Departure from Chemical Equilibrium in a Supersonic Flow. *ARS Journal*, April 1960.
6. Chung, P. M. and Anderson, A. D. Heat Transfer to Surfaces of Finite Catalytic Activity in Frozen Dissociated Flow. NASA TN D-350, Jan. 1961.
7. Camac, M. and Vaughan A. Oxygen Vibration and Dissociation Rates in Oxygen Argon Mixtures. AVCO Corp. AVCO-Everett Res. Lab. Report 24, December 1959.
8. Evans, J. S. and Schexnayner, C. J. An Investigation of the Effect of High Temperature on the Schumann-Runge Ultraviolet Absorption Continuum of Oxygen. NASA TR R-92, 1961.
9. Hertzberg, G. *Molecular Spectra and Molecular Structure I, - Spectra of Diatomic Molecules*. Second Edition, D. Van Nostrand Co., Inc., 1950.
10. Ladenburg, R. and Van Voorhis, C. C. The Continuous Absorption of Oxygen Between 1750 and 1300 Å. *Physical Review*, Vol. 43, pp. 315-321, March 1933.

THE CALCULATION AND MEASUREMENT OF
CENTERLINE FLOW GRADIENTS IN AXISYMMETRIC DUCTS

Solomon Ciolkowski
Grumman Aircraft Engineering Corporation

ABSTRACT

This paper is concerned with some characteristic properties of compressible flows through axisymmetric ducts of varying cross section. A simple technique is developed for obtaining the angularity and Mach number gradients along the centerline of axisymmetric ducts of variable cross section. In particular, relationships are obtained between angularity and Mach number gradients. The results are then used to analyze the angularity and Mach number gradients in conical nozzles. Experiments have been performed to obtain centerline flow gradients by means of the theory described.

INTRODUCTION

In studying nonviscous, compressible fluid flows through axisymmetric ducts of variable cross section it is often desirable to describe the flow behavior along and away from the axis of symmetry. The gradients of the Mach number and flow angularity are often required to determine the usefulness of these ducts. This note is concerned with the analysis of the angularity and Mach number gradients along the centerline of axisymmetric ducts of variable cross section. Axisymmetric wind tunnel nozzles, rocket exhaust nozzles, shock tubes, and shock tube wind tunnels are all examples of these ducts.

ANALYSIS OF THE PROBLEM

The equations describing the isentropic flow of a compressible fluid are

$$\frac{\partial \rho}{\partial t} + \nabla \cdot (\rho \vec{q}) = 0 \quad (1)$$

$$\rho \frac{\partial \vec{q}}{\partial t} + \rho (\vec{q} \cdot \nabla) \vec{q} + \nabla p = 0 \quad (2)$$

$$p = p(\rho, S) \quad (3)$$

$$S = \text{const.} \quad (4)$$

where ρ is the density, p the pressure, \vec{q} the velocity vector, and S is the entropy. This note treats steady axisymmetric flows. The co-ordinate system used is formed by the streamlines and the curves normal to them with the x-axis as the axis of symmetry. Because of symmetry, the x-axis is a streamline. Let ξ be the distance along the streamline and η the distance normal to the direction of ξ .

The equations in this co-ordinate system become (see Reference)

$$q \frac{\partial \rho}{\partial \xi} = -\rho \left[\frac{\partial q}{\partial \xi} + q \frac{\partial \theta}{\partial \eta} + \frac{\sin \theta}{r} \right] \quad (5)$$

$$q \frac{\partial q}{\partial \xi} = -\frac{1}{\rho} \frac{\partial p}{\partial \xi} \quad (6)$$

$$q^2 \frac{\partial \theta}{\partial \xi} = -\frac{1}{\rho} \frac{\partial p}{\partial \eta} \quad (7)$$

$$p = p(\rho, S) \quad (8)$$

$$S = \text{constant} \quad (9)$$

where θ is the angle between the streamline and the x-axis, q the absolute velocity, and r is the distance from the x-axis.

On the centerline (i.e., the x-axis) the equations become

$$q \frac{\partial \rho}{\partial x} = -\rho \left[\frac{\partial q}{\partial x} + 2q \frac{\partial \theta}{\partial r} \right] \quad (10)$$

$$q \frac{\partial q}{\partial x} = -\frac{1}{\rho} \frac{\partial p}{\partial x} = -\frac{a^2}{\rho} \frac{\partial \rho}{\partial x} \quad (11)$$

$$q^2 \frac{\partial \theta}{\partial x} = -\frac{1}{\rho} \frac{\partial p}{\partial r} \quad (12)$$

Combining Equations (10) and (11)

$$1 - \frac{1}{M^2} \frac{\partial \rho}{\partial x} = -2\rho \frac{\partial \theta}{\partial r} \quad (13)$$

Thus a density gradient along the centerline will result in an angularity gradient normal to the centerline and vice versa.

Since on the centerline $\theta = 0$, Equation (12) results in the relation

$$\frac{\partial p}{\partial r} = 0 .$$

Thus, the pressure gradient normal to the centerline is zero and therefore, the Mach number gradient normal to the centerline is zero.

DUCTS OF VARYING CROSS SECTION, ONE-DIMENSIONAL APPROXIMATION

Making use of Equations (11), Equation (13) may be written in the form

$$(M^2 - 1) \frac{1}{q} \frac{\partial q}{\partial x} = 2 \frac{\partial \theta}{\partial r} . \quad (14)$$

If the flow is analyzed using one-dimensional theory to relate area change dA/dx to change in flow velocity q , it is found that

$$\frac{1}{A} \frac{dA}{dx} = - (1 - M^2) \frac{1}{q} \frac{\partial q}{\partial x} . \quad (15)$$

Accordingly, after substitution of Equation (15) into Equation (14),

$$\frac{\partial \theta}{\partial r} = \frac{1}{2} \frac{1}{A} \frac{\partial A}{\partial x} . \quad (16)$$

Since $A = \pi R^2$, with R equal to the radius of the duct,

$$\frac{\partial \theta}{\partial r} = \frac{R}{R} \frac{\tan \theta_{\text{wall}}}{R} \quad (17)$$

where θ_{wall} is the local angle between the walls of the duct and the x-axis. Equation (15) results in

$$\frac{dM}{dx} = \frac{1}{(M^2 - 1)} \frac{q}{\frac{\partial q}{\partial M}} \approx \frac{1}{R} \frac{dR}{dx} . \quad (18)$$

CONICAL NOZZLE

For the case of a conical nozzle, Equation (17) becomes simply

$$\frac{\partial \theta}{\partial r} = \frac{1}{L} \quad (19)$$

where L is the length of the cone from its generating apex. Thus, the angularity gradient is a function only of the length of the conical nozzle.

For a perfect gas the Mach number gradient can be obtained by using the relationship

$$q^2 = \frac{a_0^2}{\frac{\gamma-1}{2} + \frac{1}{M^2}}$$

and Equation (18). It follows that

$$\frac{dq}{dM} = \frac{1}{q} \frac{a_0^2}{\frac{\gamma-1}{2} + \frac{1}{M^2}} \frac{1}{M^3}$$

so that using Equation (18)

$$\frac{dM}{dx} = 2 \frac{M^3}{M^2 - 1} \left[\frac{\gamma-1}{2} + \frac{1}{M^2} \right] \frac{1}{R} \frac{dR}{dx} \quad (20)$$

so that for large M one obtains the approximate relationship

$$\frac{dM}{dx} \approx (\gamma-1)M \frac{1}{R} \frac{dR}{dx} .$$

Accordingly,

$$\frac{dM}{dx} \approx (\gamma-1) \frac{M}{L} .$$

In order to provide some feeling for the magnitude of the angularity and Mach number gradients, consider a conical nozzle with exit diameter of 1.5 feet and 12.5° semiangle with exit $M=13$, $\gamma = 1.64$. Neglecting the

boundary layer, this nozzle will produce a flow $3\text{-}3/4$ inches from its exit with an angularity gradient at the centerline of $\partial\theta/\partial r = 1.29$ degrees per inch. The Mach number gradient is approximately $dM/dx = 0.188$ per inch.

EXPERIMENTS

The Research Department of the Grumman Aircraft Corporation has a shock tunnel which contains a conical nozzle with exit diameter of 1.5 feet and 12.5 degree semiangle. The nozzle is shown in Figure 1. It is driven by a 3-inch internal diameter shock tube shown in Figure 2.

An experiment was devised to use the results obtained in this paper to determine the nature of the flow gradients in the test section of this nozzle. Part of the model is shown in Figure 3. It is made up of eight $1/4$ -inch ball bearings and one 1-inch ball bearing supported by $1/8$ -inch steel rods. The large ball bearing is at the center. The axis of each rod is 1.25 inches from the next. The leading edge of the center ball was placed $3\text{-}3/4$ inches downstream of the exit plane of the nozzle. At this location the Mach number of the flow is 13. The Mach number was determined by measuring total pressure and then determining from a real gas calculation the free stream Mach number.

Assuming that the flow remains conical after leaving the nozzle we obtain

$$\frac{d\theta}{dr} = \frac{1}{L} \quad (21)$$

in units of radians per unit length so that since $L = 44.35$

$$\frac{d\theta}{dr} = 1.29 \text{ degree per inch.}$$

In Figure 4 we have graphed the predicted centerline angularity gradient as a function of distance along the centerline from the apex of the generating cone. By examining the line of symmetry of the shock pattern at each ball we can obtain the local angularity. The schlieren

of the flow in Figure 3 indicates that the angularity gradient is approximately 1.16 degrees per inch when this technique is applied. In addition using the shock displacement distance, Δ , on the large 1-inch ball and the formula

$$\frac{(R + \Delta)^2}{\Delta(R + \frac{\Delta}{2})} = 2 \frac{\gamma+1}{\gamma-1}$$

(see the appendix) we have that $\gamma = 1.65$. Accordingly since

$$\frac{dM}{dx} = (\gamma-1)M \frac{d\theta}{dr},$$

we obtain

$$\frac{dM}{dx} = 0.1689/\text{inch} \quad (22)$$

versus 0.1905 predicted by using Equation (21).

In Figure 5 we have run another experiment using 1/4 inch spheres only. In this case we obtain an angularity gradient of 1.4 degrees per inch which indicates that in this experiment the Mach number gradient was 0.206 per inch. The spheres in this experiment were placed 1/2 inch from the exit plane of the nozzle. The use of the theory, however, permits us to determine the Mach number gradients from the measurement of angularity gradients and Mach number. In the same way we can determine the value of the angularity gradients from measurements of Mach number gradients.

CONCLUSION

The analysis of the centerline flow gradients in a nozzle is carried out. Equations are developed for determining approximately the nature of the flow gradients along the centerline of variable ducts. These equations can be used to evaluate the performance of different types of nozzles.

Experiments are described in which the results are used to determine the characteristics of the Grumman Hypersonic Shock Tunnel nozzle. Because the boundary layer growth in the nozzle was not taken into account, the predicted gradients are too large. However, the measurements indicate that the approximate theory is valid.

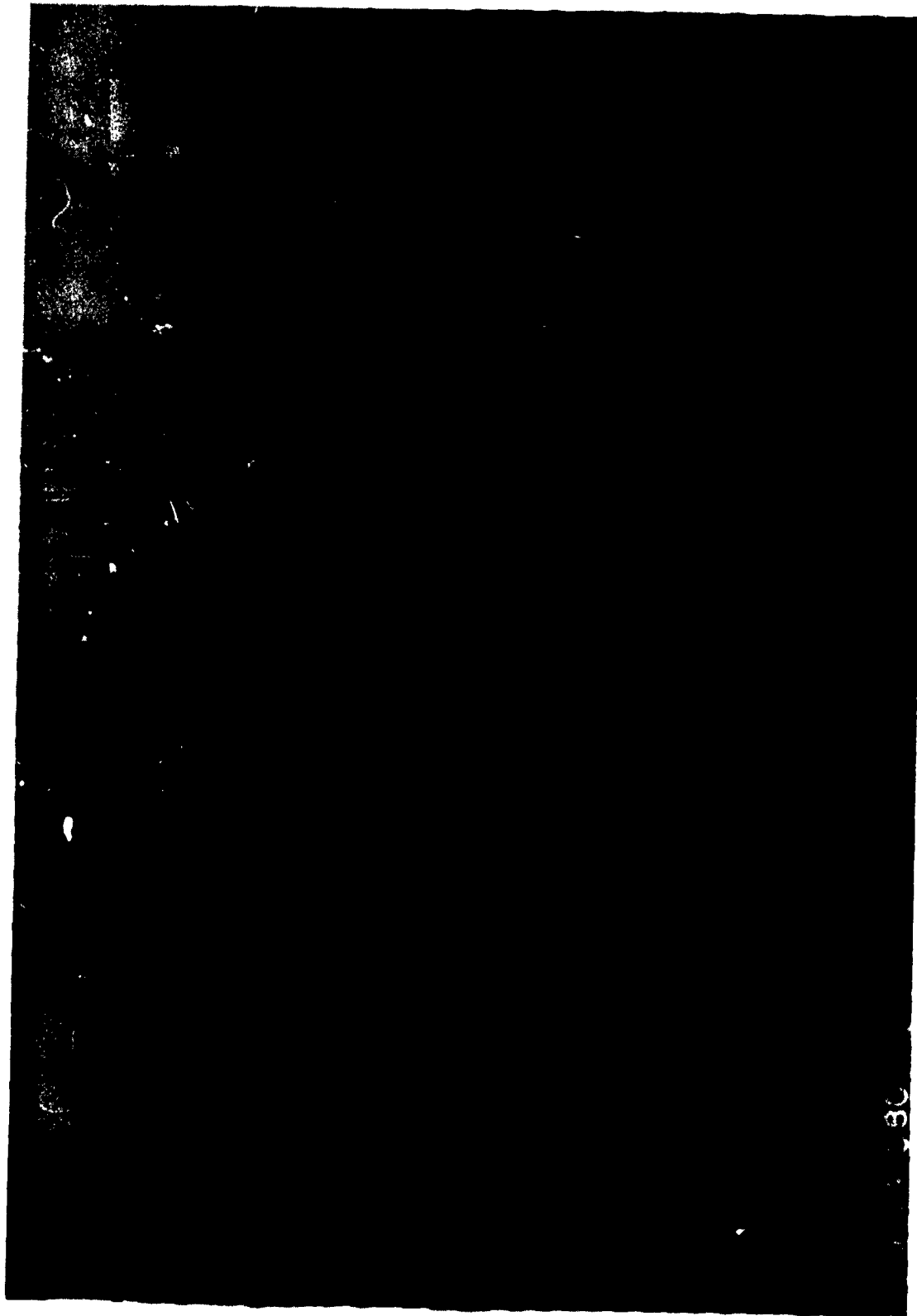
SYMBOLS

a	speed of sound
p	pressure
q	velocity
r	radius in cylindrical co-ordinate system
x	axial distance
A	cross-sectional area
L	length from apex of generating cone of conical nozzle to the exit
M	Mach number
R	duct radius
S	entropy
ρ	density
ξ	co-ordinate along streamline
η	co-ordinate normal to streamline
θ	angle between velocity vector and axis
$()_0$	quantity evaluated at $q = 0$
$()_i$	quantity evaluated in region i
Δ	shock displacement distance

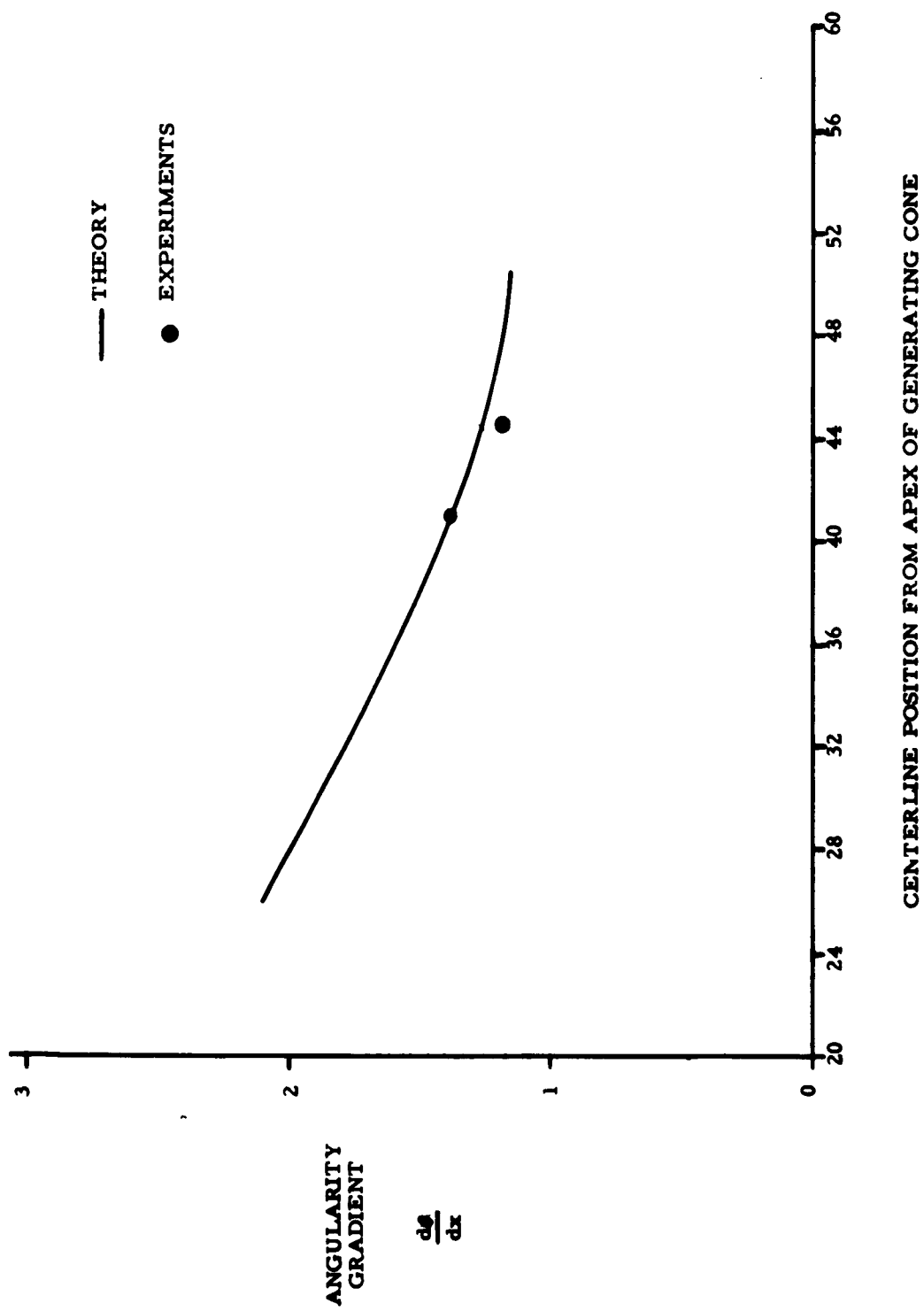
REFERENCE

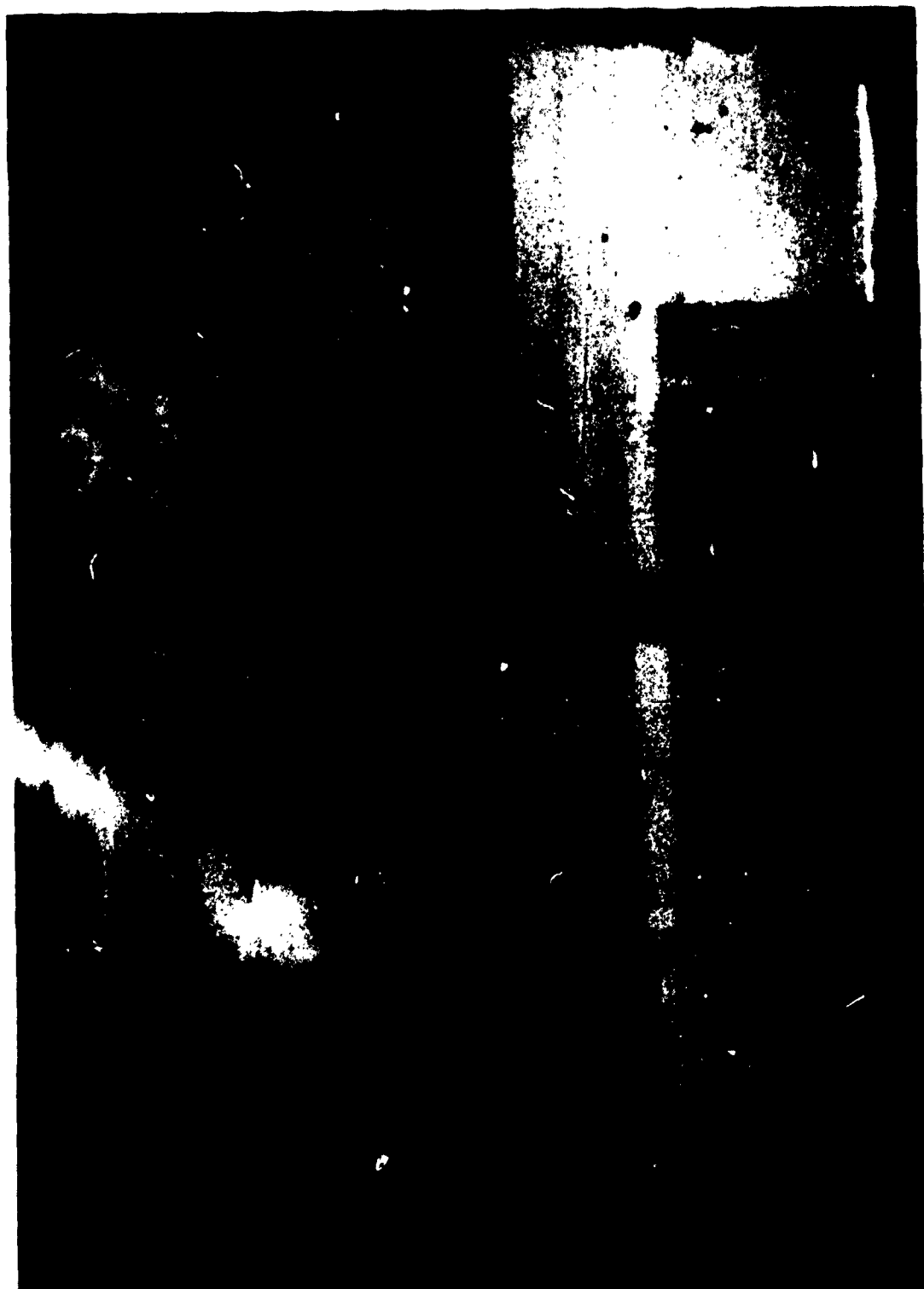
Chu, Boa-Teh. Wave Propagation and the Method of Characteristics in Reacting Gas Mixtures with Applications to Hypersonic Flow. WADC TN-57-213, ASTIA Doc. No. AD118350.











APPENDIX

To determine the relationship between shock displacement distance and the effective value of Δ of the flow impinging in a sphere of radius R we look at the conservation of mass.

The mass flow impinging on the sphere is (see Figure 6)

$$\pi \left[(R + \Delta) \sin \theta \right]^2 \rho_1 U_1$$

The mass flow out of region 2 through the cone of angle θ is

$$\rho_2 U_2 \sin \theta \Delta 2\pi (R + \frac{\Delta}{2}) \sin \theta$$

Equating these two mass flows we obtain

$$\frac{(R + \Delta)^2}{\Delta(R + \frac{\Delta}{2})} = 2 \frac{\rho_2}{\rho_1}$$

For large Mach numbers

$$\frac{\rho_2}{\rho_1} \rightarrow \frac{\gamma+1}{\gamma-1}$$

so that we obtain in the limit as $M \rightarrow \infty$

$$\frac{(R + \Delta)^2}{\Delta(R + \frac{\Delta}{2})} = 2 \frac{\gamma+1}{\gamma-1}$$

PRESSURE AND HEAT-TRANSFER INSTRUMENTATION USED
IN THE NOL HYPERSONIC SHOCK TUNNELS

Philip M. Aronson
U. S. Naval Ordnance Laboratory

ABSTRACT

A brief description of the NOL Hypersonic Shock Tunnel performance capabilities is presented in this paper. Major emphasis is given to a discussion of the pressure and heat-transfer instrumentation used in the shock tunnel facilities at low and high pressures. Two types of pressure-sensitive devices used in measuring shock velocities in the driven gas are reported. A description of the system currently used in the shock tunnel facilities to obtain combustion in oxygen-hydrogen-helium drivers with minimum likelihood of detonation is also discussed. Finally, some "anomalies" obtained in the test section flow are reported.

INTRODUCTION

The hypersonic shock tunnel has, in recent years, become a very important tool in aerodynamic research. The value of this facility depends to a large extent on the accuracy with which one knows and can determine the gas dynamical variables of the flow which it generates. The accuracy of a measurement is itself sometimes very difficult to determine, and in the shock tunnel it is further complicated by the presence of high heating rates, ionization, acceleration, erosion, turbulence, and shockwaves. The type or magnitude of the problems which any investigator faces with regard to the measurement of pressure, for example, depends on the conditions under which the pressure gages are to be used within the given facility. Also, gages which are well-adapted for use in one shock tunnel may be inappropriate in another for such reasons as poor frequency response, low sensitivity, lack of ruggedness, improper physical dimensions, etc. It is appropriate, therefore, that a brief description of the conditions encountered in the NOL Shock Tunnels be given first before any discussion is begun on the pressure and heat-transfer instrumentation used in them.

TYPICAL OPERATING CONDITIONS FOR THE SHOCK TUNNELS

At the present time there are, in the Gas Dynamics Division at the Naval Ordnance Laboratory, four hypersonic shock tunnels. Three of these, the 20-mm, the 1.5-in. No. 1, and the 4-in. No. 3, are all operated as non-reflected or straight-through type facilities. The other shock tunnels, known as the 1.5-in. No. 2, is capable of being operated in either a reflected or non-reflected fashion. Both the 20-mm and 1.5-in. No. 2 Shock Tunnels rely on cone nozzles for expanding the shock-compressed working gas. In contrast to this, the 4-in. No. 3 and 1.5-in. No. 1 Shock Tunnels utilized free-jet expansion to provide the necessary wind-tunnel operation.

The testing times for the NOL Shock Tunnels in their present form vary from approximately 250 to 2,500 microseconds. These times depend on facility, mode of operation, and loading conditions.

The table shown in Figure 1 lists some typical operating conditions for the NOL Hypersonic Shock Tunnels. Values are given for both straight-through and reflected-shock modes of operation. M_s refers to the Mach number of the incident shock-wave as obtained from a measurement of shock velocity at the muzzle end of the low-pressure chamber. P_0 is the peak pressure measured in the high-pressure chamber at a distance of 3 inches from the main diaphragm during the burning of the driver gas mixture. P_1 represents the loading pressure of the working gas in the low pressure chamber. The working gas is air for all cases considered in this paper. P_2 is the pressure measured immediately behind the shockwave at the muzzle. On the other hand, P_3 is the pressure measured immediately behind the reflected shockwave at the muzzle. Since measurements of Pitot pressure have been carried out at the muzzle and in the test section, both values are listed in the table.

It is evident that pressure varies over an extreme range of values in the shock tunnels, from .022 psi to 53,000 psi. To cover this range of pressures two types of pressure gages have been developed at the Naval Ordnance Laboratory. They are the piston-type pressure gage and the

double-crystal acceleration-compensated gage. The double-crystal pressure gage is intended for use below 500 psi. Tests conducted in a shock tube have shown that the gage is capable of compensating for acceleration quite effectively. However, in the shock tunnel environment during a run, conditions are such as to cause erosion of the gage potting material. Calibrations of the double-crystal pressure gage before and after a run have produced deviations as much as 20 percent. Because of this large change in the calibration, new potting materials must be investigated. Since the double-crystal pressure gage is still in a stage of development, no further mention of it will be made in this paper.

THE PISTON-TYPE PRESSURE GAGE

The piston-type pressure gage is used for measuring pressures over the range of 2 psi to 100,000 psi. Its main characteristics are simplicity of design and construction, ruggedness, reliability, and a high natural frequency. A very important feature of this gage is that erosion at the piston face has no effect on its calibration. As shown in Figure 2, erosion can be a serious problem in the shock tunnel, especially when the tunnel is operated so as to provide high Reynolds number flow in the test section. The erosion which appears in the photograph is around gage holes located in the wall of a steel muzzle nut. This piece was removed from the muzzle end of the low-pressure chamber of the 1.5-in. Shock Tunnel No. 1 after having been in use for about 50 firings. It was subsequently cut in half to make the erosion more visible. So long as gages are not made perfectly flush with the bore of the low-pressure section, serious erosion can develop around the gage holes. The piston-type pressure gage, unlike most diaphragm-type gages, is capable of flush mounting. Curvature at the piston face in no way affects its operation.

A sketch of a piston-type pressure gage having a flat piston face is shown in Figure 3. It is machined from a single piece of stock and consists of a piston, a column, and a threaded base which serves only to anchor the gage. As can be seen from the front view, the cross section of

the column is square or rectangular. The sensing elements for the gage are strain gages which are bonded to the faces of the column. The amount of strain which the column experiences when pressure is applied to the piston is dependent on the ratio of the areas of the piston and column. For steel and some other metals, the strain is directly proportional to pressure over a wide range. To compensate for any bending of the column while pressure is being applied to the piston face, two strain gages are placed at similar positions on opposite faces of the column. Electrically, they may be wired in series and placed in a potentiometric circuit or in one arm of a Wheatstone bridge, or they may be placed individually in opposite arms of the bridge. In those instances where the duration of the pressure measurement is sufficiently long for temperature to cause a change in the dimensions of the column and a resistance change in the strain gage, gage accuracy can be maintained by means of temperature compensation. Several types of temperature-compensated strain-gage elements are available commercially, but the temperature range over which compensation is achieved is somewhat limited. A much wider range of compensation is obtainable when two additional uncompensated strain gages are bonded to the two unused faces of the column and positioned so as to measure transverse strain. Temperature compensation is achieved when each of the four strain-gage elements is electrically connected as an arm of a Wheatstone bridge.

Some type of pressure seal is required for the satisfactory operation of these piston-type pressure gages. As shown in Figure 3 provision is made for an O-ring seal around the piston.

The equations which determine the sensitivity or voltage output of the bending-compensated two-element pressure gage to a given applied pressure appear in Figure 4. The first equation is the stress-strain relation with E being Young's modulus of elasticity. A_p and A_c are the areas of the piston and column respectively. Equation (2) defines the gage factor for the strain gage. R is the resistance of a single strain-gage element. The third equation is obtained from equations (1) and (2).

Equation (4) expresses the voltage obtained from a Wheatstone bridge which initially has been balanced and in which two opposite arms contain active elements. The simplicity of this equation is due to the omission of second order terms. Finally, equation (5) results from a combination of equations (3) and (4). For a given bridge supply voltage V , the last equation shows that the output of the bridge is directly proportional to the ratio of areas of piston and column and to the gage factor of the strain gage. It is inversely proportional to Young's modulus of elasticity. If the pressure gage is made of steel and a piston-to-column area ratio of 3 is used, for a bridge supply voltage of 12 volts, a pressure-gage sensitivity of 1.2 microvolts per psi can be expected. In this case a gage factor of 2 has been assumed. The gage sensitivity can be increased substantially by employing the semiconductor strain-gage element which has a gage factor of 120. Further increase can be obtained by using metals such as magnesium, aluminum, beryllium copper, etc., which have smaller elastic moduli. Although the signals from these pressure gages are quite low in amplitude, considerable amplification can be employed before signal-to-noise ratio becomes a problem.

A photograph of four piston-type pressure gages is shown in Figure 5. The largest gage is made of aluminum and has semiconductor elements bonded to two faces of the column. Its range of operation is from 2 to 1,000 psi, and as such it is extremely useful in test-section Pitot-pressure measurements. Its large size is due to the physical dimensions of the strain gage. A reduction in the size of these elements has been announced recently by the manufacturer, and plans have already been made for employing the new units on smaller gage bodies. The next largest gage appearing in the photograph is used to measure combustion pressure in the driver chamber and pressure in the driven section. It is made of steel, has foil strain gage elements, and is capable of measuring pressure as high as 100,000 psi.

A theoretical discussion of the natural frequency of the piston-type pressure gage appears in reference (2). Most of these gages have been found to have a ringing frequency of 40 to 50 KC. Because the

piston gages are somewhat underdamped, a simple RC filter having a 30-microsecond time constant is used to reduce the ringing which is generally present when the gage is shock loaded. These piston-type pressure gages are calibrated statically against a Heise Bourdon tube gage having an accuracy of 1/10 percent of full scale.

Typical calibration curves for two similar steel piston-type pressure gages are plotted in Figure 6. V_{cal} is the voltage obtained from the Wheatstone bridge when one arm of the bridge having a nominal resistance of 120 ohms is shunted with a 10,000 ohm resistor. In order to show that no hysteresis is present in the calibration, data points for both increasing and decreasing pressure have been plotted for gage A56. It should be noted that the calibration of gage A63 coincides with that of gage A56 within 1.5 percent. Although it is not shown on the plot, the theoretically predicted curve lies halfway between the two lines. This shows the degree of quality control possible in the gage manufacture. Since the sensitivity of the pressure gage is dependent on the cross-sectional area of the piston, but not on its shape, the piston face can be contoured without affecting gage calibration. Contouring permits a flush fit with the inner wall of shocktubes having a circular cross section.

The contoured piston-type pressure gage, unlike the flat-faced gage shown in Figure 3, is made in two parts. To permit perfect gage alignment with the bore, the threaded end is machined as a separate part. It then acts as a retaining screw.

A comparison of dynamic and static calibrations for an aluminum piston-type pressure gage is shown in Figure 7. The dynamic calibration appears to be fairly linear. The static calibration, on the other hand, deviates somewhat from the straight line, especially for increasing pressures. The semiconductor strain gages which are bonded to the aluminum column are not temperature self-compensated. The deviations from the straight line observable at the low-pressure end of the plot are due largely to small fluctuations in temperature. At high pressures

the effect of temperature becomes relatively smaller, and the deviation from linearity becomes less pronounced. Because these pressure gages are intended for dynamic pressure measurements only, the error in a measurement due to temperature fluctuation should be negligible.

SHOCK-VELOCITY MEASUREMENTS

There are a number of ways of measuring shock velocity in the working gas. One such method involves the use of ionization-sensitive probes. These probes are extremely simple in construction and can be made to be quite rugged. However, they are unreliable at shock Mach numbers below 4.5 due to the limited amount of ionization. At higher Mach numbers an erroneous shock-velocity measurement is obtained when these probes are used near the muzzle end of the low-pressure chamber and a short distance from the second diaphragm. As shown in Figure 8, the data points obtained with the ionization-sensitive probes at the 200-caliber distance deviate considerably from the extended curve. According to these points the shock velocity increases at the muzzle. On the other hand, when the last two ionization-sensitive probes are replaced with pressure-sensitive shock detectors, the data obtained at the 200-caliber distance appear to fall in line with the extended attenuation curve. In this case no increase in shock velocity is observed at the muzzle. The error in the shock-velocity measurement is 16 percent when ionization-sensitive probes are used in the last two stations which are only 7 inches apart. Since these stations are located very near the second diaphragm, which is steel, it is quite possible that the ionization-sensitive probes are triggered prematurely by electrons emanating from the surface of the diaphragm due to the photo-electric effect. No further investigation has been conducted thus far to verify this possible explanation.

Since ionization-sensitive probes cannot be used with any degree of accuracy near the second diaphragm, a special pressure-sensitive probe had to be designed which was capable of withstanding pressures as high as 30,000 psi. A drawing of this shock-wave detector is shown in Figure 9. The sensing element is a lead zirconate or barium titanate

disc, which is protected from the shock-heated working gas by a heat barrier and a thin metal diaphragm. The heat barrier is a neoprene disc. Shock mounting is supplied by a teflon cup. The design of the probe is such as to permit a change of parts in a simple manner whenever required. The output voltage from the probe is very large, and generally it must be reduced by means of a capacitor shunt.

The response of the shock-wave detector can be seen in Figure 10. Both the rise time, which is less than 5 microseconds, and the absence of any signals ahead of the shock-wave are of significance. Because of the short rise time inherent in these detectors, one percent accuracy is possible in the shock-velocity measurement over a distance of 7 inches when the shock transit time is at least 100 microseconds.

The shock-wave detector shown in Figure 9 is limited in use to pressure below 30,000 psi. Above this value a more rugged detector is required. A new type of shock-wave detector capable of working at pressures beyond 100,000 psi has been investigated recently. This detector, which appears to have considerable merit, consists of a semiconductor strain gage bonded to the outer wall of the low-pressure chamber of the shock tunnel. It responds to strain in the wall resulting from the hoop stress produced by the passing shock-wave. The signal obtained from a semiconductor strain gage used in this way is shown in Figure 11. The rise time appears to be about 10 microseconds in duration. Unlike the previously considered shock-wave detector, the semiconductor element does pick up disturbances in the metal wall ahead of the shock. However, the amplitude of these disturbances is still sufficiently low compared with the peak reached behind the shock-wave to permit good accuracy in timing.

The semiconductor shock-wave detector is simple to install and has the advantages of ruggedness and durability, since the element in no way comes in contact with the flow of air or the driver gas. Because this type of detector does not require an access hole in the wall of the low-pressure section, erosion at the inner wall is kept to a minimum. A typical semiconductor strain gage installation on the outer wall of the

low-pressure chamber of the 4-in. Shock Tunnel No. 3 is shown in Figure 12. In general, an epoxy cement is used as the bonding agent. Protection of the element and its leads is furnished by plastic electrician's tape which is wrapped around the outer wall.

HEAT-TRANSFER INSTRUMENTATION

The measurement of heat transfer over the surface of models undergoing testing in the NOL Hypersonic Shock Tunnels is made with thick film or calorimeter gages. These gages are similar in design to the one developed by the AVCO Research Laboratory as described in reference (3). Since a different gage material, thermal insulator, and gage-mounting technique are used by the Naval Ordnance Laboratory, these are to be described briefly at this time.

An artist's conception of a calorimeter heat-transfer gage mounted in the surface of a model appears in Figure 13. The groove shown in the drawing is milled into the surface of the aluminum model to a depth several thousandths of an inch greater than the thickness of the iron sensing element. After all machine work has been completed on the surface of the model, the model's surface is chemically converted to aluminum oxide by a special commercial process. The depth of the oxide layer is about two mils. It is sufficient to provide a much harder surface to the abrasive flow in the test section as well as some thermal and electrical insulation. However, the main thermal insulation is furnished by a layer of glyptol which is painted in the groove before the iron sensing element is added. By the passage of a heated roller over it, the element is forced into the softened glyptol until its outer surface becomes flush with that of the model. The calorimeter element is held in place by means of technical B cement which is placed in the four drilled holes designed to accept the voltage and current tabs and their wires. The cement, after hardening, is sanded flush with the model surface. Measurements on a completed model have shown the gage elements to be flush to within 0.2 mil of the model surface.

A close-up view of a typical calorimeter gage installation is shown in Figure 14. During a measurement a constant DC current of 2 amperes is maintained through the element. The electrical circuitry employed is conventional for a constant-current low-impedance device. A full discussion of the circuitry is given in reference (4), and no further details of it will be presented in this paper.

IGNITION SYSTEM USED WITH COMBUSTION DRIVERS

The NOL Hypersonic Shock Tunnels are generally powered by the combustion of oxygen-hydrogen-helium mixtures. The performance of these tunnels depends very strongly on how the explosive mixture is ignited, and on the percentage of gas burned before the main diaphragm opens. Diaphragms are designed to open when the combustion pressure has reached 95 percent of the maximum pressure obtainable under closed-bomb conditions. Ignition at all points in the gas simultaneously is one way of guaranteeing combustion without detonation. However, in most cases such a step is not feasible. Exploding wires have been used for ignition purposes with considerable success. When large amounts of wire are needed, such as in long driver chambers, the amount of electrical energy required to heat or explode the wire is quite appreciable. One method of reducing the energy is by crimping the wire at uniform intervals. Another method, which was first conceived at the Naval Ordnance Laboratory about 1.5 years ago and seems to have considerable merit, employs the exploding foil ignition tape. A sketch of a section of this tape appears in Figure 15. It consists of a strip of aluminum foil backed with Scotch cellophane tape for support. The holes as shown are punched through the tape near an edge leaving small amounts of foil between them and the nearest edge. When the larger amount of foil is removed from the opposite side of the hole, a high resistance current path is formed at each hole site. Along the length of the tape these ignition points are all in electrical series. While the amount of energy required to explode the foil at these points is not large, it has been found that smooth ignition results when an energy of approximately 10 joules per point is supplied

from a charged capacitor. In Figure 16 a view of the exploding foil ignition tape is shown with its support assembly. The long stainless-steel rod which fastens to the breech plug is used to support one end of the tape and supply a ground return for the system.

During burning of the explosive driver gas mixture, its pressure is measured at both the front and rear of the high-pressure chamber. Typical combustion pressure traces obtained with the foil ignition tape are shown in Figure 17. Since the main diaphragm opens before the gas mixture is completely burned, the rear pressure gage normally reads higher by several thousand psi.

MISCELLANEOUS MEASUREMENTS

The measurement of shock velocity in the 1.5-in. Shock Tunnel No. 1 over a distance of 160 calibers has revealed an attenuation of about 17 percent. Because of this large change in shock velocity, one cannot expect the pressure measured at some given point along the low-pressure chamber to remain unchanged with time. Since energy losses continually occur in the working gas prior to its expansion into the test section, the pressure increase with time at a point is much less than might be expected. An accurate knowledge of the static pressure-time history at the muzzle of the low-pressure chamber is essential for an accurate determination of the total enthalpy-time variation in the test section. By measuring pressure simultaneously at two different locations in the same vertical plane at some point along the low-pressure chamber, one can determine what amount of agreement in the pressure measurement is possible. Two pressure traces obtained under these conditions at the muzzle are shown in Figure 18. Quantitative measurements made along these traces show variation in the amount of disagreement between them, the maximum disagreement being about 7 percent. From run-to-run even the amount of variation has not been constant, and in some cases the amount of disagreement has been so low as to be indistinguishable. It should be emphasized at this point that the tests discussed here were performed with piston-type pressure gages having their flat piston faces

tangent to the bore of the low-pressure chamber. Contoured pressure gages which provide flush mounting with the bore have been fabricated recently and are presently undergoing testing in the 1.5-in. Shock Tunnel No. 1. Preliminary data indicate that the amount of disagreement between pressure gages located in the same vertical plane has been reduced by 50 percent as a result of the contouring and elimination of the cavities.

The velocity of each portion of the working gas leaving the muzzle can be computed if a Pitot pressure measurement at the muzzle is also made. The measurement of Pitot pressure in this region is complicated by the size of the probe which tends to produce flow blockage, as well as by the very high pressures encountered there. The blockage problem becomes greater as the flow Mach number decreases and the density increases. A muzzle Pitot pressure trace is shown in Figure 19. The measured pressure initially behind the shock-wave is about 20,700 psi and this agrees very closely with the predicted value of 20,000 psi. However, at much higher barrel loads, where the predicted Pitot pressure is 53,000 psi, measurements of 100,000 psi have been obtained. These are obviously in error since a calculation of reflected shock pressure reveals values 20 percent lower. Because flow blockage is appreciable under these conditions, a much slimmer Pitot probe has been designed, and is soon to be tested.

There are many causes for shock-wave attenuation in the working gas. One such cause which can easily be overlooked, especially when operating over a wide range of initial conditions, is the size or length of the high-pressure chamber. It is important that the dimensions of the chamber be such as to prevent under all operating conditions the reflected rarefaction wave from overtaking any of the shock-compressed working gas before it has left the muzzle. The effect produced by too short a high-pressure chamber is shown in Figure 20. Over a total distance of 160 calibers the measured shock attenuation is 26.5 percent for the 40-inch-long high-pressure chamber as compared to 17.3 percent for the 80-inch

chamber. It is evident from these curves that when the 40-inch chamber is used, much better flow characteristics are obtainable by shortening the low-pressure chamber at least 40 calibers.

Shock-wave attenuation has a marked effect on the Pitot pressure measurement made in the test section. This effect is very noticeable in Figure 21. With the 40-inch chamber, the Pitot pressure is substantially lower than that obtained with the longer chamber. In addition, the pressure appears to drop continually after the peak is reached. The pressure trace for the 80-inch chamber, on the other hand, exhibits a broad plateau approximately 250 microseconds following the peak. The magnitude of the pressure along the plateau is about 75 percent of that measured at the peak.

The pitot pressure traces which thus far have been displayed are all characteristic of free-jet expansion. The effect of a 28-degree conical nozzle on this characteristic trace is shown in Figure 22. A comparison between free-jet and cone nozzle expansion is made in this case under nearly identical conditions in the working gas prior to expansion and for the same flow Mach number of 8 in the test section. An examination of the traces reveals that flow establishment time for the nozzle is at least twice as long as for the free-jet. Since it takes about 400 microseconds to establish the flow in the conical nozzle and 600 microseconds are required for all the working gas to leave the muzzle, only 200 microseconds remain useful for aerodynamic testing. In this particular case twice as much testing time is available with free-jet expansion. The peak which appears early in the flow is characteristic of free-jet expansion, since it is not evident in the Pitot pressure measurement made in cone nozzle flow.

CONCLUSIONS

For very high Reynolds number flow in a shock tunnel, erosion at the inner wall of the low-pressure chamber becomes a serious problem. The erosion is especially serious around gage holes. The piston-

type pressure gage is extremely rugged and its calibration is unaffected by erosion. In addition, it can be designed such that a perfectly flush fit with the bore is obtainable, thereby minimizing erosion around the gage hole.

Ionization-sensitive probes used in measurements of shock velocity are not reliable below shock Mach number 4.5 or near the end of the low-pressure chamber in the vicinity of the second diaphragm. Pressure-sensitive probes have been used in place of ionization-sensitive probes with considerable success. Strain gages bonded to the outer wall of the low-pressure chamber have been used to detect shock transit times and have been shown to be extremely useful at very high working gas pressures.

ACKNOWLEDGEMENTS

The research reported in this paper was supported largely by the Special Projects Office, Department of the Navy.

The author wishes to express his appreciation to the following individuals in the Gas Dynamics Division of the Ballistics Department, for their assistance and helpful suggestions in the preparation of this paper: Messrs. V. C. Dawson, J. W. Watt, D. F. Gates, J. M. Marshall, and R. H. Waser.

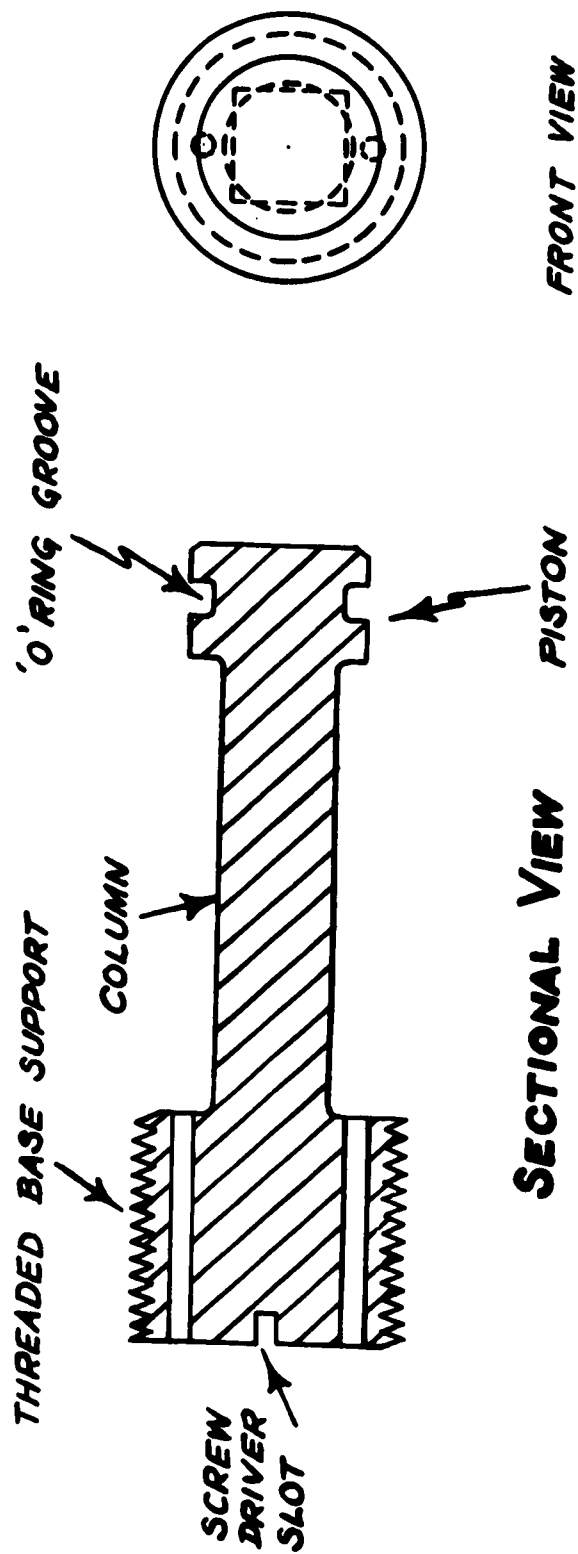
TYPICAL OPERATING CONDITIONS
N.O.L. HYPERSONIC SHOCK TUNNELS

Type of Operation	Non-reflected	Reflected
Re_{∞} /ft.	35.2×10^6	75×10^3
M_{∞}	8.0	11.3
h_{total}	1145 BTU/lb.	4832 BTU/lb.
M_s at muzzle	4.9	9.0
P_0	39×10^3 p.s.i.	39×10^3 p.s.i.
P_1	460 p.s.i.	20 p.s.i.
P_2	13×10^3 p.s.i.	2000 p.s.i.
P_3	-----	18.4×10^3 p.s.i.
P_{pitot} at muzzle	53×10^3 p.s.i.	-----
P_{pitot} test section	475 p.s.i.	4 p.s.i.
P_{∞}	5.2 p.s.i.	0.022 p.s.i.

FIG. 1



FIG. 2



PISTON TYPE PRESSURE GAGE

FIG. 3

EQUATIONS GOVERNING SENSITIVITY OF PISTON TYPE PRESSURE GAGE

$$\frac{PA_P}{A_c} = E\epsilon \quad (1)$$

$$(G.F.) = \left(\frac{\Delta R}{R}\right) \frac{1}{\epsilon} \quad (2)$$

$$\Delta R = PR \left\{ \left(\frac{A_P}{A_c}\right) \frac{(G.F.)}{E} \right\} \quad (3)$$

$$\Delta V = \frac{V}{2} \left(\frac{\Delta R}{R}\right) \quad (4)$$

$$\Delta V = \frac{V}{2} \left\{ \left(\frac{A_P}{A_c}\right) \frac{(G.F.)}{E} \right\} P \quad (5)$$

FIG. 4

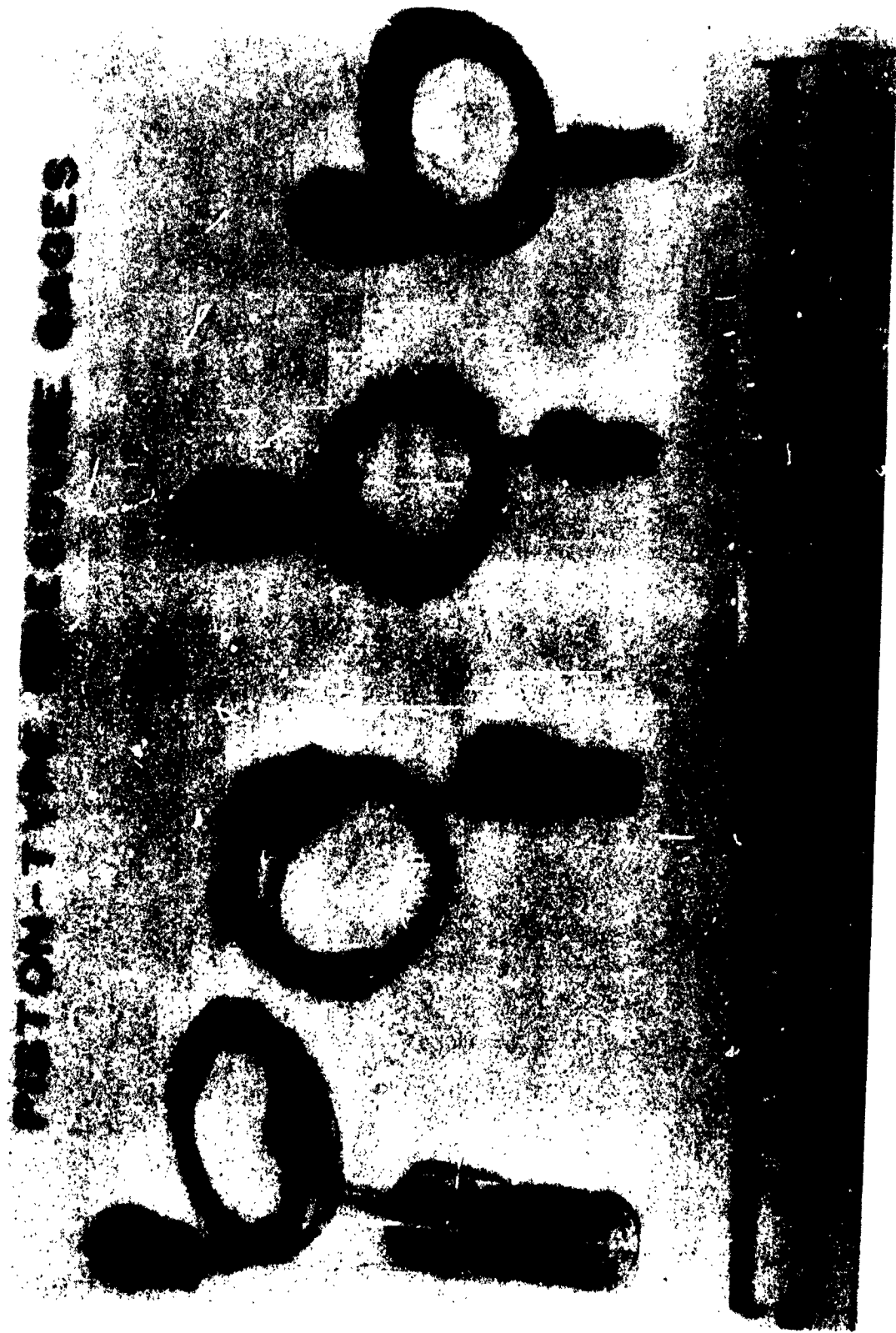


FIG. 5

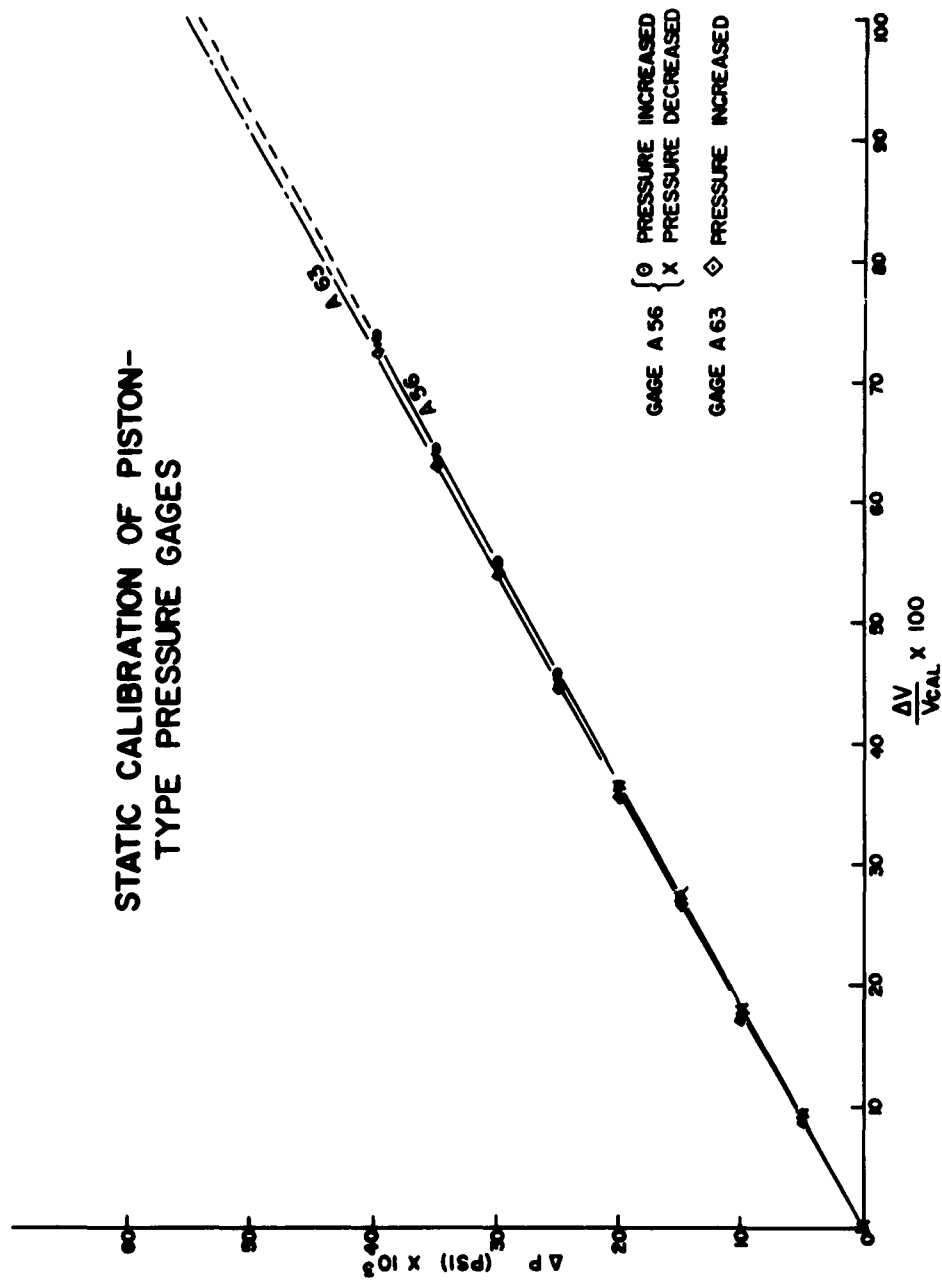


FIG. 6

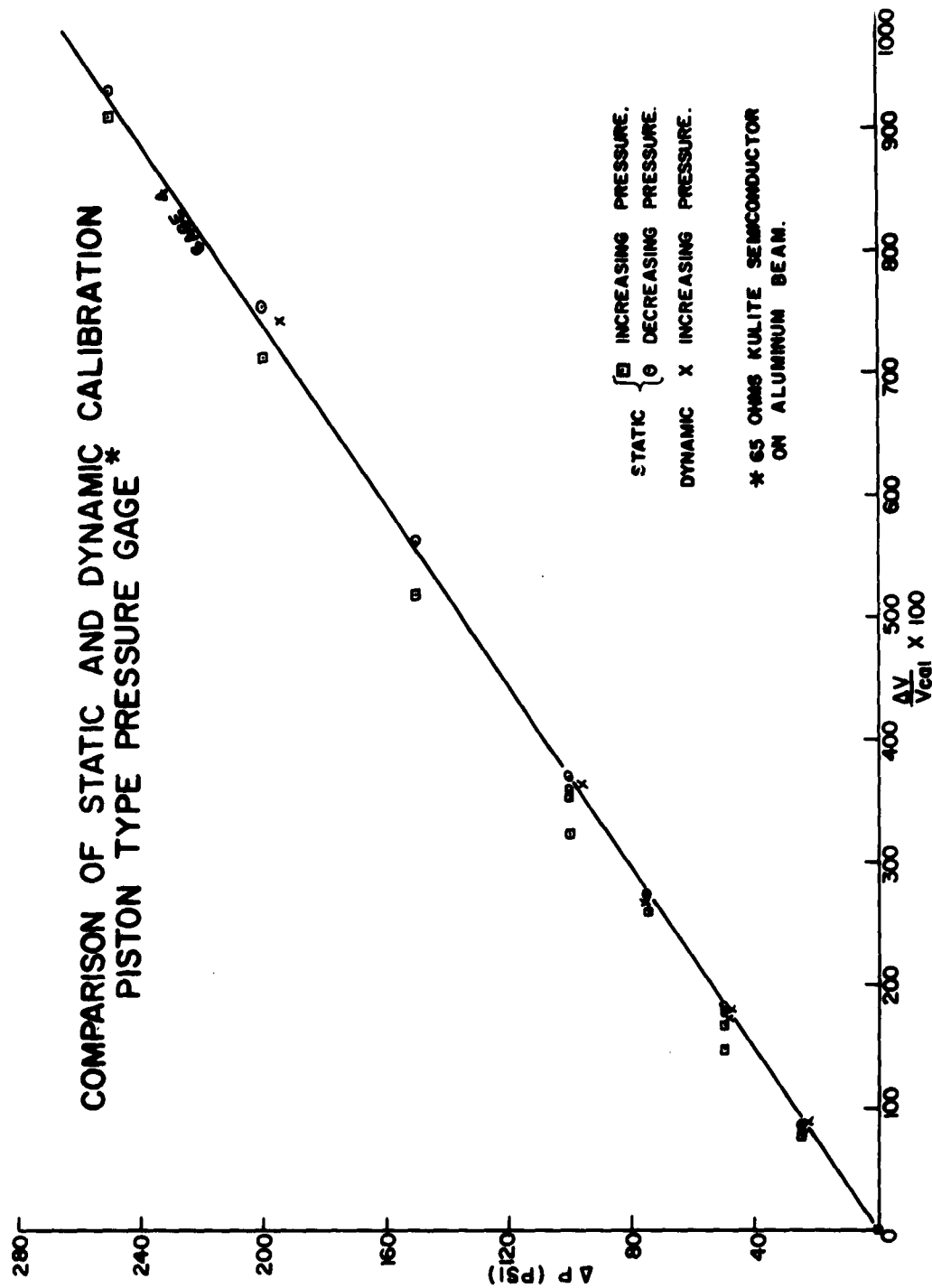


FIG. 7

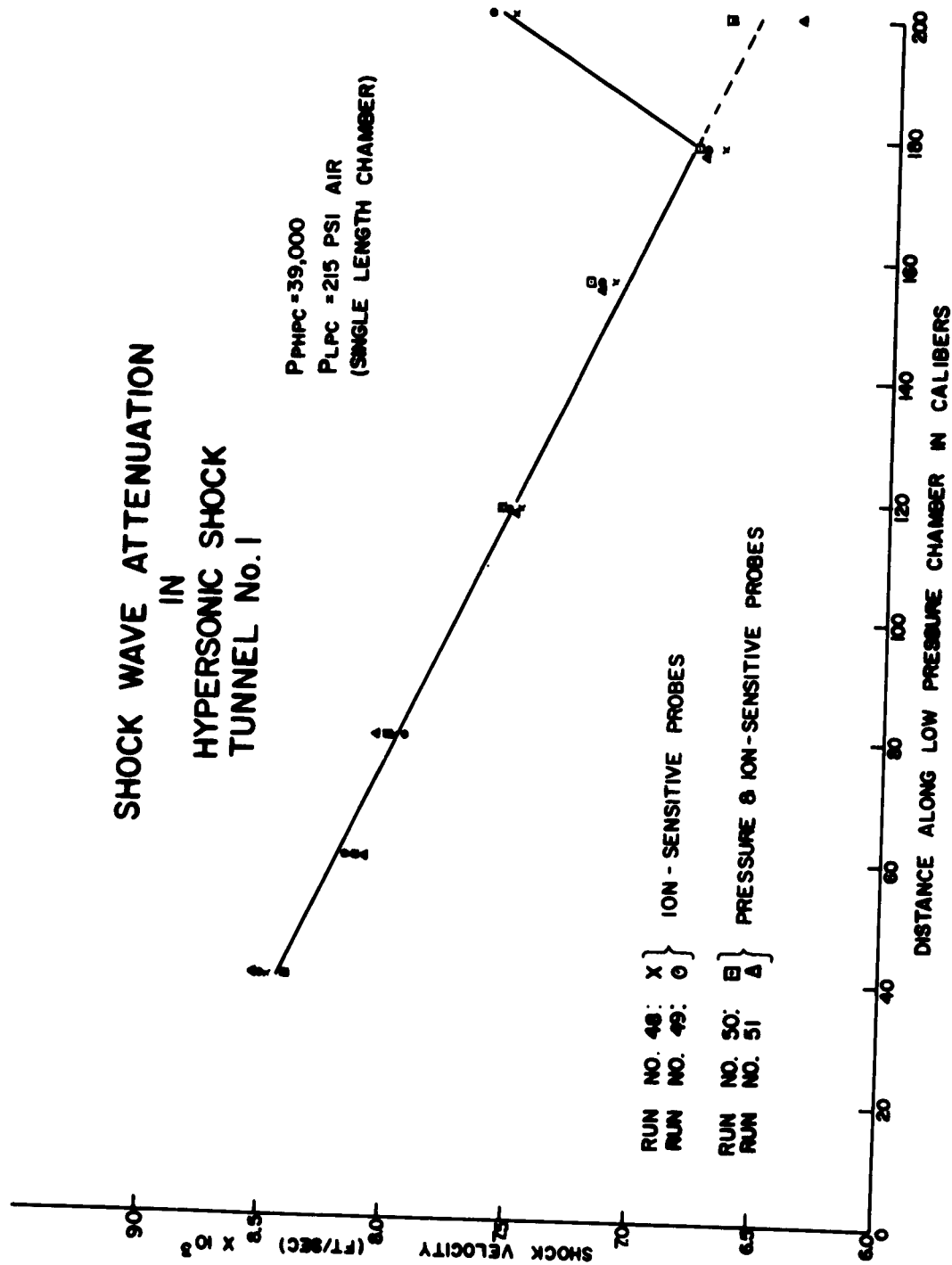


FIG. 8

SHOCK WAVE DETECTOR

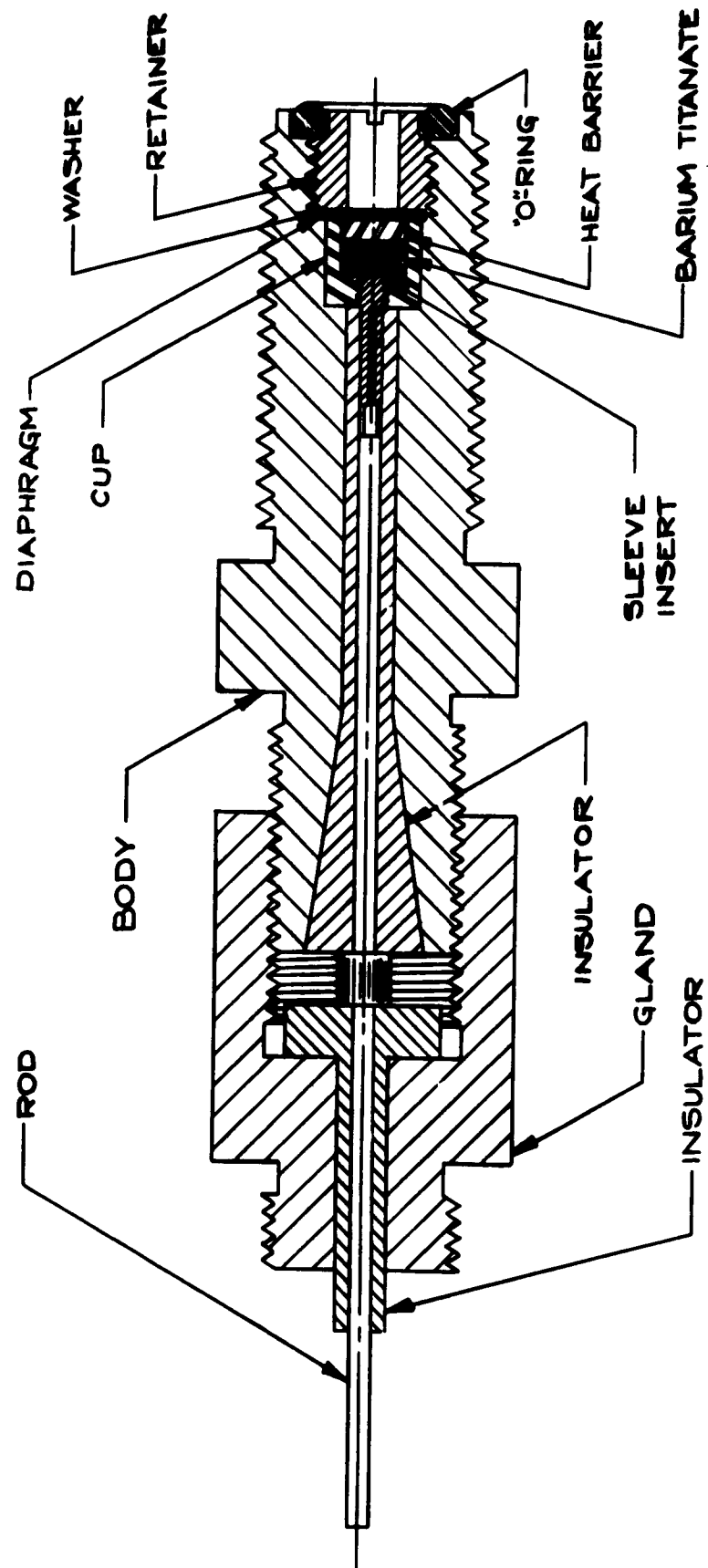


FIG. 9

Response of Shock Wave Detector
to a Shock Wave in the Driven
Gas of a Hypersonic Shock Tunnel

OUTPUT
(.25 volt/div)



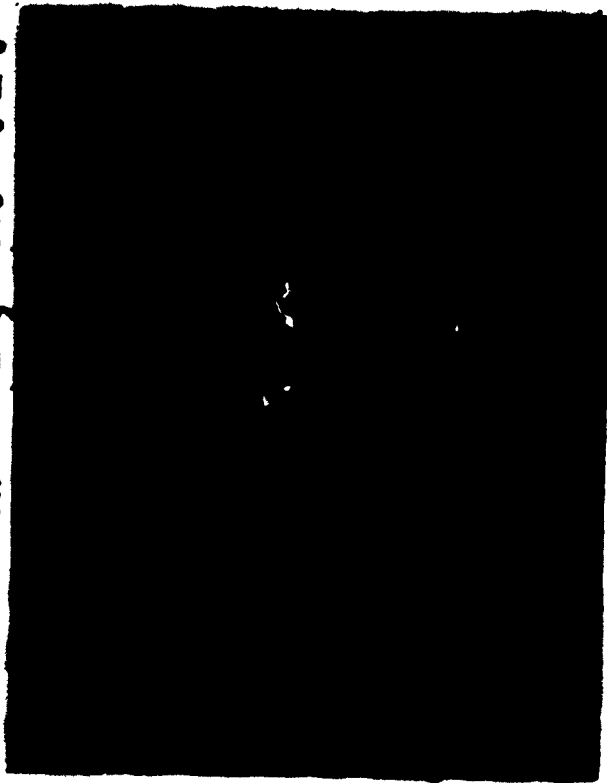
Time Base: 20 usec/div

FIG. 10

Response to Shock Disturbance
of Semiconductor Strain Gage
Mounted on Outer Wall of Low
Pressure Chamber, H.S.T. #2

(.05 volt/div)

GAGE OUTPUT



Time Base: 50 usec/div

FIG. II



CALORIMETER GAGE MOUNTING TECHNIQUE

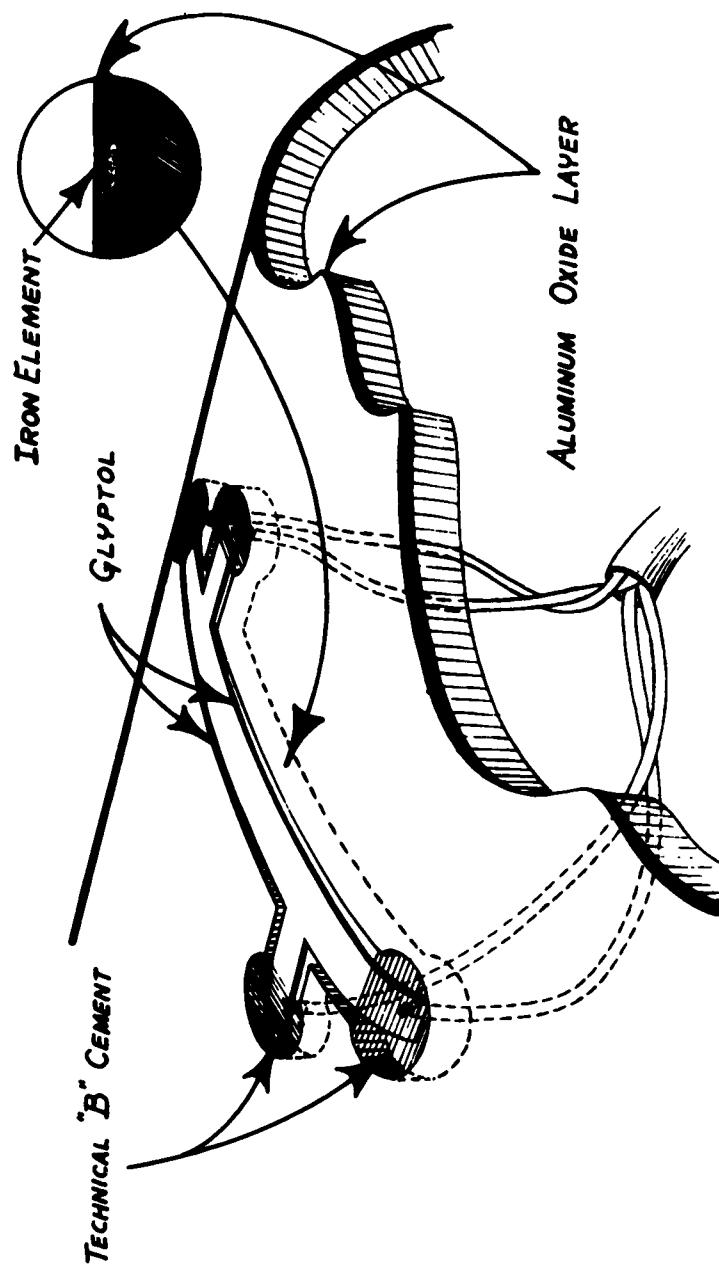


FIG. 13

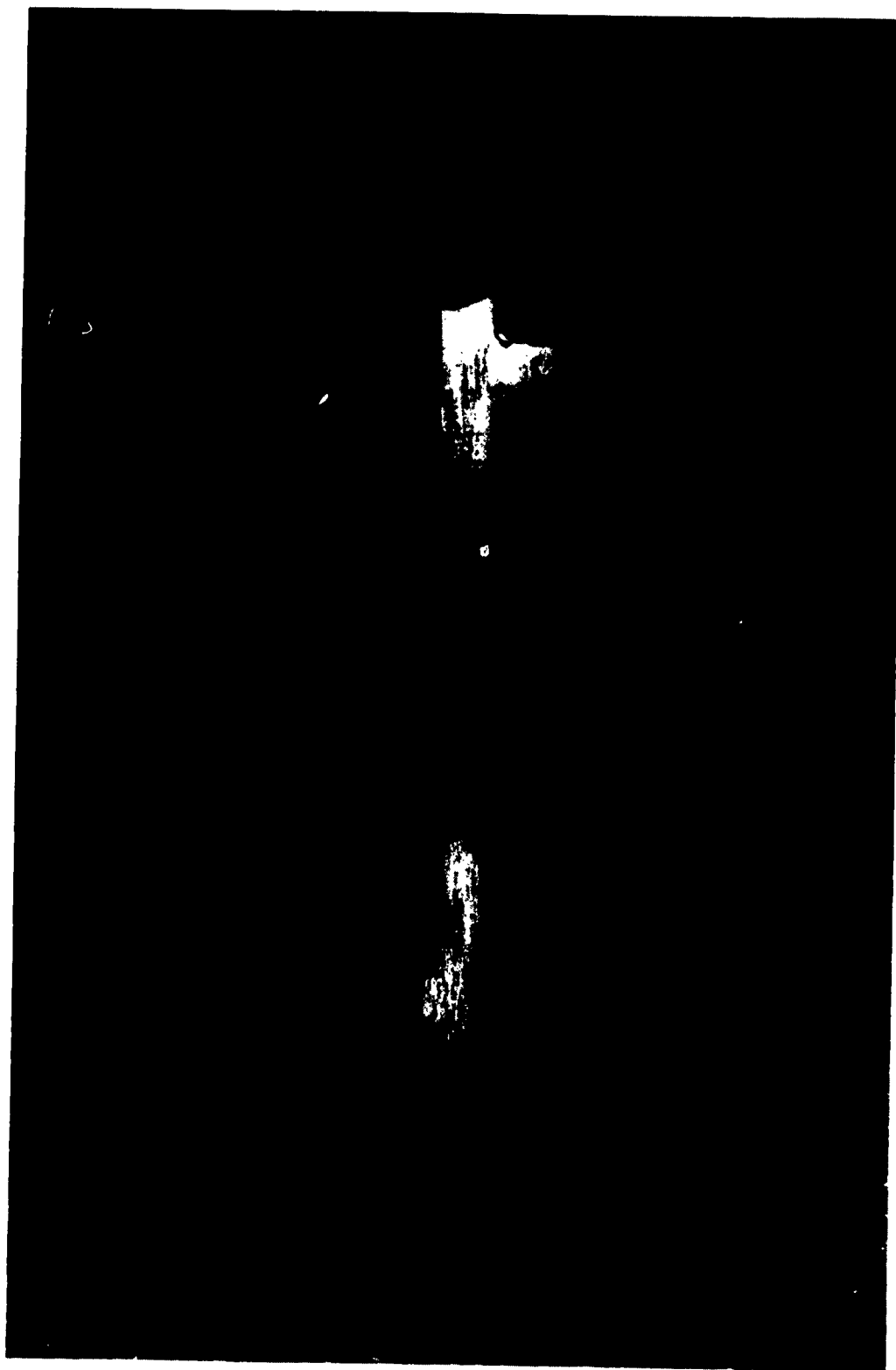
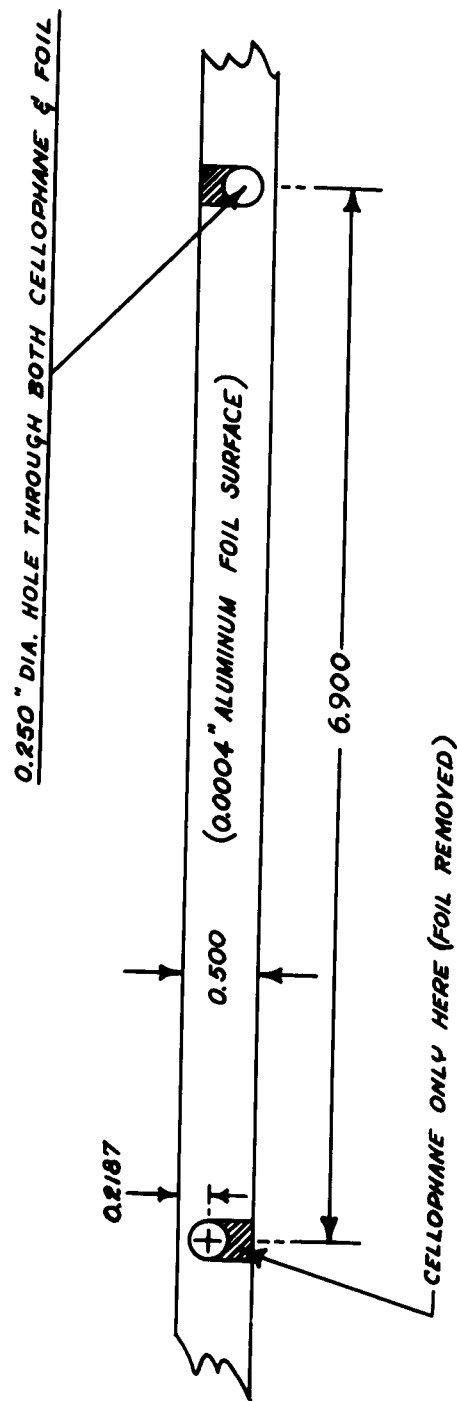


FIG. 14



EXPLODING FOIL IGNITION TAPE

FIG. 15

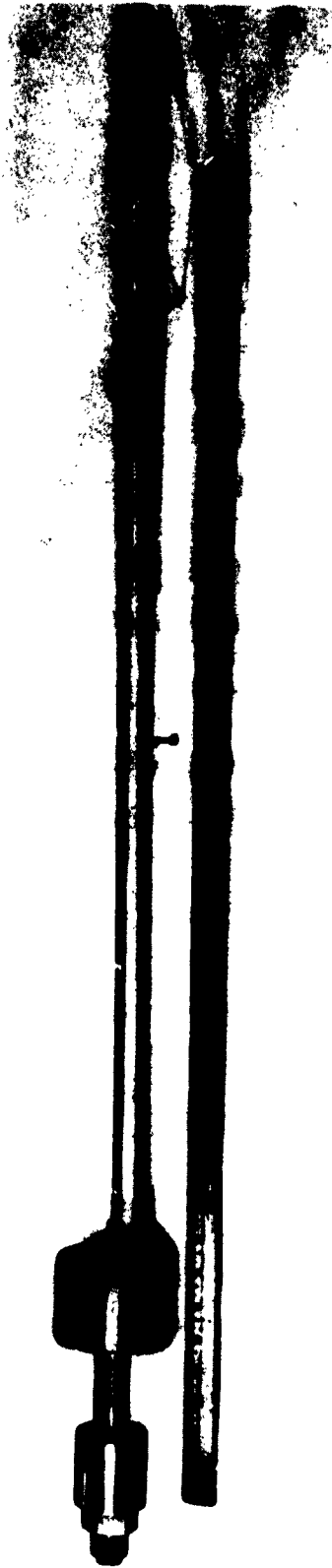


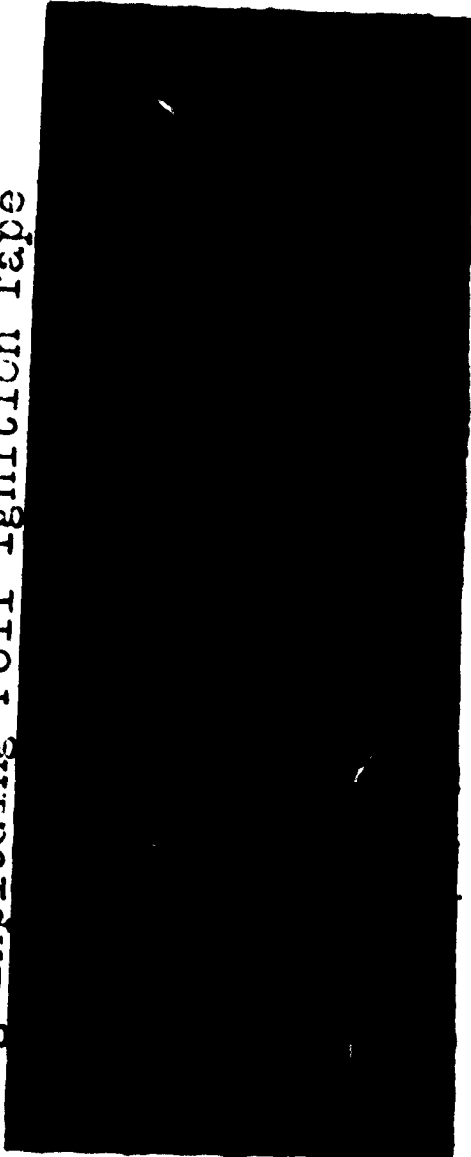
FIG. 16

240

Characteristic Combustion Pressure Traces
 Obtained in 40 inch Driver Chamber of S.F.#2
 Using Exploding Foil Ignition Tape

Pressure
 (6500 psi/div)

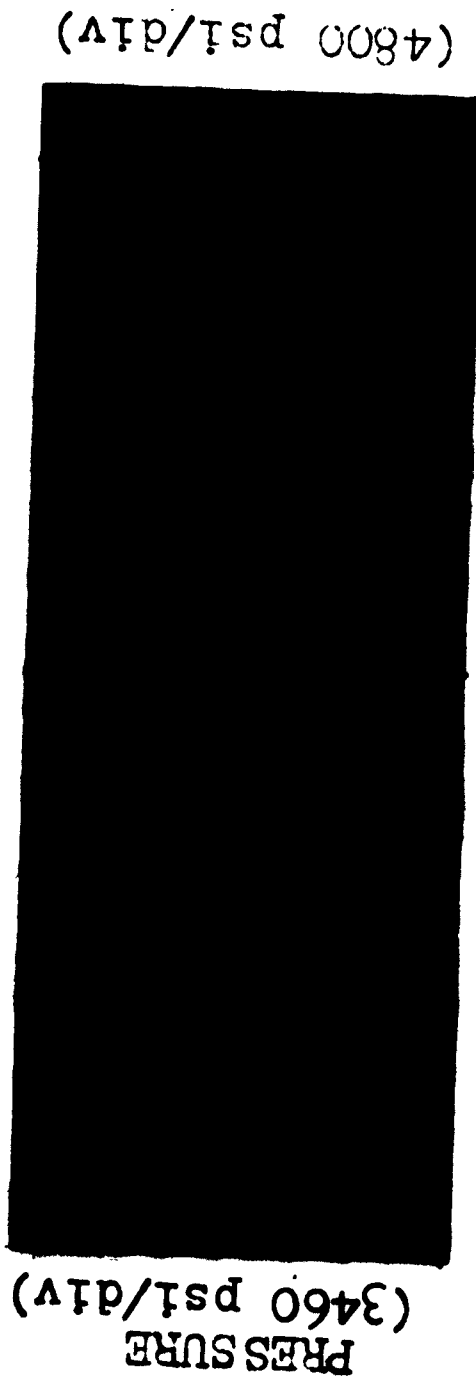
(7160 psi/div)



Front Gage: A-1 Rear Gage: A-52
 Time Base: 5 millsec/div

FIG. 17

Static Pressure Measured at Two Locations
in Same Vertical Plane in Muzzle of Shock
Tunnel No. 1 During Same Run



Static Pressure Measured at Two Locations
in Same Vertical Plane in Muzzle of Shock
Tunnel No. 1 During Same Run

Static Pressure Measured at Two Locations
in Same Vertical Plane in Muzzle of Shock
Tunnel No. 1 During Same Run

Static Pressure Measured at Two Locations
in Same Vertical Plane in Muzzle of Shock
Tunnel No. 1 During Same Run

Static Pressure Measured at Two Locations
in Same Vertical Plane in Muzzle of Shock
Tunnel No. 1 During Same Run

Pitot Pressure at Muzzle
End of Driven Section
1.5 Inch Shock Tunnel #1

Pressure
(9200 psi/div)



Time Base: 100 usec/div

FIG. 19

SHOCK WAVE ATTENUATION IN HYPERSONIC SHOCK TUNNEL No. 1

PHPC = 39000 PSI
PLPC = 460 PSI AIR

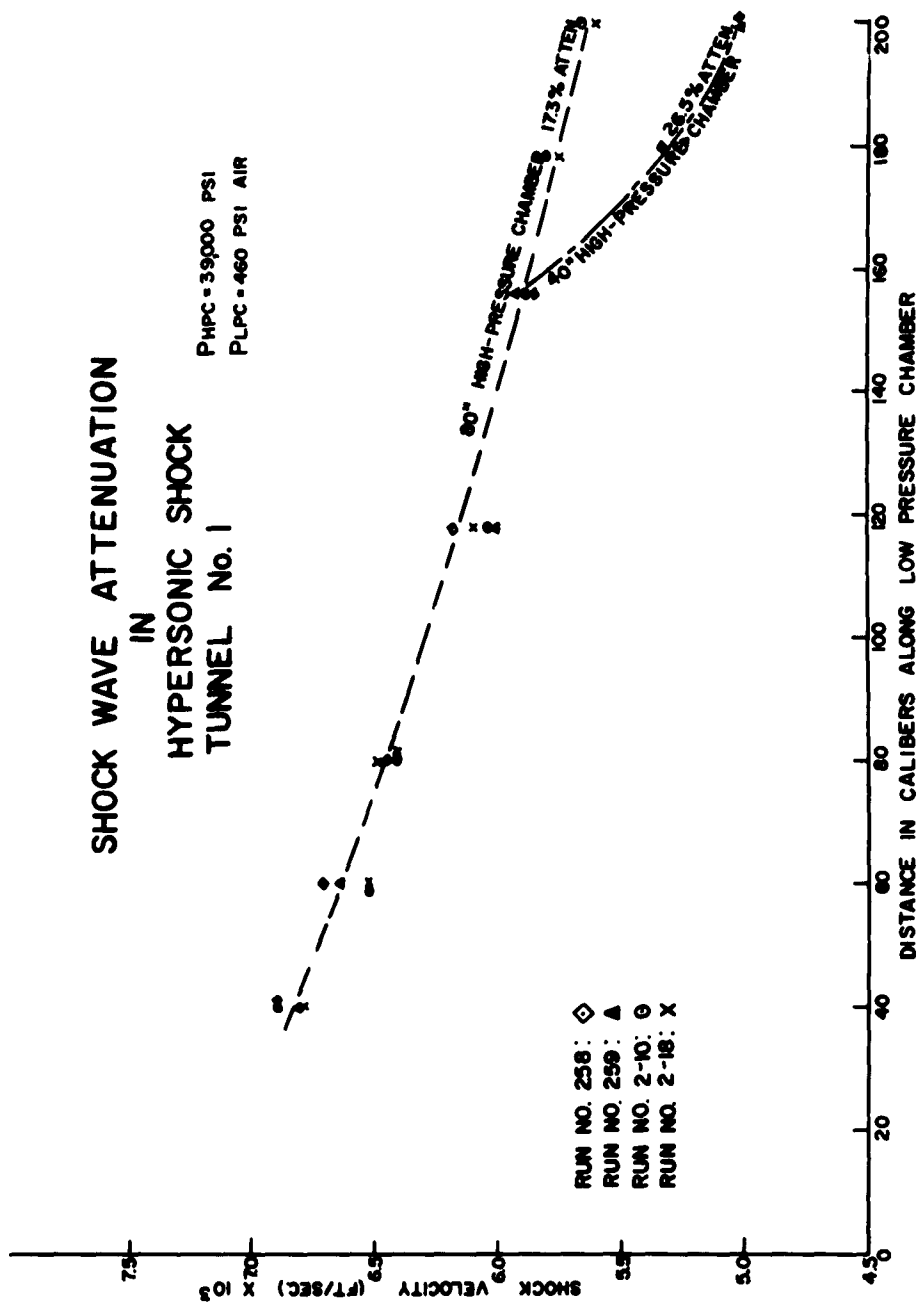


FIG. 20

Effect of Single & Double-Length Driver Sections on Test Section Pitot Pressure

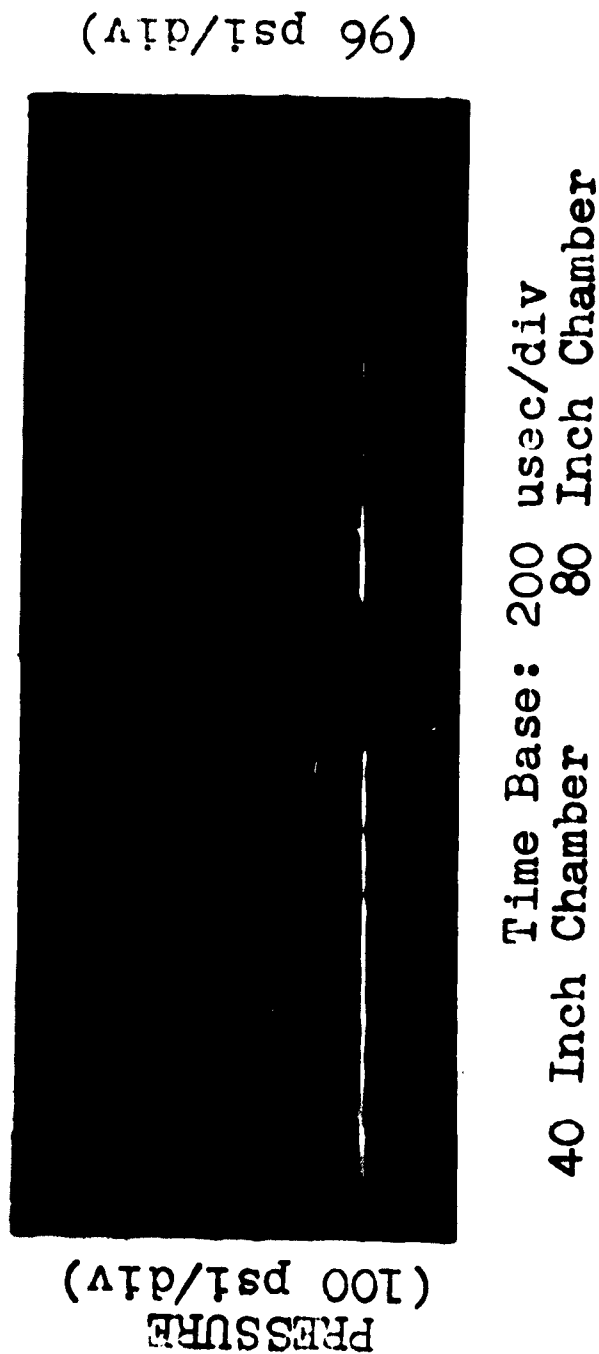


FIG. 21

Characteristic Test-Section Pitot Pressure
Traces for Free-Jet & Cone Nozzle Runs

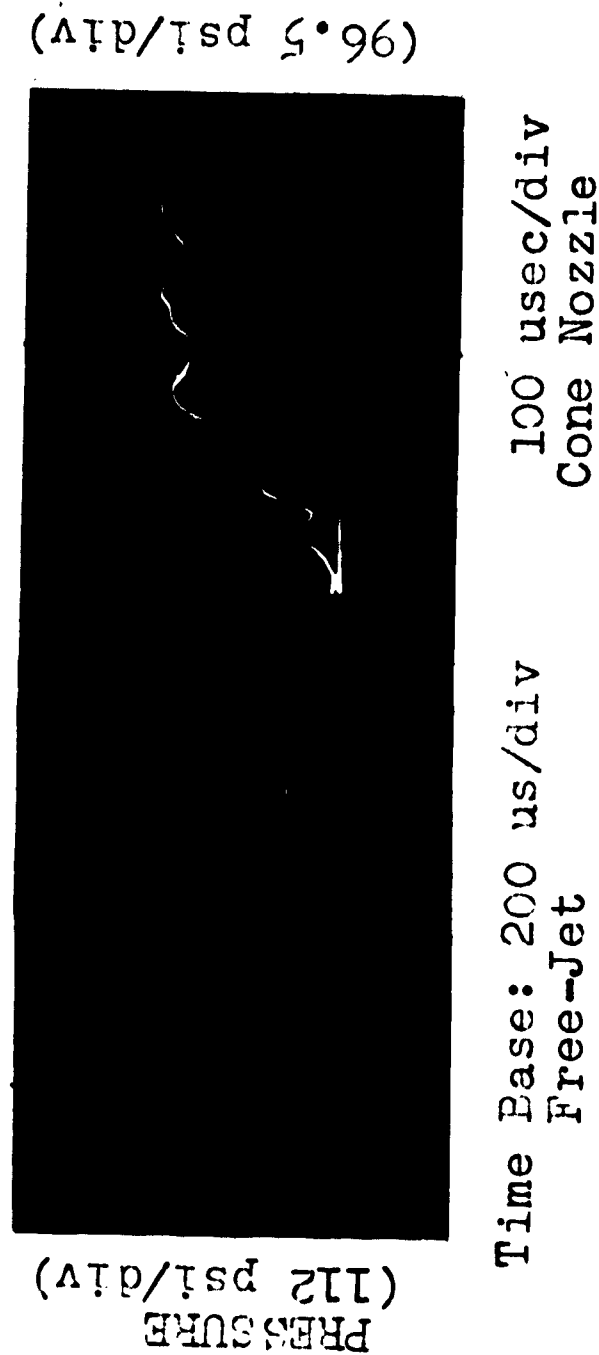


FIG. 22

REFERENCES

1. Aronson, P. M., Marshall, T., Seigel, A. E., Slawsky, Z. I., and Smiley, E. F. Shock Tube Wind Tunnel Research at the U. S. Naval Ordnance Laboratory, Proceedings of the Second Shock Tube Symposium, SWR-TM-58-3, Air Research and Development Command, Kirtland Air Force Base, New Mexico, March 1958.
2. Dawson, V. C. D. "Piston Type Strain Gages", NavOrd Report 6251, January 1959.
3. Rose, Peter H. "Development of the Calorimeter Heat Transfer Gage for Use in Shock Tubes", AVCO Research Laboratory Research Report No. 17, February 1958.
4. Gates, D. F. and Watt, J. W. "Stagnation Point Heat Transfer to a Sphere in the NOL 6-In. Shocktube", NavOrd Report 6788, January 1960.
5. Dawson, V. C. D. "Pressure Gage Design for the Measurement of Pressures in Shocktube Wind Tunnels, Shocktubes, and Guns", NavWeps Report 7326 (in publication).

THE PSEUDO-STATIONARY BEHAVIOR OF VORTICES

(EXPERIMENTS IN SHOCK WAVE TUBES)

H. Reichenbach
Ernst Mach Institut, Germany

The following relationships can be asserted for those flux processes in which friction, heat conduction and capillary forces can be disregarded.

To a process which satisfies the given conditions, there is always a geometrically similar one arising from it owing to the multiplication of all the lengths and times by a random constant factor (positive, real). In so doing the velocities, with respect to direction and magnitude, as well as the thermodynamic entropies at the corresponding spatial-temporal points are unaltered. Even when shock waves are encountered these assertions retain strict validity .

Non-stationary flux processes which remain invariant during application of the so-called similarity-transformation--specifically of a space-time-extension--are designated as pseudo-stationary. It can easily be shown that this type of flow depends only on variables of the form $\xi = \frac{z}{t}$; $\eta = \frac{y}{t}$ $\xi = \frac{z}{t}$ and no longer depends explicitly on the time t . From this you may deduce the following. An observer, proceeding in a straight line from the point on earth $x=y=z=t=0$ and moving with a constant velocity, will encounter locally stationary conditions. On the basis of this assertion, designating this particular class of non-stationary flows (the class being distinguished by a constancy factor in contrast to a similarity-transformation) as pseudo-stationary is justified.

As soon as the forces of friction noticeably influence the flux processes, this property of constancy is lost. The viscosity, in other words the property of the medium governing the friction, is not maintained during the similarity-transformation of a space-time-extension. Furthermore the viscosity which is defined familiarly as the ratio factor between

the tangential tension and velocity gradient, should be converted by the same factor as the time and space coordinates, as is easily deduced from methods of dimension similitude considerations. But this requirement cannot normally be realized. On the basis of this it can be expected that flow processes in which friction plays a role, will not easily behave pseudo-stationarily. In particular one may expect deviations during turbulence which will be taken into account in the following.

An examination of the behavior of spiral vortices can be achieved in various ways. Here, only the experimented side of the problem is given into, and a few experiments are described which we recently conducted. The question concerning the pseudo-stationariness of a plane process can be most simply decided by the following two methods:

- 1) Enlarging and/or reducing a high speed photograph and comparing it with an original photograph of the corresponding time phase.
- 2) Determining the path-time curves of characteristic flux properties.

Concerning the first method it can be said: since a plane pseudo-stationary process is determined alone by the variable of the form $\frac{x}{t}$, $\frac{y}{t}$ all the later, respectively, earlier phases can be obtained by optical enlarging respectively, reducing of a high speed photograph. A comparison with original photographs at the time which results on the basis of the enlargement scale, determines the pseudo-stationariness.

If, as indicated in the second method, the path-time diagrams of a flux process are photographed with the aid of a radio-motion picture series, then these curves-when behaving in a pseudo-stationary fashion-have to be straight lines which pass through the origin of the coordinates. The process of course depends only on $\frac{x}{t}$ if the simplicity is limited to a halfway one dimensional process. All the conditions must therefore remain unaltered on curves of the form $\frac{x}{t} = u = \text{const}$ or $x = ut$. However, that is exactly the analytical representation of a straight line.

A shock wave tube is very well suited for such examinations of a non-steady process.

The following described experiments were conducted with air on both sides of the membrane of such a tube with a constant diameter. In order to make the process visible, the so-called focused shadow principle was employed where the experiment chamber is irradiated with parallel light (Figure 1). In order to achieve the course of the rays for the various light sources of the spark aggregates (we use a 6-fold layout), which follows, as much as possible, a vertical course at the optical axis of the shock wave tube, the point sparks are mirrored in by movable mirrors, standing spatially very close to one another, and are mirrored out again on the camera side. The diameter of the point-sparks is 0.5 mm. The camera lenses are installed so that not the middle of the experiment chamber, but rather the so-called reference plane D' is sharply defined on the photographic plates. The sensitivity of the procedure, to indicate alternations of light deflection in the measuring chamber, depends in this case on the interval DD'.

The circumflow of an edge after encountering a shock wave was chosen as a simple example for a non-steady process in the shock wave tube. The following series of shadow photos (Figure 2) should give an overall view of the time-wise course of this process. Against the vertical wall, whose upper edge is scarfed with an angle of 25° , flows a shock wave with a pressure relationship of 2.12, which corresponds to a shock Mach number of $M_s = 1.4$ and to a flux Mach number of $M = 0.51$. The shock waves are reflected on the wall, whereby an increase in pressure to a pressure relationship of 4.16 occurs. An attenuation wave proceeds from the edge, lowering the shock pressure. The primary shock wave bends around the cutting edge at which a spiral vortex forms. The turbulence is then disturbed if the wave fronts reflected on the walls intersect the vortex.

If a multiple spark camera is used for the study, the path-time measurements can be measured very exactly. As an example for an arbitrarily selected trial (Figure 3) reproduces the path-time curve of the primary shock wave and of the shock wave reflected on the model. All curves are exact straight lines which cross through the zero point. The

conditions for the pseudo-stationary behavior of the shock wave fronts are thus satisfied. This knowledge is not new, for it is known that heat conduction and friction do not play any role in the range of normal shock waves; the conditions for the initially formulated procedure are satisfied.

It behaves differently if one examines the propagation of the vortex region and chooses the coincidence of the wave front on the leading edge of the cut as the time point zero (Figure 4). The path-time curves for the directions are given as parallel and vertical to the afflux. The designations result from the sketch. All the curves no longer follow a straight line course but bend in at the origin of the coordinates. However, for times, $t > 30 \mu\text{sec}$, these curves can be considered as straight lines, but the point of intersection of these straight lines lies to the left of the origin of the coordinates. From this results the fact that the entire process of the circumflow of a cut with the inclusion of the vortex region is not strictly pseudo-stationary. However, after a determined period of time and after assuming a fictive origin, one can speak of pseudo-stationary behavior for a vortex region.

The kinematic viscosity of the medium will be the decisive factor for the transitional region in the first stage of the turbulence. For this reason the way in which the Reynolds number influences the process was examined. As is known, the shock wave propagation is dependent only on the pressure ratio at the wave front. The shock Mach number, the flow Mach number and the temperature do not change if the pressure and, with it, the density in the expansion channel during preservation of a constant across of the pressure ratio are altered. During the experiments an egress pressure ratio of $\frac{P_4}{P_1} = 5$ was set up, whereupon the pressure in the compression chamber changed between 1 and 25 atu (atmospheres absolute (excess) pressure) and that in the expansion chamber of the shock wave tube was correspondingly changed between 0.2 and 5.

Since a change of the absolute density corresponds to the pressure change in the expansion channel, the Reynolds number also changes by whose definition a difficulty results, due to the size of the characteristic dimensions of the model. One can relate the Reynolds number to the interval or - as we do - take only the relative change of the Reynolds number into consideration.

On the basis of the experiment conditions (identical model, identical shock strength, identical shock and flow Mach numbers, identical gas) the determining quantities ($R_e = \frac{\rho \cdot \mu \cdot l}{\eta}$ ρ = density μ = velocity of flow; l = characteristic lengths η = viscosity) for the Reynolds number remain unchanged up to the density, respectively, the kinematic viscosity $\nu = \frac{\eta}{\rho}$.

Since we are interested only in the relative change of the Reynolds number, one can refer to a certain density and find then that the relative change of the Reynolds number is proportional to the relative change of the density.

$$R_{e \text{ rel}} = \frac{R_e}{R_{e1}} = \frac{\rho \mu l}{\eta} \cdot \frac{\eta_1}{\rho_1 \mu_1 l_1} = \frac{\rho}{\rho_1} \text{ because } \mu = \mu_1; l = l_1; \eta = \eta_1$$

Should one desire to compare the shadow photographs of two series of pictures having varying egress density with one another; the following must be taken into consideration on the basis of the individuality of the plate processing. The deflection of a light ray depends on the index of refraction and, relative to the Gladstone - Dale - relationship ($n - 1 = k \cdot \rho$), on the density. Because of this effect one is forced to alter the sensitivity of the plate processing in the individual series of pictures by varying the interval of the reference plane. In so doing the very simple relationship is retained that the intervals of the reference planes (r, r_1) behave inversely to the absolute densities in the expansion chamber.

$$\frac{r}{r_1} = \frac{\rho_1}{\rho}$$

If this optical ratio is considered, the following dependences of the extents of propagation are found. As was expected (Figure 5), the period of time which elapses until the propagation velocity of the vortex

reaches a constant value, vertical as well as parallel to the direction of discharge, is dependent on the relative Reynolds number. As can be deduced from the mean measured values, proportionality with the root consists of the relative Reynolds number (respectively, of the density). In our case the times lie between 18 and 30 μ sec. A constant velocity with appears to be practically independent of the Reynolds number, comes about only after this time is up.

Theoretically, we could next expect that the period of time generally increases with the Reynolds number. The formation of the vortex is a function of the kinematic viscosity of the system. The greater the viscosity, the more rapidly the vortex forms. Frictionless flow is described by the border line $Re \rightarrow \infty$. The acceleration time in this is infinitely large, i.e. formation of a vortex is no longer a consideration.

The vortex comes about by the stripping off and rolling up the boundary layer by the cutting edge. The thickness δ of a boundary layer is generally set up to be inversely proportional to the root of the Reynolds number.

Thus:
$$\delta \sim \sqrt{\frac{1}{Re}}$$

The proportionality factor results from the type of model over which the flow passes and has dimensions. Therefore the assertion concerning the independence of the acceleration time of a vortex can be thus interpreted: the acceleration times are inversely proportional to the boundary layer thickness. This assertion is very plausible.

Let us again consider the complete process of the turbulence. The separation and coiling up of a vortex at a cutting edge is a process in which friction plays an important role. Thus, this process cannot be pseudo-stationary. This process is indicated in the shown curves by the non-linear climb. When the vortex reaches a certain volume, it separates from the cutting edge and can be considered more and more as a closed system in which friction and viscosity are negligible. Thus, the conditions

for pseudo-stationary behavior are given. If, however, one assumes that the vortex should have reached a critical volume up to the beginning of the pseudo-stationary state, then the running time is determined with what speed the separating boundary layer subsequently delivers material to fill up this volume. Since the velocity was constant in the experiments, it can be expected that the slip stream speed of the boundary layer is also constant. In this case, however, the subsequently delivered volume depends only on the thickness of the boundary layer. Thus, the assertion that the running time for the vortex is inversely proportional to the thickness of the boundary layer has found an explanation.

Originally there was still another method for proving pseudo-stationary behavior which proceeded from the fact that the photos of the flow process which were taken at various times, should be geometrically similar to one another. Through optical enlarging or reducing it would then be possible to obtain pictures equal in coverage. A few experiments were even conducted in this direction. Both the following illustrations (Figure 6 and 7) show the results. Four photographs corresponding to various time phases were selected from a photo series of the same process and copied in the same scale. If the optical enlargement scale is chosen reciprocal to the photographing times and if the same geometrical dimensions are present, the process behaves pseudo-stationarily. It can be seen from Figure 7 that this behavior holds true by and large after a certain running time during the propagation of the vortex. The external geometric form agrees well; in the details there are, to be sure, a few deviations.

It is self-explanatory that the latter two illustrations were worked out with varying sensitivity of the shadow process. During the pseudo-stationary propagation, the density gradient in the vortex region decreases and along with it, the light deflection. This effect has to be compensated for by a corresponding change in the sensitivity of the plate processing.

In addition the adherence to strict geometrical similarity during the photographic process makes necessary the use of experimental chambers of varying depth. Since this is prohibitive for experimental reasons (multiple exposures), a corresponding correction of the sensitivity of

the shadow process has to be applied. It can easily be shown that the reference planes in nearest proximity have to behave as the squares of the interval of the shock front from the cutting edge in order to obtain pictures with a mutually corresponding optical sensitivity.

In summary, it is established that: the overall process of the circumflow of a cutting edge upon encountering a shock wave with the inclusion of the vortex region does not in a strict sense flow pseudo-stationarily. The shock fronts and attenuation waves do fulfill the conditions of a pseudo-stationary state within the considered range. The vortex region by itself behaves almost pseudo-stationarily if a transitional region is dispensed with and if an imaginary origin is referred to. The transitional stage lasts in our case from 18 to 30 μsec , calculated from the arrival of the shock wave at the cutting edge. This time period depends on the Reynolds number; so the process can be interpreted thusly, that the starting time behaves inversely proportional to the thickness of the boundary layer.

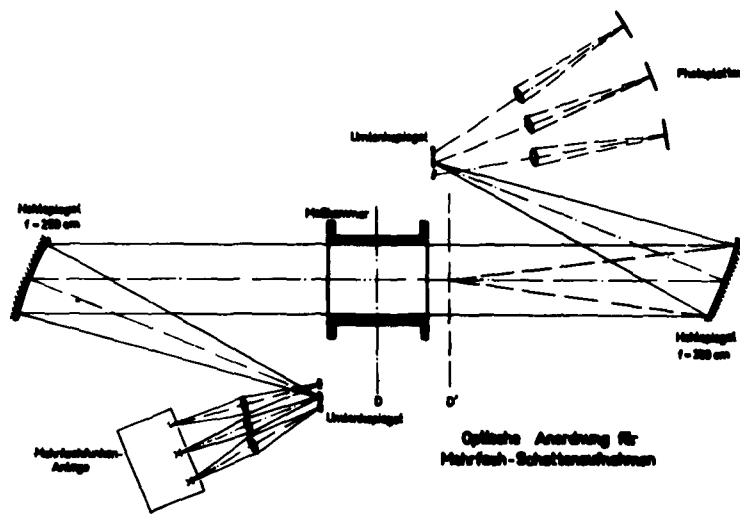


Abb.1
Optische Anordnung für Mehrfach-Schattenaufnahmen
nach dem fokussierten Schattenverfahren

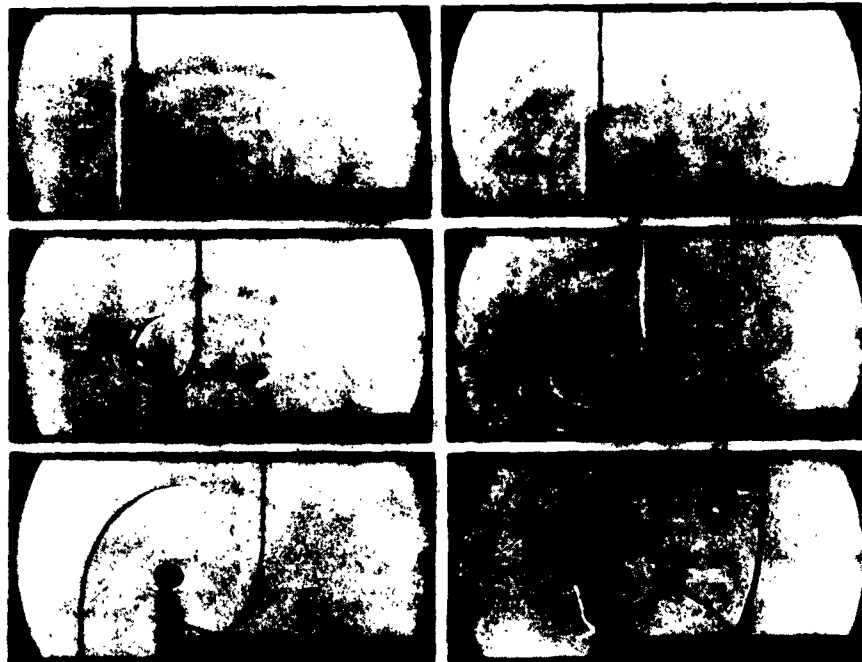


Abb.2
Beaufschlagung und Umströmen einer Schneide. Mehrfach-
funkenaufnahmen nach dem Schattenverfahren

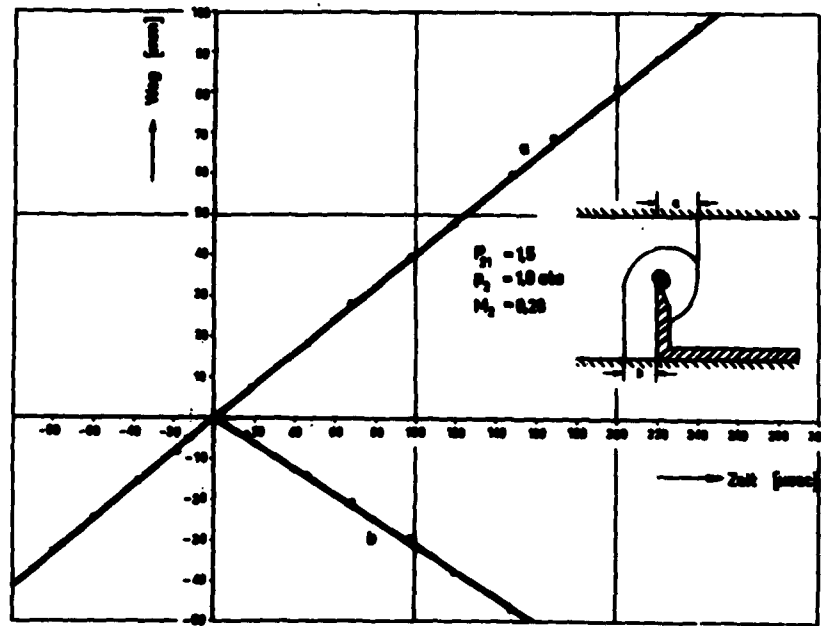


Abb. 3

Weg-Zeit-Kurven der primären bzw. reflektierten Stoßwelle

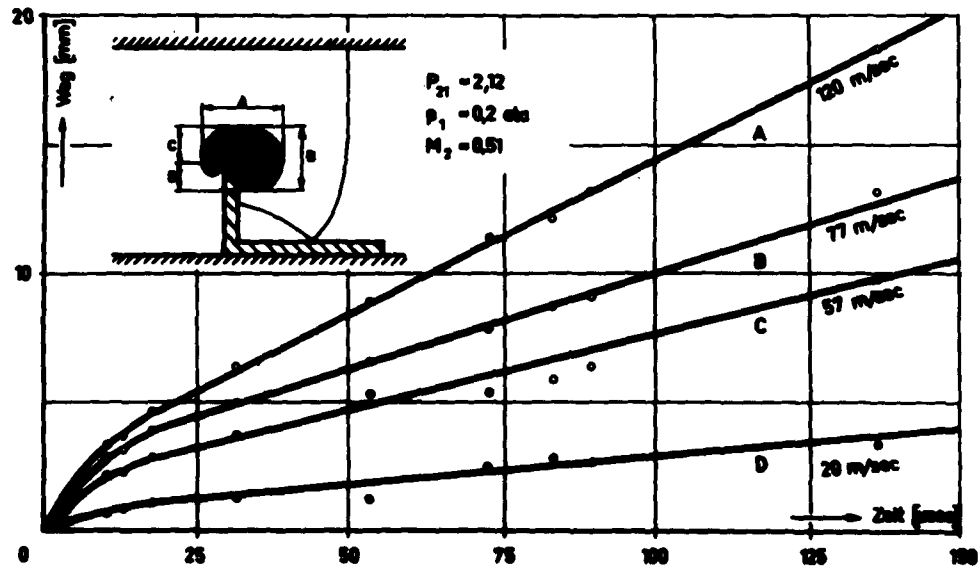
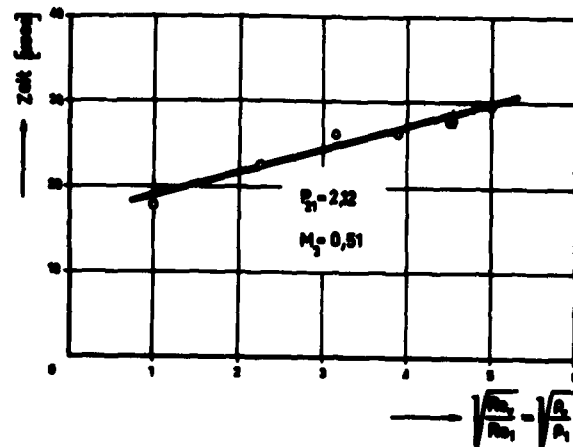


Abb. 4

Weg-Zeit-Kurven für die Wirbelausbildung

Mittlere Anlaufzeit bis zur Ausbildung einer konstanten Geschwindigkeit der Wirbelausbreitung in Abhängigkeit von der Reynold's-Zahl.



Geschwindigkeit der Wirbelausbreitung für $t > 50 \mu\text{sec}$ in Abhängigkeit von der Reynold's-Zahl parallel und senkrecht zur Anströmrichtung

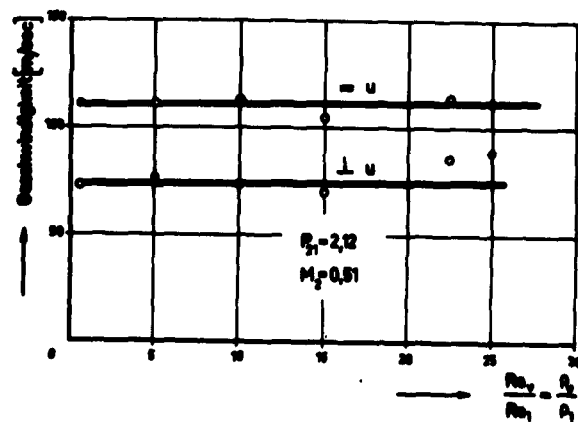


Abb. 5

Mittlere Anlaufzeit bis zur Ausbildung einer konstanten Geschwindigkeit und konstante Geschwindigkeit der Wirbelausbreitung in Abhängigkeit von der Reynold's-Zahl

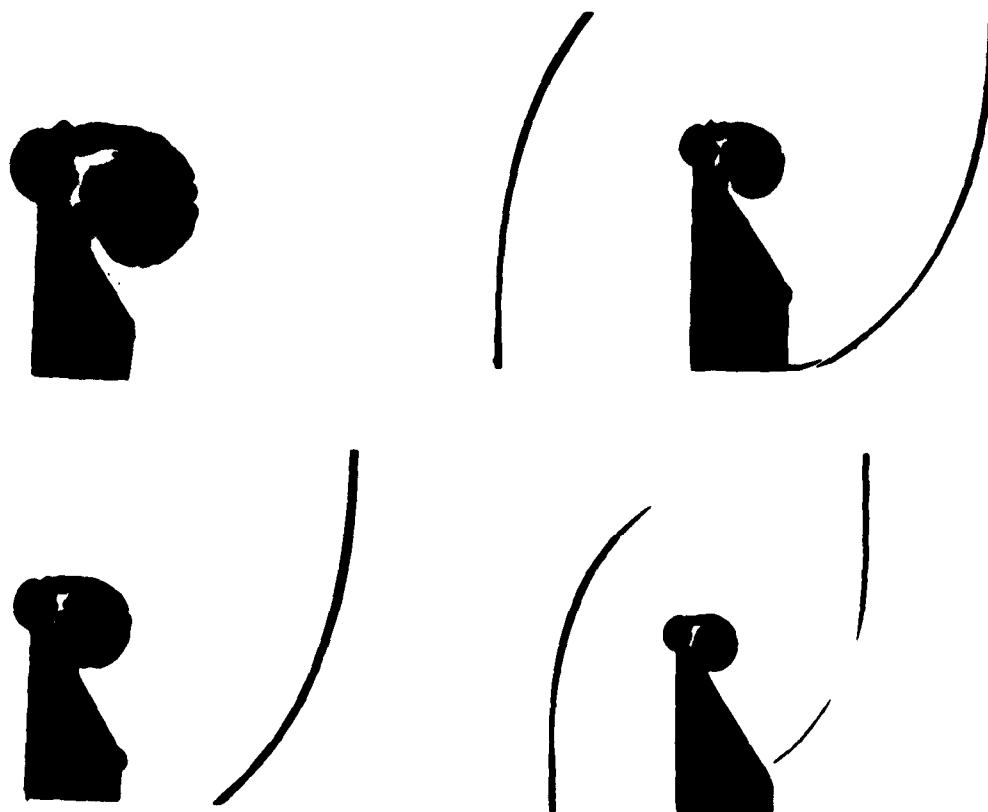


Abb.6

Wirbelausbildung um eine Schneide
zu verschiedenen Zeiten

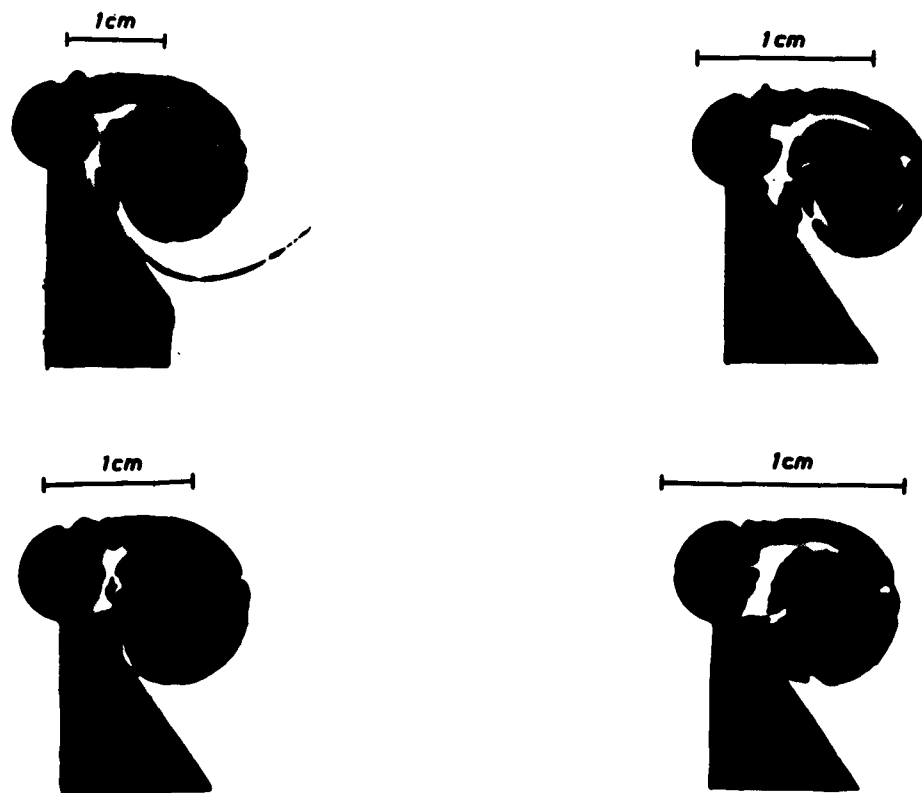


Abb.7

Gleiche zeitliche Phasen wie in Abb.6, jedoch im Verhältnis der Aufnahmezeitpunkte vergrößert. Der auf das Original bezogene Maßstab ist bei jeder Aufnahme angegeben.

LOCALIZED SHOCK VELOCITY MEASUREMENT TECHNIQUES

Dr. Ralph L. Haslund
Robert J. Charlson
Boeing Airplane Company

ABSTRACT

Due to restriction on shock tube operating conditions, complexity of associated optics and electronics and shock front thickening and curvature, the methods of shock velocity measurement dependent upon flow properties whose effects are integrated across the shock tube cease to be feasible. For a given range of shock strengths and initial gas densities, one can choose a particular type of pick-up utilizing localized gas flow properties initiated by the presence of the shock front to determine shock velocity. To minimize the effects of shock attenuation, velocity determinations must be made over a short base line requiring a gage frequency response on the order of one to ten megacycles. Three such fast response pick-ups and corresponding operating ranges are considered. They are: (1) the glow discharge probe for weak shocks, (2) the thin film resistance gage for moderate strength shocks and (3) the ionization probe for strong shocks. The principles of operation, the limitations on the operating range and the appropriate associated circuitry for each is described. Typical results from the operation of each are presented.

INTRODUCTION

Due primarily to simplicity in basic concept and design, the shock tube has and will continue to satisfy a variety of purposes. Perhaps foremost among current applications is the study of shock wave interactions in a particular and often rarified gas medium over a wide range of incident shock strengths. Fundamental to any such study is an accurate determination of shock strength just before interaction. Inasmuch as most pressure transducers are limited in response time,

linearity and sensitivity, shock strength is usually obtained by calculation from a measured mean shock velocity. Such a measurement may be made by using a sensing device the information for which is integrated across the shock tube or by using a sensing device the information for which is obtained locally, usually at the very shock front. The former method, in general, requires a rather complex system of optics and electronics and requires an undue amount of alignment when used with very low gas densities and with shock fronts exhibiting thickening and curvature.

The purpose of this paper is to consider in practical detail three sensing devices of the latter type with their appropriate operating ranges and principles of design. To better evaluate the merits of the probes to be considered, some initial discussion on timing probe systems and timing accuracy limitations is included.

CRITERIA FOR TIMING PROBE DESIGNS

When designing a set of probes for the purpose of measuring the travel time of a shock wave between two points, many criteria must be borne in mind. For the probe itself, the usual requirements are manageability, durability, simplicity of construction and associated circuitry, and adaptability. Depending upon application, the probe design may be limited by operating range (initial gas density and shock strength), physical dimensions, reproducibility, and interference or effect on the shock wave and test gas. To meet accuracy requirements for a given shock strength, over as short a base line as possible (e.g. in order to minimize the effects of attenuation), the probe and associated circuitry must provide adequate sensitivity, a minimum frequency response (vitiating probe "memory" or circuit compensating characteristics), and a minimum probe sensing width, in the direction of shock travel, in order to limit shock front transit time.

When the shock wave is the primary source of energy in furnishing the probe signal (e.g. pressure transducers) a relatively large portion of the shock wave pressure step is required, increasing effective shock front transit time and decreasing effective signal rise time. If the probe circuit is the primary source of energy in furnishing the probe signal, the signal rise time is limited only by the transit time of the shock front itself (assuming a probe circuit frequency response greater than 10 megacycles per second). The latter approach lends itself more readily to timing shock waves with irregular pressure profiles.

EFFECT OF TIME ERROR ON BASE LINE CALCULATION

In setting up a velocity measuring system it is best, especially with shock tubes with small internal dimensions, to use three rather than two timing probes. The last probe should be stationed as close as possible to the point of shock interaction under study. A linear extrapolation of the two consecutive mean velocities then gives a shock velocity upon interaction from which shock strength can usually be calculated with sufficient accuracy. The accuracy of the mean velocity measurements is (disregarding nonlinearity in shock velocity attenuation over short enough base lines) limited mainly by the probe response and triggering characteristics of the electronic interval timing device employed. These, in turn, determine the necessary length of the two consecutive base lines for a given desired accuracy. In general, the necessary base line, d , is equal to the product of U_s , the shock velocity (expressed perhaps most conveniently in millimeters per microsecond), Δt , the time variation in probe response in giving a particular trigger level voltage, and the reciprocal of the allowable percentage error in time interval determination. For example, if the time variation in producing say a 1 Volt signal is 0.1 microsecond, for a required time interval accuracy of 0.1 percent, the base line would have to be about 70mm for a Mach 2 shock in air. Of course, Δt will increase due to variation in electronic timer trigger level, but this increase can usually

be minimized to less than 0.1 microsecond. If the timer triggers at 1 Volt \pm 0.05 Volt and the signal rise time from 0.95 Volt to 1.05 Volts is less than 10^{-7} second, the trigger level response variation will give what is usually a negligibly small contribution to Δt from the electronic timer in the calculation of d .

PROBE SIGNAL SHAPE

Essential to accurate shock timing is reproducibility in shape of the probe output signal. The probe signal output can be broken down into a two step process. For the localized timing probe the shock front acts as a high speed switch, the switching time being equal to the transit time of the shock front across the sensing width of the probe in the direction of shock travel. To provide maximum accuracy, the frequency response of the probe must be large enough to exceed that corresponding to the switching time. Depending upon circuit design, this switching response is followed by either a charging or discharging response of the external probe circuit (except for the case of the thin film). For short initial time intervals, within which the timing pulse is utilized, the potential is inversely proportional to the effective circuit output RC product and increases linearly with time. Because of the high output impedance of most timing devices, a cathode follower is usually used between it and the electronic timer. With low output impedance of the cathode follower, capacitance introduced by the output cable does not appreciably reduce the over-all circuit frequency response.

For identical timing probes and signal output circuits, the variation in output potential level in time is due primarily to difference in shock transit time across the identical probe sensing widths, each usually less than a millimeter. For a slow rate of attenuation or for short base lines, this variation is much less than 10^{-7} second.

The error due to variation in signal output characteristics which always exists, because no two physical systems can be made identical, can be resolved by comparing signals taken concomitantly at the same shock timing station.

THE IONIZATION PROBE

A shock wave of sufficient strength propagating through a particular gaseous medium will cause substantial ionization of the gas which it has overtaken (see Reference 5). This is true for a shock traveling faster than about Mach 5 in air, for example. At a given instant during shock propagation the gas in the expansion chamber is composed of a low pressure and low electrical conductivity region ahead of a high pressure and high electrical conductivity region sharply separated by a shock front. A metal probe is initially charged to a high negative potential, relative to ground, in the nonconducting (i.e. comparatively) low pressure gas. As the shock front passes the probe a fast jump in gas conductivity occurs giving rise to a corresponding fast drop in potential between the probe and ground which is subsequently used as the timing pulse.

Figure 1a shows an ionization probe composed of a steel pin, about 0.8mm in diameter, inserted in a teflon insulating plug. Using the circuit of Figure 2a coupled with the cathode follower of Figure 2b, an output signal is obtained as shown in Figure 3a. The output signal in Figure 3a is for a Mach 8.9 shock in Argon at an initial pressure, P_1 , equal to 10mm Hg. A Zener diode used in the probe output circuit clips the signal at about 5 Volts to prevent overloading the timer circuits. The probe circuit is essentially a high speed discharge circuit with a frequency response in excess of that necessary to keep up with the rate of onset of gas conduction corresponding to passage of the shock front.

Fortunately, with increase in shock velocity, U_s , there is a corresponding decrease in signal rise time. The faster signal rise time reduces the error in timing, Δt , by a factor nearly equal to that of the increase in U_s . The net result is that the base line requirements are only slightly affected over a wide range of incident shock strengths. Indeed, the base line may be kept the same and still satisfy over-all accuracy requirements in time interval measurement for nearly the entire range within which the ionization probe is operable.

THE GLOW PROBE

A stable glow discharge may be set up between a cathode and an anode in a gaseous medium whose pressure lies within a certain range. This range is about 0.1mm Hg to about 25mm Hg pressure in air, for a "normal" glow discharge (see Reference 4). The nature of the glow discharge is determined by electrode spacing and geometry, applied voltage, and gas density. For the purposes of shock timing, the glow discharge current should be kept as low as possible and still be stable. With too small currents the potential drop across the electrodes becomes quite erratic due to randomness in gas conduction characteristics and sensitivity to cosmic radiation. Once glow discharge is established, the applied voltage may be lowered below "firing" voltage and still maintain a stable glow discharge. A higher firing voltage is required for gas pressures above and below about 10mm Hg in air. With too large currents the potential drop across the electrodes is steady but the conducting gas diffuses out from the electrodes and increases the volume of the glow (high positive ion density) and dark space (high electron density) conducting regions. Using the shock tube wall as the anode (usually grounded) is a drawback because the glow region around the cathode is relatively large and requires a correspondingly large shock transit time. The switching action of the shock front comes about by extinguishing or effectively "blowing out" the glow.

Except for very slight pressure jumps across the shock front, the shock will blow out the glow even though the total shock pressure is within the normal conduction range for the initial applied voltage. This is because of the large velocity gradient presented by the shock front. The probe has been shown by the authors to be operable even for compression waves, the principle difficulty in this case being that the potential drop due to change in gas conductivity (a function of gas density) is relatively small. This probe could be used for determining the rate of shock formation from a compression wave, thus complementing the more usual shock tube timing mechanisms for measuring the rate of decay of an already formed shock.

Figure 1b shows a glow discharge probe, composed of two shaped electrodes set in a teflon insulating plug, utilizing a point-to-plane design. This geometrical design, with negative pin and grounded plane, has been shown to be one of the better designs not only because of very little noise with small currents (see Reference 4) but because it introduces the least possible circuit capacitance which is of utmost importance in over-all probe frequency response. Using this probe in air at pressure P_1 (expansion chamber pressure) equal to 0.3mm Hg, with an applied voltage of 435 Volts limited by a load resistor to a current of 0.1 ma., a glow region of about 1mm in diameter is created. With these initial conditions and a probe circuit as given in Figure 2c, the output pulse, timing a Mach 2 shock, is given in Figure 3b. Clipping of the signal can be accomplished with a Zener diode as shown for the ionization probe in Figure 2a. If long signal cables are required, a coupling capacitor and cathode follower would be used as well as clipping. Because the circuit of Figure 2c is essentially a charging circuit over a range of potential equal to the drop across the load resistor while conducting, it is important to note that signal reproducibility requires only that the conduction current be the same at each timing station for a given applied voltage, assuming the probes to be physically identical. Current is controlled by varying the load resistance, the change in load resistance being compensated by an equal change in range of charging potential for very small charging times.

There is some indication that with appropriate probe geometry and applied voltages, the glow discharge may be formed in gases whose pressure lies outside the range of normal glow discharge. The authors have not explored this possibility mainly because our present shock tube investigations do not require expansion chamber pressures in this range.

THE THIN FILM

A short discussion of the thin film timing probe is included in this paper primarily to bridge the gap in operating range from the glow probe to the ionization probe. Its signal output is about three orders of magnitude smaller than either of the two previously discussed probes.

The thin film is usually a platinum or gold strip about 10^{-4} mm thick and a fraction of a millimeter wide (see Reference 1). Because its heat capacity is very small it contributes virtually no thermal lag to signal response time. An increase in resistance with temperature, upon passage of the shock front, provides an increase in potential which is used as the timing signal. The magnitude of this signal is small because the thin film power dissipation characteristics prevent drawing continually more than a few milliamps. While the amplifying circuits and electronic timer triggering level may introduce error in timing, the response time of the thin film itself is limited only by shock front transit time. The shock wave in this case does not act as a high speed switch to a fast response charging or discharging circuit.

Figure 1c shows a platinum thin film mounted on a pyrex cylinder which, used with the circuit of Figure 2d, gives the unamplified signal seen in the top trace (1) of Figure 3c. This was for a Mach 4 shock and an initial expansion chamber pressure equal to 75mm Hg.

With low initial expansion chamber pressures and weak incident shocks, the thin film is only slightly heated and is unreliable at best. At higher shock Mach Numbers the resulting ionization creates a low resistance conduction path across the thin film surface and counteracts the increase in film resistance through heating.

RESUME OF OPERATING RANGES

For the purposes of comparison, a piezoelectric crystal pressure transducer* was mounted with its center in line (in the plane of the shock front) with the center of the thin film. The signal from each pickup was fed directly into a dual beam oscilloscope giving the traces seen in Figure 3c. There are two features that should be noted: first, the pressure transducer signal starts before that of the thin film due to the larger sensing width over which the shock passes before reaching

* PZ-6 Pressure Transducer, Kistler Instrument Corp., Tonawanda, N.Y.

the thin film and second, the relatively slower rate of rise of the pressure transducer signal. The oscillation in the latter portion of the pressure transducer signal is generated by crystal ringing.

The range of operation of each probe is summarized by means of a regional graph in Figure 4. The limiting curves on the graph were calculated from maximum available bottle pressure using a Helium driver at the lower Mach Numbers (see Reference 6) and the shock tube structural limits using a combustion driver at the higher Mach Numbers (see Reference 7) for two of the Boeing Airplane Company shock tubes. It is to be understood that the regions depicted in the graph will vary in extent as a function of overall probe design and kind of test gas, the graph being drawn primarily for air.

SUMMARY

A close look has been given to the principles to be considered for optimum design of a localized effect, as opposed to integrated effect, shock timing probe. The principles of design have been examined from the viewpoints of:

- 1) probe construction, geometry and appropriate circuitry
- 2) effect of error in timing on base line calculation
- 3) probe output signal shape
- 4) probe operating range.

Insofar as the shock front is employed as a high speed switch, the effect of shock front transit time and necessity for sub-microsecond probe circuit time constants have been emphasized.

In particular, at low initial expansion chamber pressures, the glow probe and ionization probe, for weak and strong shocks, respectively, provide output pulses on the order of volts. The operation of each is dependent upon the relative electrical conductivity across the shock front and breaks down for moderate strength shocks. Within the latter range the thin film, which is sensitive to shock heating and provides a signal on the order of millivolts, is suggested as a timing pickup.



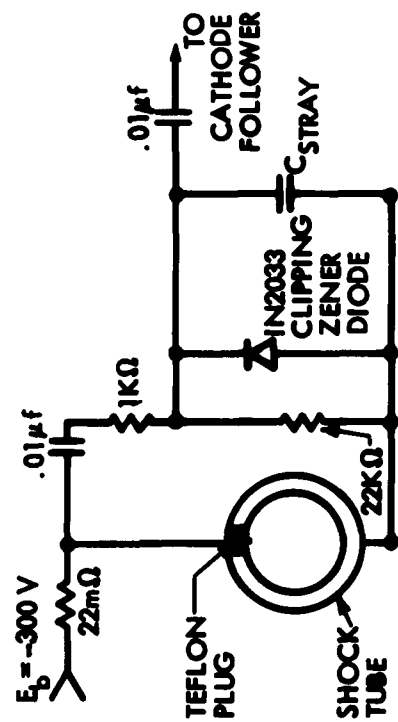
a. IONIZATION PROBE

b. GLOW PROBE

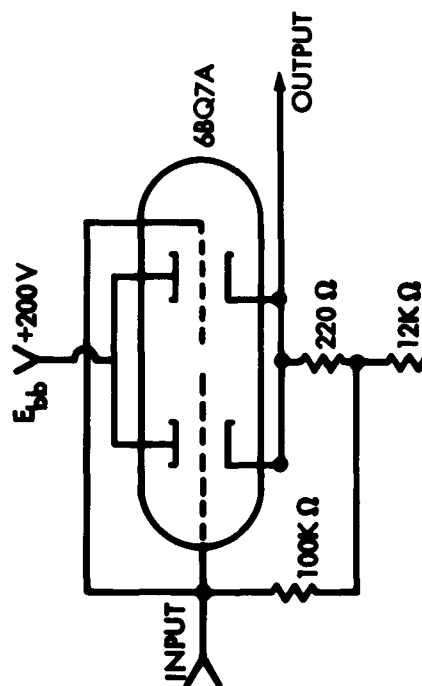
c. THIN FILM

FIGURE 1

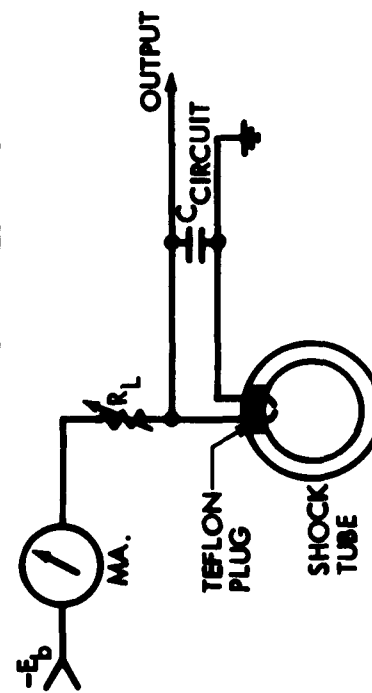
SHOCK TIMING PROBES



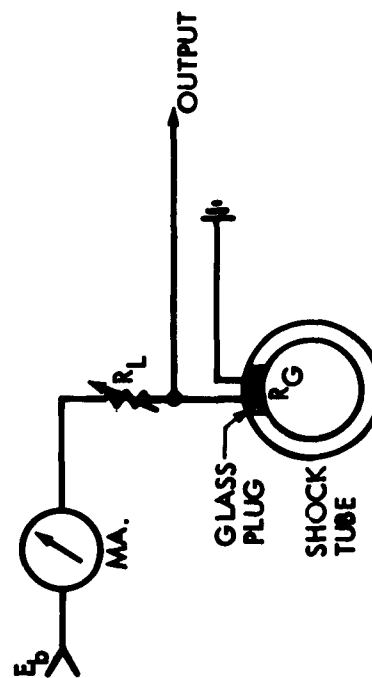
a. IONIZATION PROBE



b. CATHODE FOLLOWER



c. GLOW PROBE



d. THIN FILM

FIGURE 2

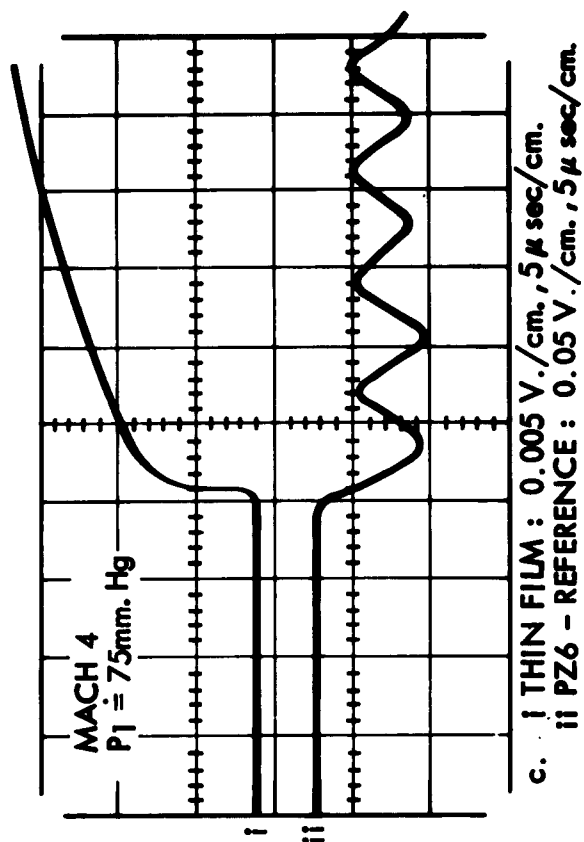
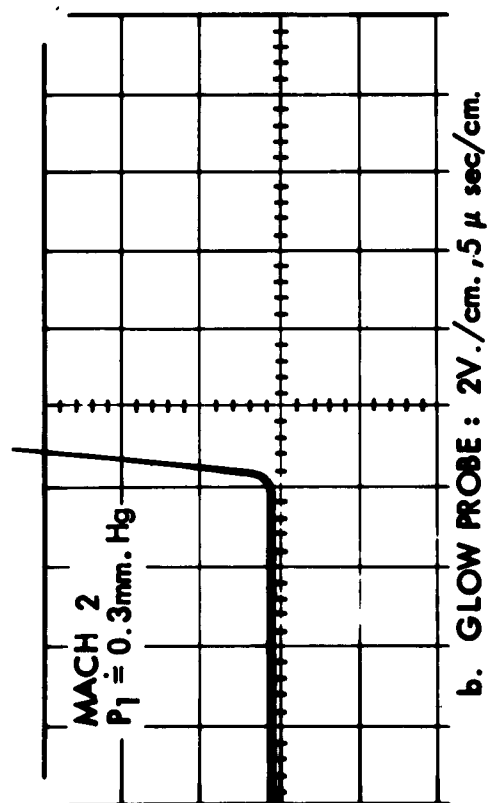
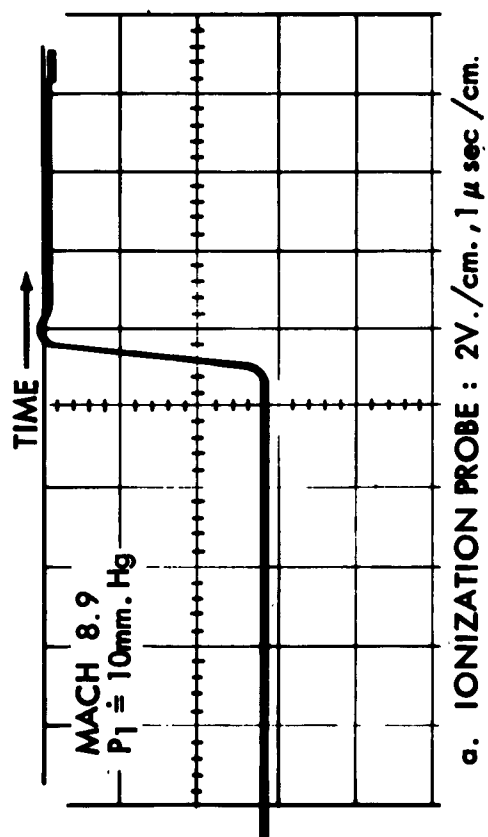


FIGURE 3

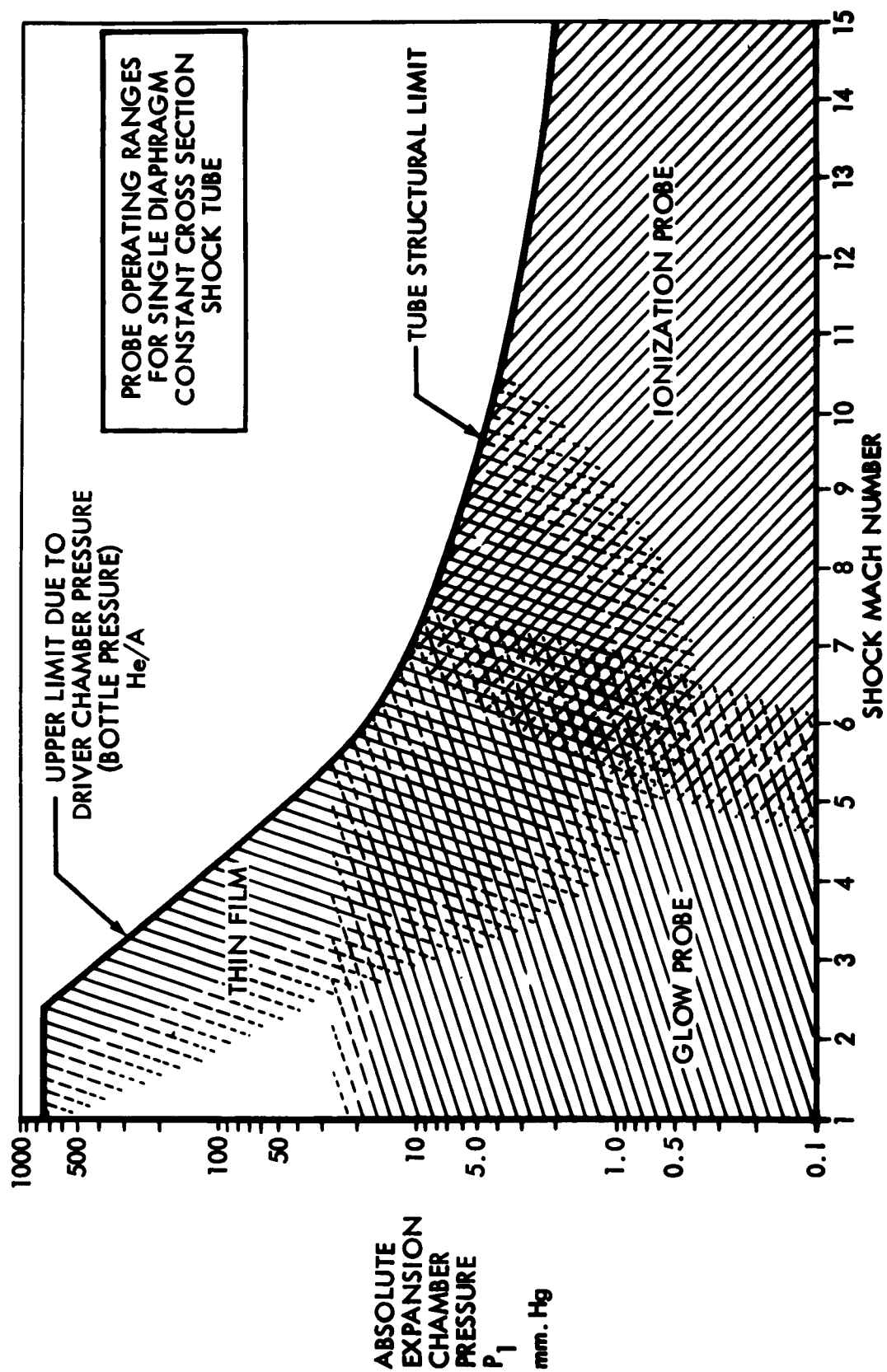


FIGURE 4

REFERENCES

1. Hall, J. Gordon. "Shock Tubes, Part II. Production of Strong Shock Waves; Shock Tube Applications, Design and Instrumentation". UTIA Rev. No. 12, May 1958, pp. 250-259.
2. Harrison, H. "Glow Discharge Trigger for Shock Wave Studies". Rev. Sci. Inst., Vol. 29, No. 2, February 1958, pp. 175-176.
3. Hecht, G. J., Laderman, A. J., Stern, R. A. and Oppenheim, A. K. "Determination of Flame Velocities in Gaseous Predetonation". Rev. Sci. Inst., Vol. 31, No. 10, October 1960, pp. 1107-1108.
4. Cobine, James Dillon. Gaseous Conductors - Theory and Engineering Applications. Dover Publications, Inc., New York, 1958.
5. Bond, John W. Jr. "Electrical Potential in an Argon Shock Front". The Proceedings of the Conference on Chemical Aeronomy, Cambridge, Mass., June 1956, pp. 249-258.
6. Grippe, R. P. "Proposed Research Program and Associated Instrumentation Requirements for the One Inch Shock Tube". Boeing Airplane Company Memo. 2-5740-207, February 1960.
7. Boeing Airplane Company Wind Tunnel Hypervelocity Systems. Summary Report 14-2.

DEVELOPMENT OF A MINIATURE DYNAMIC PRESSURE GAUGE

Kenneth Kaplan
Broadview Research Corporation

INTRODUCTION

Measurement of dynamic pressure is commonly made by obtaining the difference between stagnation pressure and side-on pressure. At low overpressure levels, where the velocity of flow is much smaller than the speed of sound, this difference is very nearly equal to dynamic pressure. Even with shock flows of Mach 1, the difference between stagnation pressure and side-on pressure is within 25 per cent of true dynamic pressure.

For a long time, there have been field instruments to measure this difference. A typical instrument consists of a probe with a stagnation pressure sensor at its tip and a side-on pressure sensor back far enough from the tip for tip interference to be minimized. For measurements at relatively low overpressure levels, for measurements in short duration flows, and for measurements where fast time response is critical, this design has a number of major drawbacks.

At low overpressure levels, where stagnation and side-on pressure are not greatly different, extreme accuracy of measurement of either pressure is required to assure accuracy of the measurement of their difference. For example, at an overpressure level of 5 pounds per square inch, a 5 per cent uncertainty in side-on and stagnation pressure would result in a 64 per cent uncertainty in their difference. At an overpressure of 10 pounds per square inch, this same 5 per cent uncertainty would result in a 36 per cent uncertainty in the value of the pressure difference.

For measurement in short duration flows, the distance between the sensors can result in stagnation and side-on pressure being sampled in portions of the shock wave in which the flow differs significantly.

For measurement where fast time response is critical, the time response of the gauge design is lengthened by the time for the shock to travel between the points of measurement.

The gauge to be described largely eliminates these drawbacks. A single sensor responds to the difference between stagnation and side-on pressure directly, and the points for sampling stagnation and side-on pressure are quite close together.

DESCRIPTION OF THE GAUGE

The basic gauge design is shown in Figure 1. The gauge is in the form of a thin disk oriented with its flat surfaces parallel to the direction of flow. Stagnation pressure is sampled in the center of one side of the disk and side-on pressure, in the center of the other side. A piezoelectric ceramic tube is mounted in the center of the disk with its axis perpendicular to the disk faces. The two pressures act on either side of a plastic cap rigidly fastened to one end of the tube. The sensitive element -- the tube -- senses only the difference of the forces applied to its cap.

Stagnation pressure is produced on the front surface of a small block (stagnation baffle) mounted in the center of the stagnation pressure side of the disk. The disk minimizes the effects, on the side-on pressure sampling port, of the flow disturbance created by the stagnation baffle, but it still allows the two sampling points to be in close physical proximity to one another.

Note that there is an adjustable sealing ring on the stagnation side of the cap. The area of the stagnation side of the cap is larger than that of the side-on side. The sealing ring is adjustable to equalize these areas. The stagnation baffle is removable, and when it is removed, side-on pressure is applied to both sides of the cap. By this means, the equality of the cap face areas to which pressure is applied can be tested.

A photograph of two gauges is shown in Figure 2. On the right is a standard gauge with its cap and cover plate removed and the cap on the piezoelectric tube exposed. On the left is a gauge designed to measure dynamic pressure close to a surface, with its stagnation baffle in place.

GAUGE EVALUATION AND CALIBRATION

In verifying the correct operation of the gauges the first step is to be certain that the gauge is balanced, i.e., that the sensitivity of the gauge is the same for pressures applied to either side of the disk. As noted earlier, this is accomplished by removing the stagnation baffle so that equal (side-on) pressures are applied to both sides. If the gauge is balanced, no signal will be generated.

The stagnation baffle is then replaced and the gauge calibrated by exposing it to shock waves of various strengths in a shock tube. When this is done it is found that the gauge responds linearly to the difference between stagnation and side-on pressure calculated from the Rankine-Hugoniot relations for the shock front. Since the type of sensor used responds linearly to applied pressure, this linear response of the gauge indicates that it is operating correctly.

There is additional indirect evidence that strongly confirms the correct operation of the gauge.

1. The arrival of the contact surface, across which pressure is uniform but density is not, should be seen on a record of dynamic pressure but not on a record of side-on pressure. The gauges repeatedly exhibited a decided signal increase at a time after the start of the pulse that corresponded to the calculated arrival time of the contact surface. In addition, the overall magnitude of the signal increase corresponds to the expected magnitude of increase from the Rankine-Hugoniot relations.

No such discontinuity was observed in records from side-on pressure gauges.

2. When the reflected wave from the closed end of the shock tube passes over a gauge during the time of measurement, the signal decreases sharply virtually to zero -- while the signal from a side-on overpressure gauge increases sharply. This is the proper pattern, for the air flow should be halted by the reflected shock, and free-field overpressure should increase.

The linearity of the calibration of one gauge with calculated dynamic pressure is shown in Figure 3. Note that the gauge response to overpressure is far from linear.

The calibration of a later model gauge is shown in Figure 4. A different piezoelectric material was incorporated in the gauge. Its sensitivity is larger than that shown in Figure 3 by more than a factor of 8.

The inset in Figure 4 shows a comparison of the calculated and measured times of arrival of the contact surface as a function of incident overpressure.

The next three figures show typical oscillograph traces from a number of gauges. Figure 5 is a trace from an early gauge taken at an overpressure of 14.7 pounds per square inch -- a dynamic pressure of 4.6 pounds per square inch. The traces of Figure 6 are from a later model gauge. They were taken at overpressure levels of 18.0 and 21.0 pounds per square inch -- dynamic pressure levels of 6.7 and 8.9 pounds per square inch. In Figure 7 are shown a number of traces from a modified version of the same gauge -- taken at various overpressure levels. This particular gauge exhibits a fairly large overshoot which results in a response time of approximately 0.8 milliseconds.

In the gauges produced to date, gauge response times of as little as 0.1 millisecond with noise levels of as little as ± 10 per cent of the basic signal have been achieved.

DIAPHRAGM GAUGE

Some development work has been done on a gauge which uses the same disk-pressure differencing principle, but which is more suited to use in very hot shock flows. The basic design of this gauge is shown in Figure 8. Note that pressure is applied to diaphragms mounted in the faces of the disk. The force on these diaphragms is transmitted to the cap on the piezoelectric tube by a rod connecting them.

Our experience to date indicates that this type of gauge can have a fast response time, but is somewhat noisier than the previously discussed design.

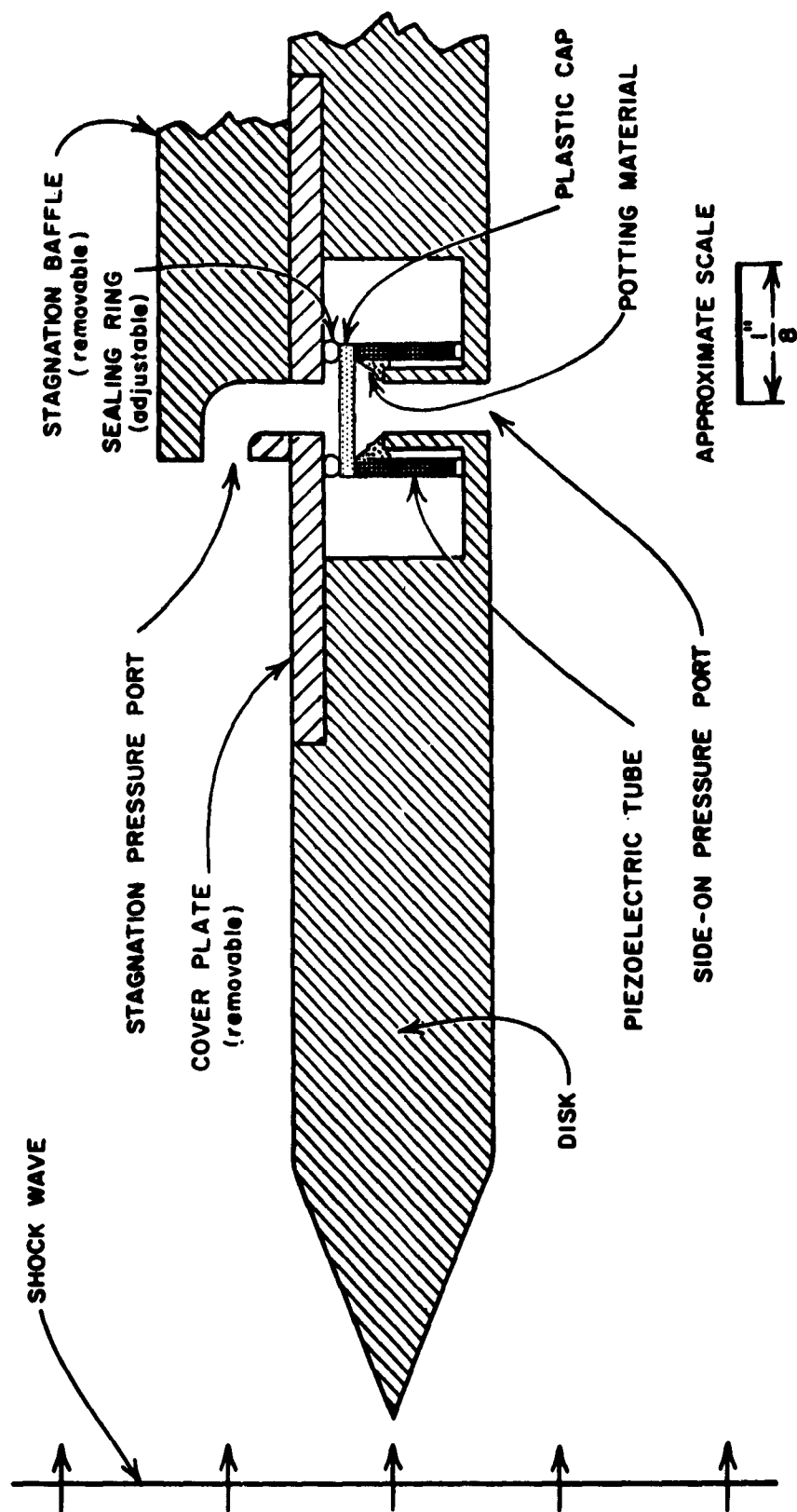


FIGURE 1
SCHEMATIC OF STANDARD DYNAMIC PRESSURE GAUGE



NOTE: The non-surface gauge is on the left the standard
full-size gauge is on the right.

FIGURE 8-2

NEAR-SURFACE DYNAMIC PRESSURE GAUGE

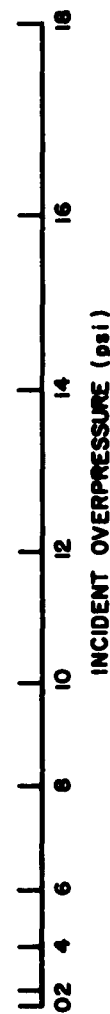
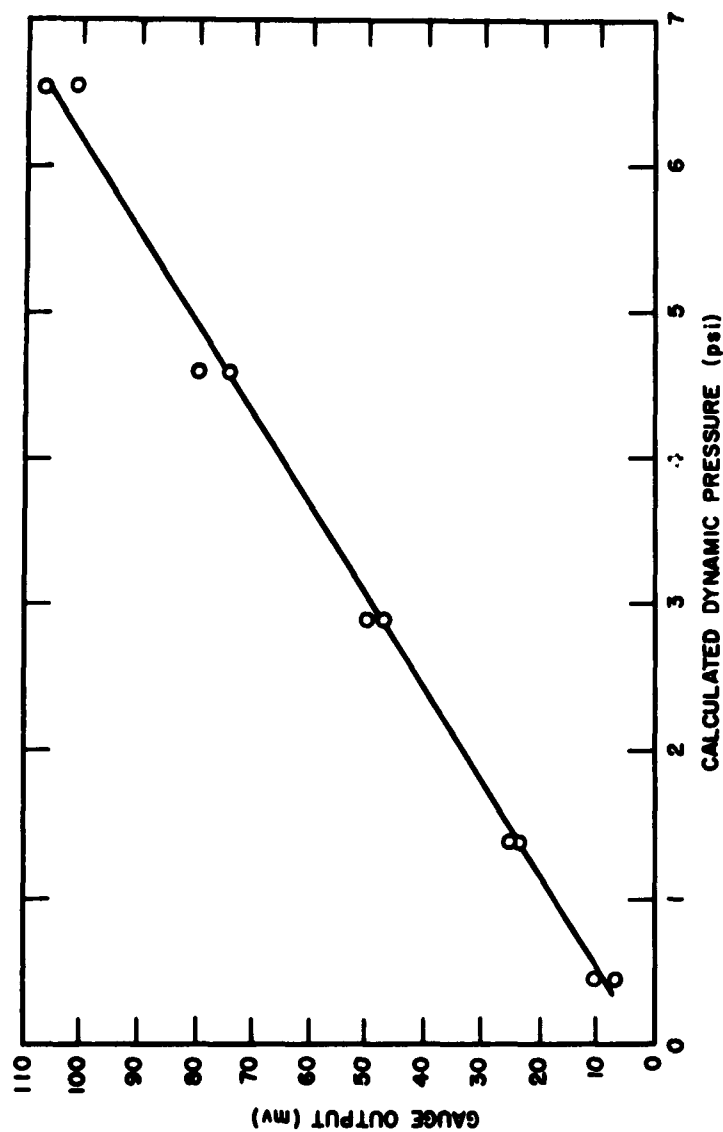
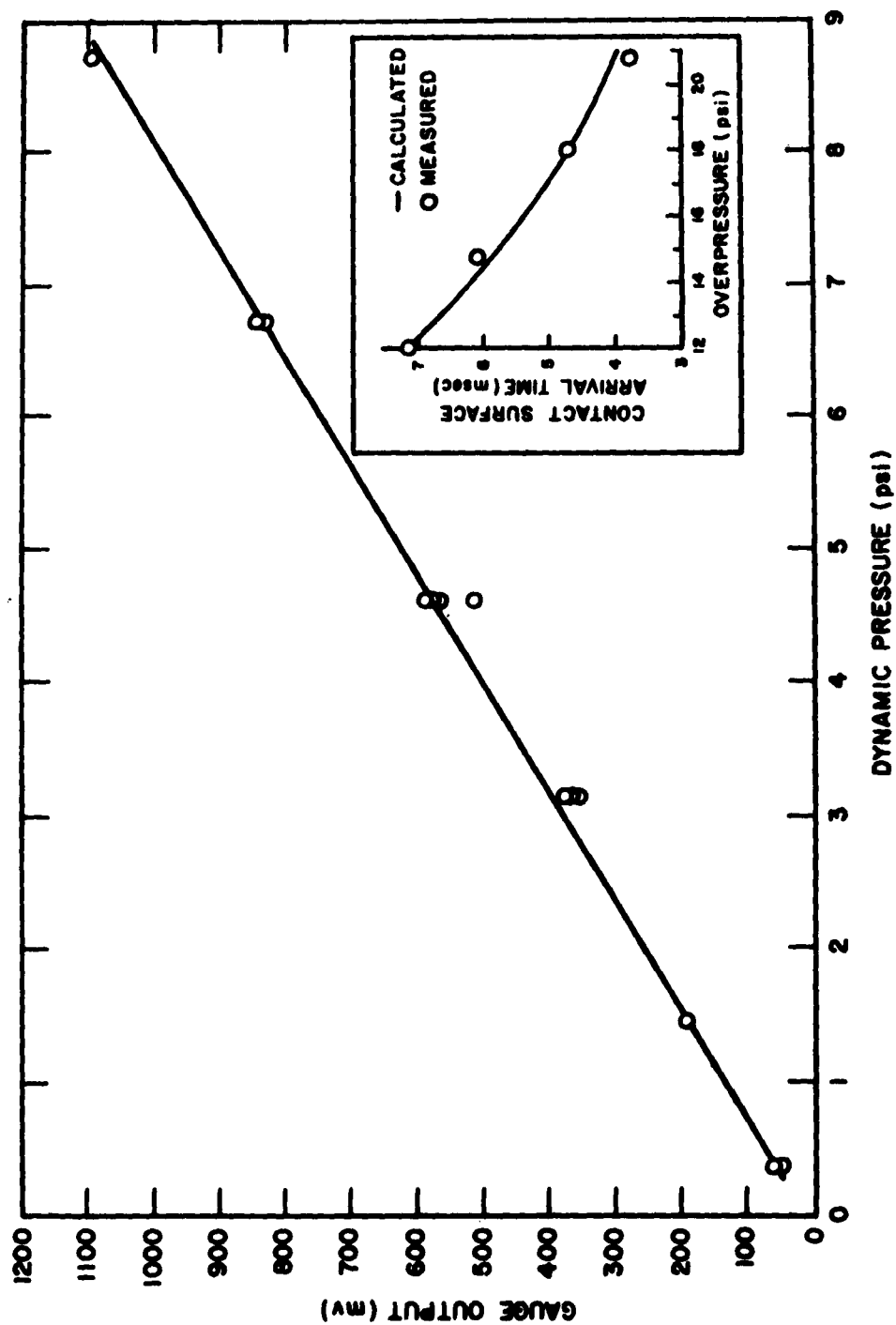


FIGURE 9-3
CALIBRATION OF GAUGE Q-2

NOTE: Dynamic pressure is calculated from

$$q = (2.5 P_1^2) / (7 P_0 + P_1)$$

Where q = dynamic pressure
 P_1 = initial shock overpressure
 P_0 = ambient pressure



NOTE: Dynamic pressure is calculated from

$$q = (2.5 P_1^2) / (7 P_0 + P_1)$$

where q = dynamic pressure

P_1 = initial shock overpressure

P_0 = ambient pressure

FIGURE 4

CALIBRATION OF GAUGE Q-5 AND THEORETICAL AND MEASURED TIMES OF
ARRIVAL OF THE CONTACT SURFACE

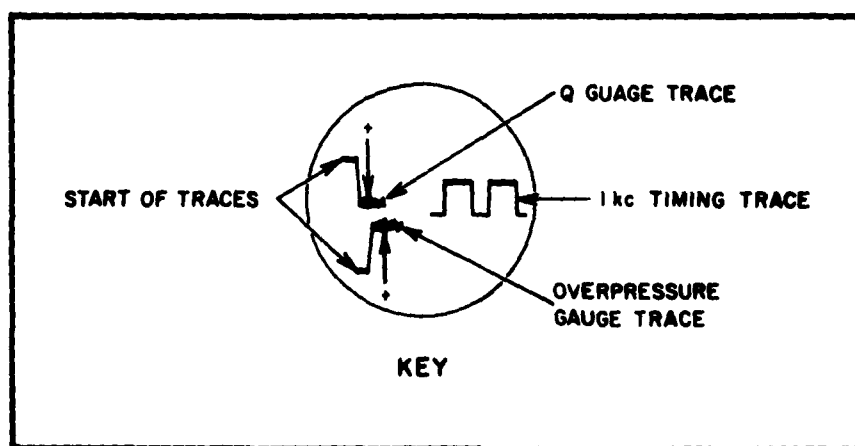


FIGURE B 5

DYNAMIC PRESSURE AND OVERPRESSURE TRACES FROM GAUGE Q-2

NOTE: The contact surface arrived approximately 4 msec after the start of the pulse, and the shock reflected from the closed end of the shock tube about 1 1/2 msec later. Shock wave overpressure was 14.7 psi; dynamic pressure, 4.6 psi.

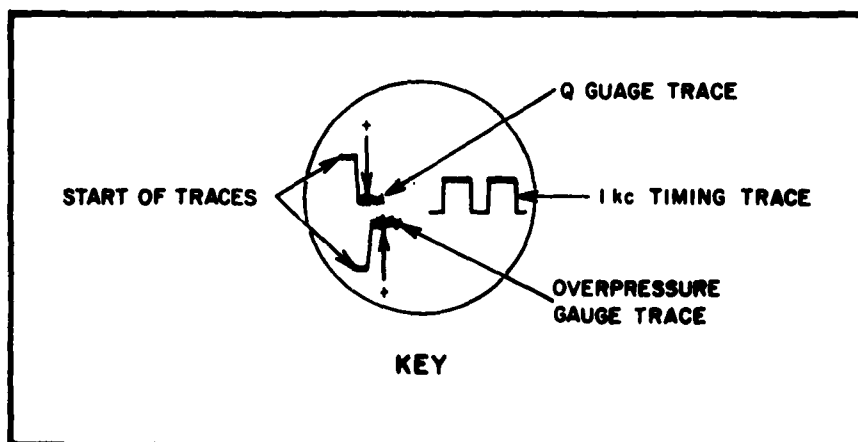
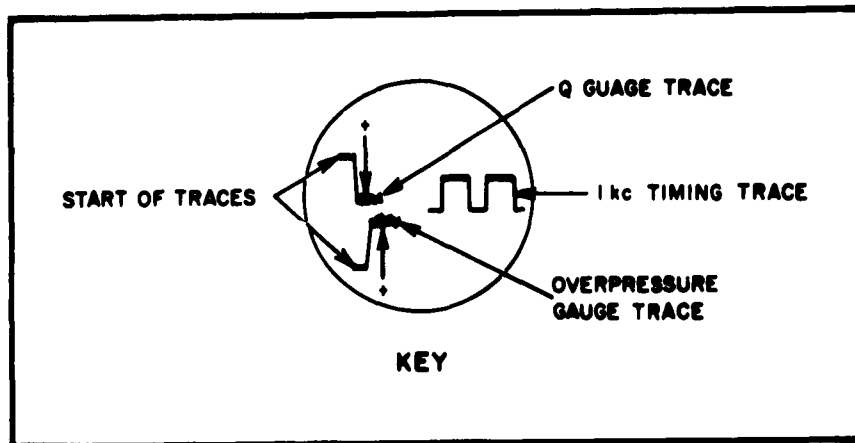


FIGURE 76

DYNAMIC PRESSURE AND OVERPRESSURE TRACES FROM GAUGE Q-5

NOTE: The upper set of traces were taken at a shock overpressure of 18.0 psi, a dynamic pressure of 6.7 psi; the center trace was taken at a shock overpressure of 21.0 psi, a dynamic pressure of 8.9 psi.



$q = 0.4 \text{ psi}; P_i = 4.0 \text{ psi}$



$q = 1.4 \text{ psi}; P_i = 8.0 \text{ psi}$



$q = 3.1 \text{ psi}; P_i = 12.0 \text{ psi}$



$q = 4.6 \text{ psi}; P_i = 14.7 \text{ psi}$



$q = 6.7 \text{ psi}; P_i = 18.0 \text{ psi}$



$q = 8.7 \text{ psi}; P_i = 20.8 \text{ psi}$

FIGURE M 7

TRACES FROM GAUGE Q-5 WITH ORIFICE RESTRICTION
OVER THE STAGNATION PRESSURE PORT

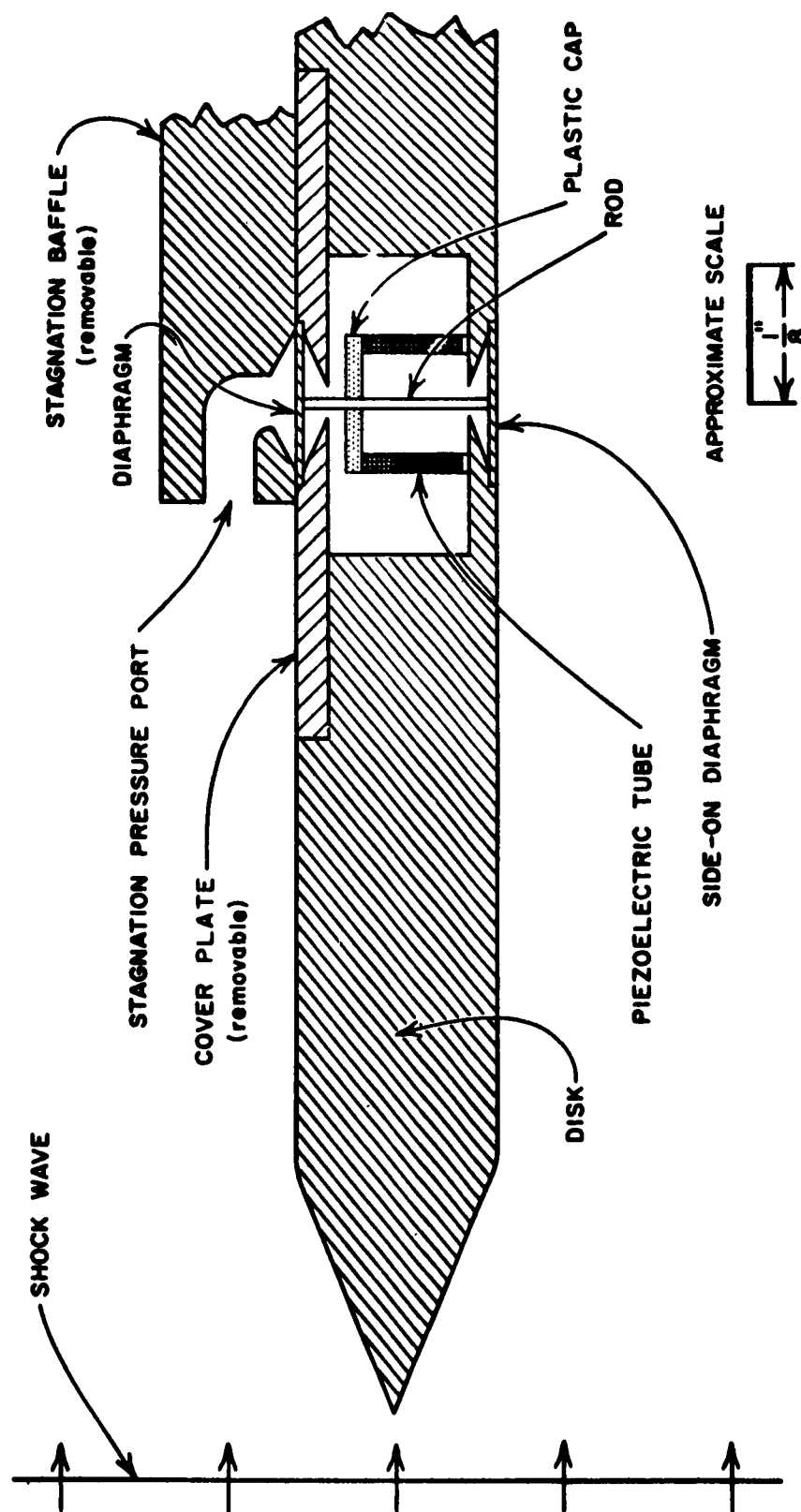


FIGURE 9-6
SCHEMATIC OF DIAPHRAGM TYPE GAUGE

AERODYNAMIC FORCE AND MOMENT MEASUREMENTS IN THE

NOL 4-IN. HYPERSONIC SHOCK TUNNEL NO. 3

David N. Bixler
U. S. Naval Ordnance Laboratory

ABSTRACT

Extremely light-weight models of missiles are suspended by very fine threads in the test section of the NOL 4-in. Hypersonic Shock Tunnel No. 3. Alongside the models a light-weight sphere is also suspended. A high-speed camera is focused on the models through a window in the side of the shock tunnel test section, and illumination of the models is provided by a rapid-response, constant-intensity light source. When the shock tunnel is fired, the light source is actuated, the fine threads holding the models are snapped, and the models are then photographed for $2 \frac{1}{4}$ milliseconds as they move freely in the shock tunnel flow. From the high-speed camera film (taken at a frequency of about one frame every 40 microseconds) data of the horizontal, vertical, and angular motions of the models as functions of time are obtained. Data of the horizontal motion of the light-weight sphere are also obtained. Since the drag coefficient of a sphere is fairly well established, this configuration is used as a test body and the motions of the models are compared to that of the sphere. From these comparisons the drag coefficients, the lift coefficients, and the moment coefficients are determined.

INTRODUCTION

Figure 1 is an illustration of the NOL 4-in. Hypersonic Shock Tunnel No. 3. To date, 95 tests have been performed in this facility; 77 of these tests were made for the purpose of determining the aerodynamic forces and moments on models of missiles while they were in actual free flight in the shock tunnel flow. The tests were performed under separate contracts with various corporations. Over 90 per cent of these tests yielded usable data from which results could be obtained.

These results consisted of the static moment and drag coefficients - and more recently, lift coefficients - of missiles as functions of missile angle of attack and Mach number.

EXPERIMENTAL TECHNIQUE

The following experimental method for obtaining forces and moments was first outlined at the Second Shock Tube Symposium in 1958 (reference 1). A more detailed description was presented by Dr. A. E. Seigel in May 1959 (reference 2). A similar technique, with several modifications, has been adopted by the Missile and Space Vehicle Department of the General Electric Company in its 6-in. Shock Tunnel (reference 3); while at Cornell Aeronautical Laboratories, the method is being used to determine damping moments of models of missiles.

The high-pressure chamber of the NOL 4-in. Hypersonic Shock Tunnel No. 3 is 14 feet long and has an inside diameter of 10 inches, while the low-pressure chamber is 60 feet long and has an inside diameter of 4 inches. The test section is 52 feet long and 8 feet in diameter. In the test section, two light-weight models and a light-weight sphere are suspended by very fine threads and positioned so that they hang between two opposing windows in the side of the test section, as shown in Figure 2. A short-duration, high intensity light source is situated outside one window and focused to pass a converging beam of light through the test section and over the models. A high-speed camera is placed on the opposite side of the test section and focused on the models. Attached to the window nearest the light source are several vertical and horizontal grid wires to be used as a reference system on the camera film. The light source is actuated by a piezoelectric pressure transducer at the muzzle of the low-pressure chamber.

The camera is a Beckman & Whitely Dynafax and is operated at a rate of approximately one frame per 40 microseconds. The models are usually machined from ethocel, although various materials are sometimes used for different parts of a model. A portion may be made of magnesium, aluminum, brass, or steel, in order to increase strength of a particular part of a model or to position the center of gravity at a desired point.

The tolerance on the machining of a model is usually kept within 0.005 inch. The model may have a length of one to 6 inches and weigh from one to 30 grams. The sphere which accompanies the models may have a diameter from 1/4 to 1 1/2 inches; the latter diameter being that of a ping-pong ball, which is sometimes used. The sphere weighs between 1/3 and 5 grams, and, except for the ping-pong ball, is made of nylon. Figure 3 is a view from the back of the test section looking into the muzzle. In this photograph a sphere and two hollow cones are seen suspended by fine threads.

In the test section, the working gas expands as a free jet from the muzzle. Along the sides of the test section, three pairs of opposing windows are located. These windows have been placed such that when the models are suspended between any pair of windows the models will be a distance of 80, 142, or 218 inches from the muzzle. At these distances the flow Mach number will be approximately 8, 11, or 14, respectively. The conditions in the shock tunnel for these various Mach numbers are listed in Figure 4. In all cases the loading conditions in the high-pressure chamber are the same. The powder charge used to heat the helium is Hercules Unique powder and is ignited by a series of explosive primers running along the inside of the chamber. In the Mach 8 and Mach 11 cases the loading conditions in the low-pressure chamber are the same, but in the Mach 14 case the initial pressure is lower in order to avoid condensation in the test section due to excessively low temperatures. The flow duration is approximately 2 1/4 milliseconds, except in the Mach 14 case, where it is slightly under 2 milliseconds.

When the shock tunnel is fired, the initial portion of the flow breaks the threads with which the models are suspended in the test section, and the models, initially at rest, are then accelerated. The magnitudes of the various components of this acceleration are directly proportional to the aerodynamic drag, lift, and moment on the models.

DATA ANALYSIS

The drag force on a model is

$$C_D q A_m = m\ddot{x} \quad (1)$$

where C_D is the model's drag coefficient, q is its dynamic pressure, A_m its characteristic area, m its mass, and \ddot{x} its acceleration in the direction of the flow. The lift on the model is given by

$$C_L q A_m = m \ddot{y} \quad (2)$$

where C_L is the lift coefficient of the model, and \ddot{y} is its acceleration normal to the direction of flow. The static aerodynamic moment on the model is

$$C_m q A_m D_m = I \ddot{\alpha} \quad (3)$$

where C_m is the static moment coefficient of the model, D_m is the characteristic diameter of the model, I is the moment of inertia about its center of gravity, and $\ddot{\alpha}$ is its angular acceleration. Similarly, for the sphere in the test section the drag is

$$C_{D_s} q_s A_s = m_s \ddot{x}_s \quad (4)$$

where C_{D_s} is the drag coefficient of the sphere, q_s is the dynamic pressure on the sphere, A_s is its cross-sectional area, m_s its mass, and \ddot{x}_s its acceleration.

After a finite period of flow time, the models and the sphere will have attained individual velocities, so that each will experience a slightly different dynamic pressure. The difference between the dynamic pressures on the model and on the sphere (i.e., q and q_s) has been as high as 4 per cent of q . However, it is generally easy to design a test so that this difference will be no greater than 2 per cent. Thus, with negligible error, q is equal to q_s . Then if each of the first three equations above is divided by equation (4), the resultant equations will be

$$C_D = C_{D_s} \frac{A_s}{A_m} \frac{m}{m_s} \frac{\ddot{x}}{\ddot{x}_s} \quad (5)$$

$$C_L = C_{D_s} \frac{A_s}{A_m} \frac{m}{m_s} \frac{\ddot{y}}{\ddot{x}_s} \quad (6)$$

$$C_m = C_{D_s} \frac{A_s}{A_m} \frac{1}{m_s D_m} \frac{\ddot{\alpha}}{\ddot{x}_s} \quad (7)$$

Now the drag coefficient of the sphere is a fairly well known quantity, and, with the exception of the accelerations, all other quantities on the right-hand side of the above three equations are readily measurable. Then the problem remaining is to determine the ratios $\frac{\ddot{x}}{\ddot{x}_s}$, $\frac{\ddot{y}}{\ddot{x}_s}$, and $\frac{\ddot{\alpha}}{\ddot{x}_s}$ by analysis of the high-speed camera film.

Obtained from the camera is a strip of film containing 30 to 60 consecutive frames of silhouettes of the models and the sphere in motion. Figure 5 contains six sample photographs taken from two strips of film of two different tests. The top, middle, and bottom photographs were taken at the beginning, middle, and end of the flow, respectively. In these pictures the silhouettes and the grid wires described earlier can be seen. A strip of this film is placed in a projector, and images of the silhouettes in one frame are magnified and cast on an opaque screen. A full-scale drawing or template of the image of each model is made on a sheet of vellum, with the centerline and center of gravity of the model also placed on each template. These templates are then superimposed upon the images of the silhouettes in each consecutive frame of the film, and the coordinates of the centers of gravity and the angles of attack of the models are measured and recorded. Also recorded are the coordinates of the sphere in each frame. Typical data obtained by this method of reduction are shown in Figure 6. The plots in this figure are shown as they are produced by the IBM 704 computer. The plot labeled "x(1) vs. Frame No." is that of the horizontal motion of the model with time. The plot labeled "y(1) vs. Frame No." is that of the vertical motion of the model with time, and the plot labeled "Alpha vs. Frame No." is that of the angle of attack with time. The last plot, which is labeled "x(1) vs. Frame No. - Model 3," is that of the horizontal motion of the sphere with time. The angles given in this figure are in units of degrees, while the linear units given here are such that 650 units equal one inch. Thus, this model moved only about 1/4 inch, while the sphere

moved more than an inch. The motion of the model is small because this particular model was one of the most massive ever used in these tests.

The data in each of these plots are now divided into short intervals of time, and a second-degree equation is fitted by the method of least squares to the data in each interval. In the same interval of time a second-degree equation is fitted to the data of the sphere motion. These equations are then differentiated twice, and the ratio of these second derivations is taken as the ratio of the model to the acceleration of the sphere. For example, the data in the plot labeled "Alpha vs. Frame No." are divided into short intervals of time. Assume that the first interval extends from frame number 3 to frame number 18. Then over this interval an equation of the form $\alpha' = a + bt + ct^2$ is fitted to the data by the method of least squares. Over the very same interval of time (frame number 3 to frame number 18) an equation of the form $x'_s = a_s + b_s t + c_s t^2$ is fitted to the data of the sphere motion. Both of these equations are differentiated twice, and the ratio of these second derivatives, $\frac{C}{C_s}$, is assumed to be the ratio $\frac{\ddot{\alpha}}{\ddot{x}_s}$. When this ratio is placed in equation (7), a value for the static moment coefficient C_m over this interval is obtained. Values for the drag and lift coefficients are also obtained in a similar manner from ratios of the horizontal and vertical accelerations of the model to the acceleration of the sphere.

Now, when a second-degree equation is fitted to the data, it is automatically assumed that the acceleration of the model is constant. However, it has been seen from Figure 6 that there is a variation in the angle of attack of the model, and thus, there is probably a variation in the forces and moments, giving rise to a variation in the acceleration components.* For each value of a force or moment coefficient determined for an interval of the data, a value of the average angle of attack over that same interval is determined. If the angular variation of a model in a given interval of time is small, as it is in Figure 6, then this average angle of attack will be a reasonably accurate value for the angle at which the calculated coefficient occurs.

* As will be pointed out later, there is also a variation in the dynamic pressure q .

However, in some tests the variation in the angle of attack is considerably larger, as in Figure 7. Here the angular motion of two cones is plotted vs. time.** In order to obtain values for the moment coefficient C_m as a function of angle of attack from the data shown here, it is first assumed that C_m is antisymmetric about zero angle of attack, as the case has always been in tests up to now. Then it is further assumed that $C_m = A\alpha + B\alpha^3$, where A and B are constants to be determined by examination of the data. These constants are calculated by first setting

$$(A\alpha + B\alpha^3) q A_m D_m = I \ddot{\alpha}$$

and integrating twice with respect to time. In the resulting integral equation

$$\frac{I(\alpha - \alpha_0)}{A_m D_m} = A \int_0^t \int_0^t \alpha q dt dt + B \int_0^t \int_0^t \alpha^3 q dt dt$$

everything is readily measurable except A, B, and q. The dynamic pressure q has been found to vary with time in the 4-in. Hypersonic Shock Tunnel No. 3, and thus, it is treated as a variable here. It is found by first fitting equations to very small portions of the sphere motion by the method described earlier, and taking the second derivatives of these equations. These derivatives are then placed in the drag equation for the sphere, and values for the dynamic pressure at various times are found. With the use of these values and the "Alpha vs. Frame Number" data, the above integral equation is numerically integrated. This equation can be integrated only over a little more than a quarter of an oscillation of the model, since there is nothing in the equation to allow for damping of the model's oscillations. Then as the integration is carried out from zero to some time t, the angle of attack is decreasing.

** The data in this figure were obtained from film taken from the Beckman and Whitely Model 192 High-Speed Framing Camera, rather than the Dynafax. These are data from one of the earliest tests made with the 4-in. Hypersonic Shock Tunnel No. 3.

The double integration is carried out twice, first to some time t_1 and then to some other time t_2 , and thus, two simultaneous equations are obtained, from which A and B are determined. Upon comparison of the results obtained by this method of analysis in different tests, and over different intervals of integration in individual tests, it has been found that the values of the moment coefficient obtained for angles near the initial angle of attack of the model generally agreed within 15 percent.

The test section conditions are determined from the dynamic pressure as obtained from analysis of the sphere motion, in conjunction with the directly measured pressure and shock-wave velocity at the muzzle.

Originally, the designers of the 4-in. Hypersonic Shock Tunnel No. 3 were hoping to be able to obtain damping moments of models in addition to the static forces and moments. Thus, a model was designed to attain as much angular motion as possible. However, with the non-reflecting method employed in this facility, there is insufficient time to obtain dynamic coefficients. Therefore, the tests in this facility are now designed only for the object of yielding data from which the static forces and moments can be reduced. It has been found from experience that these quantities are most accurately determined in tests where the angular motion of the model is small.

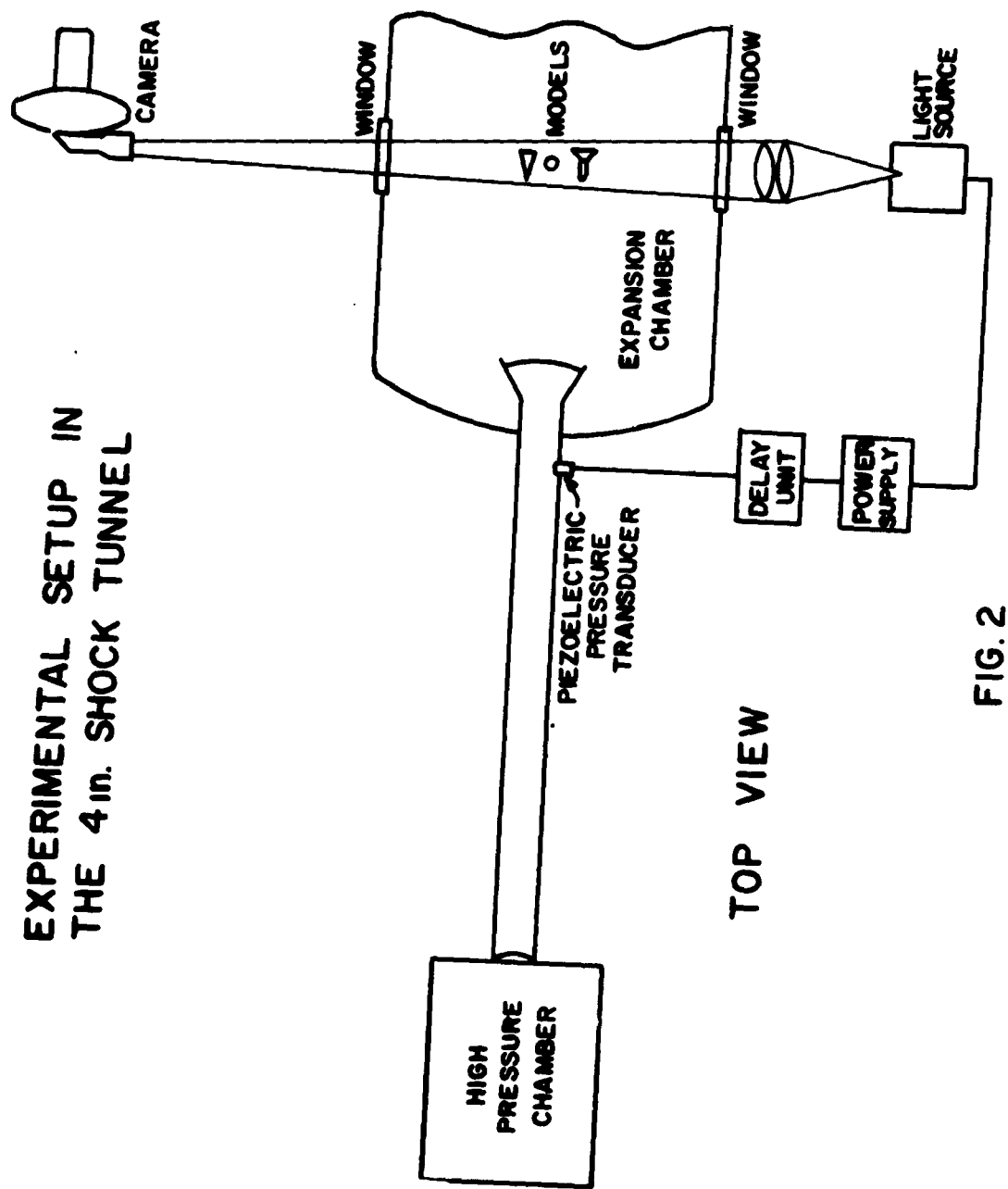
Presently, attention is focused on improving the flow in the 4-in. Hypersonic Shock Tunnel No. 3, since the variation of the dynamic pressure of this flow is the chief obstacle to obtaining greater accuracy of results. Attempts to reduce the impurities present in the flow in the test section are also being made, so as to reduce absorption and scatter of light from the light source and thus achieve optical measurements of a higher quality. With the realization of these improvements, the capabilities of the free-flight method for yielding aerodynamic information in the 4-in. Hypersonic Shock Tunnel No. 3 will be enhanced.

The author wishes to express his gratitude to Mr. David Gates for his indispensable advice and constructive criticisms and Mr. Robert Piacesi who wrote the entire data reduction program for the IBM 704 computer.



FIG. 1

EXPERIMENTAL SETUP IN THE 4in. SHOCK TUNNEL



TOP VIEW

FIG. 2

SUSPENDED SPHERE AND CONES AS SEEN FROM
REAR OF TEST SECTION IN 4 m. HYPERSONIC
SHOCK TUNNEL NO. 3

FIG 3



CONDITIONS IN THE NO. 4-IN. HYPERSONIC SHOCK TUNNEL NO. 3

Distance From Nozzle To Model		80 in.	142 in.	218 in.
High-Pressure Chamber	Initial Load	6,000 psi Hg	6,000 psi Hg	6,000 psi Hg
	Powder Charge	30 lbs	30 lbs	30 lbs
	Peak Pressure	30,000 psi	30,000 psi	30,000 psi
Low-Pressure Chamber	Initial Load	450 psi air	450 psi air	350 psi air
	Free Stream Pressure	9,200 psi	9,200 psi	9,300 psi
	Total Enthalpy	850 Btu/lb	850 Btu/lb	1,080 Btu/lb
	Free Stream Temperature	1,230°K	1,230°K	1,450°K
	Shockwave Velocity	4,800 ft/sec	4,800 ft/sec	5,400 ft/sec
	Shockwave Mach Number	4.2	4.2	4.7
	Flow Velocity	3,800 ft/sec	3,800 ft/sec	4,400 ft/sec
Expansion Chamber	Flow Mach Number	8	10.9	14.3
	Stagnation Pressure	265 psi	80 psi	25 psi
	Stagnation Temperature	1,800°K	1,800°K	2,200°K
	Free Stream Pressure	4 psi	0.5 psi	0.1 psi
	Free Stream Temperature	140°K	80°K	60°K
	Flow Velocity	6,300 ft/sec	6,400 ft/sec	7,300 ft/sec
	Density	0.04 lbs/ft ³	0.009 lbs/ft ³	0.002 lbs/ft ³
	Dynamic Pressure	180 psi	40 psi	12 psi
	Reynolds Number Per Inch	3×10^6	10^6	0.5×10^6

FIG. 4

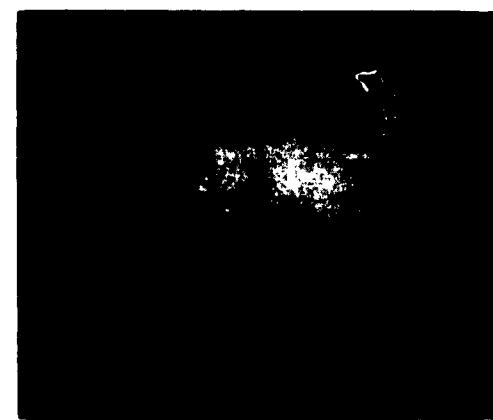
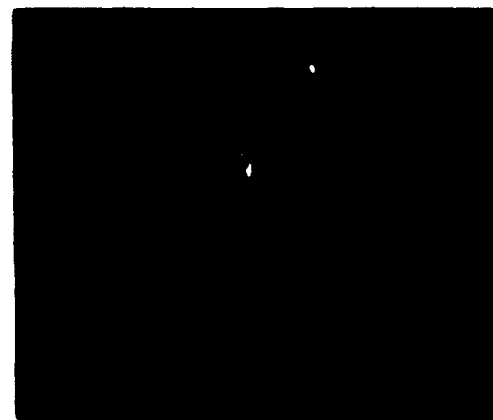
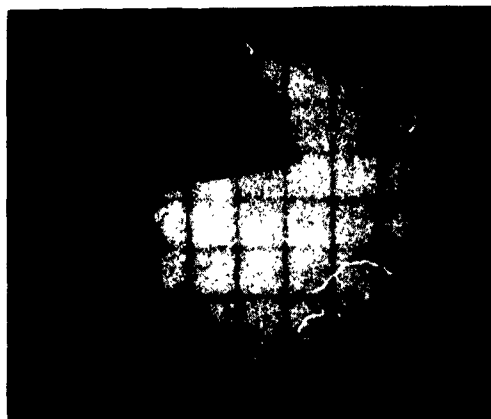


FIG. 5

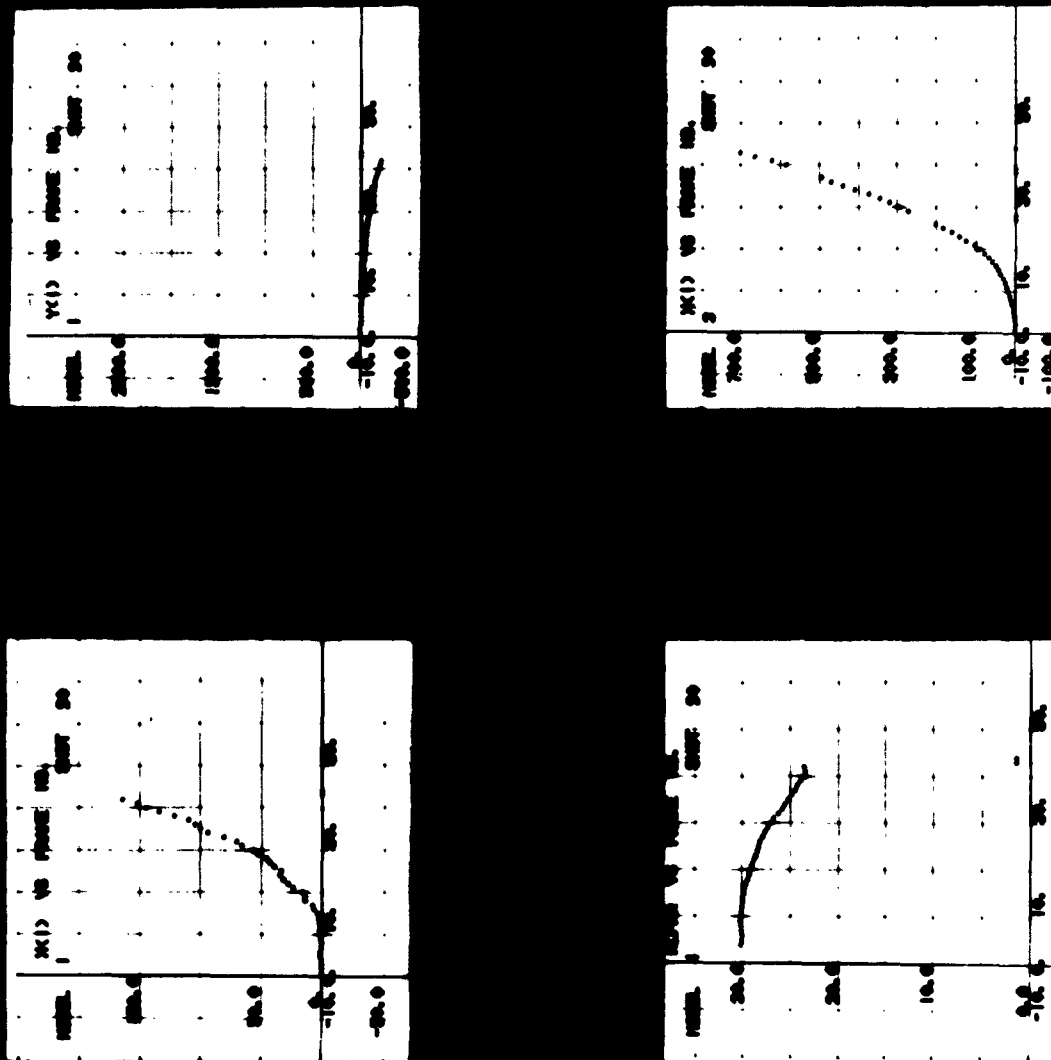
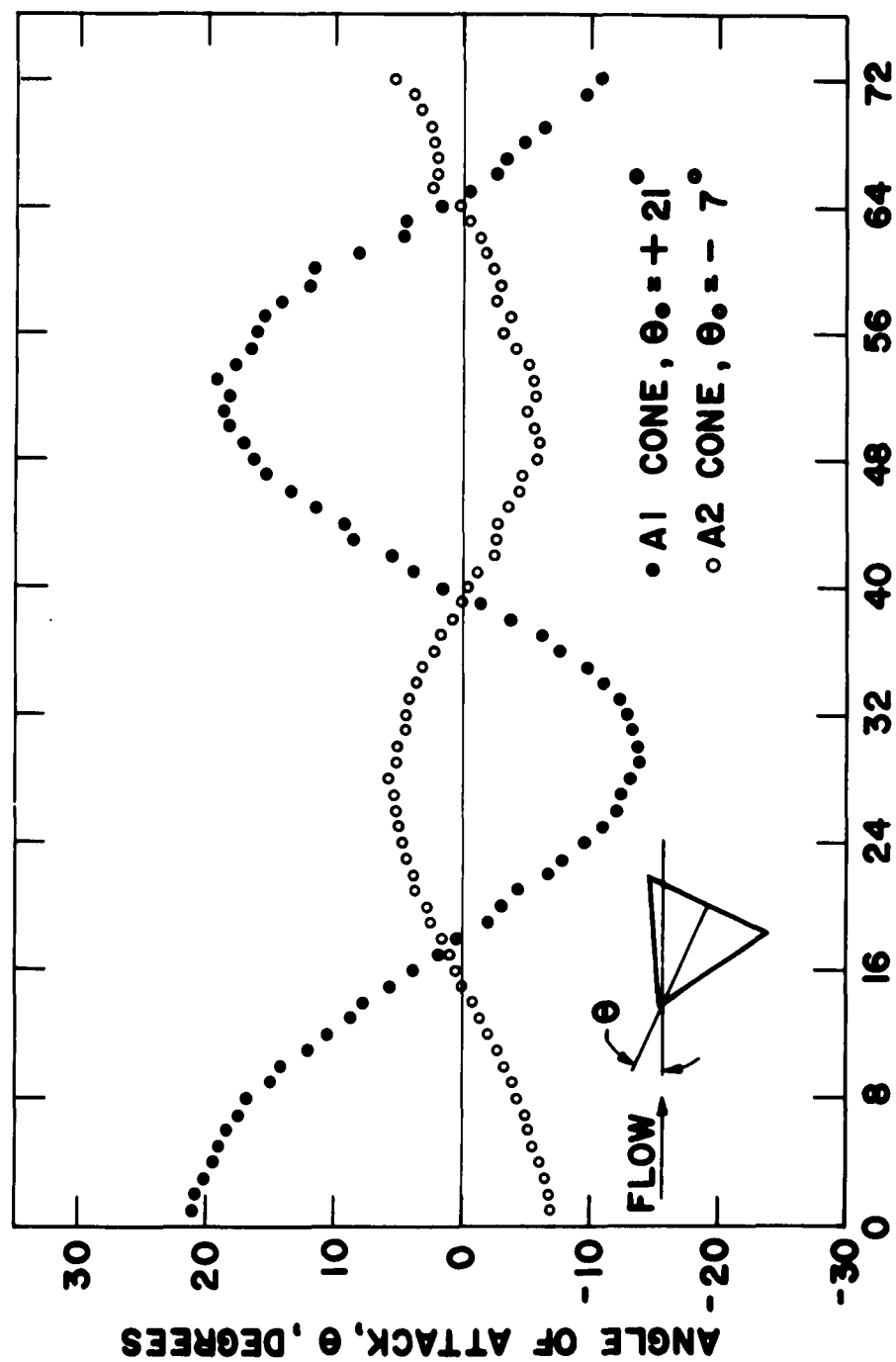


FIG. 6

CONE STABILITY DATA



REFERENCES

1. Aronson, P. M., Marshall, T., Seigel, A. E., Slawsky, Z. I., and Smiley, E. F., "Shock Tube Wind Tunnel Research at the U. S. Naval Ordnance Laboratory," Proceedings of the Second Shock Tube Symposium, SWR-TM-58-3, Air Research and Development Command, Kirtland Air Force Base, New Mexico, March 1958.
2. Seigel, A. E., "Millisecond Measurement of Forces and Moments in Hypersonic Flow," NOL Aeroballistic Research Facilities Dedication and Decennial, NOLR 1238, May 1959.
3. Kaegi, E. M., Warren, W. R., Harris, C. J., and Geiger, R. E., "The Capabilities of the Shock Tunnel in the Study of the Aerodynamics of Atmospheric Entry," ARS 15th Annual Meeting, December 1960.

EXPERIMENTAL RESULTS FROM
THE I.S.L. - HYPERSONIC SHOCK TUBE

Dr. H. Oertel
German-French Research Laboratory, France

INTRODUCTION

In the hypersonic shock tube of the joint German-French-Laboratory of St.-Louis strong shock waves in air, N_2 or CO_2 are produced by using cold H_2 as driver gas. Part of the shock heated gas is then expanded in a conical nozzle. The expansion ratio is chosen to give Mach numbers between 4 and 8. Four sorts of measurements have been done so far: Shock speed measurements, visualisation of bow waves and boundary layers, drag measurements, heat flow measurements.

SHOCK TUBE

Slide 1 shows the dimensions of this shock tube. It is a very small one. The length over all is about 10 m. The diameters are 44mm to 150mm. The driver pressure cannot exceed 40 atm. Thus at a Mach number of 8 the density is very low and the blowing time is very short. For instance at a stagnation temperature of $3000^\circ K$ the density is only about $6 \cdot 10^{-4}$ of sea level density and the blowing time is only about $2 \cdot 10^{-4}$ s, just as long as the starting time. Slide 2 shows a sketch of the nozzle and slide 3 a photo of the nozzle entrance.

SHOCK SPEED MEASUREMENTS

Shock speed measurements have been done by means of small resistance thermometers as shock detectors and by means of transistorized 10^6 cps - counters. Some results are shown in slide 4.

VISUALISATION

Three methods of visualisation have been used:

Shadow pictures have been taken by means of the optical set-up shown in slide 5.

Slide 6 shows an example.

Schlieren pictures have been taken by means of the optical set-up shown in slide 7.

Slide 8 shows an example.

The Normanski-interferometer shown in slide 9 has been used to take interferograms.

This is a differential-interferometer using polarized light split by Wollaston prisms. The interferometer (a) needs a point-light source. The interferometer (b) can work with an extended source. There is plenty of light to take color pictures. With this method fringe shifts measure density-differences between points some 0.1 mm apart.

The slides 10 and 11 compare the 3 methods of visualisation.

The splitting angle of the prism and its orientation must be well chosen, as can be seen from the slides 12 and 13. With this method we have been able to visualize the stagnation line-boundary layer of a cylinder at Mach number 8, as shown in slide 14. One of the problems studied so far was the detachment distance of the bow wave of a cylinder as a function of real gas effects. The results indicate, that no thermodynamic equilibrium was achieved with densities below 10^{-3} of sea level density. This may be seen from slide 15, where a is the shock detachment distance, D the diameter of the cylinder and M_g the shock Mach number before the nozzle. The driver pressure was fixed at 40 atm. Higher shock Mach numbers have been produced by lower initial pressures of the driven gas lower test section densities.

There was the question of really stationary flow. The answer could be given by series of pictures taken at high frequency. We worked with spark frequencies up to $2.5 \cdot 10^5$ pictures per second. Image separation has always been done on rotating film. Slide 16 shows the spark circuit. Slides 17 and 18 give examples of pictures taken at 10^4 per second and 10^5 per second.

DRAG-MEASUREMENTS

There was little hope to be able to measure drag with commercial probes. Proper frequencies of about 10^5 cps are not sufficient for measurements in some 10^{-4} s. We thus decided to use selfmade piezo-electric probes with ρ a - matched interfaces. They don't have proper frequencies. Probes of such kind have first been used in our laboratory by Turetschek 17 years ago to measure pressure variations in bow waves of small bullets. Turetschek used quartz on a aluminium bars. The slides 19 and 20 show some examples. I have been able to verify those measurements by density-measurements using corona probes. Those early quartz probes had some disadvantages, which can be overcome by the bariumtitanate probe shown on slide 21. With bariumtitanate and brass matching is not as good as with quartz and aluminium. Never-the-less there is only small residual oscillation, as can be seen from the oscillogram slide 22 showing the drag on a cylinder. The time base represents 10^{-4} seconds per cm. The bar had a length of 2 m. Slide 23 shows echos coming from the end of the bar, when the front had been knocked by a falling sphere.

HEAT FLOW MEASUREMENTS

Heat flow measurements have been done by means of the well known thin platinum surface thermometer; slides 24 and 25 show such thermometers on glass models. There was some doubt as to the reliability of the flow measurements with probes, which had suffered erosion by fragments of the second shock tube diaphragm.

Slide 26 shows the results of calibrations of a highly eroded probe. We found out that erosion does not matter, if the straight part of calibration curves is used to determine the calibration constant.

OSCILLATING BOW WAVE-RESULTS

We have used all the mentioned methods to study the oscillating bow wave of a cylinder with a stick at Mach number 8. Slide 27 shows the model.

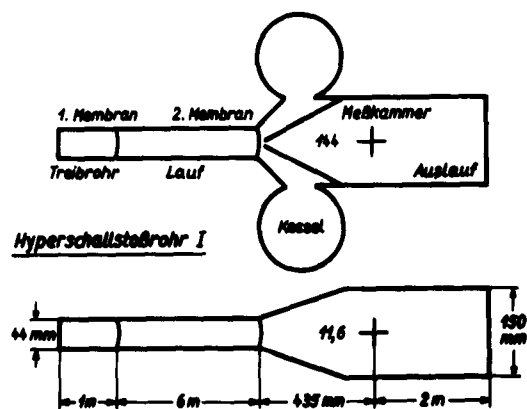
Slide 28 shows pictures of the bow wave.

Slide 29 gives an oscillogram of the oscillating drag. The frequency of the sinusoidal oscillation is $2 \cdot 10^4$ cps.

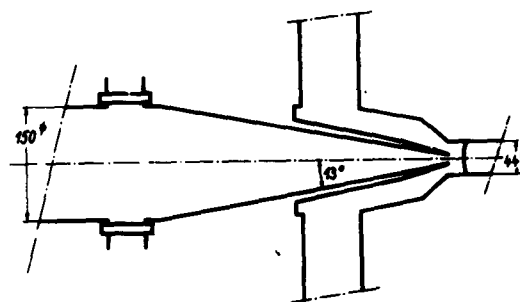
Slide 30 gives an oscillogram of the oscillating surface temperature at the point of maximum mean heat flow.

Slide 31 shows the heat flow as evaluated from this oscillogram.

The mean heat flow is shown on slide 32.



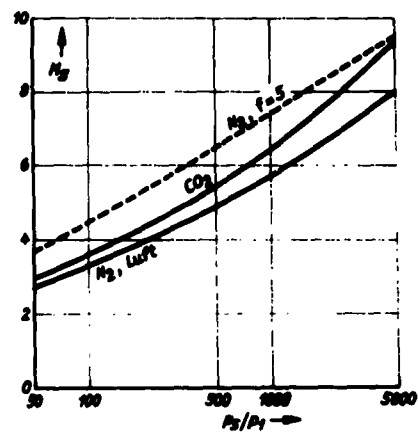
SLIDE 1



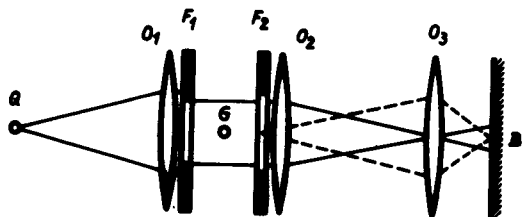
SLIDE 2



SLIDE 3



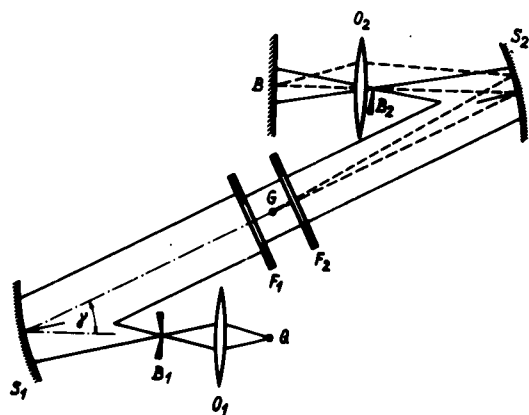
SLIDE 4



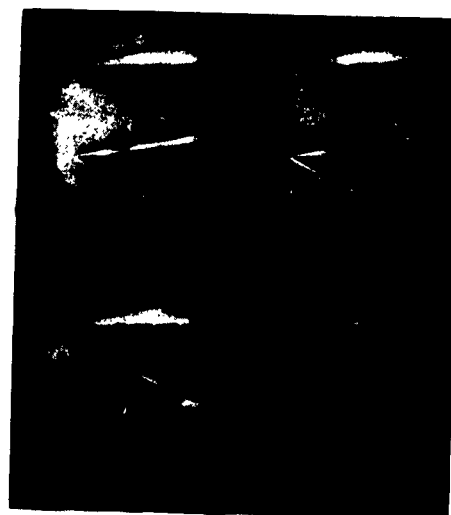
SLIDE 5



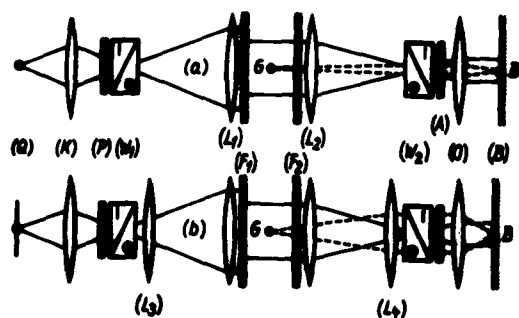
SLIDE 6



SLIDE 7



SLIDE 8



SLIDE 9



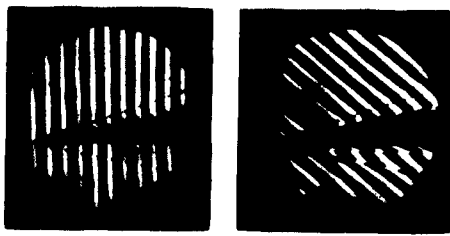
SLIDE 10



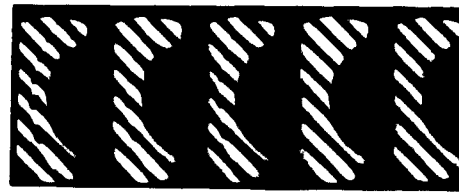
SLIDE 11



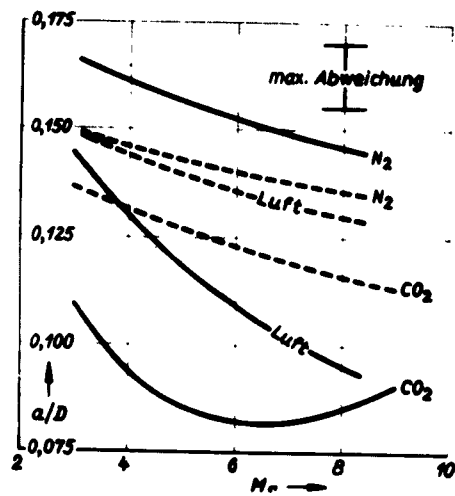
SLIDE 12



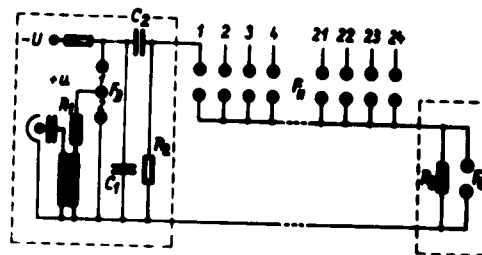
SLIDE 13



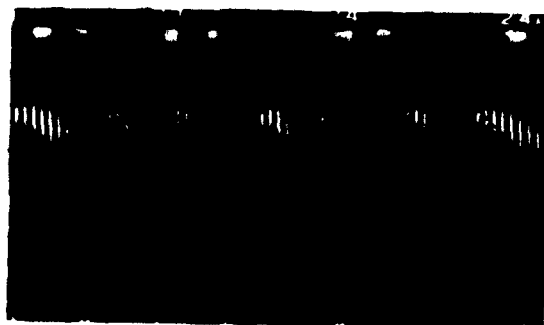
SLIDE 14



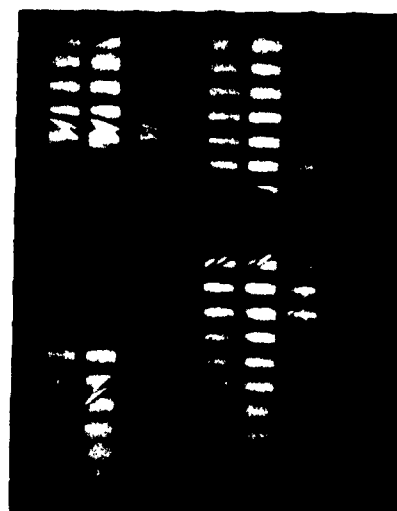
SLIDE 15



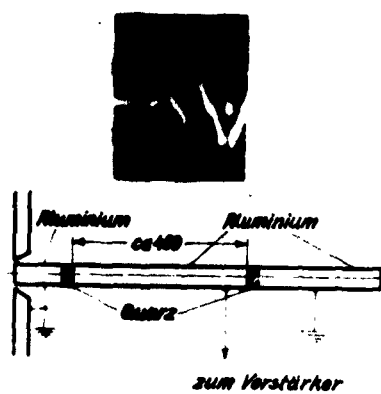
SLIDE 16



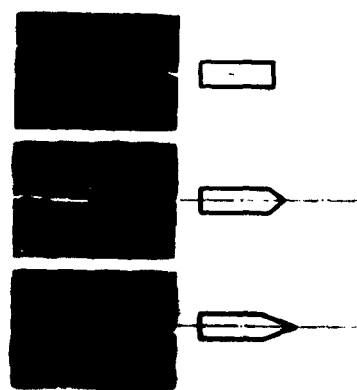
SLIDE 17



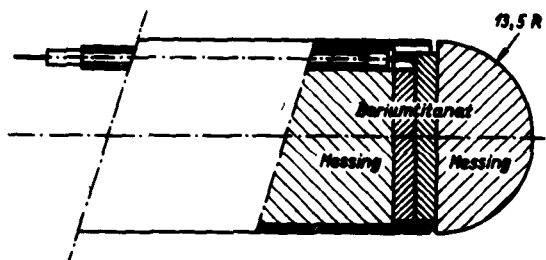
SLIDE 18



SLIDE 19



SLIDE 20



SLIDE 21



SLIDE 22



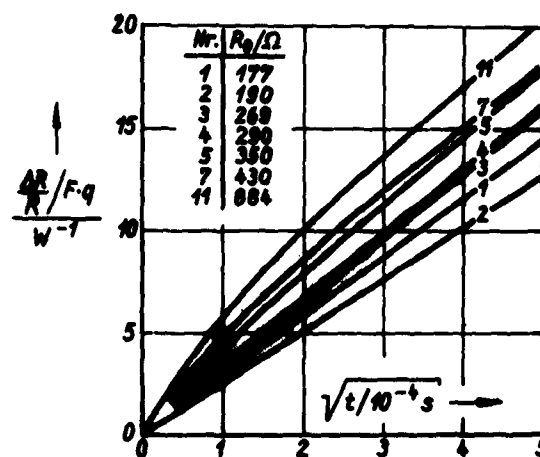
SLIDE 23



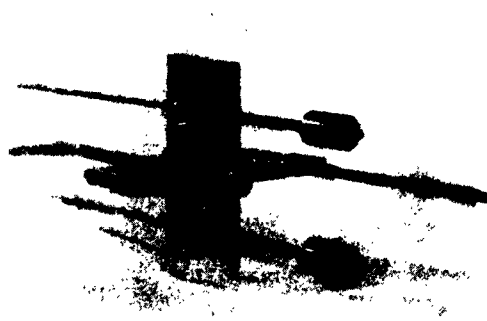
SLIDE 24



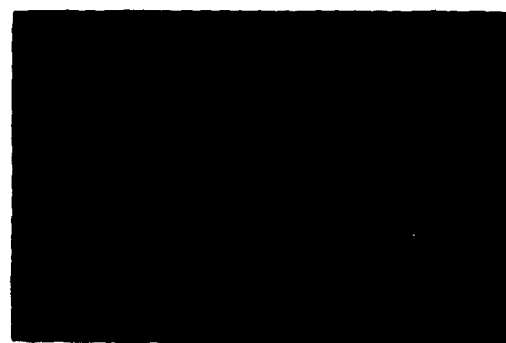
SLIDE 25



SLIDE 26



SLIDE 27



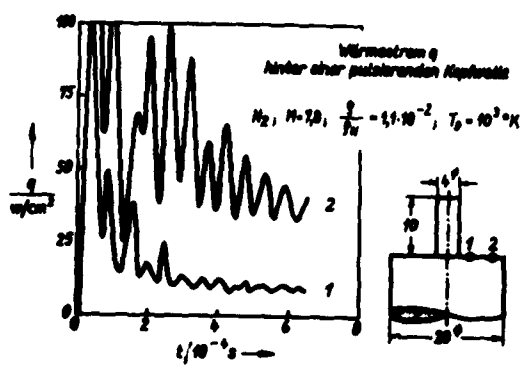
SLIDE 28



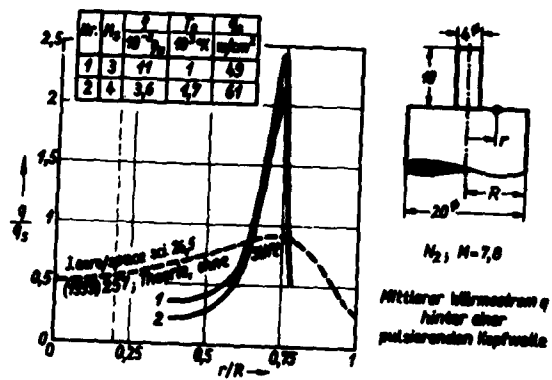
SLIDE 29



SLIDE 30



SLIDE 31



SLIDE 32

THE PRESSURE INSIDE OPEN SHELTERS FROM ENTERING SHOCK WAVES

Hjordis Celander
The Research Institute of National Defence
Sweden

The pressure conditions which are found inside open air raid shelters after bomb detonations have been investigated at the Research Institute of National Defence. The investigation was originally planned as a purely experimental one. Some relations between the pressure and the shape of the shelter were found, so the investigation was extended to include also a more theoretical treatment of the problem.

The experimental investigations were carried out with scale models. The form of these shelter models are seen in Figure 1a and 1b. (Scale 1:10). The height of the model was everywhere the same ($= 3,6$ cm). Therefore the shock expansion inside the models was two-dimensional. The two slits indicate the placing of the pressure gages. The pressure is simultaneously registered in two points, one just outside the entrance of the shelter model and one inside the model.

The shock wave was obtained from a shock tube with circular cross-section. Figure 2 shows how the models were connected to the shock tube. The following parameters were varied:

1. incident pressure p_2
2. length of the entrance tube l
3. length of the shelter model
4. width of the shelter model
5. angle of incidence α
6. placing of the pressure gage inside the model

The pressure gages were usually of the piezoelectric type (barium - titanite).

Figures 3, 4 and 5 shows typical pressure-time-curves obtained inside the shelter models with these gages. The time calibration pulses, which were obtained from a derivating RC - circuit, appear as sharp peaks on

the curves. The angle of incidence, α , was here 0° . The incident pressure p_2 is indicated on the vertical axis.

From the records obtained it appears that the pressure change inside the shelter model consists of a rather slow oscillation with superimposed shock wave disturbances. This oscillation has been compared with other oscillations in physics, particularly electrical and acoustical. These studies led to the assumption of the following analogies between aerodynamical and electrical phenomena. (The same analogies are used in all electro-acoustical comparisons).

aerodynamical

energy

pressure

gas volume

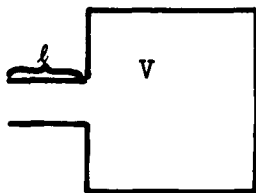
gas volume/unit time

frictional losses

$$L = \frac{\rho l}{s}$$

$$C = \frac{V}{\rho c^2}$$

$$\nu = \frac{c}{2\pi} \sqrt{\frac{s}{V}}$$



resonant circuit

electrical

energy

potential

charge

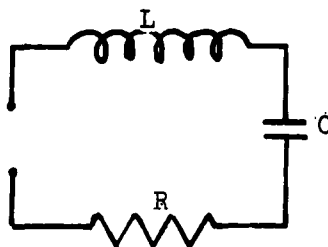
current

resistance R

L = inductance

C = capacitance

$$\nu = \frac{1}{2\pi} \sqrt{\frac{1}{LC}}$$



resonant circuit

where ρ = gas density

l = entrance tube length

s = entrance tube cross-section

c = sound velocity

V = shelter volume

ν = resonant frequency

Principally, two of these analogies can be arbitrarily chosen. In practice however, it seems suitable to let energy in one system correspond to energy in the other and to let pressure correspond to voltage, since both are potential magnitudes. Starting from these two first analogies the remaining analogies can easily be calculated from simple gas laws and electrical equations.

The air raid shelter will therefore here be regarded as an aerodynamical resonant circuit. The pressure in such a resonant circuit can be calculated from the differential equation

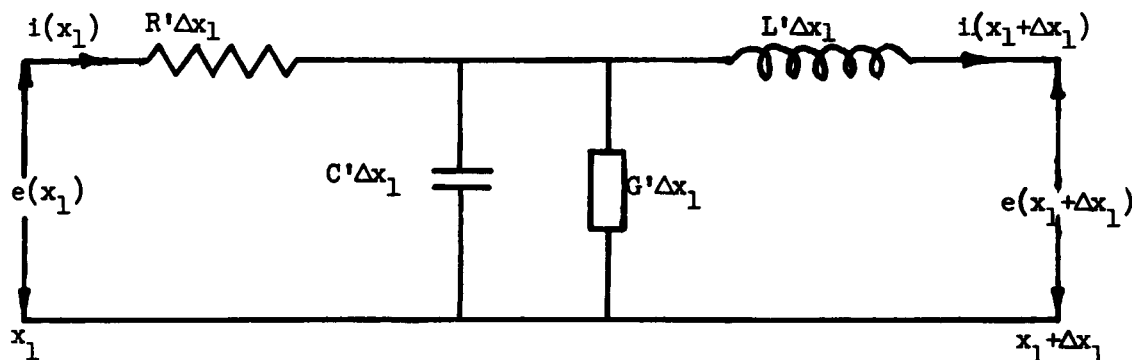
$$\frac{d^2 p}{dt^2} + \frac{R}{L} \cdot \frac{dp}{dt} + \frac{1}{LC} p = \frac{1}{LC} p_2(t)$$

where $p_2(t)$ is the pressure-time relation of the entering shock wave.

The equation has been solved with an analog computer. $p_2(t)$ is the pressure time relation of the shock wave in the shock tube. No formula for the resistance R has been introduced in this investigation. The values of R have been chosen in order to coincide with the experimental records. The curves, which were thus calculated, were compared with the records for $\alpha = 0$. Both curves are shown in Figure 6a and b. It appears from this comparison, that the calculation gives the slow oscillation, but it does not give any information about the superimposed successive shock reflections. It seems however to give rather good information about the value of the maximum pressure inside the shelter model.

Figure 7 shows records when the angle of incidence $\alpha = 90^\circ$. It appears from these figures that the frequency of the oscillation changes with the shelter volume and the entrance length. The overpressure of the incident shock wave is about 1 atm. Figure 8 shows registrations, where the incident shock wave is somewhat stronger (2-3 atm.). From these curves it seems that, for $\alpha = 90^\circ$ the oscillation disappears, when the shock strength increases to about 2 atmospheres.

The above mentioned way of calculating the pressure changes inside a shelter model works quite well in the case, where the volume of the shelter model is large compared to the volume of the entrance. But when the shelter volume is small (or = 0) the formula cannot be used. In order to obtain some possibility to estimate the pressure inside shelters of such shape (e.g. fox-holes) the entrance tube is regarded as an aerodynamic transmission line. The electrical analogies are applied to the shelter model. For an electrical transmission line



the following simple equations are obtained:

$$e(x_1; t) = R' \cdot \Delta x_1 \cdot i + L' \cdot \Delta x_1 \frac{\partial i}{\partial t} + e(x_1 + \Delta x_1; t)$$

$$i(x_1; t) = C' \cdot \Delta x_1 \cdot \frac{\partial e}{\partial t} + G' \cdot \Delta x_1 \cdot e + i(x_1 + \Delta x_1; t)$$

In the limit $\Delta x = 0$ the following equations are obtained. They are compared with the aerodynamical equations

$$\begin{array}{l} \text{Continuity eq.} \quad - \frac{\partial(\rho u s)}{\partial x_1} = S \frac{\partial \rho}{\partial t} \quad \left| \quad - \frac{\partial i}{\partial x_1} = G' e + C' \frac{\partial e}{\partial t} \right. \\ \text{Eulers eq.} \quad - \frac{\partial \rho}{\partial x_1} = \rho(u \frac{\partial u}{\partial x_1} + \frac{\partial u}{\partial t}) \quad \left| \quad - \frac{\partial e}{\partial x_1} = R' i + L' \frac{\partial i}{\partial t} \right. \end{array}$$

The changes in density are regarded as small. $\rho = \rho_0(1 - \psi)$ where ρ_0 is constant and ψ varies. ψ is introduced in the equation above. If

$u \frac{\partial u}{\partial x} \ll \frac{\partial u}{\partial t}$ the following equations are obtained

$$\begin{array}{l|l} -\frac{\partial(Su)}{\partial x_1} = s \frac{\partial v}{\partial t} & -\frac{\partial i}{\partial x_1} = G'e + C' \frac{\partial e}{\partial t} \\ -\frac{\partial p}{\partial x_1} = \rho_0 \frac{\partial u}{\partial t} & -\frac{\partial e}{\partial x_1} = R'i = L' \frac{\partial i}{\partial t} \end{array}$$

From this comparison it appears, that the electrical and aerodynamical equations are not quite corresponding. The electrical equations contain the terms $G'e$ and $R'i$, which have no equivalence in the aerodynamical formulae.

The conductance term $G'e$ is negligible in these investigations and will therefore be omitted. The resistance term $R'i$ is not negligible as can be seen in Figures 3-7. The problem will here be solved using electrical symbols. In spite of the lack of a resistance term in the aerodynamical formula a resistance term $R'i$ is introduced. Eliminating i between the two electrical formulae above gives

$$\frac{\partial^2 e}{\partial x_1^2} = L'C' \cdot \frac{\partial^2 e}{\partial t^2} + R'C' \frac{\partial e}{\partial t}$$

(= the telegraphist's equation).

Boundary conditions:

1. $e = e_0$ and $i = 0$ for $t \leq 0$ and all x_1
2. $e - e_0 = E(t)$ for $t \geq 0$ and $x_1 = 0$
3. $i = C' \cdot \frac{\partial e}{\partial t}$
or $i = 0$ for $x_1 = l$

The function $E(t)$ is the pressure-time-curve from a detonating charge. It is supposed to have the following form:

$$e - e_0 = (\hat{e} - e_0) \cdot e^{-\alpha t} \left(1 - \frac{t}{T'}\right) \quad \text{where}$$

e_0 corresponds to the atmospheric pressure

\hat{e} corresponds to the shock front pressure

e base of the natural log system

T' duration of the overpressure

This differential equation was solved with a digital computer. Some of the curves, which were obtained in this way, are shown in Figures 9a-9d together with the entering shock wave. The pressure is here measured with the entering shock front pressure as unit and the time is measured with the shock front travel time a' along the entrance tube as unit. Figure 9a shows four pressure curves obtained for different duration of the entering shock wave. Shelter volume $V = 10 \times$ entrance tube volume. Entrance tube length $l = 10 \sqrt{\text{entrance area}}$. Figure 9b shows a curve obtained at the bottom of an entrance tube, when the shelter volume $V = 0$. Figure 9c shows four pressure curves obtained in a shelter for different values of shelter volume V . Figure 9d shows four curves obtained at the bottom of an entrance tube, when $V = 0$. The duration of the entering shock wave has different values in the four curves.

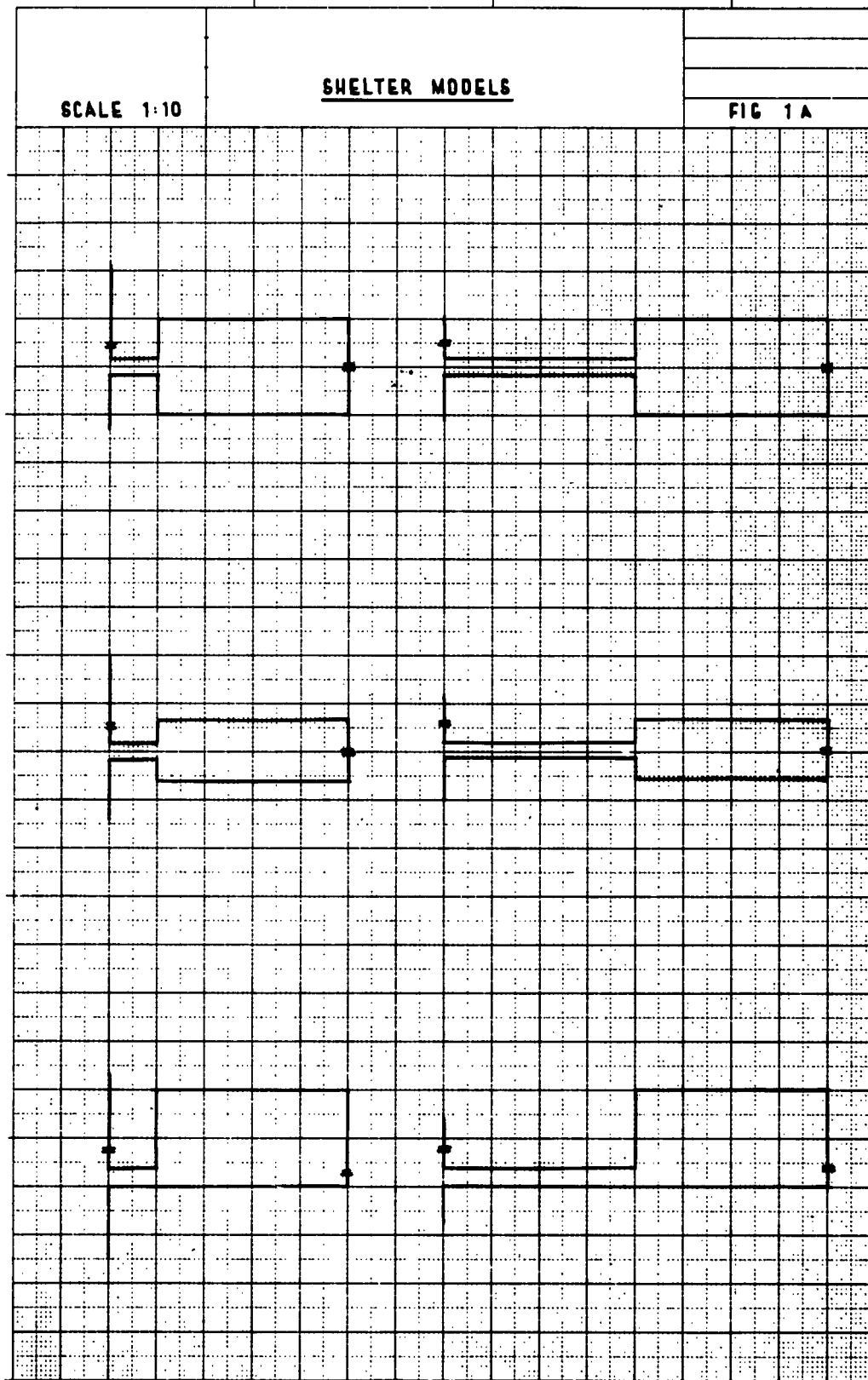
Figure 10 shows comparison between calculated curves and records.

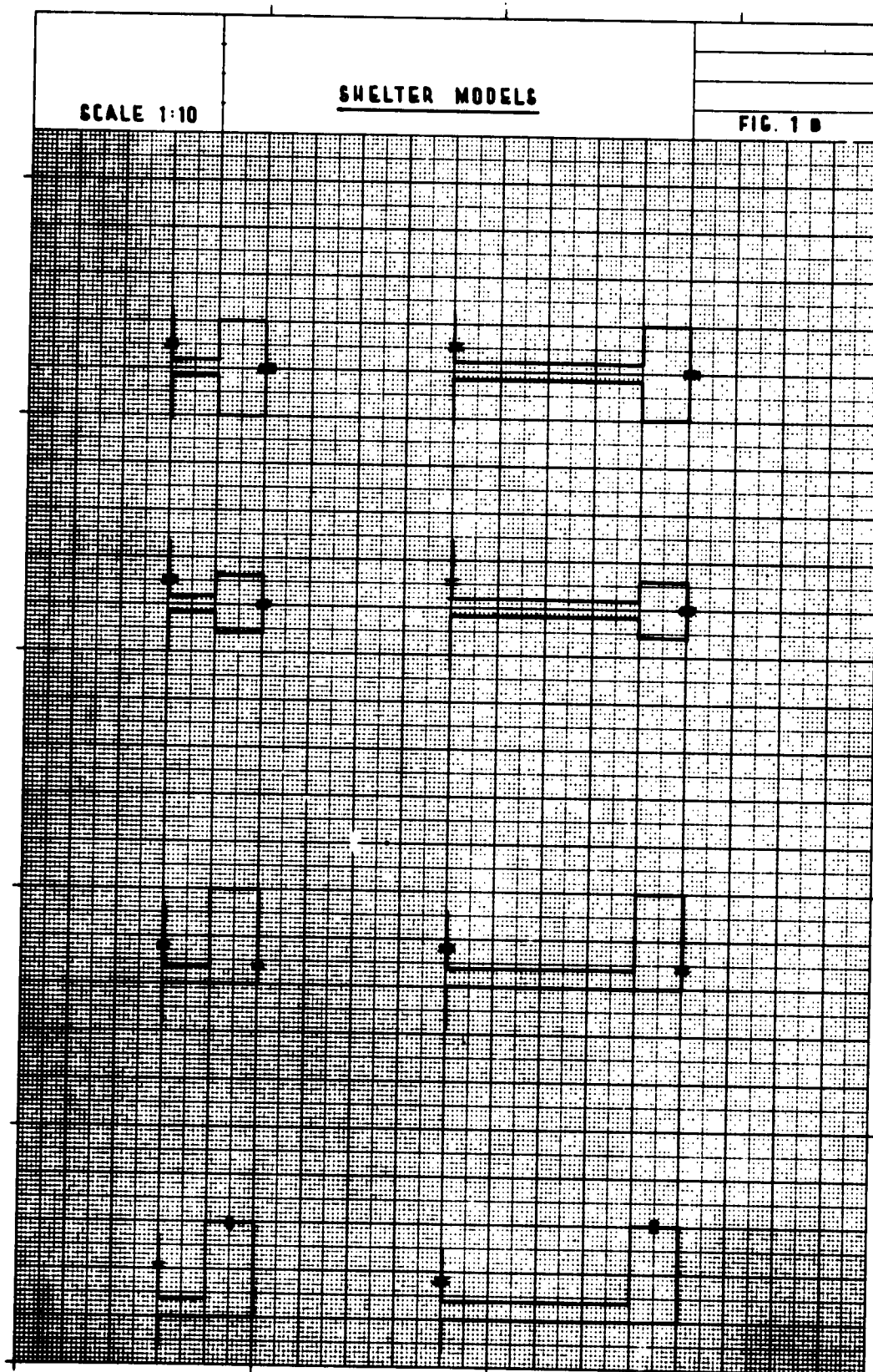
Figure 11 shows pressure records at the bottom of an entrance tube, when $V = 0$ for two different lengths of the entrance tube. (14, 4 cm and 36 cm).

SCALE 1:10

SHELTER MODELS

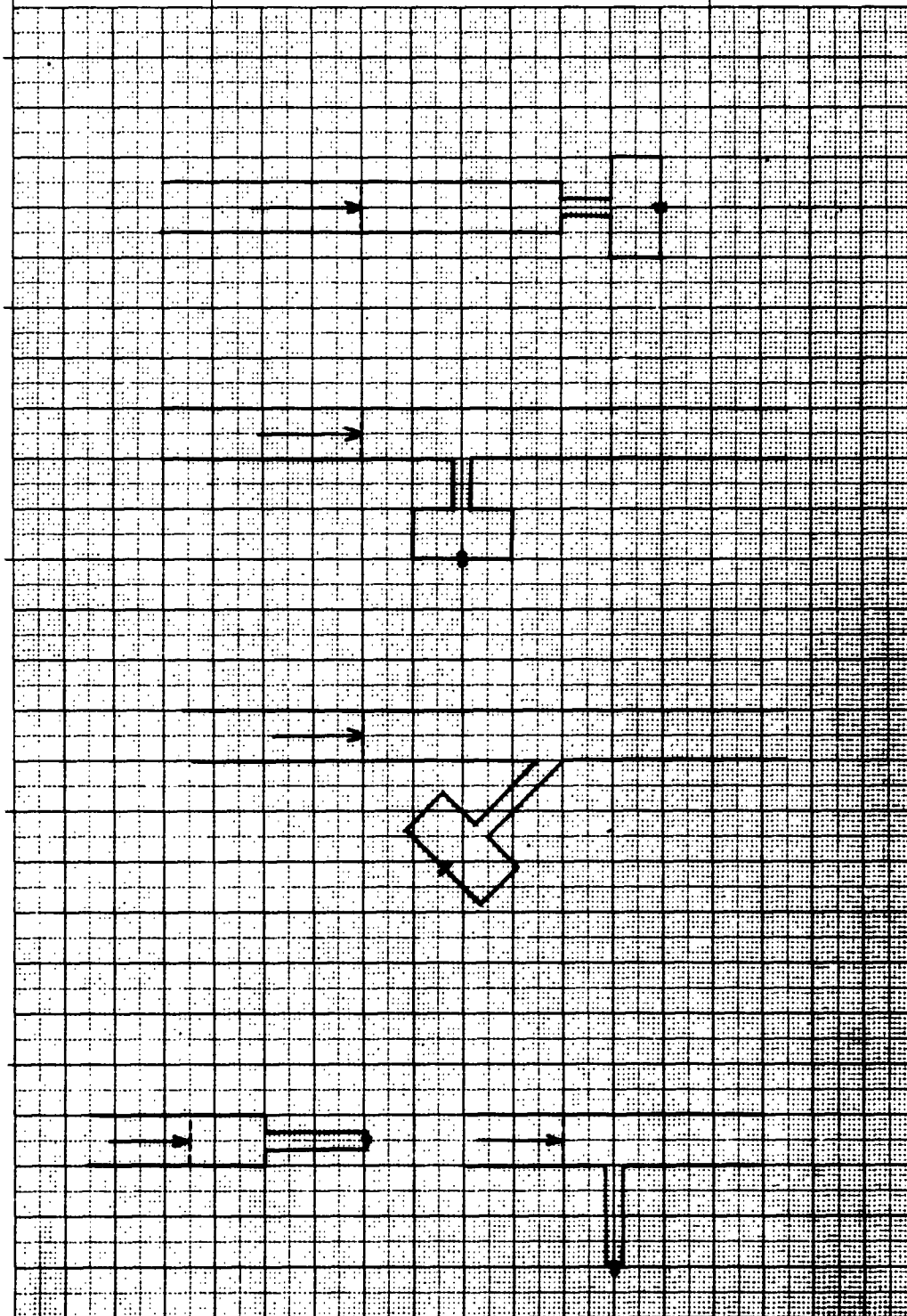
FIG 1A



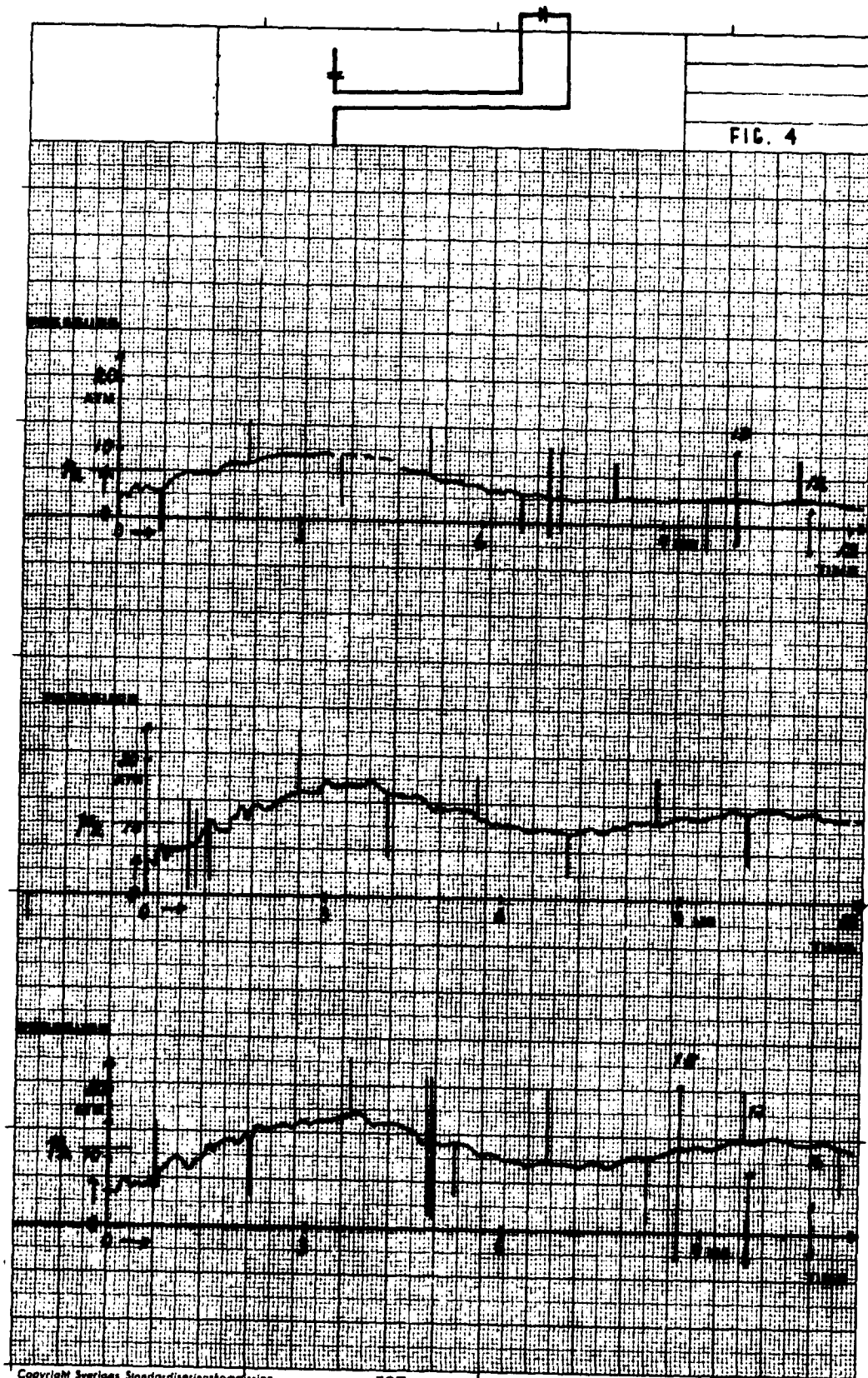


SHELTER MODELS ATTACHED
TO THE SNODE TUBE

FIG. 2







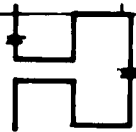
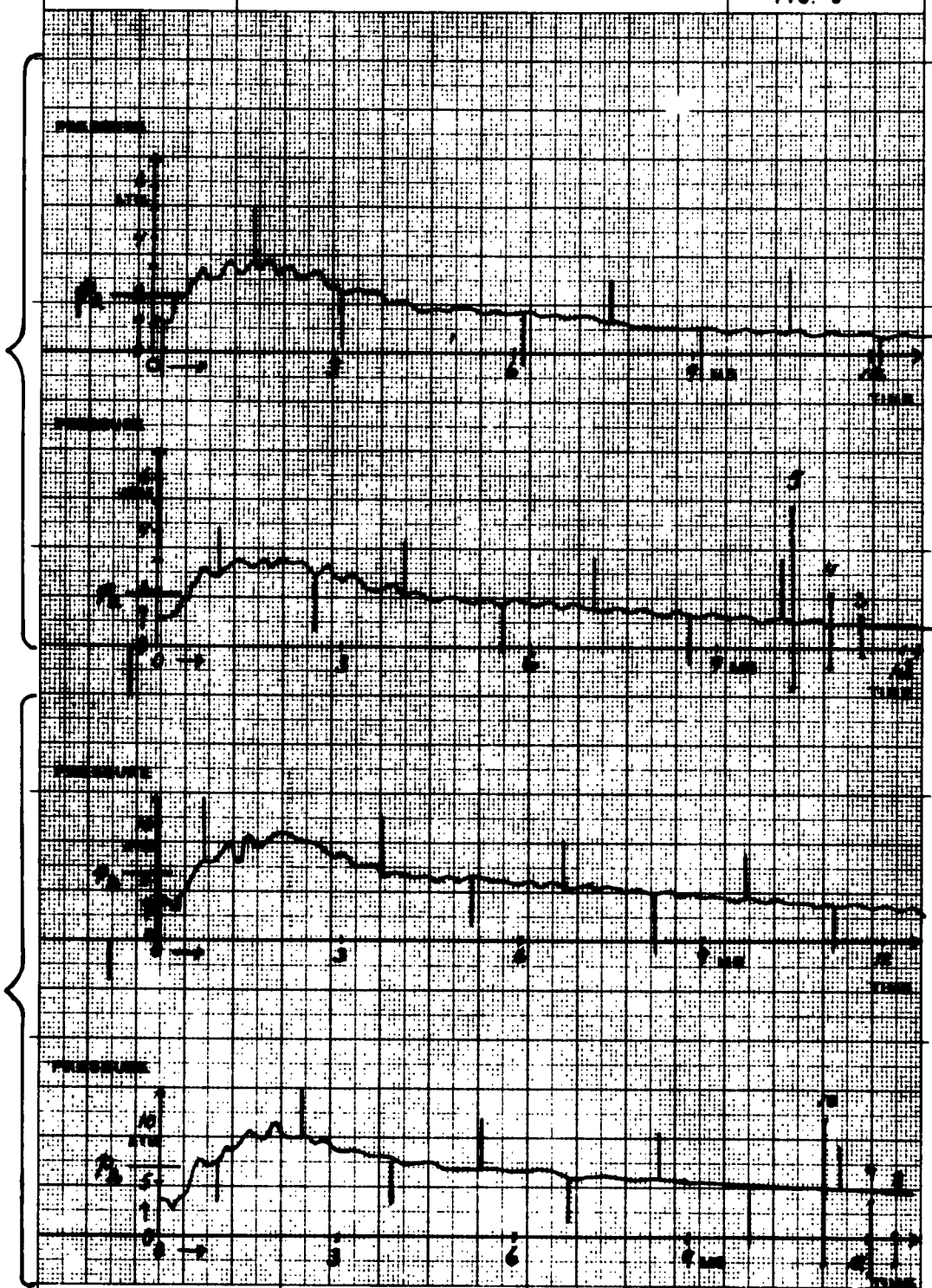
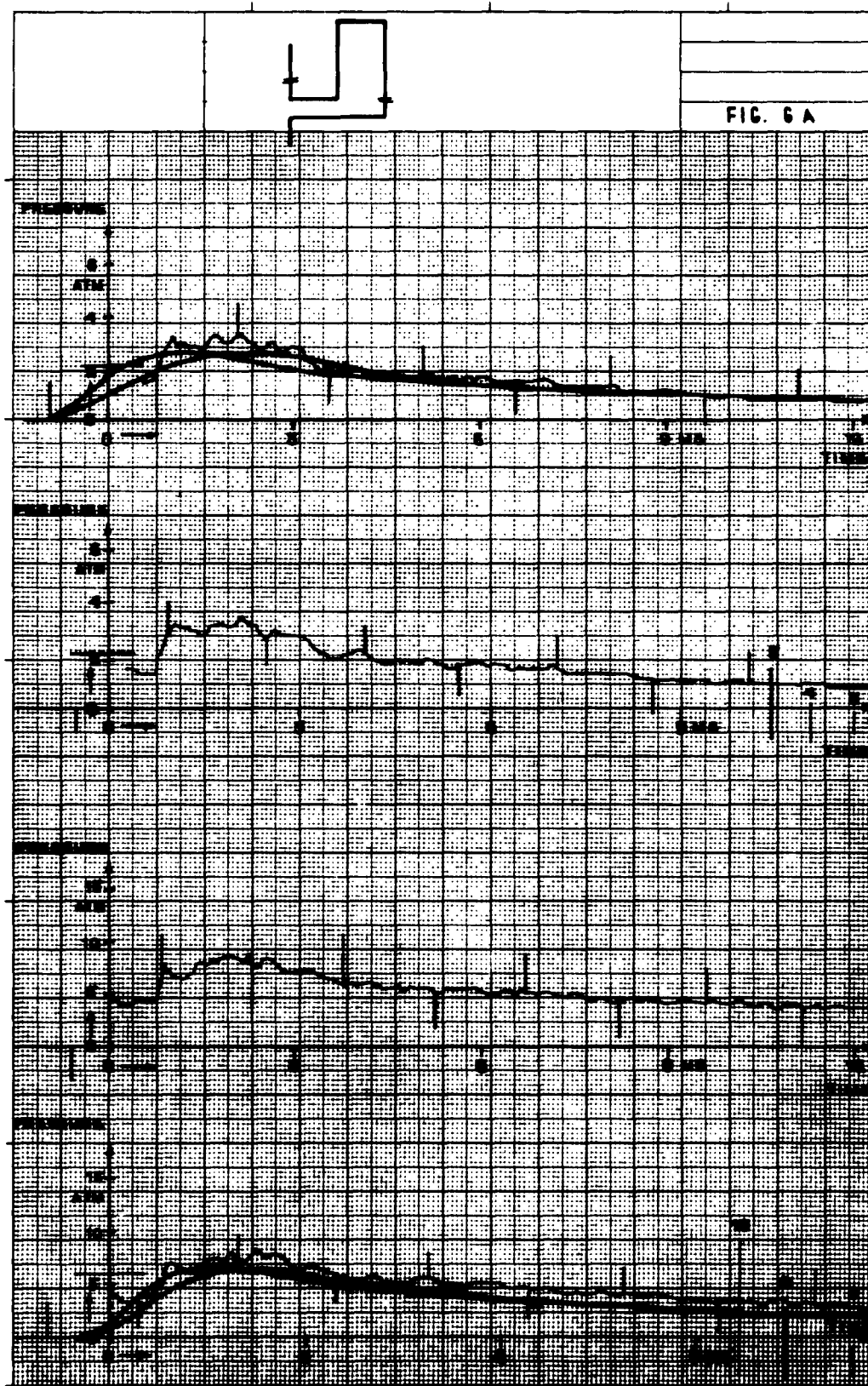


FIG. 5





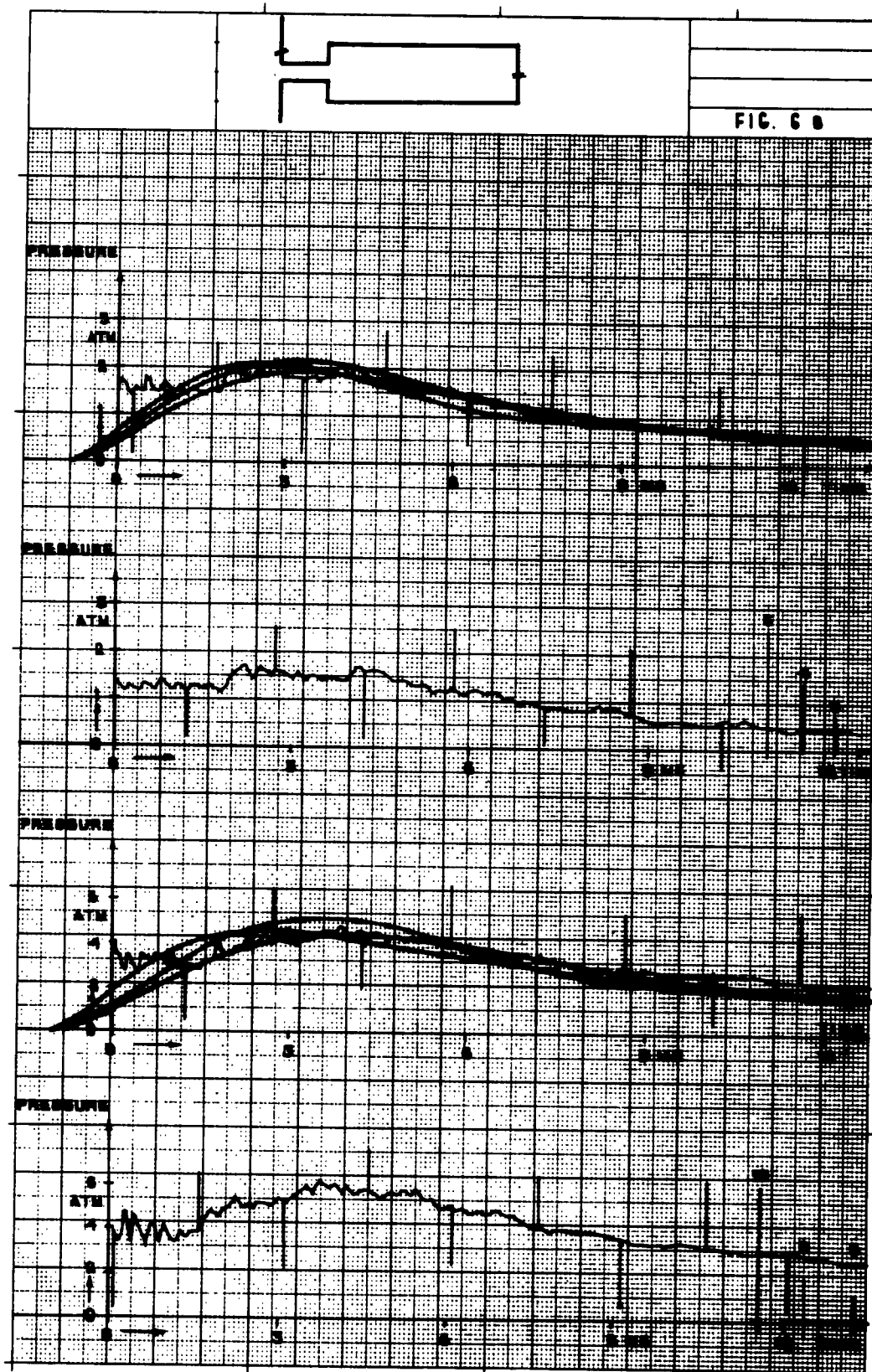
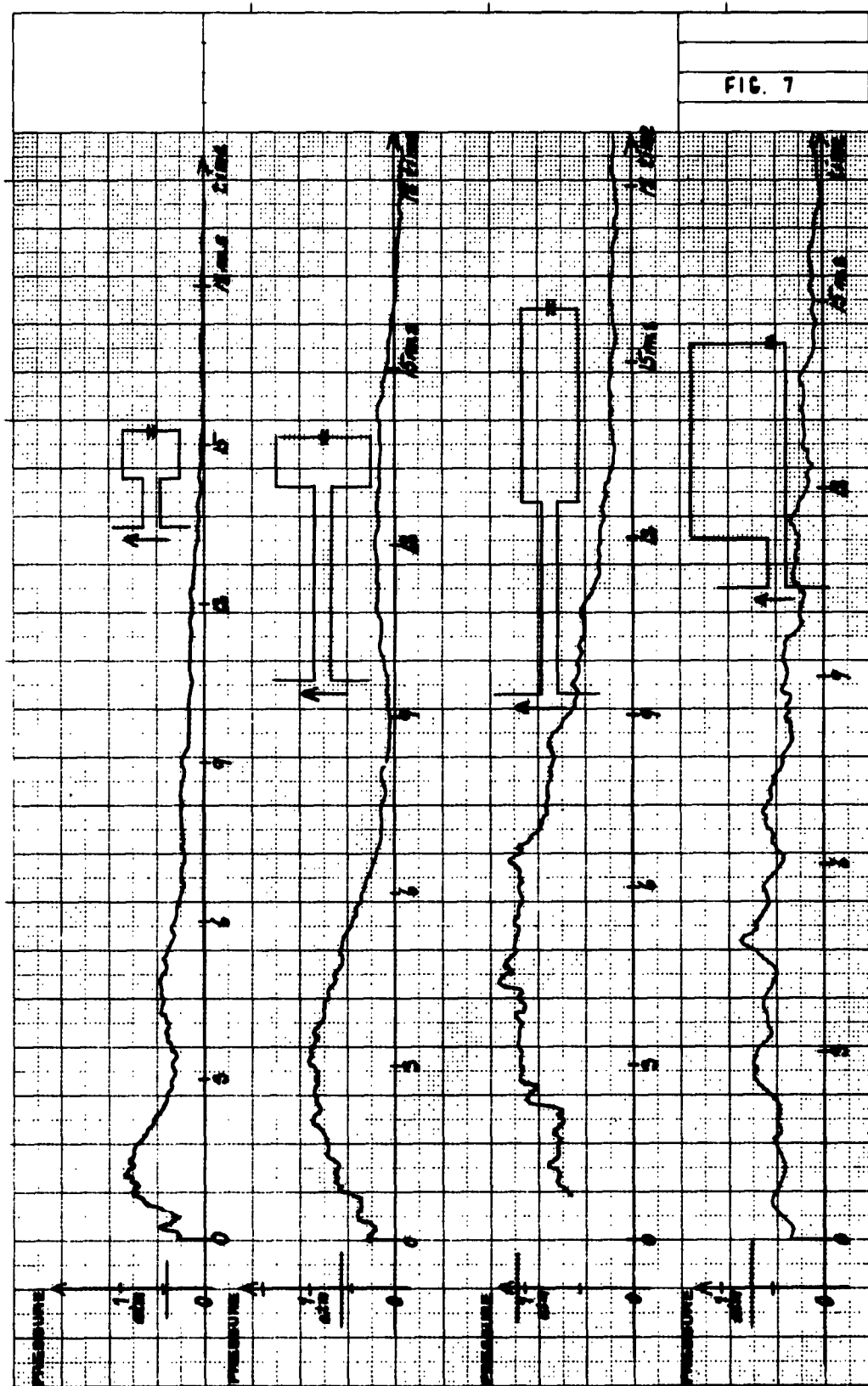


FIG. 7



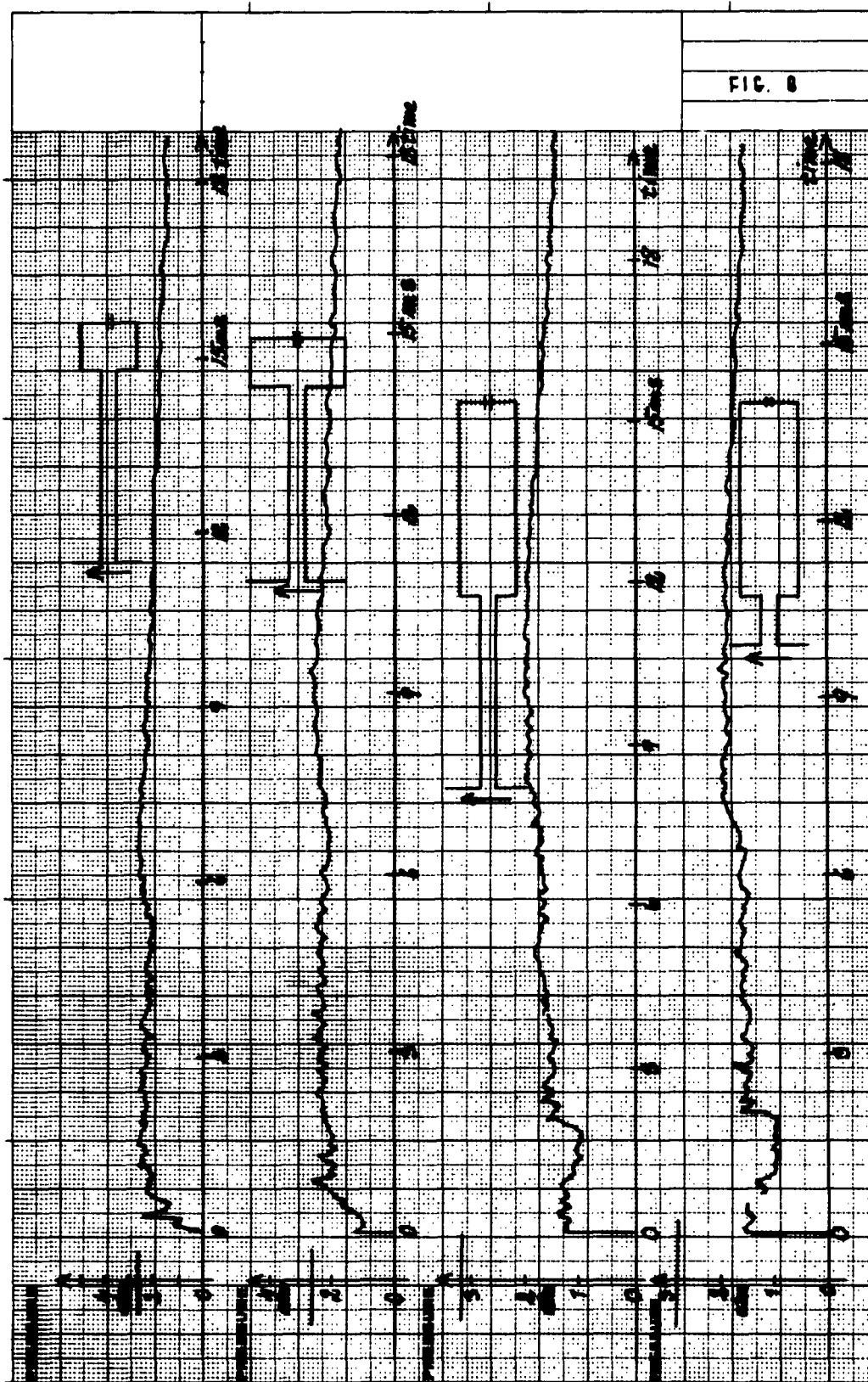


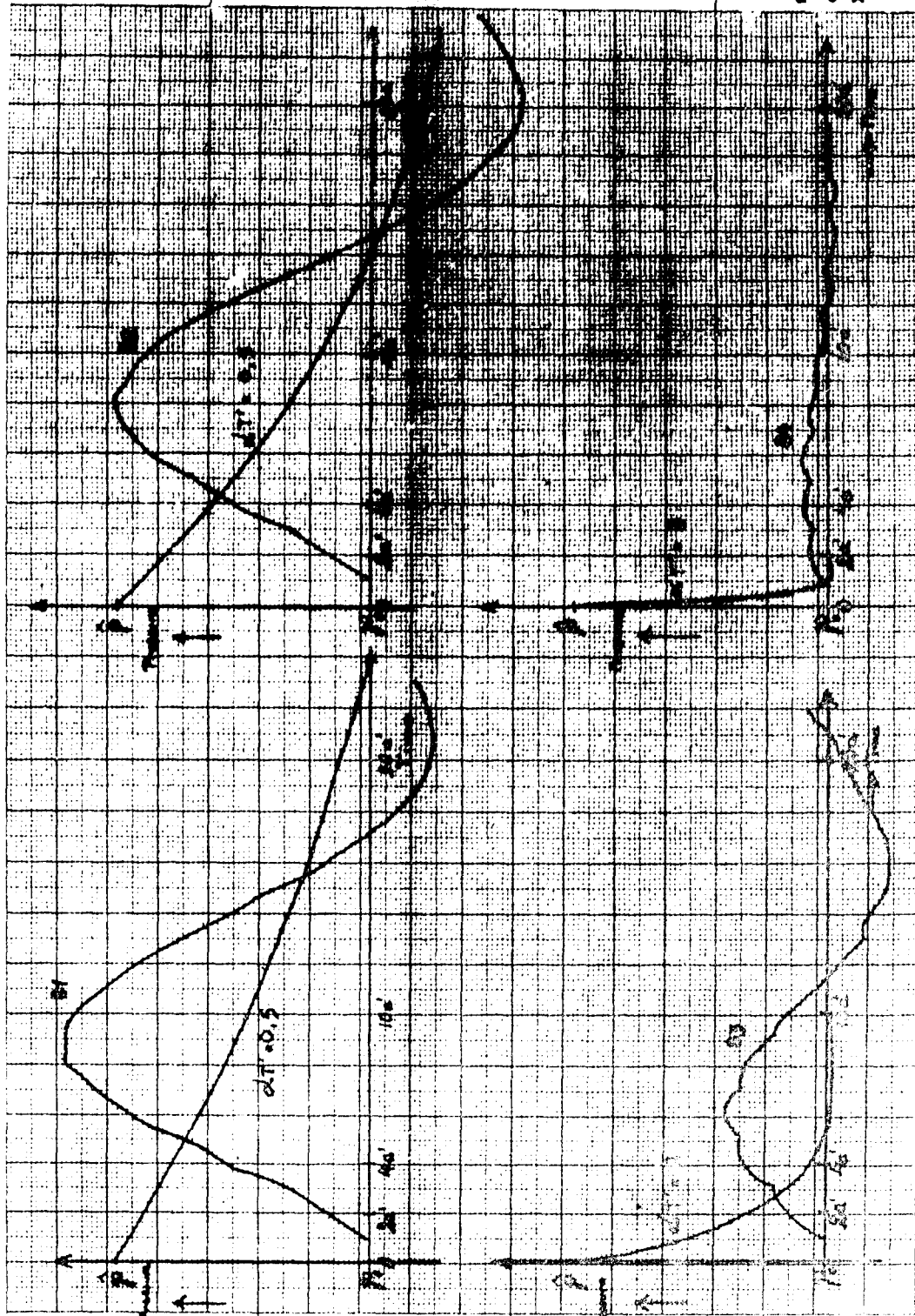
FIG. 8

$V = 10 \text{ s l}$

$l = 10 \sqrt{s}$

Pressure Relationships in a Shelter as Computed on BESK. Shelter volume = V, Entrance tunnel length = l, Entrance tunnel x-sect. area = 1
Attenuation, D = 16.2 %

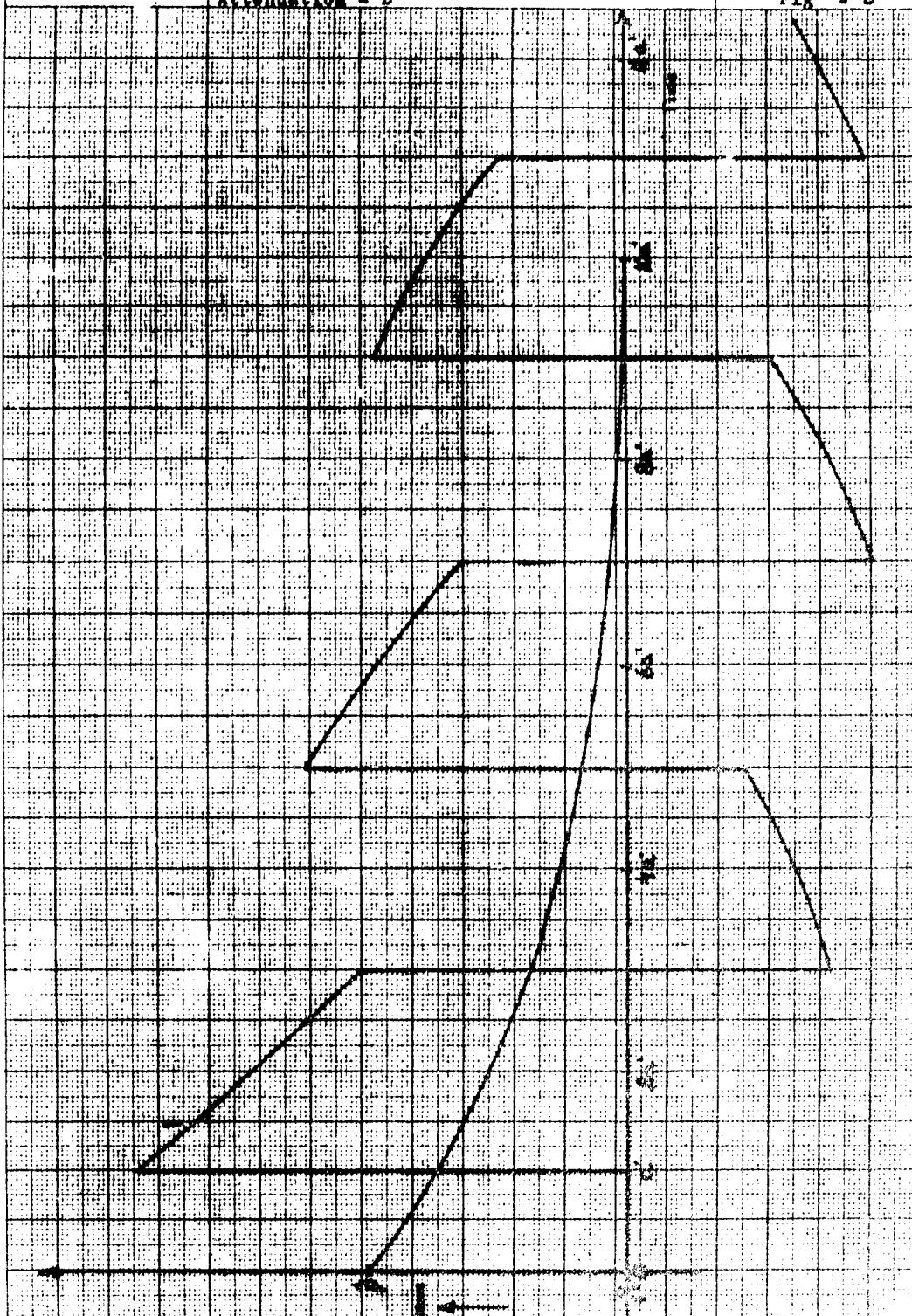
Fig 9 A



$D = 1,64 \%$
 $\alpha' T' = 2$

Pressure Relationship at Bottom of a Fox-
 Hole as Computed on BESK, Shockwave Transi-
 time from fox-hole opening to its bottom =
 α'
 Attenuation = D

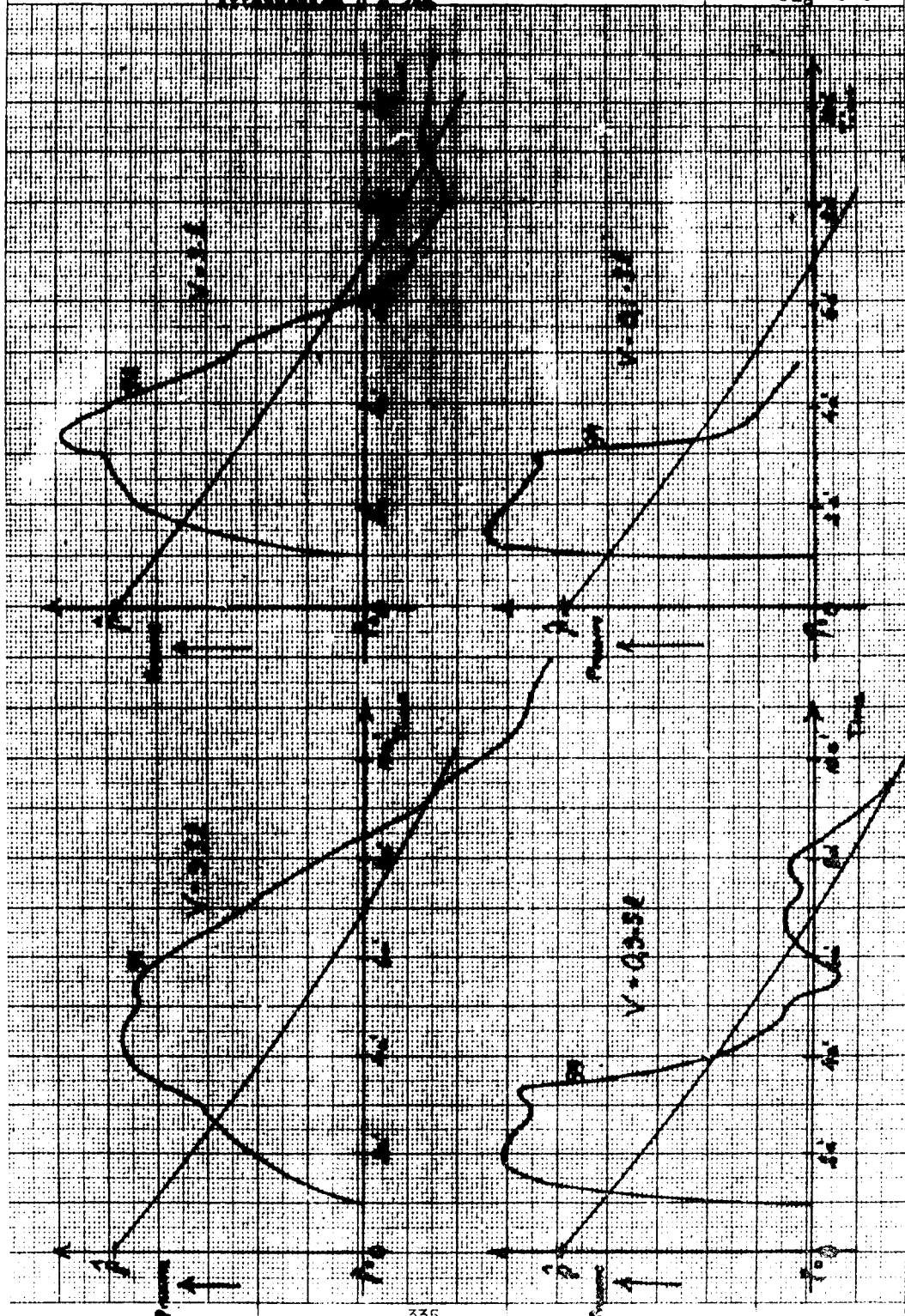
Fig 9 B



$\alpha T' = 0.143$

Pressure Relationships in Shelter as Computed on BE3K. Shelter volume = V . Entrance tunnel length = 1. Entrance area = 3. Shock wave transit-time for distance 1 = a' . 4 different shelter volumes V . Attenuation $D = 24\%$

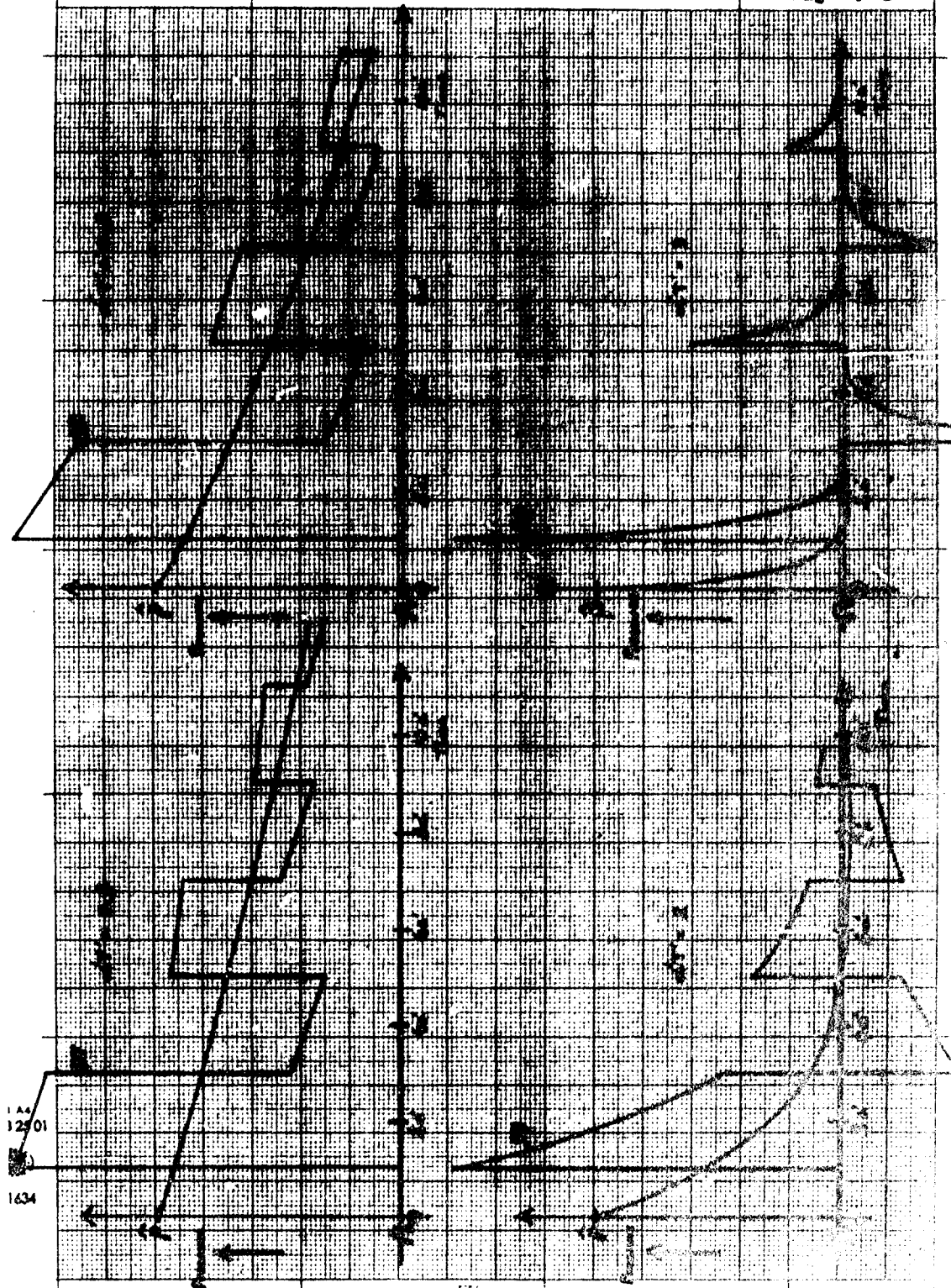
Fig 9 C



D = 15 %

Pressure Relationship at Bottom of a Fox-hole as Computed on BESK. Shock-wave Transit-time from Fox-Hole Opening to its Bottom = a' . 4 different Shock-Wave Durations. Attenuation = D

Fig 9 D



Comparison between experimental and
computed curves.

Fig. 10.

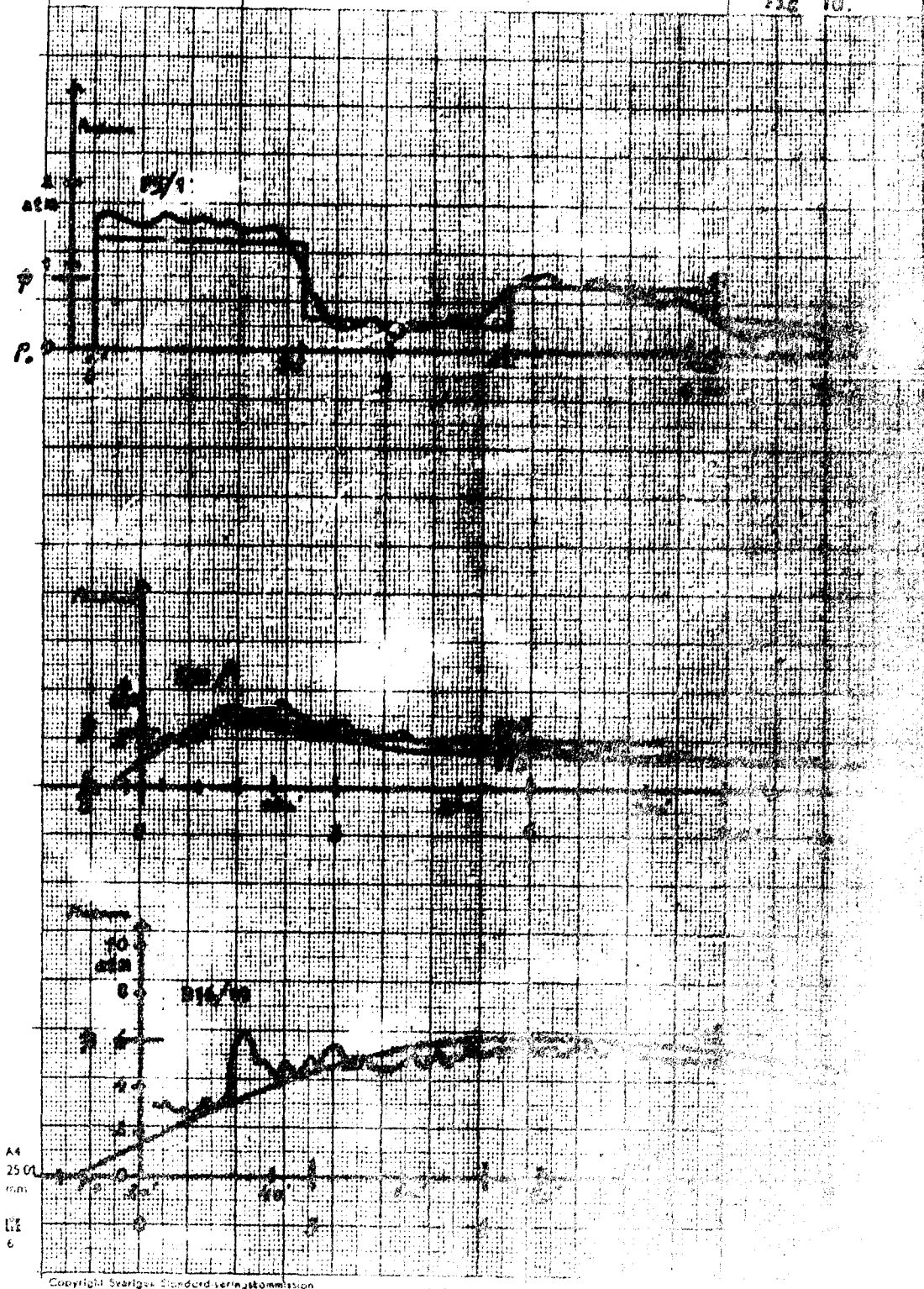
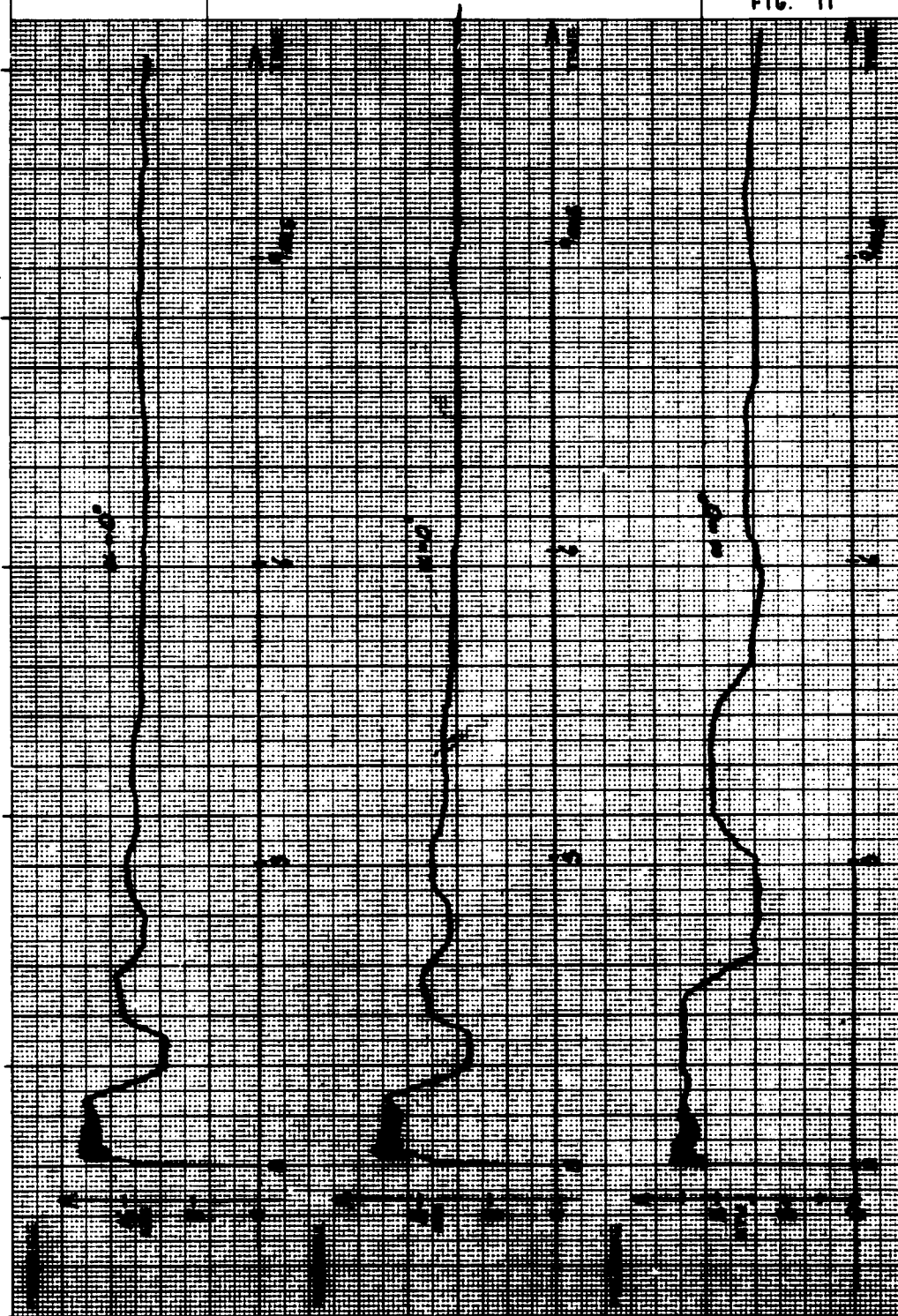


FIG. 11



SHOCK WAVE DECAY IN TUNNELS

Robert O. Clark
Ballistic Research Laboratories

As a classical shock wave advances down a tunnel, two processes act to decrease its pressure. One is the shock wave expansion in one dimension, and the other is due to viscous interaction between the wave and the tunnel wall.

The following equation accurately describes the shock front pressure versus travel distance of a classical shock wave in a straight uniform tunnel.

$$P_{21} - 1 = (P_{21}' - 1)e^{-k'x \left[\frac{7 S(1 + 2\epsilon n)^2}{A} + \frac{1}{t} \right]} \quad (1)$$

This equation is a practical solution of a differential equation which was devised in part from theory and in part from experiment. The part involving viscous decay is based mainly on experimental results, and the part involving expansion decay is based on a theory. The variables are shock front pressure ratio P_{21} at the distance traveled x . The prime pertains to conditions at $x = 0$. The quantity k' is defined by

$$k' = \frac{1}{U_2'} - \frac{1}{u_2' + a_2'}, \text{ for } P_{21}' < 2$$

$$k' = 11 \times 10^{-5}, \text{ for } P_{21}' > 2$$

where

U_2' is shock front velocity.

u_2' is shock front flow velocity.

a_2' is shock front sound velocity.

The function k' is a ratio of changes in the shock front with respect to time, to changes with respect to distance. Other parameters are physical dimensions of the tunnel and of roughness of the tunnel wall.

A is cross sectional area of tunnel.

S is the perimeter of A.

The constant (7) has dimension of velocity.

The function $(1 + 2 \epsilon n)^2$ is a roughness coefficient where ϵ is the mean height of the protuberances and n the number of them per unit length. The product ϵn is dimensionless, and approaches a maximum rough wall value of $1/2$. The maximum value is based on the idea that as the number of protuberances per unit length increases beyond $1/2\epsilon$, the roughness begins to approach the smooth wall again.

The time \bar{t} is the mean time intercept for the range x as described by the equation,

$$\bar{t} = t_0 + \frac{t_0 x}{2\tau_0 a_1} \left(1 - \sqrt{\frac{7}{1 + 6 P_{21}}} \right), \quad (2)$$

where t_0 is the time intercept at $x = 0$ of the wave front tangent line. τ_0 is the total positive wave duration at $x = 0$, and a_1 is the sound velocity ahead of the shock front.

The proof of the decay equation will be seen in its comparison with experimental results. For this purpose a broad variation of experimental conditions were put to the test; these are illustrated in Figure 1. The lines on the graphs on the left side of Figure 1 show the relative initial slope of the individual shock wave forms tested. Opposite each graph is the sketch of the tube or tunnel through which the wave travels. The numerical values associated with these test conditions are tabulated in Table 1. Here the tests are grouped according to emphasis on the effect of variation of an individual variable or parameter. Since these were all done on cylindrical tunnels, the diameter substitution $\frac{A}{S} = \frac{D}{4}$ can be made.

Certain relationships between viscous decay and expansion decay are of interest. The ratio of the term in the decay equation which accounts for viscous decay to the terms which account for total decay at $x = 0$ is,

$$R = \frac{7 \frac{S}{A} (1 + 2 \epsilon n)^2}{7 \frac{S}{A} (1 + 2 \epsilon n)^2 + \frac{1}{t_o}} \quad 100\% . \quad (3)$$

For a smooth wall cylindrical tunnel, equation 3 reduces to,

$$R = \frac{\frac{28 t_o}{D}}{\frac{28 t_o}{D} + 1} \quad 100\% \quad (4)$$

Figure 2 is a graph of equation 4. The curve is sectioned off where most of the experimental work was done. Also, a point is shown which represents a probable prototype situation of a two second positive duration wave applied to a .28 foot diameter tunnel.

This analysis of the scaling situation between models and prototype shows that the probable prototype is in the most convenient model range in scale and gives support to the value of applying the decay equation to full scale tunnels.

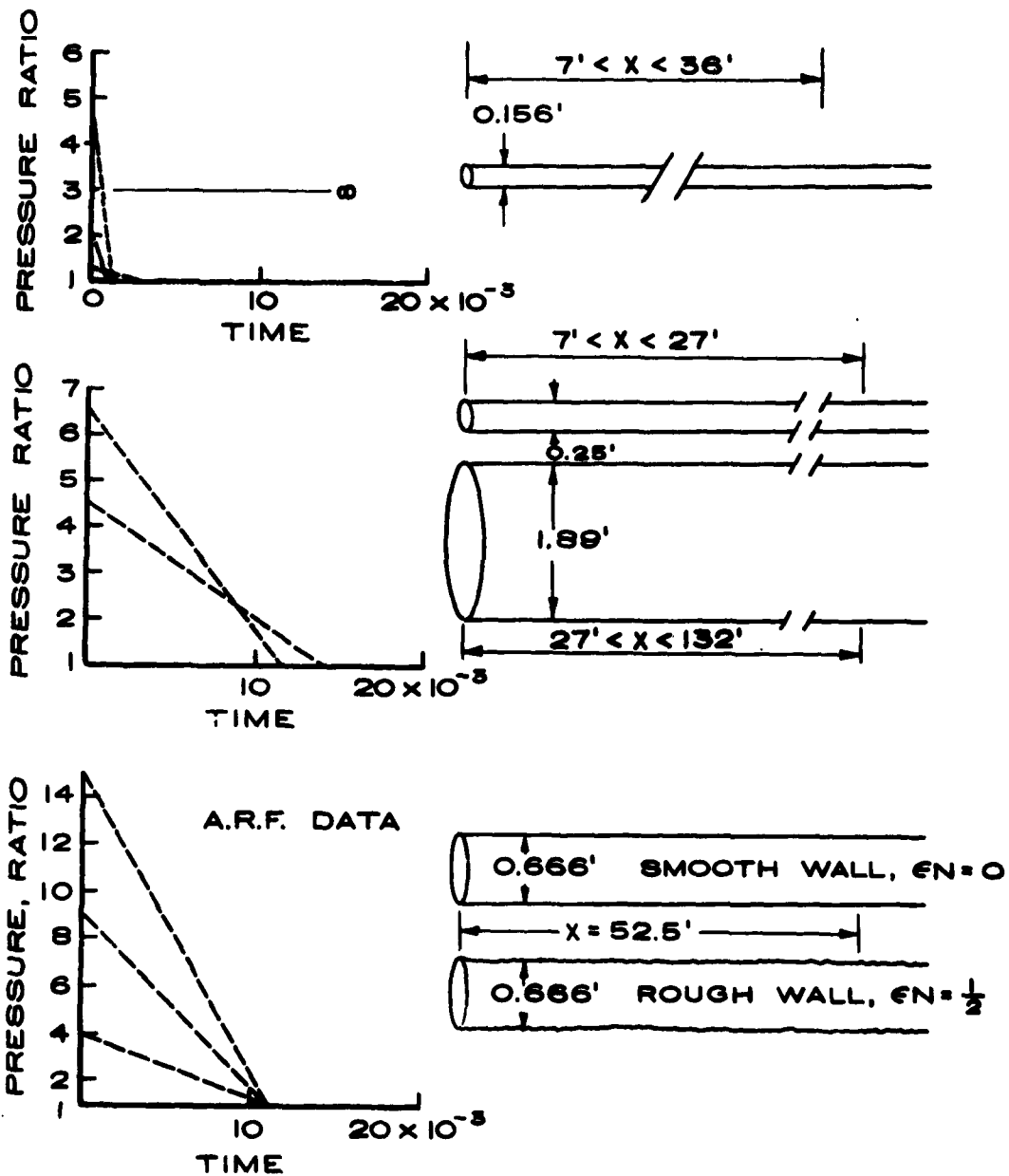


FIG. 1 - SKETCH TO EXPRESS VARIATION
OF EXPERIMENTAL CONDITION

	t ₀	D	X	PRESSURE RATIO		
				P ₂₁ ' MEASURED at X = 0	P ₂₁ MEASURED at X	P ₂₁ CALCULATED at X
	TIME INTERCEPT (SEC.)	TUBE DIA. (FT.)	DISTANCE TRAVELED (FT.)			
CHANGE IN DISTANCE	1.16 x 10 ⁻³	0.156	18	4.5	2.162	2.094
	1.16 x 10 ⁻³	0.156	36	4.5	1.589	1.599
LOW PRESSURE	2.40 x 10 ⁻³	0.156	7	1.480	1.328	1.332
	0.88 x 10 ⁻³	0.156	18	1.494	1.229	1.227
	2.70 x 10 ⁻³	0.156	18	1.229	1.181	1.172
LONG DURATION	∞	0.156	23.4	4.85	4.175	4.150
	∞	1.890	50.0	3.05	2.850	2.890
	48 x 10 ⁻³	1.890	20.0	3.09	2.850	2.820
CHANGE IN DIAMETER	14 x 10 ⁻³	1.89	.27	4.61	3.650	3.885
	14 x 10 ⁻³	0.25	27	4.61	3.145	3.145
	14 x 10 ⁻³	1.89	132	4.61	2.700	2.805
	14 x 10 ⁻³	0.25	7	4.61	4.100	4.150
	11.5 x 10 ⁻³	1.89	27	6.49	5.075	5.225
	11.5 x 10 ⁻³	0.25	27	6.49	4.110	4.150
CHANGE IN WALL ROUGHNESS A. R. F. DATA	SMOOTH WALL εn = 0	0.666	52.5	4.0	2.75	2.66
	11 x 10 ⁻³	0.666	52.5	9.2	5.70	5.70
	11 x 10 ⁻³	0.666	52.5	15.5	8.90	9.50
	ROUGH WALL εn = 1/2	0.666	52.5	4.0	2.10	1.84
	11 x 10 ⁻³	0.666	52.5	9.2	3.40	3.28
	11 x 10 ⁻³	0.666	52.5	15.5	4.90	5.08

TABLE I
COMPARISON OF DECAY EQUATION TO EXPERIMENT

SCALING RELATIONSHIP

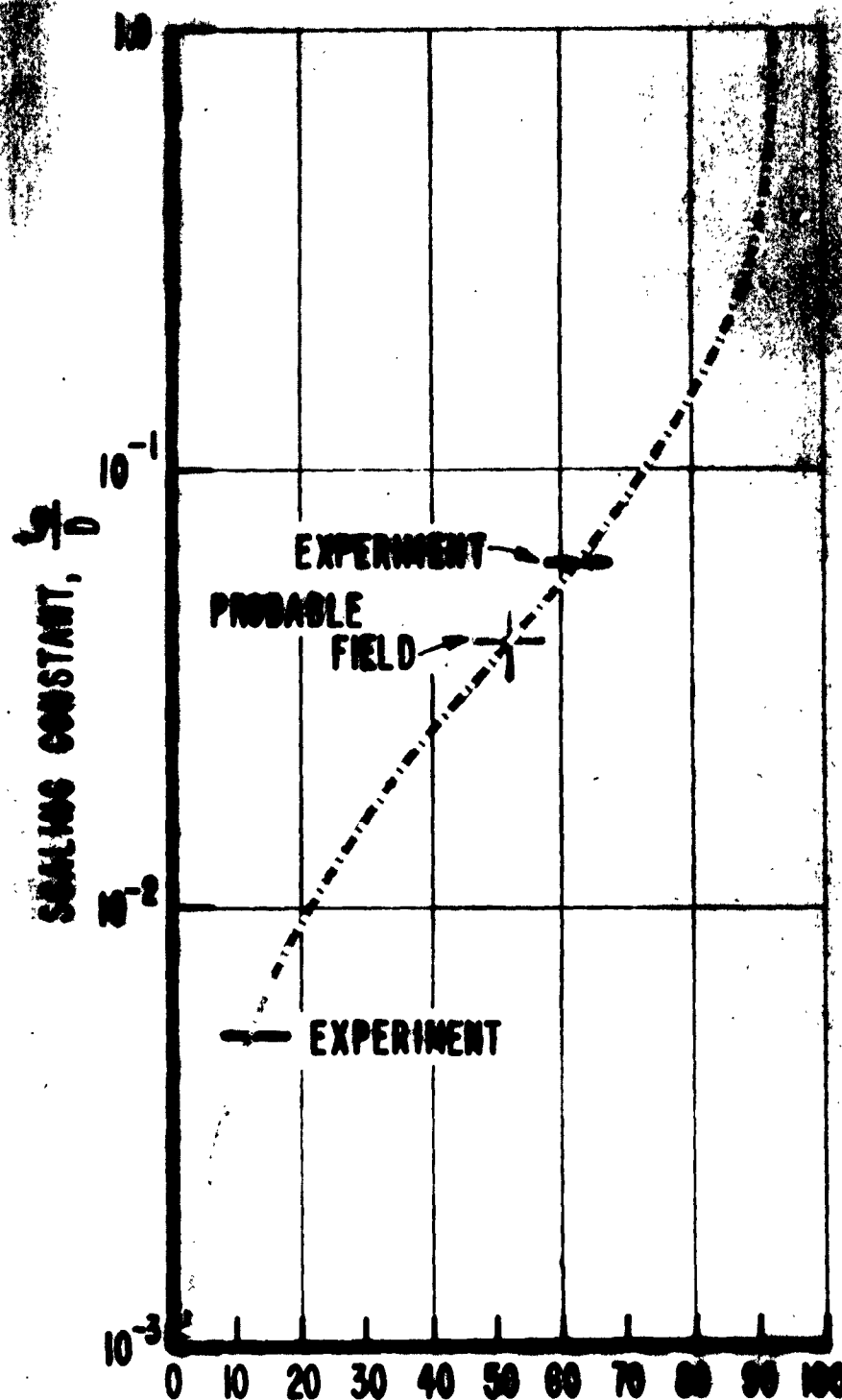


FIG. 2. R - PERCENT OF TOTAL DECAY WHICH IS DUE TO VISCOUS DECAY

SHOCK TUBE BLAST LOADING ON SCALED MODEL NAVAL VESSELS

T. H. Schiffman
E. V. Gallagher
Armour Research Foundation

This program was designed jointly by representatives of the David Taylor Model Basin and the Armour Research Foundation, and was intended as a first step in the development of a general load prediction method for ships. It was undertaken in order to obtain information for ship designers, regarding the nature of the air blast loading on three typical naval vessels.

The loads were to be expressible as an input function for response calculations. This basically means determining the pressure-time history at each point on the ship. However, for practical purposes, only the pressure-time history on a limited number of point need be known, if each point properly represents a large or important tributary area.

The effects of surging of the water, which could be expected to occur in the vicinity of a full-scale vessel, were not included, since this program utilized solid-metal, scaled models rigidly bolted to the steel test plate of the shock tube. It was assumed that a flow field existed comparable to that which could be expected to exist in the neighborhood of a ship in open water with no other significant obstacles to the flow.

MODELS

Three basic models were treated in this program. These were: (1) the transport, (2) the destroyer, and (3) the aircraft carrier. Photographs of these models are shown in the figures. However, a few general comments about the models will be given first.

Each of these models was a simplified scale model of a full-scale ship, and each was approximately 40 inches long. The 40-inch length of the model was chosen as a compromise between (1) the model small enough

to eliminate excessive wall effects resulting from reflections of the shock wave between the model and the wall of the shock tube, and (2) the model large enough to allow for sufficient scaling detail of various portions of the ship and for installation of the gages. (The gages are cylindrical, 1/4 inch long by 1/4 inch in diameter.) Since the lengths of the three full-scale prototype ships were not the same (i.e., a full-scale aircraft carrier is longer than a full-scale transport vessel), the scale factors required to yield shock tube models 40 inches long varied for each of the three ships. The over-all lengths of each of the ships and the corresponding scale factors for the shock tube models are listed in Table 1.

A brief breakdown of the number of gages utilized on the various portions of the three ships is given in Table 2, and the locations are shown in the photographs.

Figure 1 shows a photograph of the transport model. The model consisted of four basic geometric components: (1) the hull block, (2) the main deckhouse, (3) the forward deckhouse, and (4) the rear deckhouse. The gage locations are indicated by darkened dots on the photograph. For each gage on the side of the vessel which is visible in the photograph, there is a corresponding gage on the opposite side of the vessel, similarly located, which is not visible in this photograph. The important geometric irregularities of shape which influence the loading of the model vessel are observable. These are: (1) the sides of the hull block are vertical near mid-ship but slope inward and downward at the fore and aft portions of the hull, so as to create a possible re entrant corner for trapping of the shock front between the hull and the test plate. Multi-reflections of the shock front between these two surfaces are expected to cause an increase in the magnitude and duration of the peak pressures. These quantitative changes in pressure and duration at various locations on the vessel were not known prior to testing and could not be determined from theory with any reliability; (2) the main deckhouse has overhangs and recesses which are also expected to affect the loading in an unpredictable manner; (3) the forward deckhouse tends to increase the height of the hull

wall locally and should lengthen the period of reflected pressure acting on the hull; (4) the rear deckhouse is stepped in a manner similar to the main deckhouse.

Intuitively, it was felt that the loadings on these deckhouse structures should be similar to those for a simple rectangular block located on a flat plate, which is rather well known for most blast waves. The actual degree of similarity, however, was to be determined experimentally. The geometry of certain portions of this model vessel differed considerably from that of simple geometric shapes, such as blocks and cylinders, for which the loading is known. Consequently, for these portions of the vessel, the loading predictions made before this series of experiments was conducted involved a very high degree of uncertainty. For example, Figure 1 shows that the back of the hull is curved considerably, and the local angle of incidence of the shock tube surface varies significantly within a small locality. Pre-test predictions of the loading in this region could only be based upon educated guesses. Such predictions ranged from about half the incident overpressure to twice the incident overpressure--a range which is inadequate for purposes of predicting response. Although not visible in Figure 1, a gage was placed on this portion of the hull of the ship, and data obtained from this gage permitted fairly accurate prediction of the complete pressure-time history in this region for a wide range of orientations and overpressures.

Figure 2 shows a broadside view of the destroyer model placed in the test section of the shock tube. This model represents the actual geometry of the prototype vessel very accurately. No major simplifications of the geometry of the deck structures were necessary, since the prototype itself had a simple geometry. The hull block, front deckhouse, and rear deckhouse were the main components having gages. The two gun turrets at the front the deck structures and the two circular cylindrical stacks were not instrumented, but were included to simulate the flow obstruction properties of the vessel properly.

Figure 3 shows a top view of the aircraft carrier. The shape of the flight deck is exhibited here. Gages were placed on a thickened part of the overhanging flight deck, just to the rear of the tower, to study the loadings on the top and bottom on the elevators of the flight deck.

Figure 4 shows a broadside view of the starboard side of the aircraft carrier model. As with the destroyer model, the aircraft carrier model has geometry almost identical to that of the prototype. Very little simplification was required to yield a practical model. The tower (or island structure) can be seen at about midship. It consists of two blocks capped with a circular cylinder. It was heavily gaged, and is shown in more detail on a later figure. The flight deck overhangs at the front and back of the hull are visible. The flight deck, supported by sponsons can be seen at midship below the tower.

Figure 5 shows a close-up view of the tower, starboard side sponsons, and deck edge elevator. Four gages, not visible in Figure 5, were located on the deck edge elevator overhang. Two of these gages were on the top and two were on the bottom. From these gages, the top loading, the underside loadings, and the net loading on the elevator were all determined.

ORIENTATION

The orientation, or the angle of incidence between the blast wave and the ship model, is defined in Figure 6. Orientations of the ships to the direction of flow of the blast wave covered the range of zero to 90 degrees, in 30 degree increments. Orientations in the range of minus 90 degrees to zero degrees are, in most cases, accounted for by model symmetry. However, for the aircraft carrier, an orientation of minus 90 degrees was also treated for the same gage positions, in order to investigate the effects of model nonsymmetry.

Since it is possible to interpolate between the values of the angle of incidence for which records have been obtained, the values of pressure and time on the loading curves can be expressed as functions of the angle

of incidence. Thus, curves are obtained for pressure values or time values which are continuous over some interval of θ , such as $-90^\circ \leq \theta \leq +90^\circ$ in some cases, or $0^\circ \leq \theta \leq +90^\circ$ in other cases. This first range corresponds to loading orientations from normal to the starboard side, from normal to the port side, and all orientations of flow from the front of the ship between these two limits.

OVERPRESSURES AND DURATIONS

The treated overpressures varied from 5 to 50 psi; however, most of the data were obtained at overpressures in the range of 5 to 20 psi. A few shots were conducted at the higher overpressures, between 20 and 50 psi, to ascertain the dependence (or lack of dependence) of the important loading quantities upon the initial overpressure level. On the basis of these shots, a reasonable assumption is that the dependence on initial overpressure level could be normalized using only the pressure ratio for pressures from 5 to 50 psi.

TEST PROCEDURE

The models were placed in the test section of the six-foot shock tube, and a predetermined quantity of primacord high explosive was placed at some desired distance (at least 40 feet) from the model and detonated to yield the desired shock strength in the test section. The data were obtained by using barium-titanate pressure sensors in conjunction with the standard piezoelectric gage circuitry. The signals were fed through a preamplifier into oscilloscopes. The oscilloscope traces were photographed by a drum camera, producing a linear trace of pressure-versus-time on the film.

The transport model was treated first. Initial tests were conducted at an angle of incidence of $+90$ degrees (i.e., flow broadside to the ship with the starboard side upstream and the port side downstream). The point pressures at individual gage positions, as well as the average pressures on each side of the ship, were compared with shock tube and full-scale atomic field test data for the average pressure-time variation

on the front and back of a two-dimensional rectangular block. (The two-dimensional rectangular block represented an extreme idealization of the ship hull geometry, and had furnished a basis for prediction of the loading on ship structures¹.) These comparisons indicated that the loadings on the shock tube models of the ships were consistent with the predictions based upon the block model, and provided a link with the vast quantity of previous shock tube data. These comparisons also showed that data from the ship hull and the rectangular block were closely related, but were not exactly the same. The loading on the block clearly could not be substituted for the shock tube data from gages on these ship models, but the comparison was sufficiently close to assure that no major interferences were resulting from wall effects.

After data at the 90-degree orientation were obtained, the model was rotated 30 degrees in the horizontal plane to obtain data at angles of incidence of $\theta = 60$ degrees, $\theta = 30$ degrees, and finally at $\theta = 0$ degrees.

The test procedure used for each of the three vessels were essentially the same. The aircraft carrier model, unlike the transport and destroyer models, was not truly symmetrical. Examination of the pressure-time records for the aircraft carrier indicated that very similar loadings were occurring at points which would be symmetrically located if minor changes in geometry of the vessel were made.

FORM OF THE RAW DATA

The data obtained were in the form of pressure-versus-time line traces on film. A typical example of the film records obtained is shown in Figure 7. A calibration pulse, which makes possible the conversion of ordinates of the traces into pressures, was associated with each trace. This pulse is produced by impressing a known change in voltage in the gage circuit to cause a deflection on the oscilloscope screen. This deflection is called the calibration deflection. The pressure equivalent of the

¹"Proceedings of the Air Blast Conference", Navy Dept., David Taylor Model Basin, Edited by Cdr. Robert. S. Burpo, Jr., UNR and Mary C. Crook, published in April 1958, report C-860 (Confidential)

calibration deflection can be computed from the known circuit properties and the gage constant. A series of dots one millisecond apart, which permitted the conversion of the horizontal scale into time units, also appeared on each film. Four channels of instrumentation were recorded on each of two films, designated as film A and film B. The top gage of film B represents the record of the monitor gage on the shock tube wall. The other seven records represent the pressure-time histories at individual points on the models.

The various traces were then compared with one another, and with the free-stream pressure, to determine where trends existed in the loading. The records exhibited, to varied extents, the distinctive characteristics of the usual two-phase loading schemes. Figures 7 and 8 exemplify this two-phase loading curve. These two phases are the diffraction phase and the pseudo-steady-state or drag phase. The diffraction phase corresponds to the initial period of the loading, when the shock wave engulfs the model and causes comparatively rapid variations in pressure on all of the surfaces. The shape of the loading during this diffraction period is characterized by jagged straight-line segments. The second phase is the drag phase of the loading commencing as soon as the diffraction phase has been completed. The time $t = 0$ for each gage was chosen as the time at which the shock first reached that particular gage.

The diffraction phase of each trace was linearized by replacing the recorded signal with representative straight lines whose points of intersection represent critical values of pressure and time. Figure 8 illustrates the linearization of a typical record.

A smooth approximation to the pressure-time record during the early part of the drag phase was drawn in. The difference between this smooth approximation to the record and the superimposed free-stream static pressure curve represents the drag component of the total loading for the record. The free stream static pressure was measured at the tube wall. An attempt was made to compute drag coefficients on the basis of the

experimental records but it proved infeasible, primarily because the free-stream dynamic pressure could not be measured satisfactorily.

The above process yielded a form of idealized loading scheme for each record, as shown in Figure 9. While this figure shows only three critical points occurring during the diffraction phase of the loading prior to the time t_d , at which time the drag phase begins, as many as five critical points were observed on some of the records.

The pressures were normalized by dividing by side-on pressures evaluated at their respective times of occurrence. They were then conveniently referred to by utilizing the following nomenclature: $p_1 = p(t_1)/p_o(t_1)$, where p_1 is the normalized pressure at the time t_1 , $p(t_1)$ is the pressure of the gage at the time t_1 , and $p_o(t_1)$ is the free stream pressure of the monitor gage at the time t_1 . This allows for the wave shape factor, and permits extrapolation of the data over a wide pressure range.

The time of occurrence of any event on the pressure records depends on the size of the model used, as well as on the velocity of propagation of the disturbance which caused the event. This disturbance velocity is taken as the shock speed (U). Thus, critical time values were scaled linearly with model size and shock speed. For an event which occurs at the critical time t on the shock tube model of length L , when subjected to an overpressure having velocity U , new time values t' corresponding to a geometrically similar vessel of length L' , loaded at an overpressure having a velocity of propagation U' , can be computed simply by multiplying the value of t by the factor $(L'U/LU')$, to obtain $t'_1 = t_1 (L'U/LU')$. Since the results of this study are intended to be used by designers of full-scale ships, the units chosen have time dimensions corresponding to a full-scale ship of the dimensions shown in Table 1. In this program, the time values have been expressed for a shock speed corresponding to an arbitrarily selected 10 psi initial overpressure. Conversion to other ship sizes and to other shock velocities can easily be accomplished, using the scale factor $(L'U/U'L)$.

Once the records had been analyzed in the fashion discussed above, the pressure ratios and critical-time values were tabulated for each gage position with various angles of incidence, θ . The values were then plotted using Cartesian coordinates, with θ as the abscissa. This type of plot is illustrated in Figure 10.

This figure shows that the number of critical points in the diffraction phase of a gage record could well vary with the angle of incidence. Each of the three typical schematic pressure-time curves of Figure 9 are labeled to indicate the corresponding range of θ in Figure 10.

SUMMARY

Figure 10 is typical of the results of this program. Each gage on each of the three models yielded a plot similar to that of Figure 10. The shapes of the curves varied widely for different gages and different models, corresponding to the different loading phenomena which occurred. This vast body of data is unnecessary in this paper. The nature of the problem and its solution are considered understandable in terms of the one example given.

In addition to fulfilling the explicit objective of the program, i.e., determination of loading for use by ship designers, the results can also be used to provide a better understanding of the actual physical phenomena involved in the complex interaction of shock waves with solid bodies.

Table 1

SIZE AND SCALING DATA

Model Type	Over-all Length of Full Scale Vessel, ft.	Scaling Factor for Shock Tube Model
Destroyer	512	146
Aircraft Carrier	1036	306
Transport	560	168

Table 2

DISTRIBUTION OF GAGE LOCATIONS ON MODELS

Model	Portion of Model	Number of Gage Positions
Transport	Hull	8
	Deck	2
	Main Deck House	6
Destroyer	Hull	3
	Deck	1
	Deck Structures	16
Aircraft Carrier	Hull	13
	Sponsons	7
	Deck	3
	Deck Edge Elevation	4
	Island Structure	8



Fig. 1 TRANSPORT MODEL

STANBOARD GAGES ARE LOCATED DIRECTLY OPPOSITE PORT GAGES
AND ARE NUMBERED THE SAME AS CORRESPONDING GAGES ON THE PORT SIDE.



Fig. 2 DESTROYER MODEL IN SHOCK TUBE SHOWING
PORT SIDE GAGE LOCATIONS

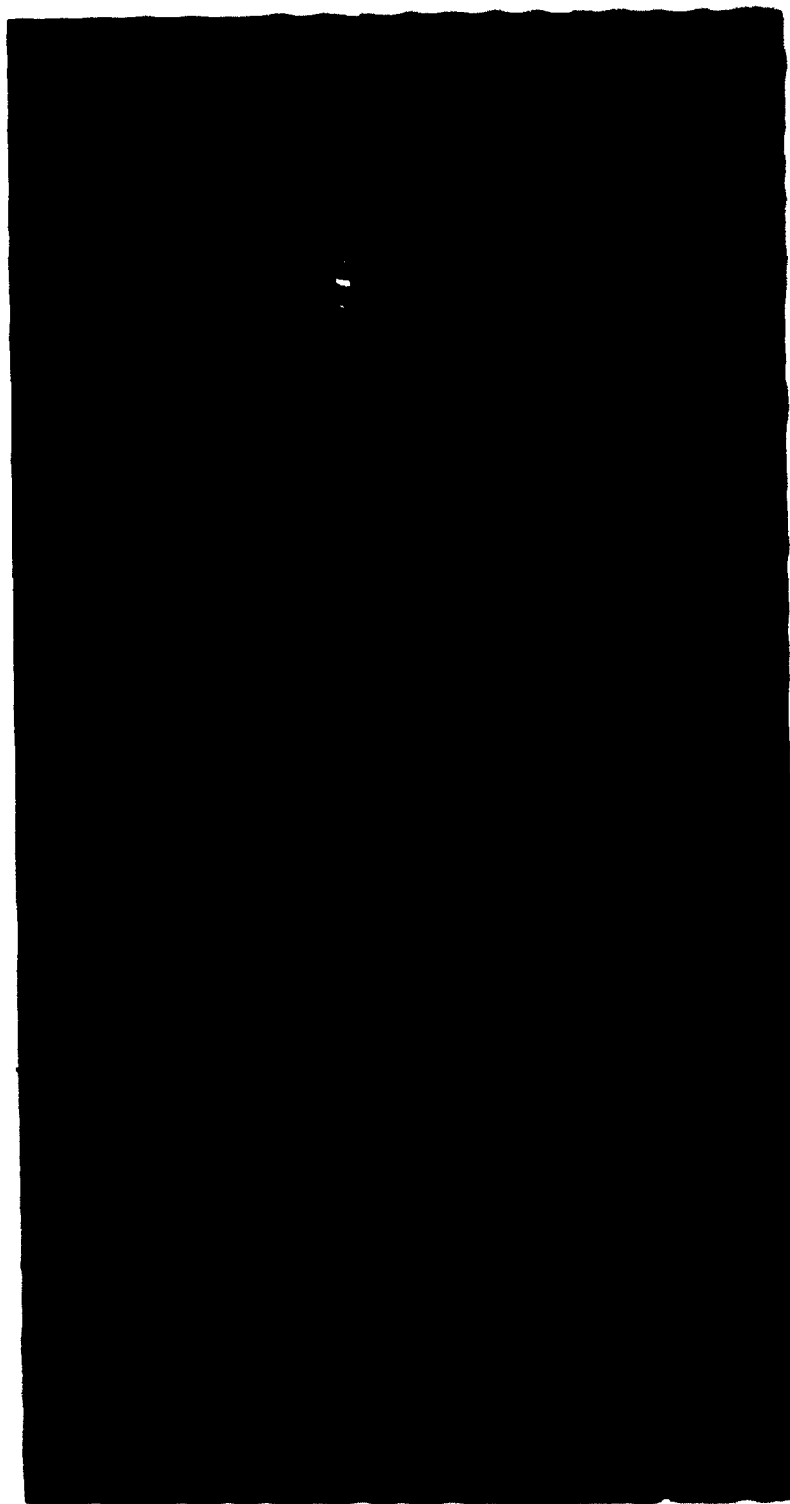


FIG. 3 TOP VIEW OF AIRCRAFT CARRIER MODEL



FIG. 4 SIDE VIEW OF AIRCRAFT CARRIER MODEL

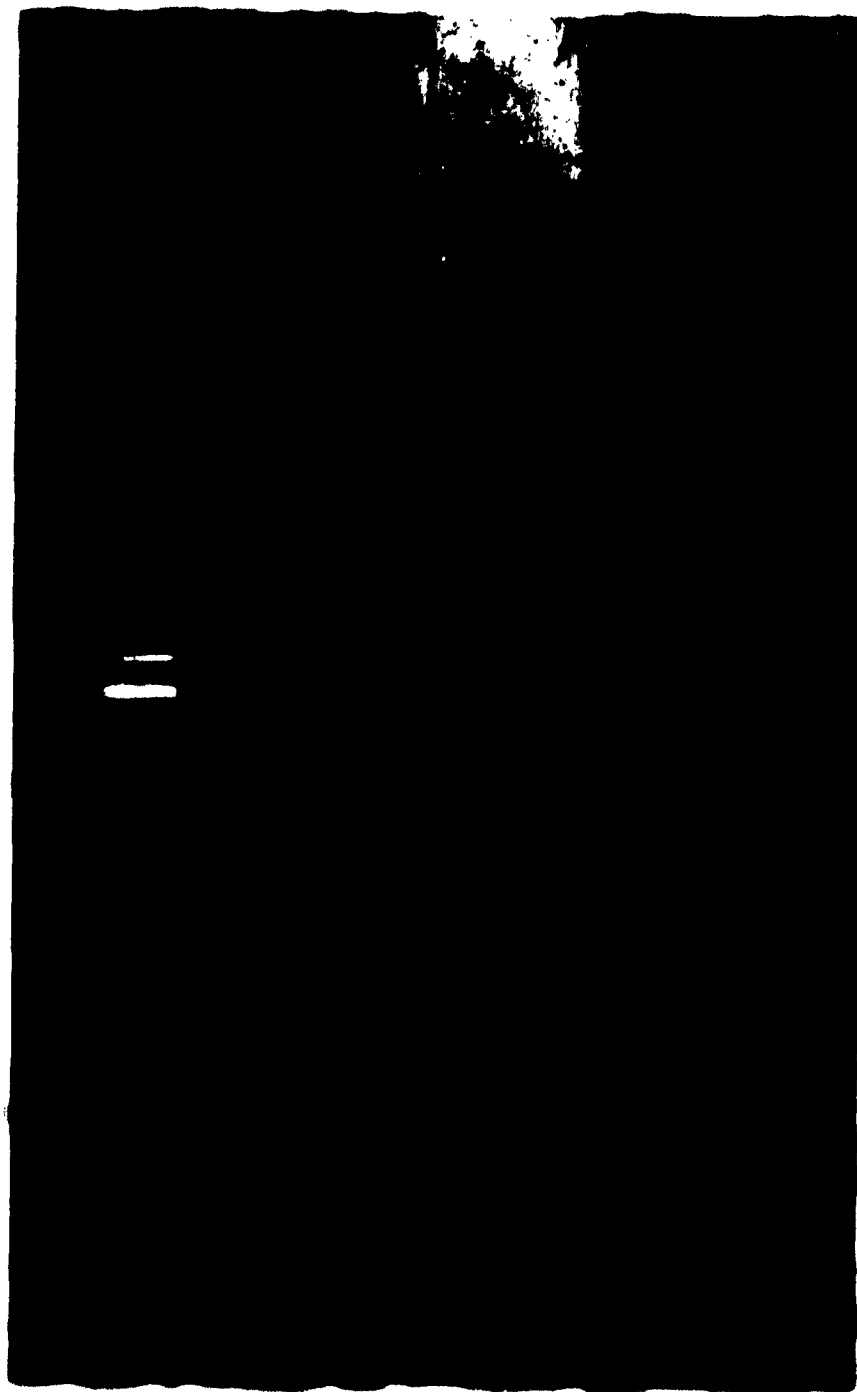


Fig. 5 CLOSE-UP VIEW OF AIRCRAFT CARRIER MODEL AT MIDSHIP

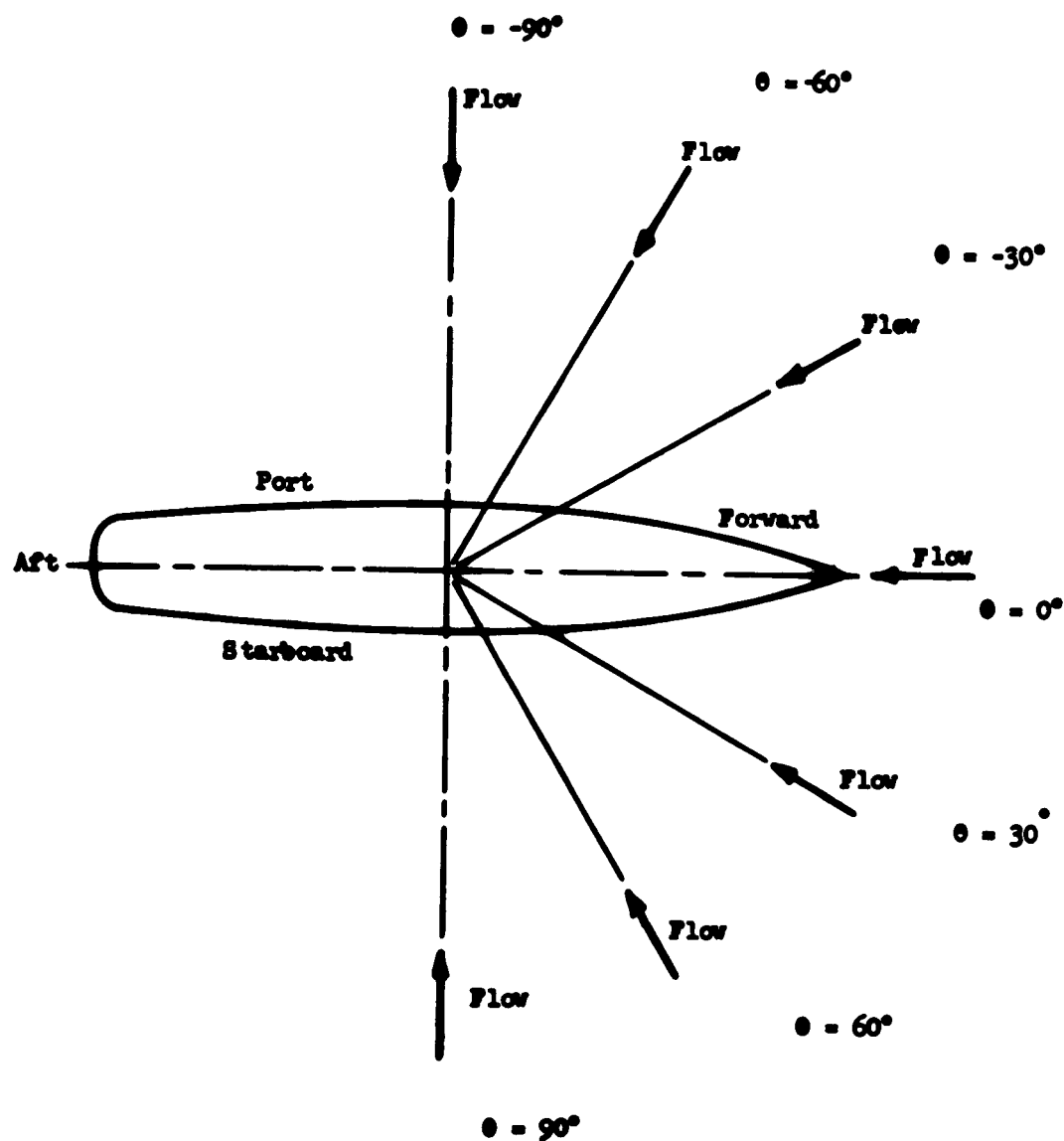


Fig. 6 DEFINITION OF ANGLE OF INCIDENCE OF FLOW DIRECTION TO MODEL SURF FOR THIS PROGRAM

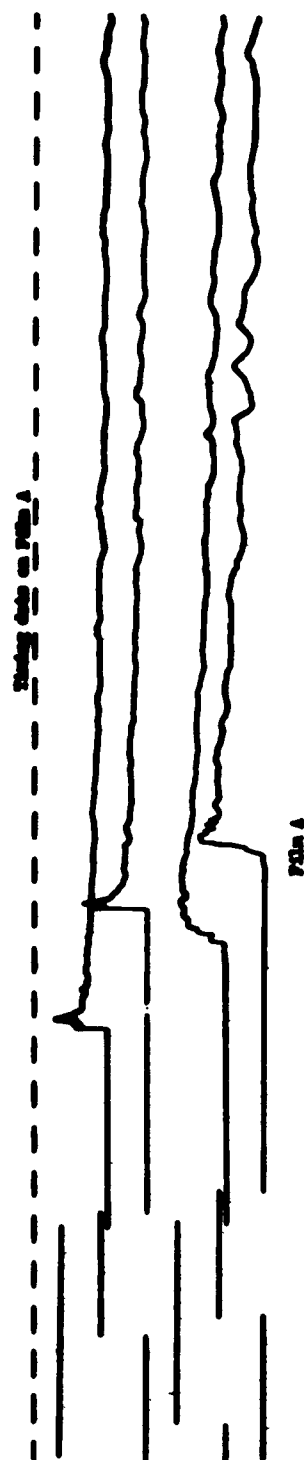
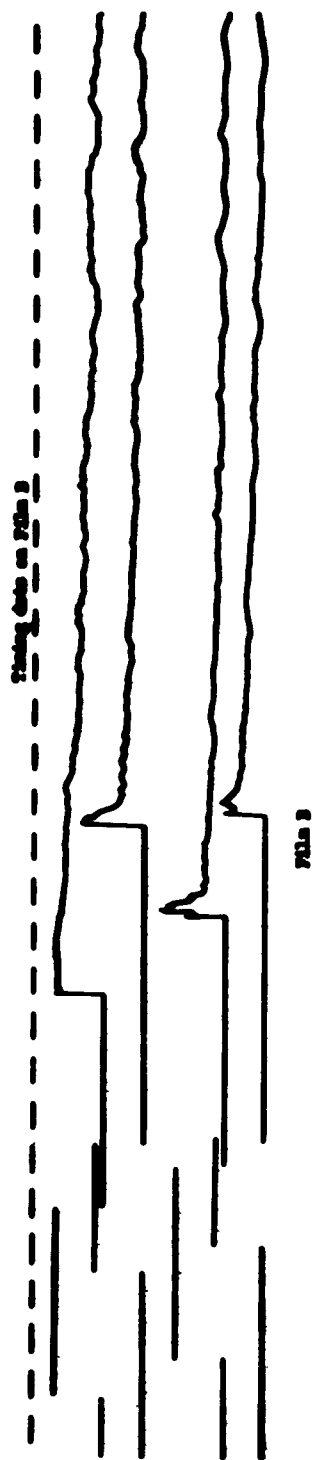
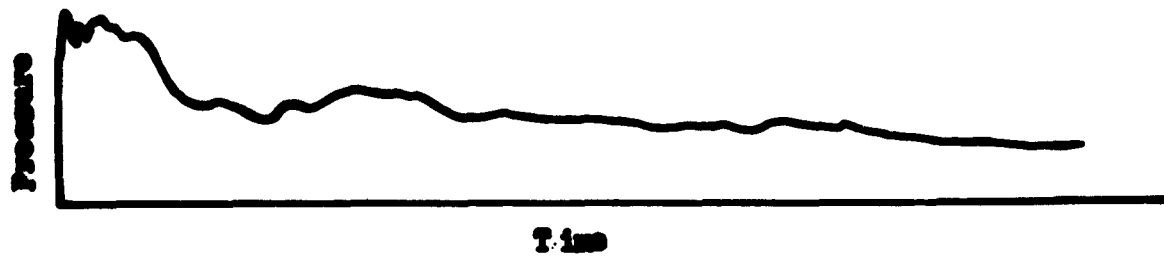
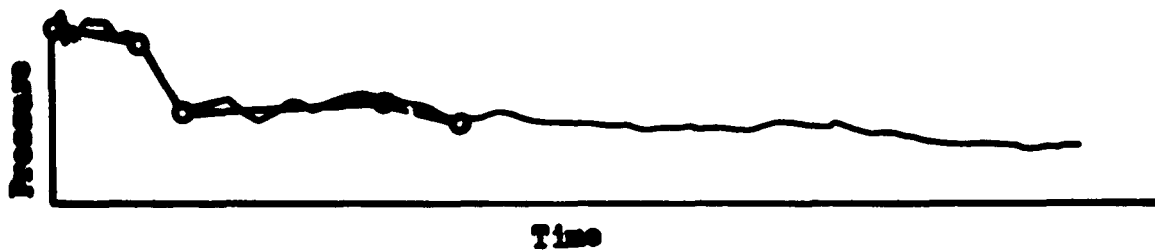


Fig. 7 **SEVEN SEPARATE FILM STRIPS**



Unlinearised Plot



Linearised Plot

Fig. 8 EXAMPLE OF LINEARIZATION OF TRACES

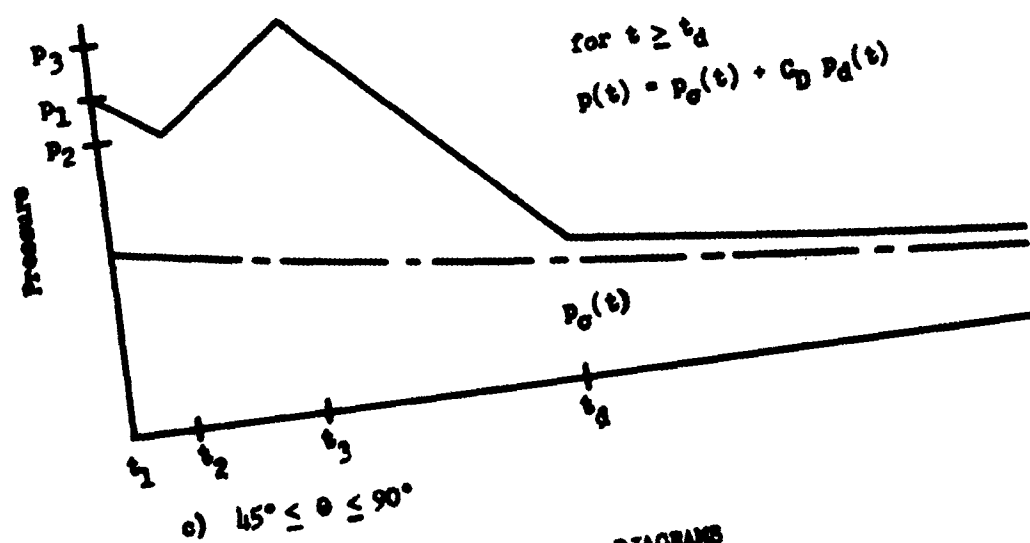
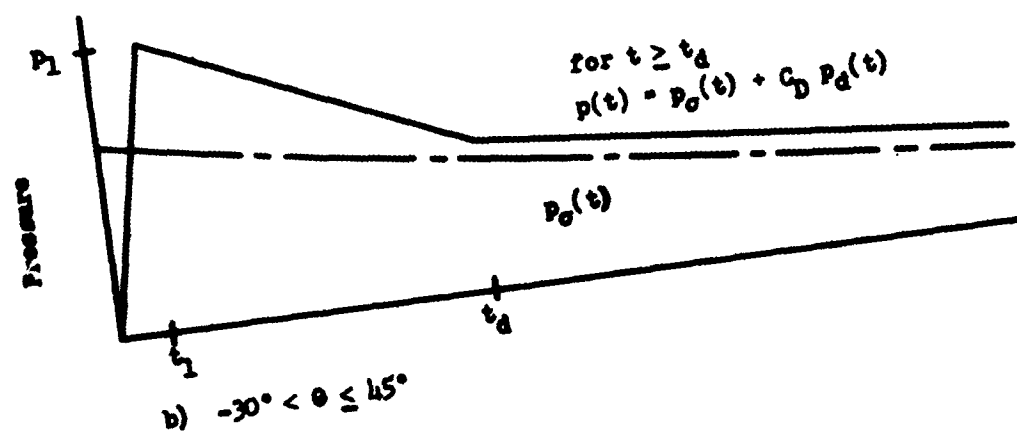
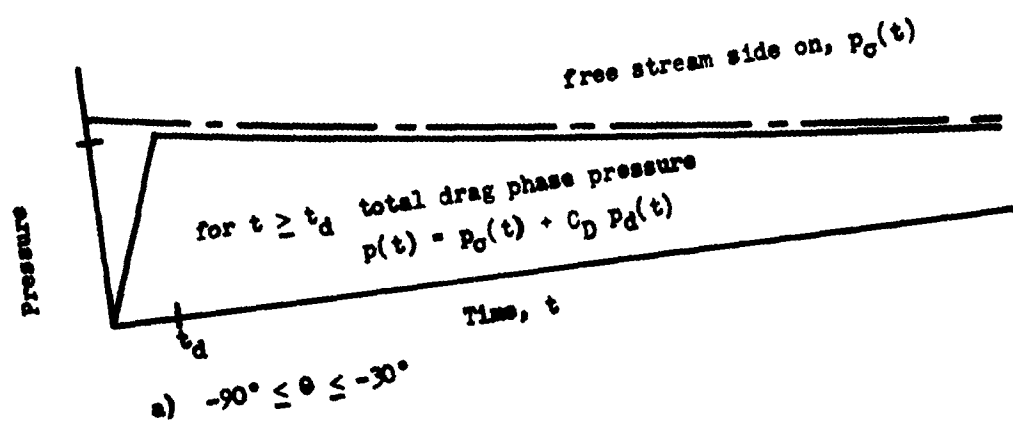


Fig. 9 SCHEMATIC LOADING DIAGRAMS

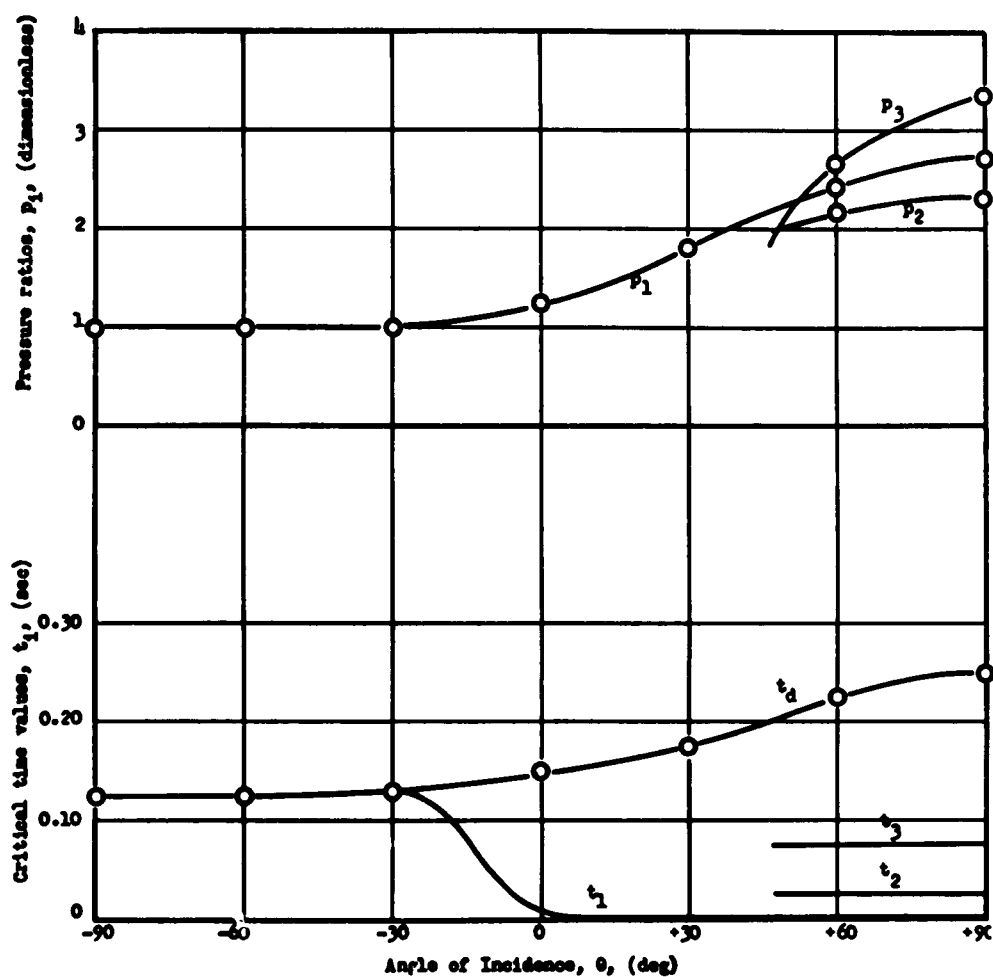


Fig. 10 TYPICAL CURVES FOR PRESSURE RATIO AND CRITICAL TIME VALUES

A PRELIMINARY SYSTEM FOR PRODUCTION OF
HIGH ENERGY PURE GAS FOR HYPERSONIC TESTING

J. E. Minardi
C. E. Pax
University of Dayton Research Institute

There exist many systems for simulating aerodynamic problems in the laboratory. A common requirement of these systems is a considerable amount of high energy pure gas. The high temperatures and pressures required to drive test systems at increasingly higher gas velocities for reasonably long durations of time, give rise to considerable difficulty in the construction of such systems. A common approach to this problem is to store a reasonably cool, high pressure gas and as it expands into a test section, energy is rapidly added to the gas. Common examples of this technique are the hot-shot tunnels and other arc-jet facilities. One notes, however, that for many tests the impurities introduced by these methods are undesirable. Another approach to this problem is the use of high pressure driver gas to compress and heat a lower pressure charge gas which is then used as the test gas. A typical system of this type is a shock tunnel. The charge gas is not contaminated in this system as it is compressed and heated by the primary and reflected shock waves. This charge gas is then at a pressure corresponding to pressure behind the reflected shock, which is considerably below the driver pressure. If then a final isentropic compression to driver pressure could be achieved, the performance of this system could be considerably improved. Of course, this final isentropic compression is not realized in a shock tube or shock tunnel since the broadened interface would permit mixing with the cold driver gas.

A method which might permit this final compression while retarding mixing and keeping heat losses low was conceived at the Aeronautical Research Laboratory at Wright-Patterson Field. A preliminary system of this type is being investigated at the University of Dayton. A layout of this system is shown in Figure 1. The three bottles shown store the

driver gas at pressures up to 200 atmospheres and join to drive a shock tube 4.9 inches internal diameter and 27 feet long. A compression chamber is shown at the end of the shock tube and in Figure 2. The orifice plate between the shock tube and the compression chamber reflects the primary shock wave at nearly the strength associated with reflection from a closed end tube. The ratio of tube area to orifice area is approximately 24. The reflected wave then heats the charge gas in the shock tube and the final phase of the compression will occur as the gases enter the compression chambers. As the charge gas enters the orifice it flows through the radial nozzle to the periphery of the main compression chamber. At this location guide vanes impart a swirl to the entering gas. The centrifugal force associated with this swirling motion tends to retard the mixing of the entering gas with gas already in the compression chambers. The ideal interface remains in the shock tube even after final compression. However, broadening of this interface may permit some portion to enter the compression chambers. Mixing of this portion of the driver gas with the charge gas is retarded by the swirl imparted to the gas as it enters. A second chamber is also shown which is separated from the main chamber by a second orifice plate which also retards mixing. In an operational system the second compression chamber would possibly be replaced by an expansion nozzle into a test facility. The electrical heating elements which form the walls of the compression chamber serve to reduce heat losses from the chambers by furnishing a hot inner surface and also serve to preheat the gas in the compression chambers. Heat losses are also reduced by the small surface area to volume ratio of the chambers. The thermal insulation separates the structural members of the chambers from the heating elements. Inserts shown in the compression chambers permit variation of the volume of these chambers. The piston shown near the inlet orifice is used in a different configuration to initiate flow. In the system described herein this piston is inoperative and retracted so that its face is flush with the plate shown. Another inlet configuration which would reduce heat losses from the entering gas would have an annular inlet at the swirl vanes rather than the central orifice and radial nozzle.

A double diaphragm section is used in the shock tube as shown in Figure 3. Clamping force is obtained by means of driver pressure acting on an angular piston. Unscored annealed aluminum diaphragms have been used.

Ideal performance of a system of this type is included on Figure 4. The initial conditions assumed for the real gas curves were air at 300 degrees Kelvin and atmospheric pressure. These curves are for air and were developed assuming no heat losses. (Reference 1)

The shock Mach number (M_s) is that of the primary shock wave and the ratios of driver pressure to initial charge pressure shown are those which produce the indicated shock Mach Number in an unheated air to air shock tube. The temperature ratios (based on initial charge temperature) obtained after the primary and reflected shock waves are T_{1s} and T_{2s} , respectively. The final temperature ratio (T_f) which could be achieved by isentropic compression from conditions after the reflected shock to driver pressure is also shown for a perfect gas with $\gamma = 1.4$ and air (real gas) at the previously stated initial conditions. The temperature ratios for an isentropic compression of air from the same initial conditions to driver pressure is also shown for comparison.

The heat losses from the high velocity hot gas in the shock tube can be estimated by using the analogy with flow by a flat plate. For laminar flow heat transfer per unit area and time is

$$q = B_L t^{-0.5}$$

where B_L is a boundary layer function which depends on initial conditions, and t is time since primary shock arrival at the station. From Reference 2

$$B_L = (T_r - T_w) \left\{ \frac{1}{\pi} (K \rho c_p)_{wg} \left[1 - (\sqrt{2} - 1) \frac{u}{u_s} \right] \right\}^{0.5}$$

T_r = recovery temperature

T_w = wall temperature

$(K \rho c_p)_{wg}$ = conductivity, density, and constant pressure specific heat of the gas at the wall surface temperature and local pressure

u = particle velocity induced by primary shock wave

u_s = primary shock velocity

By replacing the time after shock passage, t , by $\tau - x/u_s$ where τ is time after diaphragm rupture one obtains the total heat loss from the shock heated gas until passage of the reflected shock as

$$Q_L = \int_0^s \int_{\frac{x}{u_s}}^{\frac{x}{u}} \pi DB_L \left(\tau - \frac{x}{u_s} \right)^{-0.5} d\tau dx + \int_s^l \int_{\frac{x}{u_s}}^{\frac{l}{u_s} + \frac{l-x}{u_{sr}}} \pi DB_L \left(\tau - \frac{x}{u_s} \right)^{-0.5} d\tau dx.$$

The two integrals account for heat losses at a station until arrival of the interface and until arrival of the reflected shock respectively.

s = position of collision of reflected shock and interface
 $= l(1 - \rho_{1c}/\rho_{2s})$

D = tube diameter

u_{sr} = reflected shock velocity

The total heat loss during shock heating for laminar boundary layers is then

$$Q_L = \frac{4}{3} \frac{\pi DB_L}{\sqrt{u_s}} s^{3/2} \left[\sqrt{\frac{u_s}{u} - 1} + \sqrt{1 + \frac{u_s}{u_{sr}}} \left(\frac{l}{s} - 1 \right)^{3/2} \right].$$

For turbulent boundary layers $q = B_T t^{-0.2}$ where B_T is again dependent only on initial conditions and is given by

$$B_T = .0296 (T_r - T_w) \left(\frac{\mu}{\mu} \right)^{0.2} \left(\frac{T}{T} \right)^{0.8} \left(\frac{c_p}{c_p} \right) \frac{\rho c_p u}{P_r^{2/3}} \left(\frac{\mu}{\rho u u_s} \right)^{0.2} .$$

\bar{T} = mean temperature between wall and stream

μ = coefficient of viscosity

P_r = Prandtl number

Heat losses which occur after the reflected shock passage and during final compression to driver pressure can be accounted for by using a suitable polytropic exponent, n , in the equation $T_f/T_{2s} = (P_f/P_{2s})^{n-1/n}$ where subscripts, f and $2s$ refer to final conditions and conditions after the reflected shock with heat losses.

Construction of this system has recently been completed and shake down operations have been performed. However, not a sufficient amount of reliable test data have been obtained to permit performance evaluation at this time.

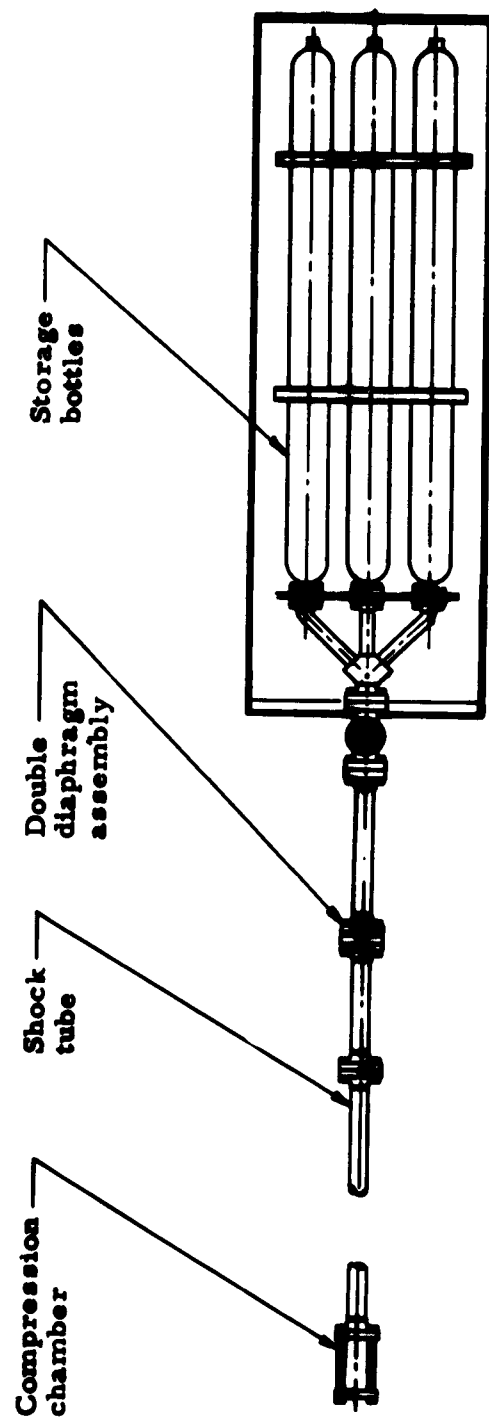


Figure 1. Layout of 200 Atmosphere System

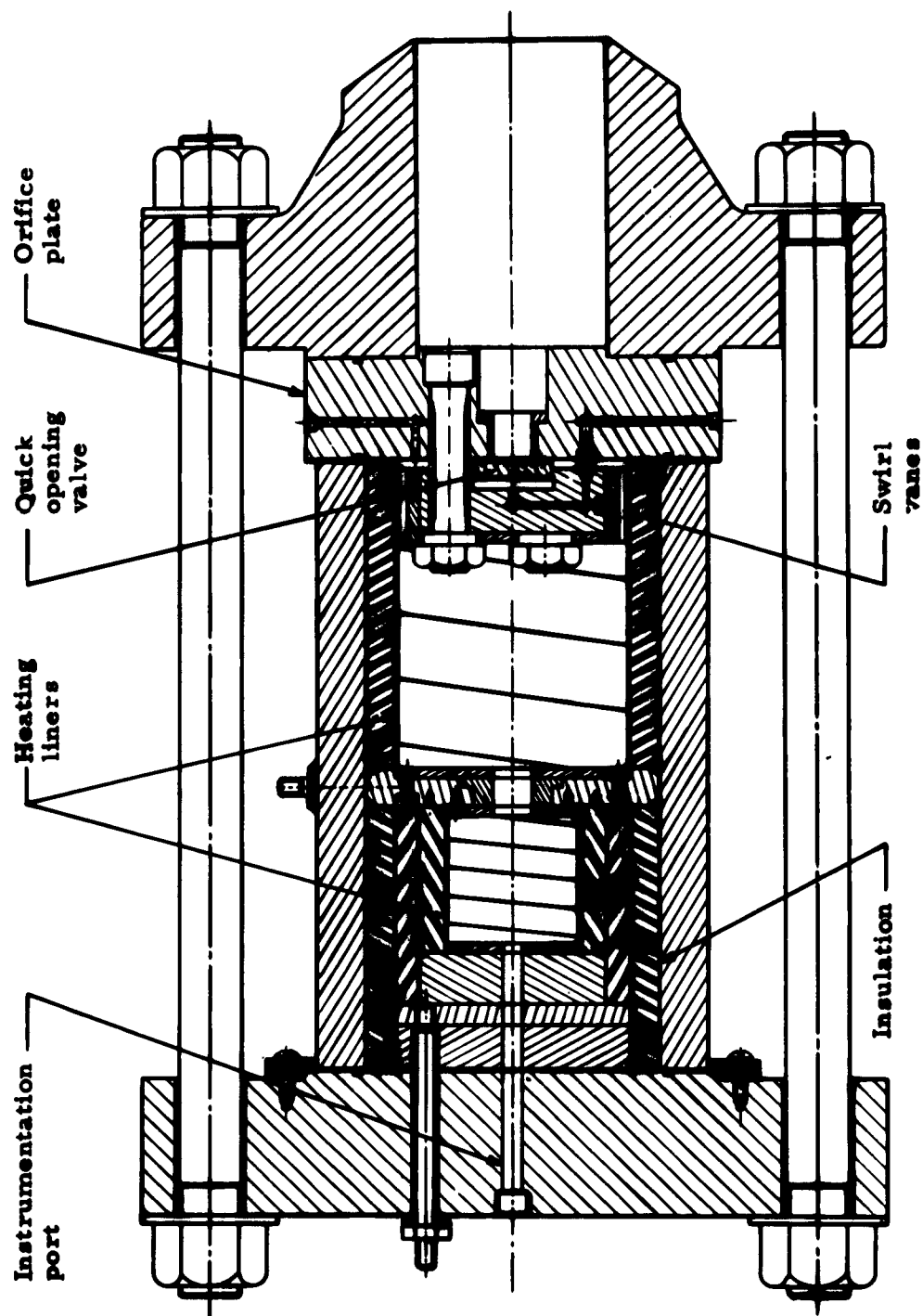


Figure 2. Compression Chamber

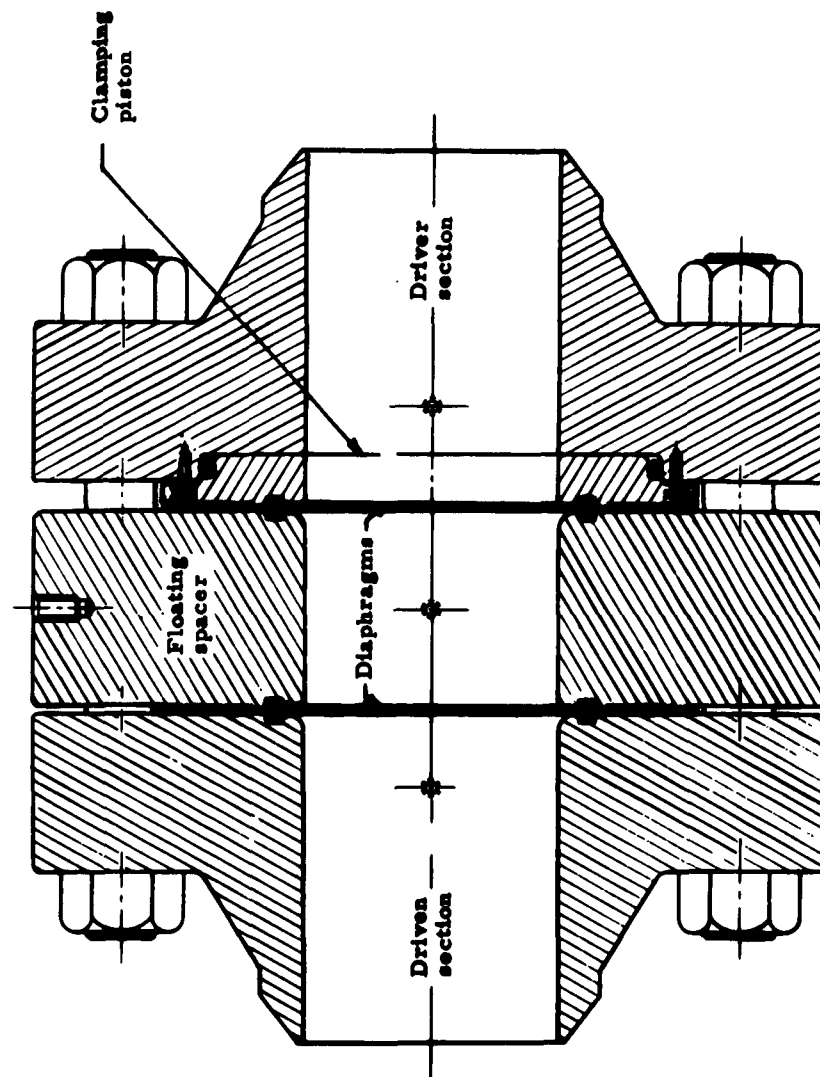


Figure 3. Double Diaphragm Assembly

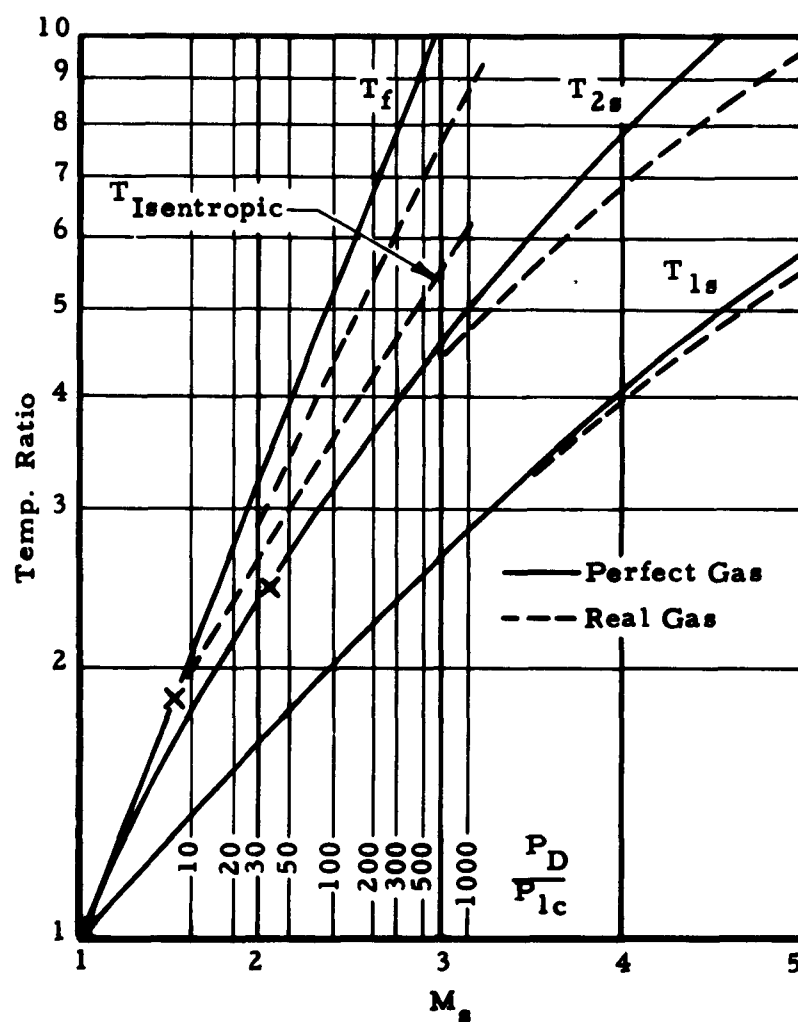


Figure 4. Theoretical Temperature Ratio Without Heat Losses

REFERENCES

1. Minardi, John E., Pax, Charles E. and Wright, Harold E.
Pressure Energy Exchange Principle. ARL TN April 1961.
2. Weatherston, R. C., Russo, A. L., Smith, W. E. and Marrone, P. V.
Gasdynamics of a Wave Superheater Facility for Hypersonic Research
and Development. AD 210 223 February 1959.

STUDY OF GAS IONIZING SHOCKS BY STREAK SCHLIEREN METHODS

G. D. Kahl
D. B. Sleator
Ballistic Research Laboratories

I. INTRODUCTION

In recent years the ionized plasma has received considerable attention from investigators interested in magnetohydrodynamics, thermonuclear processes, and high speed aerodynamics. The shock tube offers a convenient laboratory method for producing highly ionized plasmas, and magnetically driven shock tubes have been developed which are capable of producing Mach ≈ 100 shocks in low pressure gases. ^{1, 2/} The conventional pneumatically driven diaphragm-type shock tube has been abandoned in the attempt to attain these very high speed shocks, since it has an upper limit on the shock Mach number, even when the pressure ratio becomes very large. Researchers have found it easier to dispense with the diaphragm and to heat and accelerate a portion of the test gas as the driver by means of electric currents and associated magnetic fields. Such shocks usually show fairly strong attenuation, not only because of the method of driving, but also because of the energy losses due to radiation.

A new set of complications are encountered in the shock processes as the Mach number increases. In the diatomic gas, vibrational excitation, dissociation, and ionization occurs, each with its own relaxation time, and a non-equilibrium flow regime exists for some distance behind the shock.

Many techniques have been employed to examine these fast shocks, including spectroscopy, microwaves, and interferometry. However, for visualizing the flow over a finite distance the ordinary streak camera is convenient, and has been used extensively; an image of a slit window along the shock tube is swept transversely by a rotating mirror, and the self luminous ionized gas front is displayed on the film in a time-distance diagram. For the very fast shocks the luminous front is

essentially coincident with the shock; shocks preceding the luminous front by a significant distance can be located by reflecting a portion of the shock from an obstacle, thereby quickly rendering it self-luminous before the main luminous front arrives.

For flows with significant spacing between the shock and self luminous front, the addition of a fairly simple back-lighted schlieren optical system to the streak camera can, under certain conditions, locate the shock without mechanically disturbing the flow, and at the same time give a reasonable detailed picture of the flow processes.

It is the purpose of this paper to demonstrate the application of the streak schlieren method to shock-ionized argon flows produced in a small electric shock tube. Previous studies of argon shocks up to Mach 19.5 have been carried out in detail by Petschek and Byron ^{3/} and interferometrically by Alpher and White ^{4/}; thus the schlieren results can be compared to an accepted model of the ionizing shock, at least up to Mach 19.5.

II. THE SHOCK TUBE

The shock tube used in the experiments is similar to one described previously by Blackman and Niblett ^{5/}; this one is a 1" diameter pyrex tube with a vacuum pump connection at one end, and an inlet bleeder valve at the other. The shock is energized by a strap conductor, 1/4" wide, wrapped around the tube, carrying a discharge current from a .6 microfarad condenser. The electric field induced inside the tube must be sufficiently strong to cause electrical breakdown in the gas. Then currents are induced inside the tube, heating and compressing the gas in the vicinity of the external loop. Figure (1) shows the doughnut shape of glow produced when just enough voltage is used to ignite the tube. At higher condenser voltages, shocks proceed down the tube in both directions from the loop; a time exposed photograph for 30 KV on the condenser is shown in Figure (2). For most of the tests, a two turn loop was used, with 50 K.V. initial condenser voltage, and a lucite

reflector was positioned in the tube beneath the discharge coil to confine the shock to one direction. The results of shock velocity measurements 18 cm. from the coil as a function of initial tube pressure are shown in Figure 3. It was found that the velocities decreased by 20% while traversing the distance from 10 to 20 cm from the discharge loop. The velocities are seen to increase rapidly as the initial pressure is decreased.

III THE SCHLIEREN OPTICS

The optical system is illustrated in Figure (4). The backlighting source is an exploding wire (behind a slit) which is triggered on signal; this source is very bright for about 20 μ sec and maintains a lower but nevertheless usable intensity for about 80 μ sec. Both wire and slit are perpendicular to the shock tube axis; the slit width is usually set between 1/16 and 1/8 inches. A 10 inch diameter, 50 inch focal length lens is positioned next to the shock tube about 90" from the backlighting source; a .025" width slit positioned at the shock tube wall eliminates all of the backlighting rays except those which pass near the center of the shock tube. These rays converge to focus a real image of the backlighting source 100 inches from the shock tube, where a schlieren knife edge may be positioned. The backlighting rays continue through the real image and a second lens and reflect from a rotating mirror onto the film. The second lens (focal length 70 cm, and 2 inches in diameter) focusses a real image of the shock tube slit on the film; the shock tube image is demagnified by 2.5.

Each face of the 4 sided stainless steel rotating mirror is 2 inches square, and the lever arm from mirror to film is 34 1/2 inches. The mirror speed is 12,000 r.p.m., which gives a sweep rate of about 4 μ sec/cm. on the film. A small light beam (not shown), reflected into a photocell from a back face of the mirror serves to monitor the mirror speed and to trigger the shock tube and exploding wire source through appropriate delays when the mirror presents its largest aperture to the optical system.

The position of the knife edge at the real image of the backlighting source determines the pattern of backlighting on the film. If the knife edge be adjusted parallel to the backlighting slit image and cutting it off slightly, then an optical disturbance in the shock tube which deviates the light rays toward the knife edge results in some of these deviated rays being cut off; the backlighting intensity on the film is reduced at that part of the shock tube image where the disturbance is located. This schlieren principle has been used for many years in the Foucault test of optical elements. In the present application the optical element is the shock tube slit, whose image is moving transverse to its length; if the disturbance is a front moving along the slit, then a time-distance diagram of the front is displayed on the film. The streak schlieren method is not novel, and has been previously applied by others in examining non-luminous flows.

If the optical disturbance is a front across which the refractive index changes suddenly, and if the backlighting rays are incident on the front at nearly grazing angle, the deviation of the rays is ϵ , where,

$$\epsilon \simeq \sqrt{\frac{2(\Delta n)}{n}} \quad (1)$$

with n the refractive index and Δn the change across the front; the deviation is toward the region of larger index, and is independent of the thickness of the shock tube.

The aperture at the knife edge can be further masked to reduce the amount of light from the self luminous gas which reaches the film, without cutting down on the backlighting. This masking can be done until diffraction effects make image useless, or until the aperture restricts the backlighting.

IV. SCHLIEREN PICTURES

Figure 5 is a streak picture with no backlighting or aperture restrictions (except the lens) of a Mach 20-22 test in argon at 1.3 mm Hg pressure. The luminous front appears fairly sharp, and no shock is visible. Figure 6 is a slightly magnified picture under similar conditions with backlighting and the knife edge adjusted to cut off rays deviated by the shock. The self-luminosity has been reduced by the knife edge, as a comparison of the region where the backlighting was suppressed (the light horizontal streak) with Figure 5 indicates; the luminous front is fuzzier. Figure 7, at 3 mm argon pressure, (Mach 12-1/2 to 14-1/2) shows the shock and luminous region more clearly. The luminosity does not last very long in this obviously time dependent flow. There are several faint streaks apparent in the space between the shock and the main luminosity.

The knife edge can be adjusted to cut off most of the backlighting and still pass rays deviated by the shock. Then the shock streak should be darker than the background, and the self-luminosity relatively unaffected. One such example is Figure (8), where part of the back side of the shock tube was masked from the back lighting, so that the self-luminous region could be observed with no background. The conditions for this test were 1.9 mm Hg pressure, Mach \approx 20. It is notable that the region between the shock and luminosity is lighter than the background, and is lightest just in front of the luminous region. This effect is to be expected if the flow region contains an increasing concentration of free electrons as the luminous front is approached.

As ionization occurs, the free electrons begin to contribute strongly to the refractivity. The atom refractivity for argon is positive and almost independent of wavelength in the visible region; it is given by

$$(\underline{n}-1)_A = 1.07 \times 10^{-23} N_A \quad (2)$$

DISCLAIMER NOTICE

**THIS DOCUMENT IS BEST QUALITY
PRACTICABLE. THE COPY FURNISHED
TO DTIC CONTAINED A SIGNIFICANT
NUMBER OF PAGES WHICH DO NOT
REPRODUCE LEGIBLY.**